AN ABSTRACT OF THE THESIS OF

Sara E. Harris for the degree of Doctor of Philosophy in Oceanography presented on May 29, 1998. Title: The Atlantic, the Amazon, and the Andes. Neogene Climate and Tectonics Viewed from Ceara Rise, Western Tropical Atlantic.

Redacted for privacy

Abstract approved: ______________________

Alan C. Mix

High resolution proxy estimates of western tropical Atlantic sediment composition are used to determine the links between tropical climate and global climate forcing mechanisms since the middle Miocene at time scales ranging from millions to tens of thousands of years. Evaluation of relative carbonate mass accumulation rates at deep compared to shallow Ceara Rise drill sites allows estimates of late Pleistocene dissolution patterns driven by deep-ocean circulation. Compared to northern-hemisphere ice volume, North Atlantic Deep Water (NADW) responds rapidly to high northern latitude insolation forcing, intensifying during periods of ice melt and weakening during ice growth. This early deep water response may provide a link between hemispheres to translate northern-hemisphere forcing to the southern ocean. Tropical South American continental climate also responds rapidly to insolation forcing, leading ice volume changes. Precipitation cycles in the Amazon Basin, estimated from the balance of hematite and goethite in Ceara Rise sediments, appear to be driven by high-latitude summer insolation in the northern hemisphere, with wet conditions during high insolation at both tilt and precession frequencies. Low-latitude climate may respond non-linearly to precession forcing, producing significant variance in both the 1/100 ky^{-1} and 1/413 ky^{-1} eccentricity bands, a response not present in ice volume. Early phases in

Amazon precipitation, relative to $\delta^{18}O$, indicate that low-latitude climate may partly drive slow-responding high-latitude climates dominated by ice in the Pleistocene. A similar phase relationship between Amazon precipitation cycles and insolation forcing at orbital frequencies extends to the middle Miocene, overprinted on the signal of slow tectonic development of the present day Amazon drainage. Two events of rapid change, near 8 and 4.5 Ma, which initiated major erosion of terrigenous material to the Atlantic, likely were triggered by tectonic events in the eastern Andes. During the second of these events (~4.5 Ma, a globally warm interval), Amazon precipitation cycles briefly responded to local low latitude southern hemisphere summer insolation, perhaps aided by the recent development of tectonic-driven high topography. Throughout the development of the Amazon drainage basin, external insolation forcing drives orbital scale tropical climate cycles and ocean circulation, which may ultimately influence Pleistocene glaciation cycles.

The Atlantic, the Amazon, and the Andes. Neogene Climate and Tectonics Viewed from Ceara Rise, Western Tropical Atlantic.

by

Sara E. Harris

A THESIS

submitted to

Oregon State University

in partial fulfillment of
the requirements for the
degree of

Doctor of Philosophy

Completed May 29, 1998
Commencement June 1999

Doctor of Philosophy thesis of Sara E. Harris presented on May 29, 1998

APPROVED:

Redacted for privacy

Major Professor, representing Oceanography

Redacted for privacy

Dean of the College of Oceanic and Atmospheric Sciences

Redacted for privacy

Dean of Graduate School

I understand that my thesis will become part of the permanent collection of Oregon State University libraries. My signature below authorizes release of my thesis to any reader upon request.

Redacted for privacy

Sara E. Harris, Author

ACKNOWLEDGMENTS

Alan Mix, my major advisor, has provided unflagging scientific, editorial, and financial support throughout this process. Nick Pisias has been a source of inspiration, advice, and much computer assistance. I am grateful to both Alan and Nick for their flexibility and for directing me toward numerous and various research and teaching opportunities. Committee members Bob Duncan and John Baham have provided advice and encouragement. Thanks to Bill Liss and Larry Flick for alternating serving on my committee as graduate school representative, and to Dave Christie for filling in at the last minute. Gary Klinkhammer, Jack Dymond, and Jim McManus answered many questions about sediment geochemistry. Thanks to Reed Glasman for XRD advice and the use of his lab. Michael Weber gave advice on bulk density iterative calculations, orbital solutions, and signal correlation. Many thanks are due Suzanne O'Connell from Wesleyan University, who first introduced me to paleoceanography and deep sea drilling and encouraged me to pursue this subject in graduate school, and to Tim Herbert from Brown University, who guided me through my first research project and introduced me to UNIX and time series analysis.

Many people at COAS have helped me along the way. Bill Rugh saved the day numerous times with the OSU-SCAT. Andy Ungerer, Bobbi Conard and Chi Meredith were wonderful sources of laboratory help. Ann Morey, June Wilson, and Mysti Weber were always available for advice, or assistance with teaching, or anything. Lori provided much assistance with carbonate analyses. Thanks to the computer guys, especially Tom. Sue Pullen helped me in uncountable ways, as did both Irma Delson and Robin Hlobeczy. All the students who have passed through the paleo group in the last six years have made this experience memorable; thanks to my fellow students Terri King, Leigh Welling, Joe Ortiz, Jim Watkins, Ann Sabin, Carolyn Viscosi Shirley, Dave Lund, and Melissa Feldberg. Special thanks to Terri for being an intensive mentor both in

computing and grad school in general. The shipboard scientific party of ODP Leg 154 was a marvelous group of people. Thanks to Bill Curry and Nick Shackleton for support and encouragement, and to my fellow sedimentologists, Dave and Ralf (The A Team), and Graham (spiritually on the A Team).

I thank Aletha, for finally moving to Oregon (just as I am leaving!), Joanie and Glynnis, for reminding me that art and literature should not be forgotten, Jen and Jan for making AGU in San Fransisco always fun, Robin, for the hundreds of miles of swimming, the Thousand Oaks house for all the good food and talk, my parents and sisters, for their constant support, diversions, and political and gardening inspirations, and Jim for all the food, fun, and forays.

CONTRIBUTION OF AUTHORS

Alan Mix provided scientific inspiration, interpretation and editorial advice on all chapters. Joe Ortiz did much work defining a "standard" processing procedure for reflectance spectroscopy data (Chapter 2). Terri King aided in the application of non-intrusive proxies and provided editorial comments (Chapter 3). Nick Pisias provided directional guidance, interpretation, and statistical and editorial advice (Chapter 5, and others).

TABLE OF CONTENTS

TABLE OF CONTENTS, Continued

TABLE OF CONTENTS, Continued

LIST OF FIGURES

LIST OF FIGURES, Continued

LIST OF FIGURES, Continued

Figure Page

LIST OF TABLES

LIST OF APPENDICES

LIST OF APPENDIX FIGURES

The Atlantic, the Amazon, and the Andes. Neogene Climate and Tectonics Viewed from Ceara Rise, Western Tropical Atlantic

1.

Introduction

Ceara Rise, an aseismic ridge in the western tropical Atlantic Ocean, is ideally situated for paleoceanographic and paleoclimatic studies of the Atlantic and South America. Located southeast of the Amazon Fan, beneath a relatively low productivity region of the tropical Atlantic, the Rise receives sediments from two primary sources: (1) biogenic calcium carbonate from overlying surface waters and (2) terrigenous sediment from South America, today dominated by Amazon River sediments. During Ocean Drilling Program (ODP) Leg 154 in 1994, five sites were drilled in a depth transect on Ceara Rise. Three to five overlapping holes were drilled at each site and complete recovery of the sedimentary section was documented (Curry et al., 1995). This approach provided exceptionally long and complete records of sedimentary variability over the past 55 million years. Sedimentation rates are high enough to resolve orbital scale variability over most of the record, providing a unique opportunity to study climate change on time scales ranging from millions of years to tens of thousands of years.

Based on sedimentary records from Ceara Rise, the goals of this thesis are (1) to test the hypothesis that during the late Pleistocene, the deep Atlantic Ocean provided a link between the northern and southern hemispheres, causing early climate responses in the southern ocean, (2) to define the role of South American tropical climate within the late Pleistocene global climate system, assessing whether the tropics responded to Northern Hemisphere ice volume changes or more directly to external insolation forcing, (3) to determine the driving forces of Amazon and proto-Amazon Basin climate since the middle

Miocene; has this region responded to a constant forcing since 13.2 Ma?, and (4) to evaluate the connection between Andean tectonics and the development of the Amazon River drainage to the Atlantic considering whether tectonic uplift influences the Amazon Basin climate system, and assessing the timing of erosional events.

According to the orbital theory of Pleistocene climate, Earth's climate system responds to cyclic changes in the amount and distribution of solar energy received by the Earth as a function of time and latitude (e.g. Hays et al., 1976). During the late Pleistocene, the major manifestation of global climate cycles is the growth and decay of massive northern hemisphere continental ice sheets, which vary at the same frequencies as external insolation forcing. Within the framework of an insolation-driven climate system, we seek to understand the relationships between different climate components internal to Earth's system, both during the Plio-Pleistocene and older time periods.

The length and resolution of the sedimentary sections recovered at Ceara Rise are ideal for the application of non-intrusive proxy approaches to paleoceanographic questions. These methods are rapid, automated, and therefore can be made at high resolution over long sections of core. Reflectance spectra measured from the surfaces of wet split cores and magnetic susceptibility measured on whole rounds are the two non-intrusive proxies used to estimate sedimentary components in order to address the above goals. Chapter 2 documents procedures for processing reflectance spectroscopy data for use in estimates of sediment composition. This relatively new proxy has proved useful for estimating concentrations of several sedimentary components including calcium carbonate, hematite, and goethite. Calibrations and applications of these proxies are discussed in Chapters 3-5.

Chapter 3 utilizes reflectance- and magnetic susceptibility-based estimates of %$CaCO_3$ coupled with the depth transect drilling strategy at Ceara Rise to assess the timing of deep Atlantic circulation changes over the past one million years. The five Ceara Rise sites span a water depth range of 3000-4300 meters, which covers the transition between the two major deep water masses in the western tropical Atlantic, North Atlantic Deep Water (NADW) and Antarctic Bottom Water (AABW). The mixing zone between these water masses coincides with the present-day lysocline, providing a link between carbonate preservation and deep water circulation, since underlying AABW is more corrosive to $CaCO_3$ than overlying NADW. All sites are located within a relatively small geographic area. Assuming that the input of biogenic carbonate from surface waters at a given time is equal at all sites, the differences in carbonate accumulation between shallow and deep sites reflect the relative dissolution of carbonate at depth, and thus provide a measure of deep ocean circulation patterns through time. If these dissolution patterns are a response to temporal changes in the relative strengths of NADW and AABW, then the timing of Atlantic deep ocean circulation relative to global climate extremes during the Pleistocene may be assessed. Periods of maximum dissolution (inferred low NADW flux) at the deepest site relative to the shallowest site occur during ice growth, while maximum preservation (inferred high NADW flux) occurs during ice melt. The results of this study indicate that changes in Atlantic deep ocean circulation precede ice volume extremes during the Pleistocene, providing a possible mechanistic link between hemispheres for early climate response in the southern hemisphere.

Another early climate response in the Pleistocene is discussed in Chapter 4. A new proxy for Amazon Basin lowland precipitation is introduced, based on the relative proportions of hematite and goethite in the terrigenous fraction of sediment at Ceara Rise. The ratio of goethite/(goethite+hematite) (G/(G+H)) is proportional to precipitation with high ratio values coinciding with high precipitation levels. Based on sparse and discontinuous continental records, the Amazon Basin is thought to have been colder and drier during the last glacial maximum (LGM) than it is today, with climate extremes in phase with N. Hemisphere ice volume. This work, with high-resolution, continuous records spanning several complete glacial-interglacial cycles, shows a different timing of tropical climate extremes with the tropics responding to insolation forcing earlier than the northern hemisphere ice sheet response. This result suggests that tropical climate changes in the Amazon Basin do not respond to high latitude ice sheets. Rather, the early tropical response suggests that the tropics react rapidly to northern hemisphere insolation forcing and thus may play a role in driving or amplifying high latitude climate during the late Pleistocene.

The rapid response of lowland Amazon Basin precipitation cycles to insolation forcing in the Pleistocene proves to be consistent over much of the time from the middle Miocene to the present, even prior to the initiation of the Amazon drainage to the Atlantic. In Chapter 5, the changing phase relationships among G/(G+H), %$CaCO_3$, and insolation forcing suggest that precipitation cycles and %$CaCO_3$ both maintain a nearly constant and similar in-phase relationship to insolation since 13.2 Ma, with two exceptions: (1) the early Pliocene (~4.5-5.0 Ma) and (2) the late Plio-Pleistocene (~2.5-0 Ma). Are the phase shifts observed in these intervals due to a change in the processes driving precipitation, %$CaCO_3$, or both? During the early Pliocene interval, Amazon Basin precipitation cycles appear to respond to a different forcing while %$CaCO_3$ maintains phase with high latitude northern hemisphere summer insolation. The new forcing is probably low latitude insolation, likely during southern hemisphere summer. This forcing would drive a monsoonal precipitation system, which may be aided by tectonic development of high Andean topography. From 2.5 Ma to the present, Amazon precipitation cycles lead %$CaCO_3$. The results of Chapter 5 suggest that the process driving %$CaCO_3$ in Ceara Rise sediments changes near 2.5 Ma. The initiation of large northern hemisphere ice sheets at about this time provide a mechanism, sea level, to change the dominant process controlling %$CaCO_3$ during the Plio-Pleistocene, causing carbonate variability to lag insolation, while precipitation, an atmospheric phenomenon monitored by G/(G+H), continues to respond rapidly to insolation forcing.

Orbital scale climate variability since the middle Miocene is superimposed on long-term changes in the structure of the Amazon drainage itself. The timing of tectonic activity in the eastern Andes is loosely linked to step-like changes in the accumulation of terrigenous material at Ceara Rise and the composition of that material. Ceara Rise sediments document two episodes of Amazon Basin restructuring, which occur near the end or after dated discrete tectonic events in the Andes and within a broad range of dates for deformation in easternmost Andean provinces. These results, discussed in Chapter 5, show that increased deposition of terrigenous sediments at Ceara Rise may lag discrete tectonic activity in the Andes.

Since the middle Miocene, tropical South American climate has been influenced by both external orbital forcing, on time scales of 10^4-10^5 years, and by tectonic activity, on time scales of 10^6 years. Precipitation cycles, inferred from a reflectance spectroscopy proxy, G/(G+H), responded rapidly to orbitally-driven insolation forcing throughout, although the source of the forcing, in terms of latitude and season, was not always constant. From 2.5-0 Ma, precipitation cycles in the Amazon lead changes in %$CaCO_3$ in Ceara Rise sediments, due to significant sea level control on %$CaCO_3$ linked to slow-responding Northern Hemisphere ice sheets. Late Pleistocene deep Atlantic circulation, inferred from carbonate dissolution patterns at deep Ceara Rise sites, responds quickly to northern hemisphere high-latitude summer insolation, as do Amazon precipitation cycles. The early responses in these proxies suggest that (1) the deep ocean may translate climate changes from high northern latitudes to the southern hemisphere and (2) that tropical climate may play an internal role in forcing high northern latitude climate systems.

2.

Processing Digital Reflectance Spectroscopy Data for Use in Estimating Deep-Sea Sediment Composition

Sara E. Harris, Alan C. Mix and Joseph D. Ortiz

ABSTRACT

Throughout the following chapters, reflectance spectroscopy data are used to develop proxies for a variety of sedimentary parameters. The purpose of this chapter is to discuss the rationale behind using reflectance data and to document data treatment and analysis methods.

BACKGROUND

Sediment "color" holds clues to sediment composition and has been used as a qualitative descriptor by geologists for many decades, if not centuries. While color is a synthesis of reflectance and absorption of energy at wavelengths in the visible range, the spectrum itself (reflectance as a function of wavelength) provides a quantitative measure of the nature of a substance.

Various minerals display different characteristic reflectance spectra (Clark et al., 1990 and references therein). Spectral shape and locations of absorption bands are functions of characteristic electronic and vibrational processes within specific minerals (Hunt, 1977; Hunt and Ashley, 1979). These characteristics are the basis for using reflectance spectra as proxies for sediment composition.

The first automated instrument for measuring reflectance spectra from the surfaces of split sediment cores was deployed on Ocean Drilling Program (ODP) Leg 138 (Mix et al., 1992). Its purpose was to provide another independent non-intrusive sensor for sediment composition. Other examples of such sensors include magnetic susceptibility, natural gamma, and gamma ray attenuation porosity evaluator (GRAPE) measurements. These measurements do not consume sediment and are rapid and relatively easy to make. Provided they can be calibrated to real sedimentary composition, non-intrusive proxies can provide records with high temporal resolution over long time series (tens of thousands of samples), which are highly impractical to construct using traditional laboratory techniques.

Subsequent versions of the Oregon State University Split Core Analysis Track (OSU-SCAT) have been used to measure the reflectance spectra of sediments from the western tropical Atlantic (Version 2.1, ODP Leg 154, discussed in subsequent chapters), the north Atlantic (Version 3.1, ODP Leg 162; Ortiz et al., in press), the California Current (Version 3.2, ODP Leg 167), the Chile margin (Version 3.2), and the Subantarctic Atlantic (Version 3.3, ODP Leg 177). These regions represent a highly diverse sampling of deep sea sediments with varying composition. To date, reflectance data from the OSU-SCAT have been used to estimate % $CaCO_3$, % biogenic opal, % organic carbon, % hematite, and % goethite (Mix et al., 1995b; Harris et al., 1997; Harris and Mix, in press; Ortiz et al., in press).

THE OSU-SCAT

The OSU Split Core Analysis Track is an automated machine that moves a split sediment core along a track for measurement at user-defined increments. The major components of this system are a core track, light sources, fiber optic cables, a beam steerer, a 6-inch integrating sphere with an attached lander, spectrograph with a diffraction grating, a thermoelectrically cooled charge-coupled device (CCD) detector, a PC for instrument control and data acquisition, and a SUN Microsystems™ computer for data processing and storage (Figure 2.1).

At each sample location, the core stops along the track and the integrating sphere is lowered to the core surface. Strain and conductivity sensors on the landing board detect when the surface of the split core is reached. The conductivity probes sense the surface easily in soft, wet sediments, while strain gauges are used to detect the surface of compacted sediment cores. After the integrating sphere has landed, three measurements

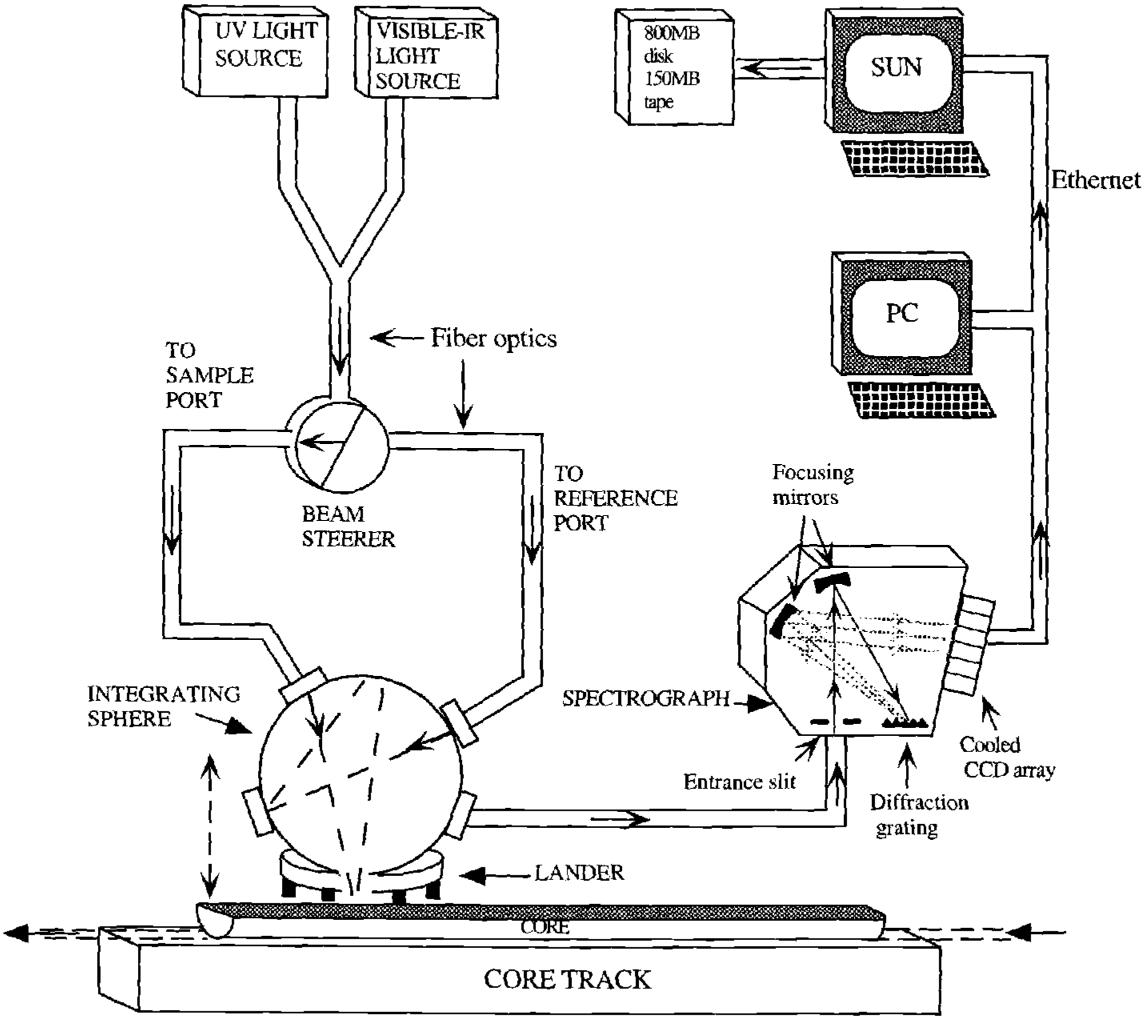

Figure 2.1 Diagram of the Oregon State University split core analysis track (OSU-SCAT). Figure by June Wilson.

are taken at each sample location: (1) a background reference measurement, referred to as "black" (BLK), (2) an internal standard reference representing theoretical 100% reflectance, referred to as "internal white" (IW), and (3) the sample measurement, referred to as "sample" (SMP) or "standard" (STD) for external standard measurements. Two light sources, a deuterium lamp for the ultra violet (UV) range and a quartz-tungsten-halogen lamp for the visible (VIS) and near infrared (NIR) ranges provide the incident beam of light. For the black measurement, the beam steerer, a revolving mirror, guides the incident beam into a light trap. For the internal white measurement, the incident beam is directed to the integrating sphere via fiber optic cables and shines on an inside surface of the integrating sphere. The inside of the integrating sphere is coated with Spectralon®, which is a near-perfect diffuse reflector over the wavelength range considered here. During sample measurement, the incident beam is steered to an open port of the integrating sphere and illuminates the surface of the split core at an incidence angle of 8° from the vertical. For all of these measurements, diffuse and specular reflectance are collected by the integrating sphere and delivered to the spectrograph, where a diffraction grating splits the light into a spectrum, which is delivered to the cooled detector array. The detector measures the reflected spectrum in 1024 channels (or pixels) ranging from 250-950 nm (UV-VIS-NIR) at 0.68 nm resolution. Raw data in beam intensity at each wavelength are written to ascii files on a PC computer, then transferred to a SUN Microsystems™ computer for storage in direct access binary format and further processing, discussed in the next section.

DATA PROCESSING

The end product desired from the OSU-SCAT is percent reflectance at each wavelength. Several steps are required to calculate the spectrum from raw beam intensities measured by the detector. Further processing of the final percent reflectance spectrum reduces the data set from the original 0.68 nm resolution to lower resolution, typically 10 nm. These steps are described below.

External standards

A set of external standards with known reflectivities is measured in exactly the same configuration as the samples in order to calibrate sample measurements to true percent reflectance. The standard "boat" is shaped like a split core and covered with a electrically conductive foam to sense landing of the integrating sphere. Holes in the foam hold the standards so that they are flush with the foam surface, approximating the geometry of core sample measurements. The four external standards are approximately 2%, 40%, 75%, and 100% reflectance. Calibrated reflectance values for the standards are provided by Labsphere Inc. at 50 nm intervals for the 2%, 40% and 75% standards (value at 250 nm for the 2% standard is not certified) and at 1 nm intervals for the 100% standard. The desired spectral quality of such standards is a nearly constant reflectivity over the range of wavelengths measured, which is achieved with these standards (Figure 2.2).

The first step to obtain % reflectance for external standards from raw beam intensity at each wavelength (λ) is to calculate a raw reflectance ratio (RRR) as

$$RRR_{STD}(\lambda) = 100*(STD(\lambda)-BLK(\lambda))/(IW\ (\lambda)-BLK(\lambda)) \qquad (2.1)$$

The raw reflectance ratio for each standard is then normalized to the RRR for the external 100% standard. To reduce noise, this is typically an average of several standard runs, culled by pixel, discarding runs with RRR values greater than three standard deviations from the pixel mean. The raw reflectance ratio for the average external 100%

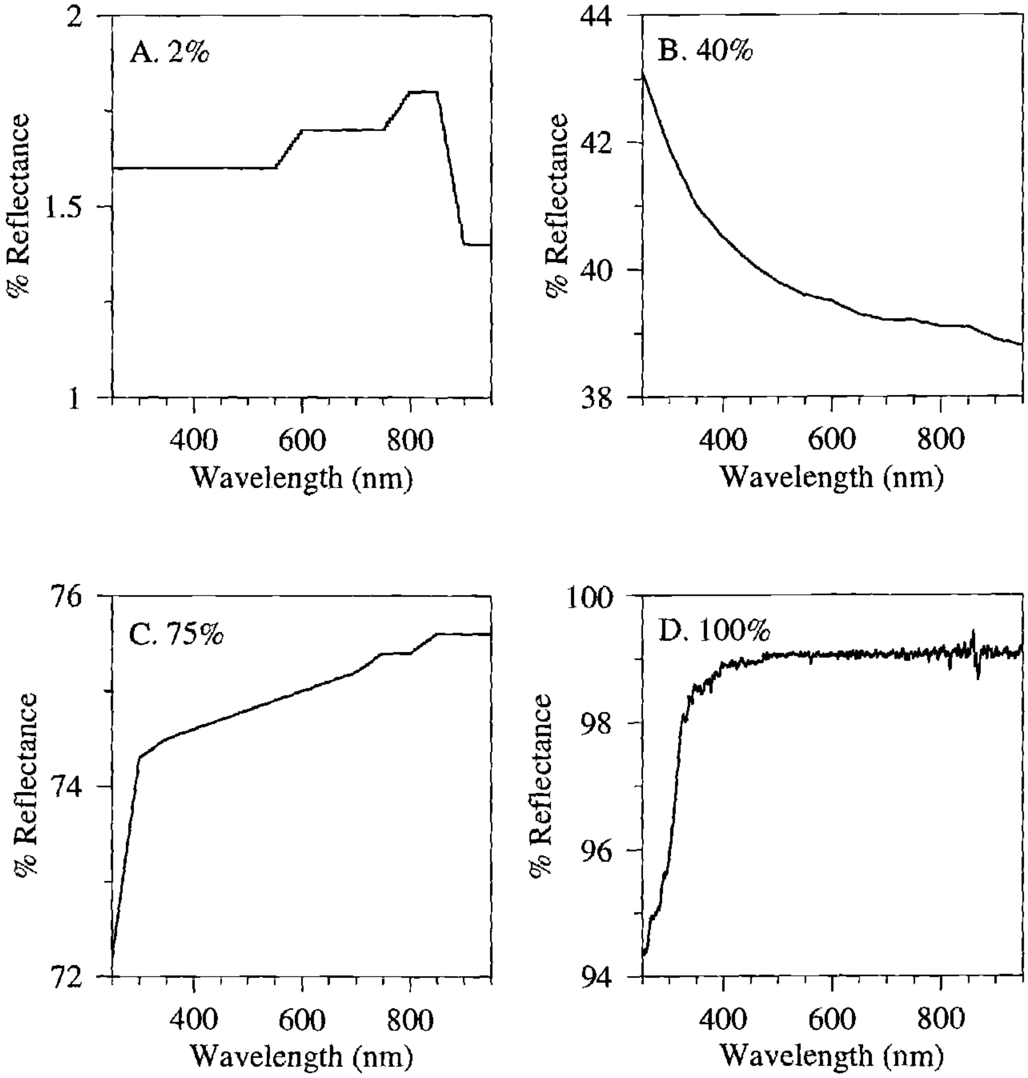

Figure 2.2 Known reflectance spectra for the 2%, 40%, 75%, and 100% external standards. Data provided by Labsphere Inc.

standard for 61 standard sets run during Leg 154 post cruise measurements is 53.5-56.5, about half of 100% (Figure 2.3). Internal white counts are higher than counts for the 100% external standard, causing this difference. The normalization equation is

$$NRR_{STD}(\lambda) = RRR_{STD}(\lambda)/RRR_{100\%}(\lambda) \tag{2.2}$$

where STD is the 2%, 40%, 75%, or 100% external standard. Note that in the case of the 100% external standard, the normalized reflectance ratio (NRR) is defined to be exactly 100% in this step. Typically, normalized reflectance ratios for each standard from several standard runs are averaged and culled by pixel with a three standard deviation cutoff. Figure 2.4 shows the culled average standards for 61 runs from the Leg 154 data set, normalized to the average 100% raw reflectance ratio.

"Ball" corrections

The normalized reflectance ratios for the set of four standards are then used to correct percent reflectance to the known reflectivities of the standards. This is a additive correction, which is a function of both wavelength and percent reflectance from the normalized reflectance ratio. One reason this correction is necessary is that the incident beam shining through the integrating sphere onto the sample surface is not perfectly focused. A "halo" of incident light reflects off the inside of the sphere before encountering the sample surface, artificially increasing the measured % reflectance for the sample. The effect is larger at lower reflectivities, since the proportion of reflected light in the halo increases relative to the total reflectance for dark samples (Clarke and Compton, 1986). A second reason for the correction is that the sample in the sample port is effectively a part of the integrating sphere. Therefore, the total reflectance of the

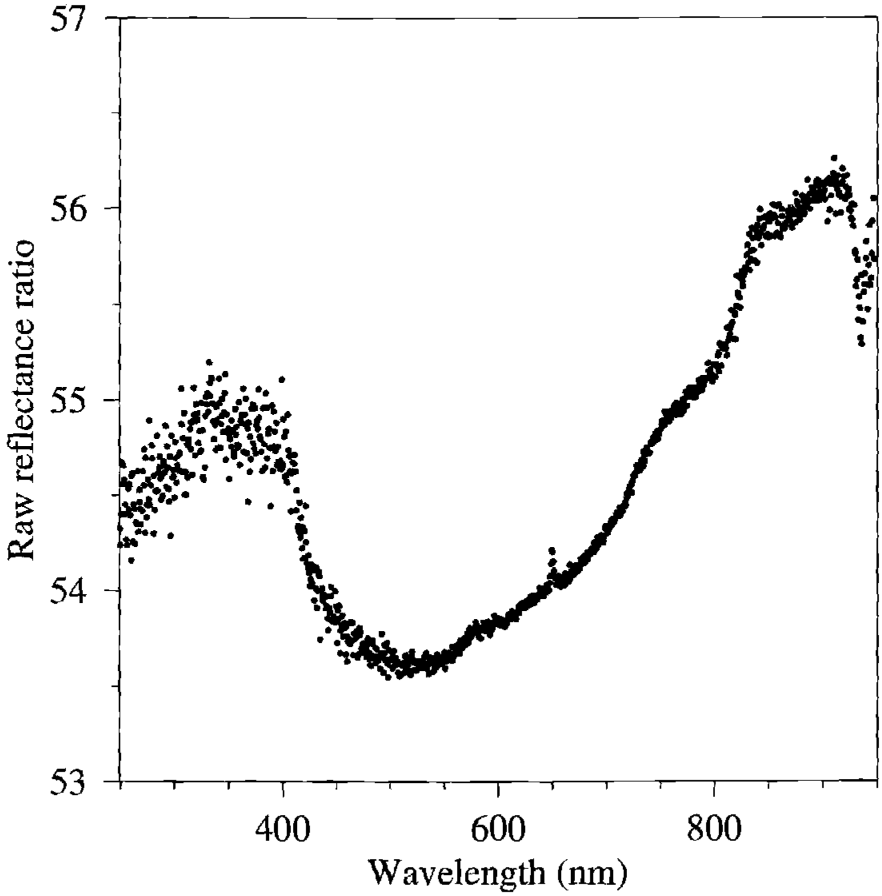

Figure 2.3 Average raw reflectance ratio (culled by pixel with a 3 standard deviation cutoff) for 61 external 100% standard measurements from the Leg 154 data set.

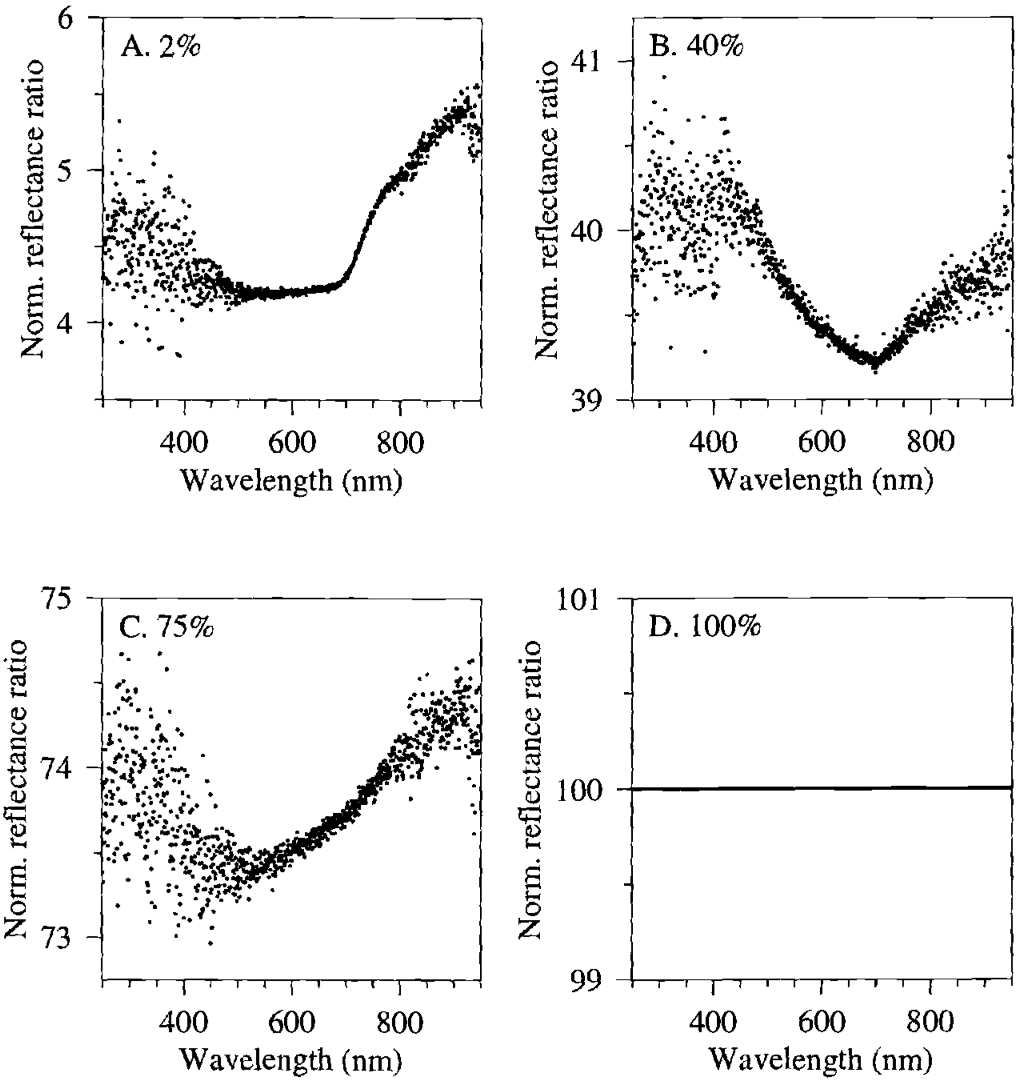

Figure 2.4 Average normalized reflectance ratios for (A) 2% standard, (B) 40% standard, (C) 75% standard, and (D) 100% standard.

sphere-sample system is lower for a "dark" sample than for a "bright" one. Corrections for these effects will be called "ball" corrections.

Ball corrections (BC) are calculated as the difference between known reflectivities for the four standards and measured normalized reflectance ratios. A polynomial of degree three fit to this difference as a function of % reflectance (normalized reflectance ratio)defines the ball corrections at each wavelength over the range of % reflectance from 0- 100%. Examples at three wavelengths are shown in Figure 2.5, while Figure 2.6 shows a contoured field of ball corrections calculated from the Leg 154 data set. Note that the correction is positive in some portions of this field, indicating that processes additional to the halo effect, possibly related to the sphere configuration or distance to the samples, must be operating.

For Leg 154 data, all standard runs were culled by pixel, averaged and one field of ball corrections defined and applied to the whole data set. This approach reduced noise in the corrections and, since the data were collected on shore post cruise, the geometry of the instrument setup should have remained constant throughout the six weeks of data collection. Alternatively, ball corrections may be defined for a single run or an average of multiple recent runs. An average is desirable to reduce the effect of anomalous standard runs on a subset of samples.

Sample data processing

Samples are processed in a manner similar to the external standards, with the additional step of ball corrections. The black, internal white, and sample raw beam intensities (Figure 2.7) are used to calculate the raw reflectance ratio as

$$RRR_{SMP}(\lambda) = 100*(SMP(\lambda) - BLK(\lambda))/(IW(\lambda) - BLK(\lambda)) \qquad (2.3)$$

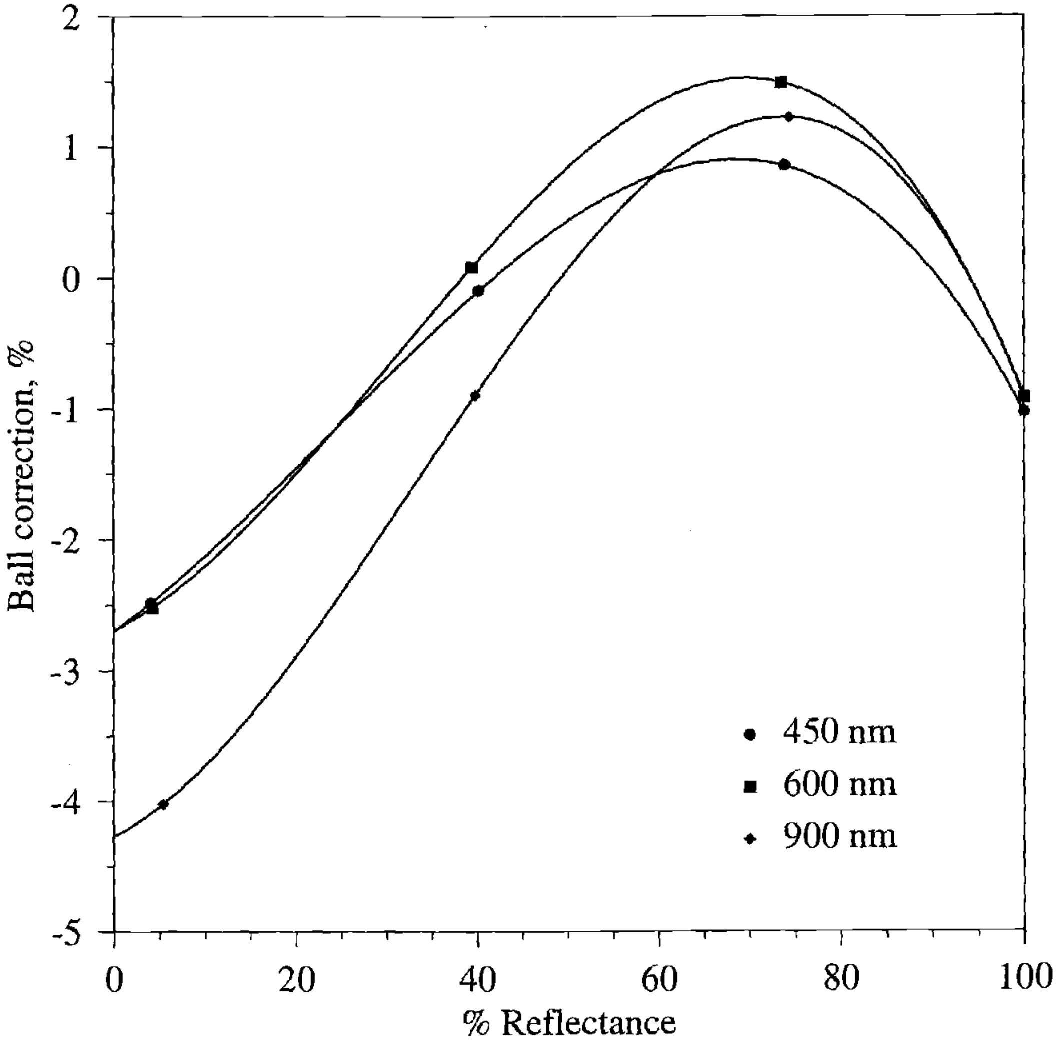

Figure 2.5 Examples of the polynomial fit for ball corrections to external standards at three wavelengths (450 nm, 600 nm, 900 nm). % Reflectance on the x axis is the normalized reflectance ratio.

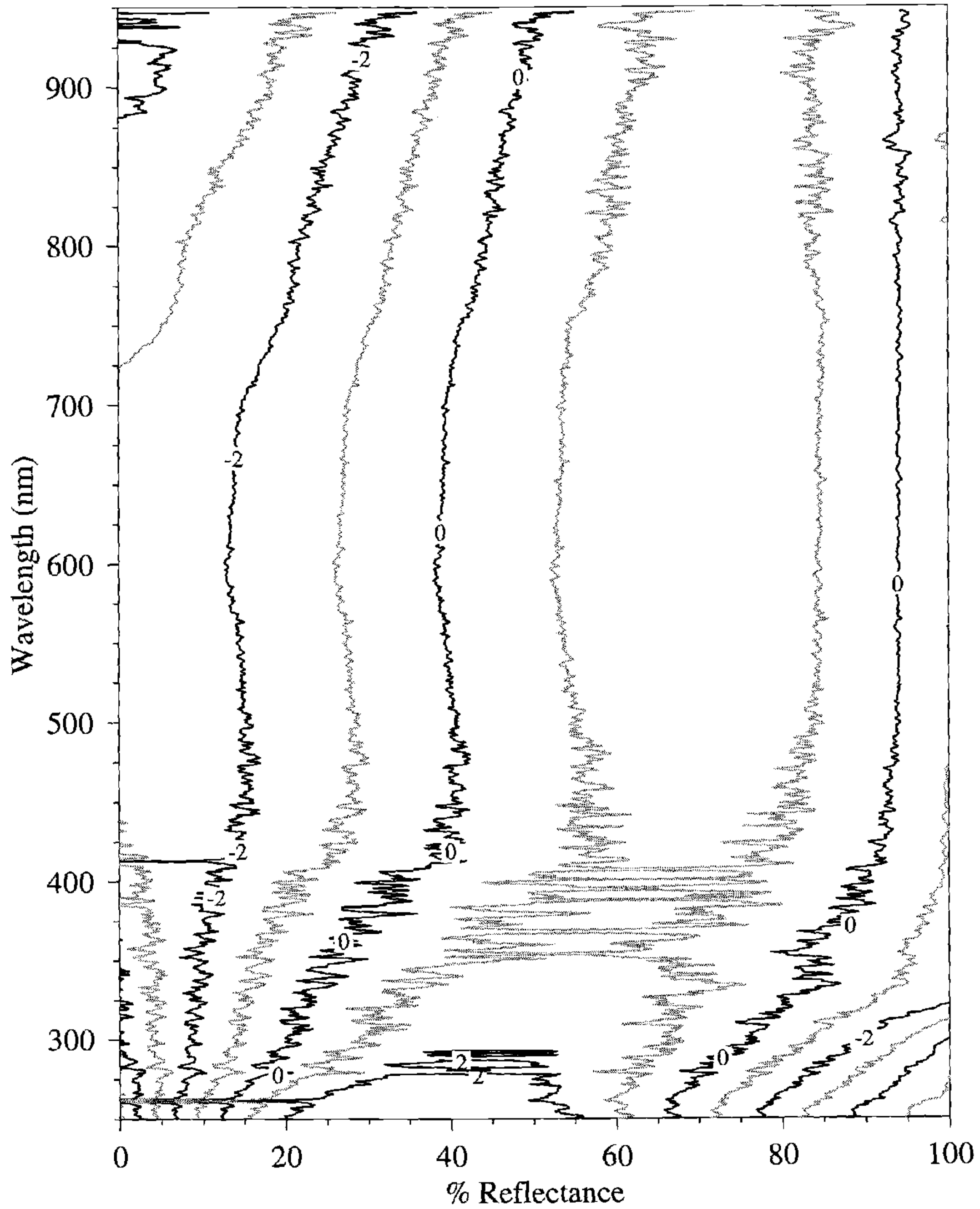

Figure 2.6 Contoured field of ball corrections as a function of % reflectance (normalized reflectance ratio) and wavelength. Ball corrections for the Leg 154 data set are typically between -2% and +2%.

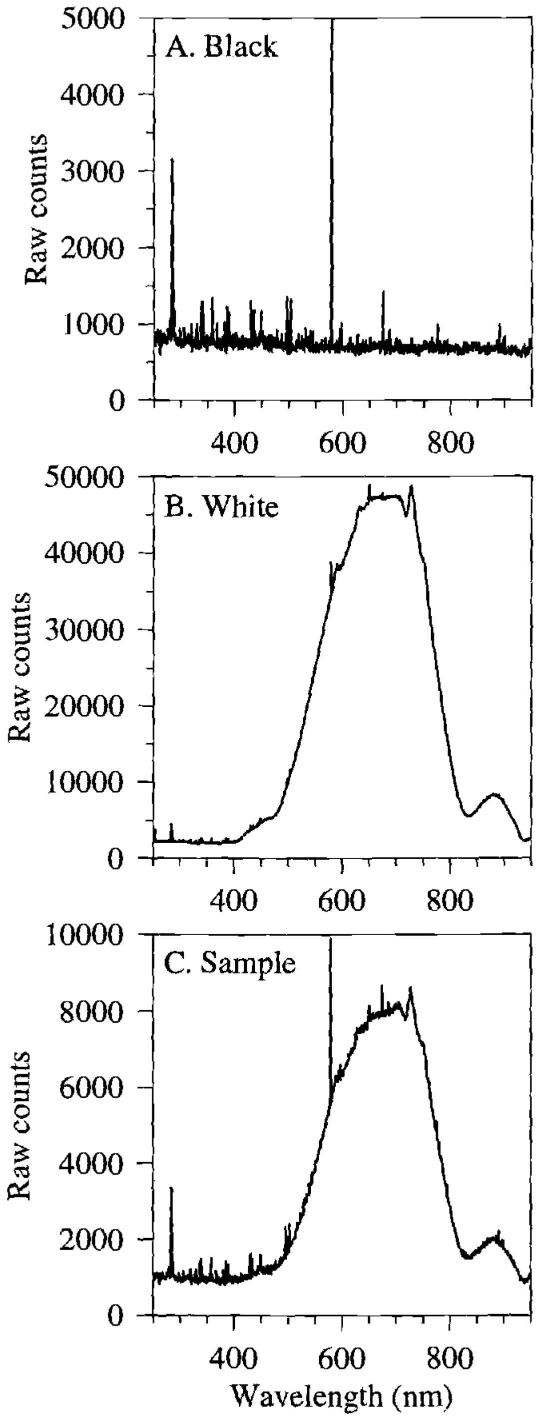

Figure 2.7 Example of (A) black, (B) white, and (C) sample measurements in raw beam intensities as a function of wavelength for one sample (926C01H2, 1-3 cm). Note that some spikes, for example near 280 nm and 580 nm are due to malfunctioning detector pixels, which read high values consistently. The correction procedures eliminate this apparent across-pixel noise.

then the normalized reflectance ratio is calculated as

$$\mathrm{NRR}_{\mathrm{SMP}}(\lambda) = \mathrm{RRR}_{\mathrm{SMP}}(\lambda)/\mathrm{RRR}_{100\%}(\lambda) \tag{2.4}$$

Final corrected % reflectance (%R) values are calculated as

$$\%\mathrm{R}(\lambda) = \mathrm{NRR}_{\mathrm{SMP}}(\lambda) + \mathrm{BC}(\lambda,\%) \tag{2.5}$$

Where BC is the ball correction as a function of wavelength and NRR (Figure 2.6). These final spectra are tested for data quality. Using a running mean 11 pixels wide, any of the 1024 corrected %R measurements more than 5 standard deviations from the running mean is replaced with that mean. Figure 2.8 shows a graphical illustration of these steps for one sample. After correcting all samples in a core or a hole, 50 nm wide band averages are examined downcore for anomalies (e.g. Figure 2.9). Any values more than five standard deviations from an eleven sample running mean are culled. This step is intended to eliminate bad landings and cracks or voids in the core section.

Sources of error

Variations in both the instrument and the split cores introduce several sources of error to the final % reflectance spectrum. This section outlines these sources and describes solutions where possible. Some errors due to inconsistencies in instrument behavior and core condition were not corrected for in the Leg 154 data and remain in the final data set.

Landing, or sensing the core so that the integrating sphere stops a constant distance above the core surface, was somewhat inconsistent during Leg 154 data

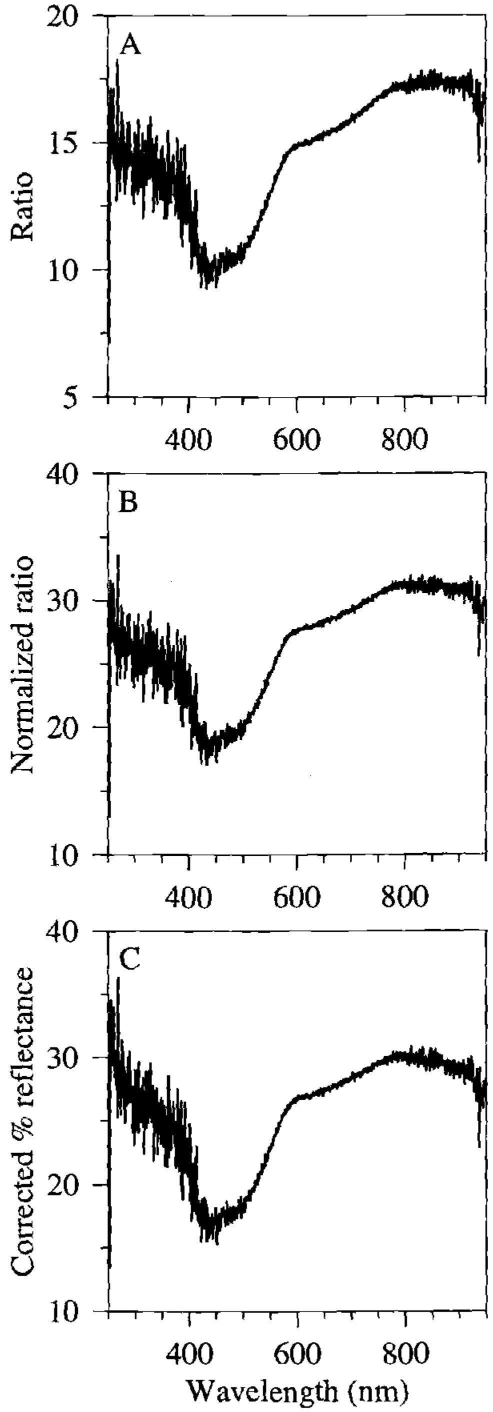

Figure 2.8 Example of the corrections process for one sample. (A) Raw reflectance ratio, (B) normalized reflectance ratio, and (C) corrected % reflectance after ball corrections.

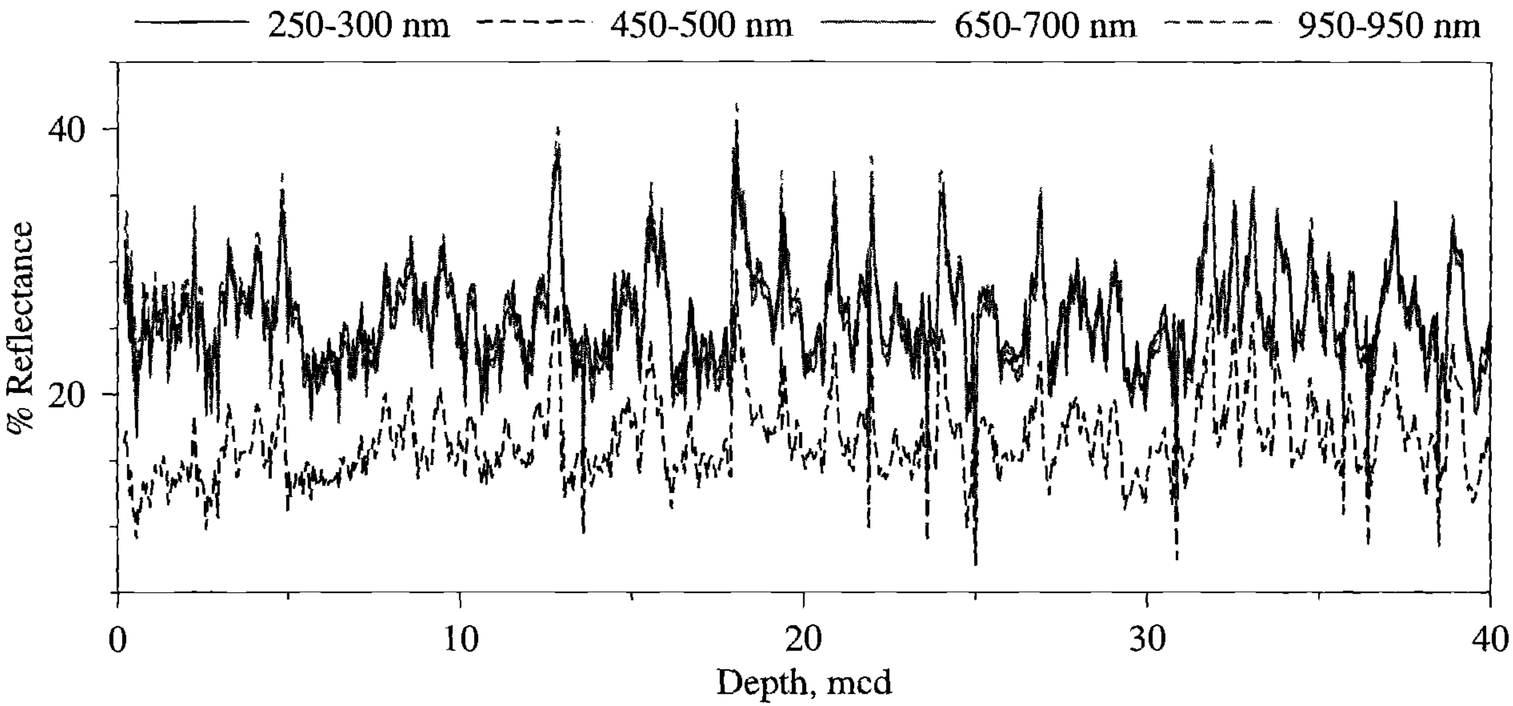

Figure 2.9 Downcore % reflectance in four 50-nm wide band averages across the spectrum. Mcd = meters composite depth.

collection, due to some variation in the sensitivity of the landing sensors. The result was some variation in the distance from the core surface to the sample port, with the range likely less than 2 mm. Clearly unsuccessful landings, where the integrating sphere stopped significantly above the core surface and % reflectance was anomalously low, were culled from the data set, based on downcore trends. Minor anomalies in the distance between the core surface and the integrating sphere port cannot be corrected.

A related effect is the varying tilt of the core surface itself. This effect can be quite pronounced with a twisted core liner. Ideally, the plane of the core surface should be parallel to the sample port. If the surface is tilted, the calculated percent reflectance decreases, since less of the reflected light is collected by the integrating sphere. In post-Leg 154 models of the OSU-SCAT, this effect was corrected with a gimbaled integrating sphere, which could land on variably tilted surfaces. Any errors due to this effect remain in the Leg 154 data set.

The standard surfaces may become contaminated over time by dust or grease from fingerprints, affecting the reflectivity of the standards and subsequently the ball corrections to the data. This effect is reduced by blowing the standards frequently with compressed air and averaging standard runs to calculate ball corrections. The standards may also be cleaned by light sanding or washing.

Temporal changes in detector cooling, or thermal drift, will affect noise levels. The detector is cooled by a water chiller and also a thermoelectric cooler. If the cooling components are not working properly, noise levels increase, and background "black" measurements increase. To correct for variable temperature control, it is essential to use individual black measurements for each sample in corrections (Equations 2.1 and 2.3), rather than, for example, to take one black reading per section. Anomalous black readings do not propagate into final % reflectance values if individual black measurements are used.

The light sources for the input spectrum evolve over time. During data collection for Leg 154, neither the UV nor VIS-NIR bulbs were replaced in the course of six weeks. The quartz-tungsten-halogen bulb gave progressively lower counts over time particularly in the visible range. The effect of bulb evolution is eliminated from final % reflectance values if individual internal white measurements are used, rather than an average, or one internal white measurement per section. The most important reason for using individual internal white measurements in the correction procedure is that the internal white measurement is a function of the reflectivity of the material in the sample port, which covers a small portion of the integrating sphere. A dark sample or standard in the sample port will produce lower internal white values than a bright sample, therefore it is essential to use individual internal white measurements for both samples and standards (Equations 2.1 and 2.3).

Band averaging and first derivatives

The final step before using these reflectance spectra for estimates of sedimentary parameters is to reduce the data set and calculate first derivative spectra. The goal is to reduce both noise across the spectrum and the number of spectral variables so as to preserve the information in the spectrum while avoiding redundancy.

Band averaging can be done in several different ways. We rejected a method utilizing a Fast Fourier Transform for smoothing in favor of a simpler "boxcar" average. Results from the two methods are statistically very similar for near-equivalent effective bandwidths. We chose to band average % reflectance data in 10 nm wide bands centered on wavelengths as close as possible to those ending in 5, e.g. 255, 265, 275,..., 945 nm. The practical reason for centering on the "5's" is for ease of comparison to previous work (Balsam and Deaton, 1991; Deaton and Balsam, 1991). No measured pixel falls directly on these nominal center wavelengths (Table 2.1), but they are offset by an average of

Table 2.1 Wavelength range, center wavelengths, number of pixels per band and center offset from nominal center wavelengths for 70 averaged bands from 250-950 nm.

Band No.	Wavelength Range (nm)	Center Wavelength (nm)	No. Pixels	Center Offset (nm)
1	250-260	254.785	15	-0.215
2	260-270	265.039	15	0.039
3	270-280	274.951	14	-0.049
4	280-290	284.864	15	-0.136
5	290-300	295.118	15	0.118
6	300-310	305.030	14	0.030
7	310-320	314.942	15	-0.058
8	320-330	325.196	15	0.196
9	330-340	335.108	14	0.108
10	340-350	345.020	15	0.020
11	350-360	354.933	14	-0.067
12	360-370	364.845	15	-0.155
13	370-380	375.099	15	0.099
14	380-390	385.011	14	0.011
15	390-400	394.923	15	-0.077
16	400-410	405.177	15	0.177
17	410-420	415.089	14	0.089
18	420-430	425.002	15	0.002
19	430-440	434.914	14	-0.086
20	440-450	444.826	15	-0.174
21	450-460	455.080	15	0.080
22	460-470	464.992	14	-0.008
23	470-480	474.904	15	-0.096
24	480-490	485.158	15	0.158
25	490-500	495.071	14	0.071
26	500-510	504.983	15	-0.017
27	510-520	514.895	14	-0.105
28	520-530	524.807	15	-0.193
29	530-540	535.061	15	0.061
30	540-550	544.974	14	-0.026
31	550-560	554.886	15	-0.114
32	560-570	565.140	15	0.140
33	570-580	575.052	14	0.052
34	580-590	584.964	15	-0.036
35	590-600	594.876	14	-0.124
36	600-610	604.788	15	-0.212
37	610-620	615.042	15	0.042
38	620-630	624.955	14	-0.045
39	630-640	634.867	15	-0.133
40	640-650	645.121	15	0.121
41	650-660	655.033	14	0.033
42	660-670	664.945	15	-0.055
43	670-680	675.199	15	0.199
44	680-690	685.111	14	0.111
45	690-700	695.024	15	0.024
46	700-710	704.936	14	-0.064

Table 2.1 Continued

Band No.	Wavelength Range (nm)	Center Wavelength (nm)	No. Pixels	Center Offset (nm)
47	710-720	714.848	15	-0.152
48	720-730	725.102	15	0.102
49	730-740	735.014	14	0.014
50	740-750	744.926	15	-0.074
51	750-760	755.181	15	0.181
52	760-770	765.093	14	0.093
53	770-780	775.005	15	0.005
54	780-790	784.917	14	-0.083
55	790-800	794.829	15	-0.171
56	800-810	805.083	15	0.083
57	810-820	814.995	14	-0.005
58	820-830	824.907	15	-0.093
59	830-840	835.162	15	0.162
60	840-850	845.074	14	0.074
61	850-860	854.986	15	-0.014
62	860-870	864.898	14	-0.102
63	870-880	874.810	15	-0.190
64	880-890	885.064	15	0.064
65	890-900	894.977	14	-0.023
66	900-910	904.889	15	-0.111
67	910-920	915.143	15	0.143
68	920-930	925.055	14	0.055
69	930-940	934.967	15	-0.033
70	940-950	944.880	14	-0.120

0.09 nm (absolute value), and at most 0.22 nm. We averaged all pixels that fell within the limits of each 10 nm band, 5 nm to either side of the center wavelength, including the lower limit and excluding the upper limit to ensure that no pixel is averaged into more than one reflectance band. Data were not smoothed before band averaging. Given the wavelength interval of 0.68, the number of % reflectance pixels that fall within each band is 14 or 15 (Table 2.1).

An alternate option is to keep the number of measured pixels included in each band constant at n=15. This method results in a bandwidth of 10.3 nm. Statistical tests show that the mean derivative spectrum, standard deviations and communalities in R-mode factor analysis are nearly identical given the two bandwidth possibilities described (Figure 2.10). Factor loadings for six R-mode factors are also very similar between the two bandwidth techniques (Figure 2.11), with the largest differences at the UV end of the spectrum. This result is expected since (1) the UV is the noisiest section, and (2) the center wavelengths of the 10.3 nm bands were chosen so that they fell near the "5's" in the mid-VIS (565, 575, and 585 nm being the wavelengths of primary interest to hematite estimations). These statistical tests demonstrate that the data are relatively insensitive to the method of binning employed. For ease and consistency, we adopt the method of band averaging at 10 nm intervals, centered on the "5's".

First derivatives of reflectance spectra with respect to wavelength were calculated using the centered difference method described in Numerical Recipes (Press et al., 1992; section 5.7, Eqn 5.7.7) as

$$D_n = (\%R_{n+1} - \%R_{n-1})/(2*bw) \tag{2.6}$$

where D_n equals the first derivative value centered at wavelength n, $\%R_{n+1}$ and $\%R_{n-1}$ equal the % reflectance band value at wavelengths n+1 and n-1 respectively, bw equals the bandwidth (10 nm). This method is referred to as a "centered" derivative because it is

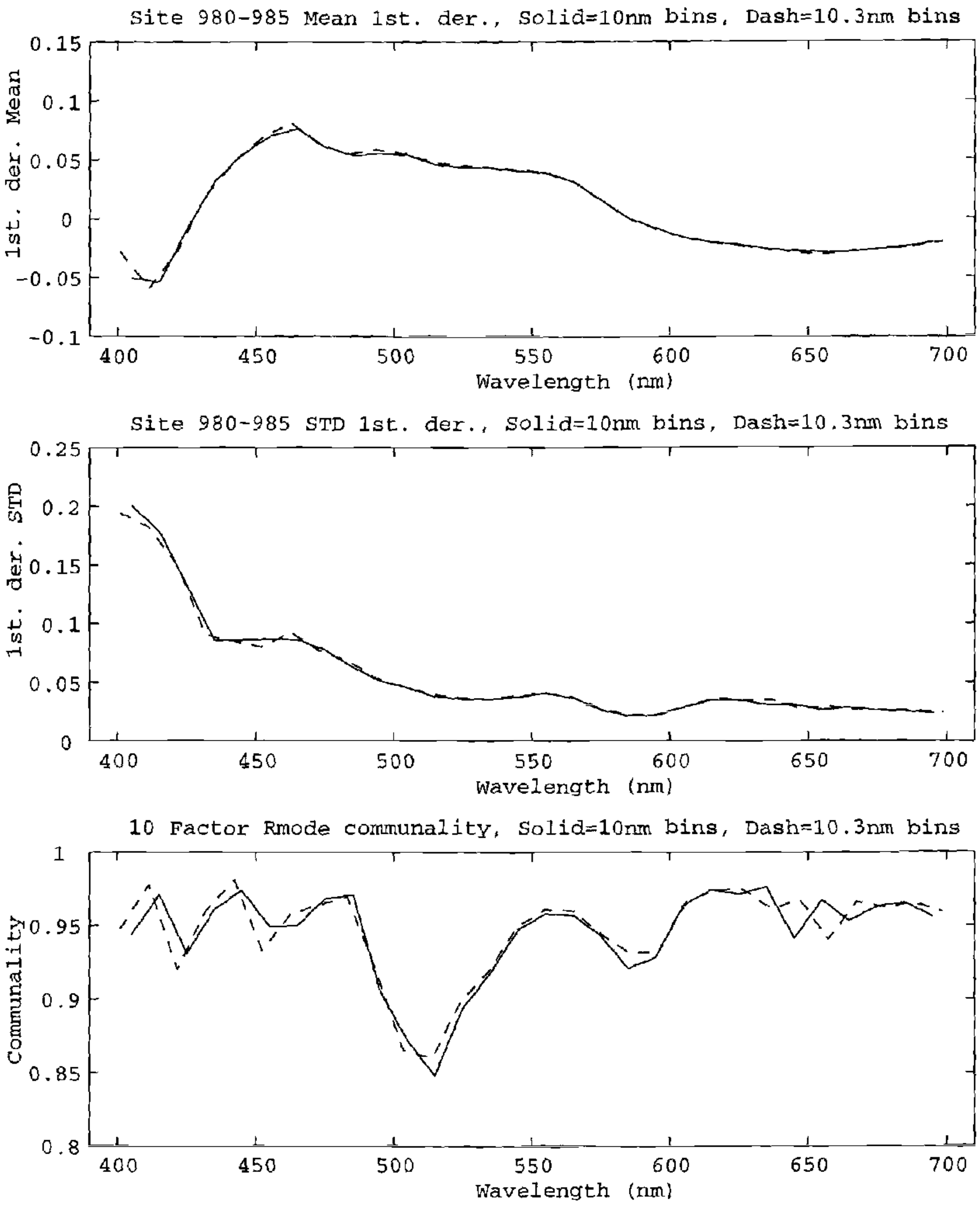

Figure 2.10 Comparison between 10 nm bins and 10.3 nm bins as a function of wavelength, in terms of the average first derivative spectrum, the standard deviation by wavelength, and the communalities from an R-mode factor analysis of first derivative spectra. Data are from Leg 162 (Ortiz et al., in press). The 10.3 nm bins were designed such that the center wavelengths of the bins fall as close as possible to 565 nm, 575 nm, and 585 nm, thus the differences between the two binning methods are greatest at the ends of the spectrum. In general, the two binning methods are in good agreement. Figure by J. Ortiz.

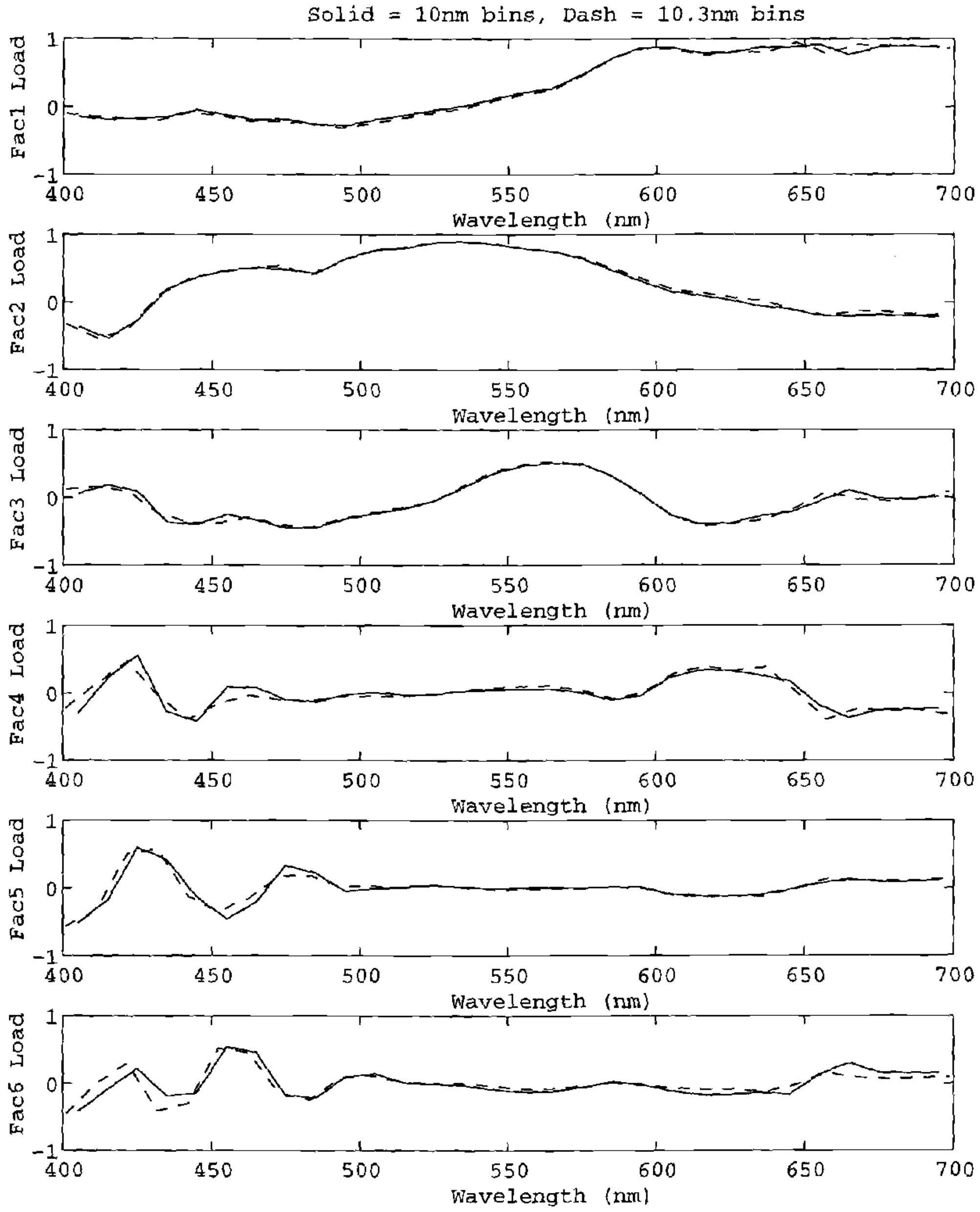

Figure 2.11 Comparison of R-mode factor loadings for an analysis of first derivative spectra from Leg 162 (Ortiz et al., in press). Factors are very similar between the two methods. See Figure 2.10 caption for details. Figure by J. Ortiz.

essentially the average of the slopes between (1) n-1 and n, and (2) n+1 and n. The effective bandwidth of the first derivative calculation as defined here is 20 nm. The number of resulting first derivative bands is two less than the number of % reflectance bands calculated, since the endpoints cannot be calculated. This method has an additional advantage in that the first derivatives are centered on the same wavelengths as the % reflectance bands, excluding the endpoints. We rejected the "first difference" method for calculating first derivatives because the results were significantly noisier, and the method results in first derivative values centered on wavelengths between % reflectance band values, rather than on the same wavelengths as % reflectance bands. An example of the results of band averaging and first derivative calculations is illustrated in Figure 2.12. This type of data is used to develop calibration equations for estimating sediment composition.

Error estimates for band averages and derivatives

The same standards are measured multiple times, producing many realizations of the same measurement. Estimates of precision, or reproducibility, of % reflectance and first derivative calculations may be made by comparisons among external standard measurements, after treating standard runs like samples (including ball corrections, band averaging, and first derivative calculations). Two measures of reproducibility are: (1) the standard deviation at each 10 nm reflectance band among 54 standard runs, excluding standard runs that were often culled during processing ("external % reflectance precision"), and (2) the standard deviation at each first derivative band among 54 standard runs ("external first derivative precision"). The external % reflectance precision increases with increasing % reflectance of the standards, from < 1% reflectance for the 2% standard to about 2.2% reflectance for the 100% standard (Figure 2.13). Reproducibility is most constant over the wavelength range from about 420-850 nm in all four standards. For all

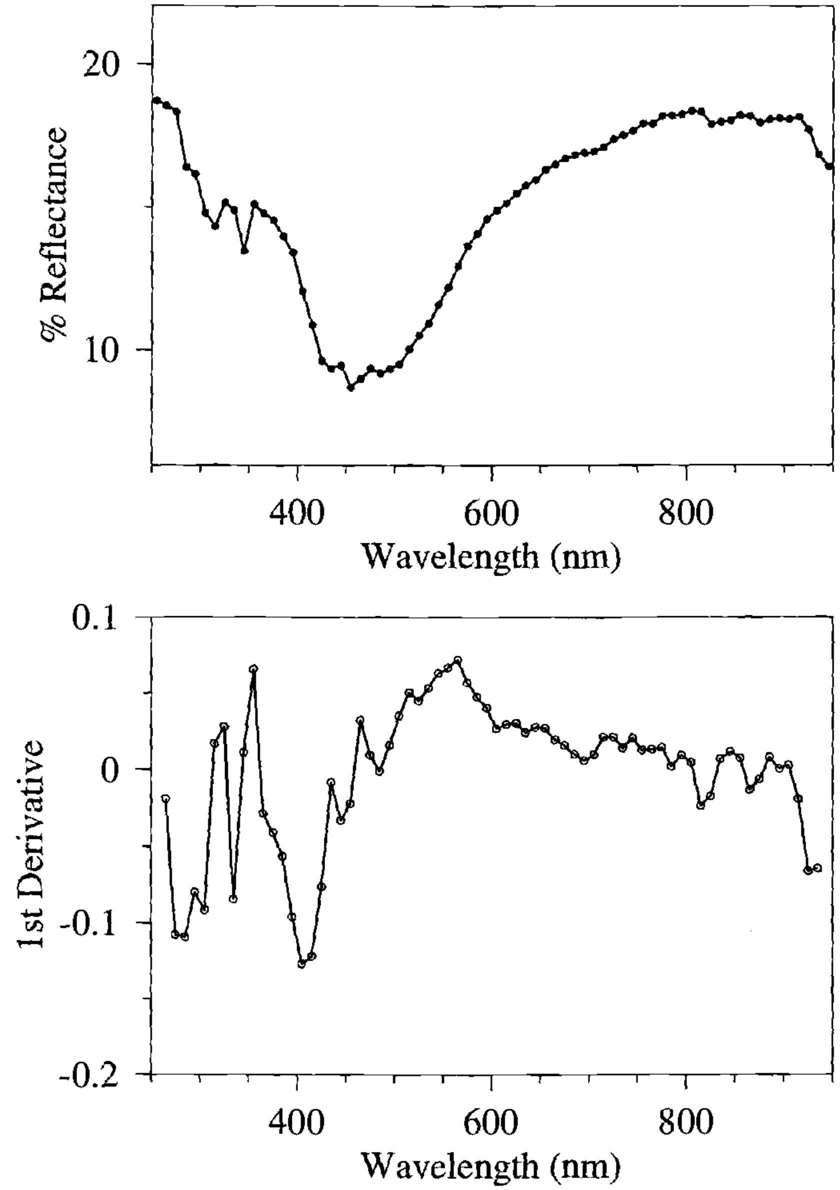

Figure 2.12 Example of one spectrum after band averaging to 10 nm intervals and calculating the first derivative spectrum as described in the text.

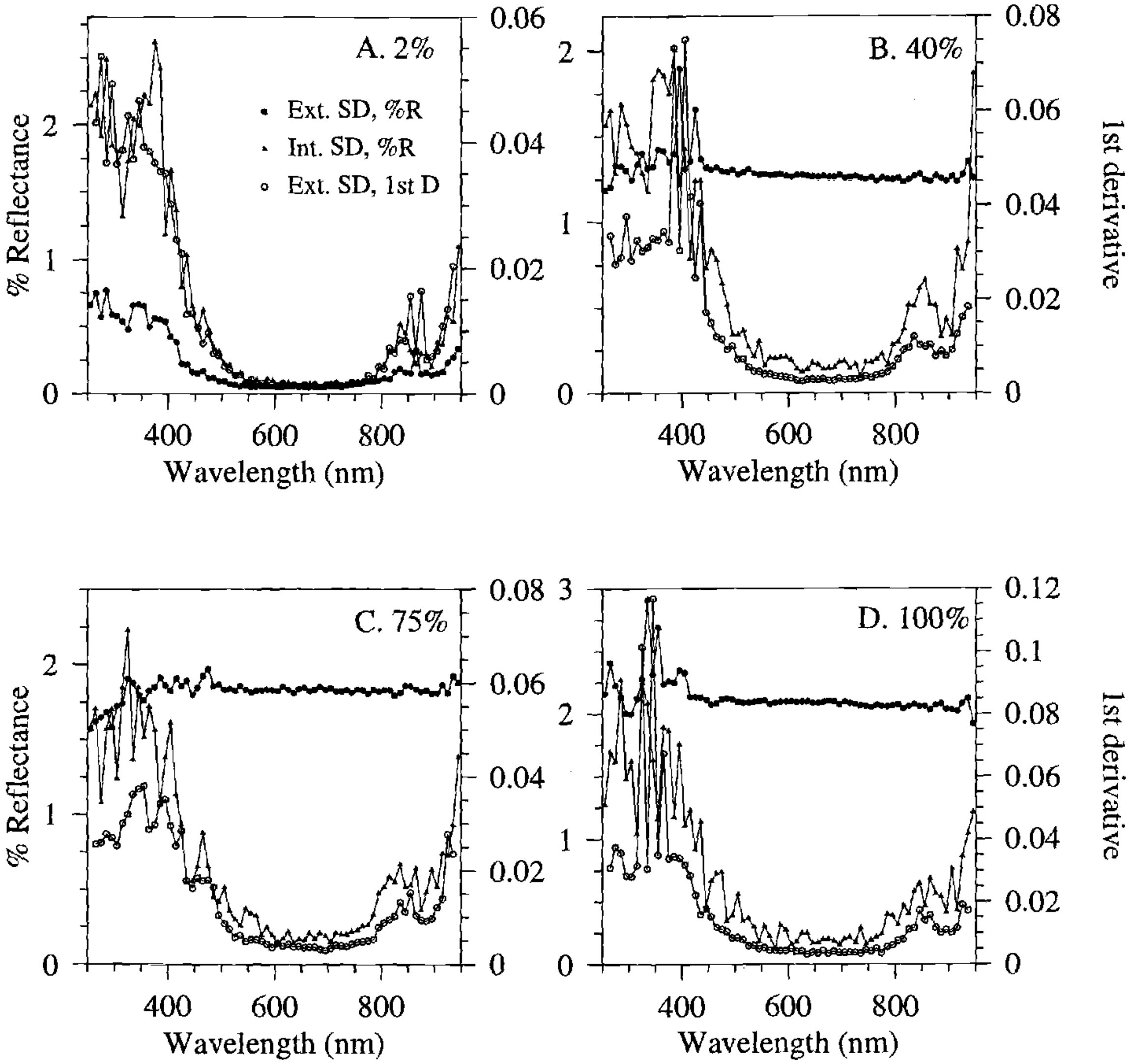

Figure 2.13 Standard deviations with respect to wavelength for 10 nm % reflectance bands among 54 standard runs (external SD for % reflectance, filled circles), 10 nm first derivative estimates among 54 standard runs (external SD for first derivatives, open circles), and pixels within each 10 nm band for one example standard run (internal SD for % reflectance, filled triangles).

standards, first derivative band values are most reproducible (lowest standard deviation) in the wavelength range from about 500-800 nm (Figure 2.13). First derivatives in the UV range are least precise.

A third statistical comparison documents the variations in % reflectance within each 10 nm reflectance band ("standard deviation of internal % reflectance"). This calculation groups the 14 or 15 pixels averaged in each band within one spectrum. The standard deviation of each group is due in part to (1) true changes in % reflectance across a 10-nm wide band, and (2) across pixel noise. These standard deviations are smallest from about 500-800 nm in all standards and greatest in the UV where the signal is noisier (e.g. Figure 2.4). The small standard deviations of internal % reflectance in the visible range imply that 10 nm band averages do not oversmooth the true signal.

In general, the best precision in both % reflectance and first derivative calculations is obtained in the visible wavelength range, while the UV is noisiest.

SUMMARY

Reflectance spectroscopy is a useful non-intrusive proxy for estimating the composition of sediments, particularly biogenic components (% CaCO3, % opal, % organic carbon) and iron oxides and oxyhydroxides. For Leg 154 reflectance data, the methods described in this chapter were used to correct and reduce the data set. Software developed for reflectance data processing is included in Appendix B.

ACKNOWLEDGMENTS

Special thanks to Bill Rugh for designing, building, programming, and troubleshooting the OSU-SCAT. June Wilson drafted Figure 2.1.

3.

Biogenic and Terrigenous Sedimentation at Ceara Rise, Western Tropical Atlantic, Supports Plio-Pleistocene Deep-Water Linkage Between Hemispheres

Sara E. Harris, Alan C. Mix, and Terri A. King

Reprinted in its entirety with permission from the Ocean Drilling Program from:
Shackleton, N.J., Curry, W.B., Richter, C., and Bralower, T.J. (Eds.), 1997. *Proc. ODP, Sci. Results,* 154: College Station, TX (Ocean Drilling Program)

ABSTRACT

Calcium carbonate percentages at five Ceara Rise sites were estimated at 1-2 thousand year intervals over the past 5 million years, using reflectance spectroscopy and magnetic susceptibility proxies. From these estimates and detailed correlations between sites, gradients of calcite and terrigenous sediment accumulation rates in a depth transect of sites reveal variations in local climate and calcite dissolution related to deep water masses. Relative to shallow sites on the southern Ceara Rise, accumulation rates of terrigenous sediments at deeper sites near the Amazon Fan were higher during glacial periods. Analogous variations in terrigenous sedimentation prior to the expansion of northern-hemisphere ice sheets ~3 million years ago suggests that tropical climate cycles occurred independently of polar glaciation. Decreasing accumulation rates of calcite with increasing water depth reveal patterns of carbonate dissolution, which varied on orbital time-scales (10-100 k.y. periods) throughout the Plio-Pleistocene. Maximum dissolution at deep relative to shallow sites occurred in the transition from interglacial to glacial conditions, and maximum preservation occurred during global warming, at all orbital periods. If the local dissolution gradient is linked to relative contributions of North Atlantic Deep Water and Antarctic Bottom Water, this phasing of events confirms a key prediction of SPECMAP that deep water adjustments may translate climate changes between hemispheres. Dissolution and preservation events, however, may also reflect a transient response to a net flux of organic matter between the continents and the oceans during ice-age climate transitions.

INTRODUCTION

Background

Ocean thermohaline circulation patterns change on glacial-interglacial time scales (e.g., Curry and Lohmann, 1983; Oppo and Fairbanks, 1987; Curry et al., 1988; Raymo et al., 1990). Much of the evidence for these changes comes from stable carbon isotopes, a nutrient-like tracer in benthic foraminifera. Carbon isotopes can be affected by both local/regional circulation and by global shifts in the mean isotopic value of the ocean. This global mean signal also correlates with Pleistocene glacial cycles. Shackleton (1977) suggested that this global signal reflected ice-age deforestation in the world's major rain forests, which would add isotopically light carbon to the atmosphere and ocean. Because the effect described by Shackleton should occur on the same time scales globally, one can look at local circulation effects with carbon isotope gradients. Carbon isotope records from the Atlantic generally indicate a reduction in North Atlantic Deep Water (NADW) production during glacial maxima (Curry and Lohmann, 1983; Curry et al., 1988; Raymo et al., 1990).

SPECMAP (Imbrie et al. 1992, 1993) quantified relationships between several climate proxies and global ice volume (as reflected in oxygen isotope records). SPECMAP found earlier climate transitions in the southern than northern hemisphere, and predicted that deep-water circulation translates early climate transitions from the Nordic Seas to the southern ocean. A problem with this prediction is that reconstructions of deep water circulation (for example %NADW relative to southern source water in the North Atlantic based on carbon isotopes; Raymo et al., 1990) vary with the wrong phase. Can we reconcile these differences? Perhaps the deep water records were too close to the source of North Atlantic Deep Water to track the large-scale circulation of NADW. For example, Mix et al. (1995a) argued that deep-water export from the South Atlantic was decoupled from formation processes in the north. It is this large-scale circulation process that would translate signals between the northern and southern hemispheres as envisioned by Imbrie et al. (1992, 1993). Perhaps the complex blend of records used in the carbon isotope indices, which requires differences between three different stable isotope records, preclude precise phase calculations because the global component of carbon isotope variation is not sufficiently known.

Ceara Rise provides an opportunity to test the SPECMAP hypothesis, because it is bathed at different depths by NADW and Antarctic Bottom Water (AABW), thus monitoring the import of these water masses far from either source. At present, AABW is much more corrosive to calcite, and a strong dissolution gradient marks the deep watermass boundary (Curry and Lohmann, 1990). The dissolution signal, like carbon isotopes, probably contains some global component as well as local watermass component. An argument for dominance by local circulation effects is that carbonate dissolution records from the Atlantic are often out of phase with dissolution events in the Pacific (Crowley, 1985). This would not be expected if the major dissolution signal were global (Peterson and Prell, 1985). Decreased production of NADW or a northward shift of AABW would cause the lysocline to shoal at Ceara Rise, which would cause increased dissolution at depth.

Setting

Ceara Rise is located in the western tropical Atlantic (Figure 3.1). Drill sites, at water depths from ~3.0 to 4.4 km, span the present-day mixing zone between NADW and AABW (Table 3.1). The transition between these water masses is presently between 4.0 and 4.5 km depth, with NADW overlying AABW.

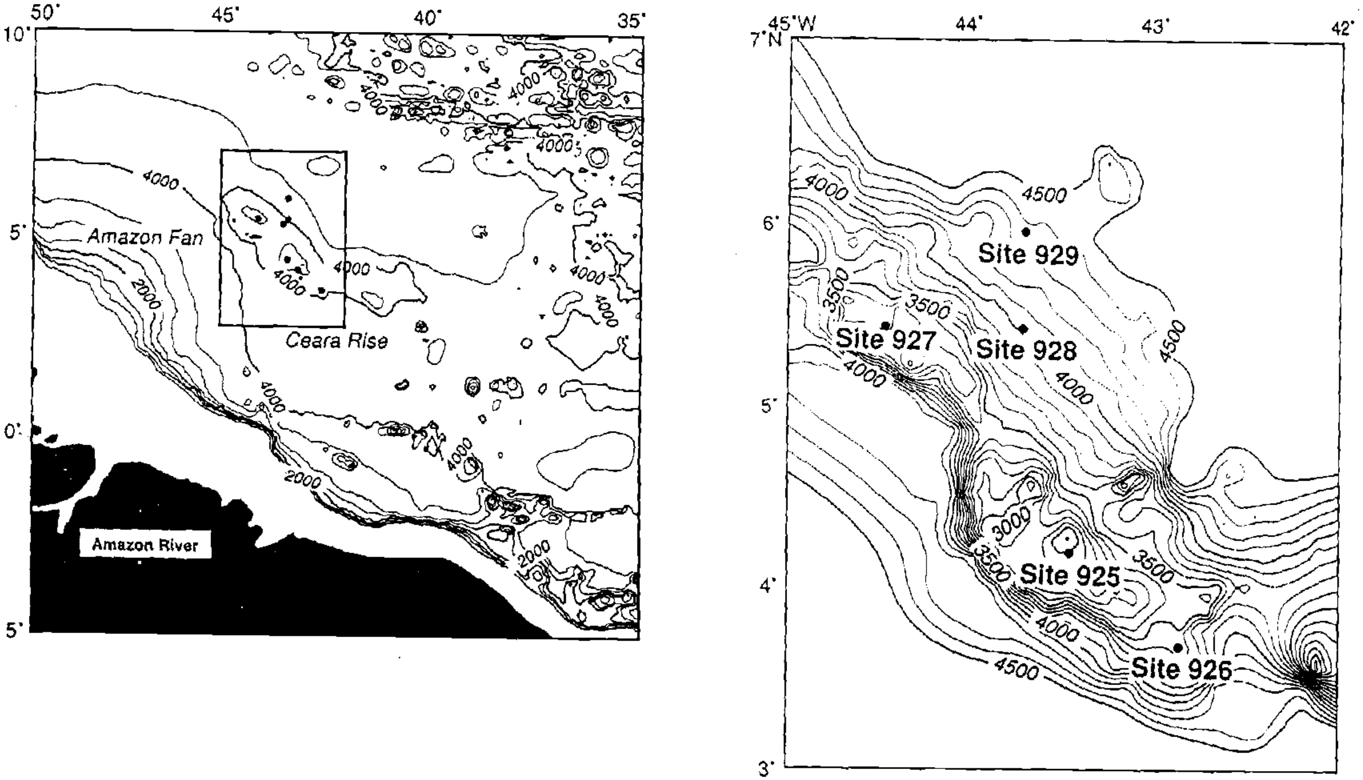

Figure 3.1 Map showing locations and depths of Ceara Rise sites. Dominant sediment types deposited here are biogenic calcium carbonate from surface waters and terrigenous material from South America, primarily from the Amazon drainage. The assumption in drilling this depth transect is that carbonate input from surface water productivity is equal at all sites. See Table 3.1 for water depths.

Table 3.1 Site locations and depths.

Site	Latitude	Longitude	Water Depth (m)
925	4°12'N	43°29'W	3041
926	3°43'N	42°54'W	3598
927	5°28'N	44°29'W	3314
928	5°27'N	43°45'W	4010
929	5°59'N	43°44'W	4358

Sediments on Ceara Rise come from two main sources: biogenic carbonate, produced in the upper water column by calcareous plankton, and terrigenous clays and quartz coming mostly from the Amazon and other South American Rivers, although trace amounts may come from Africa by aeolian transport (Balsam et al., 1995). We assume that the geographic area covered by the sites is small enough that the input of biogenic carbonate from overlying surface waters is approximately equal at all the sites. Differences in accumulation rates of calcite at sites of varying depths can therefore serve as a index of carbonate dissolution.

METHODS

Proxy data

We used nonintrusive proxies (i.e., rapid measurements that do not consume sediment) to construct detailed estimates of sediment variability over long time scales. The proxies, reflectance spectroscopy and magnetic susceptibility, were measured at 5-10-cm intervals (a temporal sampling interval of a few thousand years). This resolution required more than 3000 measurements per site covering the past five million years, more than 15,000 analyses. Such a large number of samples would be inefficient to measure discretely in the laboratory using traditional chemical methods. A trade-off for high temporal resolution and long time series is precision. While errors on laboratory calcium carbonate measurements by coulometer are typically better than 1% (e.g. Ostermann et al., 1990), errors on our proxy estimates average 5.5%. However, given the range of carbonate content in Ceara Rise sediments (0-90%), this precision is acceptable.

Reflectance spectra were measured on split cores using a second-generation automated instrument developed at Oregon State University (an improved version of Mix et al., 1992). This type of instrument was first used in applications to marine sediment cores on Ocean Drilling Program (ODP) Leg 138 in the eastern equatorial Pacific (Mix et al., 1995b). The newer instrument has an expanded wavelength range, higher spectral resolution, and a new detector that provides approximately a 10-fold increase in signal/noise ratios over the prototype instrument used on ODP Leg 138. It measures 1024 channels of reflected light from the unprepared surfaces of split cores. Wavelengths measured range from 250-950 nm (ultra violet-visible-near infrared) with a spectral resolution of 0.68 nm.

During measurement, a split sediment core moves along a track and is measured at specified depth intervals. An integrating sphere with ports for a light source (quartz-tungsten-halogen and deuterium bulbs) and detector (Charge Coupled Device) is automatically lowered to the core surface at each sampling interval. The surface is sensed by an array of electrical conductivity probes and strain gauges. This combination of "landing" sensors provides a means to position the integrating sphere a consistent distance from the core surface. Soft sediment surfaces with low wet bulk density are easily sensed by conductivity probes. More compacted sediment surfaces from deeper sections are often sensed by triggering a strain threshold.

Each reflectance spectrum measurement is a combination of diffuse and specular reflectance from a circle approximately 2 cm in diameter. A light trap for specular reflectance is possible with this instrument, although the surface roughness of unprepared cores makes it difficult to eliminate the specular component. A 2-cm spot is a reasonable sample size to smooth effects of bioturbation (i.e., individual burrows) without seriously degrading the paleoclimatic signal in these sediments.

Percent reflectance is calculated with reference to a background measurement (lights off), an internal white standard (Spectralon®) and 4 external standards with known reflectivities (roughly 2%, 40%, 75%, and 100% reflectance). The external standards are measured in exactly the same way as split core samples, providing a means to calculate percent reflectance through the 0%-100% reflectance range at each wavelength measured.

Reflectance measurements were made during August and September 1994 at the ODP Core Repository in Bremen, Germany, approximately 6 months postcruise. Some oxidation of iron sulfides occurred between April and August, although comparisons to shipboard reflectance measurements (visible range only, 400-700 nm) indicate that the spectra 0-5 Ma were not significantly altered by core storage. Magnetic susceptibility was measured shipboard on whole cores with the Multi-Sensor Track on the JOIDES Resolution. We used a combination of reflectance and magnetic susceptibility to develop proxy carbonate signals.

Calibrating the proxies

Multiple linear regression techniques define empirical relationships between calcium carbonate content and proxy variables. The "ground truth" data used for calibration is about 2200 chemical measurements of calcium carbonate percentages, from four sources (Table 3.2; Curry and Cullen, 1997; King et al., 1997; shipboard measurements in Curry et al., 1995). If reflectance or susceptibility measurements did not match discrete sample depths exactly, but were within 5 cm, we interpolated the proxy data between adjacent samples.

Input terms to the regression fall into three categories: (1) percentage reflectance in block-averaged, 10-nm-wide bands, (2) first derivatives of the reflectance spectrum with respect to wavelength in block-averaged, 10-nm-wide bands, and (3) magnetic susceptibility (in SI units). We also input the square of each variable to allow the regression equations to simulate weak nonlinearity in the relationship to carbonate. Inclusion of squared terms improved statistical relationships in all cases. From all the above input terms, those terms included in the equations (Table 3.3) were selected

Table 3.2 Laboratory percent carbonate analyses.

Sample ID	top (cm)	bottom (cm)	$CaCO_3$ (%)	Sample ID	top (cm)	bottom (cm)	$CaCO_3$ (%)
925A03R1	57	58	50.65	929B01H4	83	85	23.64
926A01H3	62	64	43.53	929B01H4	133	135	17.75
926A02H4	98	100	28.94	929B01H4	53	55	26.06
926A03H6	91	93	27.42	929B01H4	3	5	0.05
926A04H6	97	99	36.19	929B01H4	33	35	11.61
926A05H2	100	102	14.89	929B01H4	23	25	17.91
926A05H6	97	99	40.60	929B01H4	13	15	5.43
926A06H6	66	68	56.63	929B01H4	73	75	32.18
926A07H6	30	32	50.63	929B01H4	93	95	17.76
926A08H6	95	97	40.09	929B01H4	43	45	24.15
926A09H4	18	20	57.28	929B01H4	103	105	2.56
926A10H5	126	128	61.33	929B01H4	143	145	30.51
926A11H6	34	36	71.14	929B01H4	63	65	29.79
926A12H6	64	66	56.79	929B01H4	123	125	12.33
926A13H6	42	44	51.34	929B01H5	143	145	1.15
926A14H7	75	77	68.63	929B01H5	33	35	13.26
926A15H5	10	12	69.95	929B01H5	23	25	32.49
926A16H6	70	72	65.07	929B01H5	123	125	10.07
926A17H6	60	62	48.12	929B01H5	133	135	10.71
926A18H6	89	91	64.91	929B01H5	53	55	14.35
926A19H5	32	34	47.21	929B01H5	13	15	47.74
926A19H6	80	82	41.41	929B01H5	83	85	10.83
926A20H5	108	110	64.30	929B01H5	113	115	12.07
926A21H4	58	60	76.23	929B01H5	73	75	11.15
926A22H4	82	84	76.45	929B01H5	93	95	16.07
926A25H6	15	17	60.01	929B01H5	63	65	17.82
926A26H5	105	107	18.48	929B01H5	43	45	20.85
926A26H5	105	107	18.52	929B01H5	3	5	44.54
926A26H6	44	46	2.90	929B01H5	103	105	13.91
926A27H6	24	26	64.32	929B02H5	115	117	0.17
926A28H6	29	31	23.62	929B02H5	95	97	9.78
926B17H5	98	100	70.28	929B02H5	75	77	24.57
926B18H5	97	99	62.89	929B02H5	125	127	1.64
926B19H5	58	60	64.25	929B02H5	65	67	19.86
926B20H5	70	72	46.09	929B02H5	135	137	27.73
926B22H3	121	123	58.18	929B02H5	35	37	9.38
926B24H5	121	123	69.61	929B02H5	145	147	49.04
926B27H3	121	123	53.05	929B02H5	105	107	11.21
926B36X3	61	63	64.89	929B02H5	45	47	1.31
926B37X4	129	131	68.16	929B02H5	85	87	7.27
926B41X4	28	30	60.76	929B02H6	15	17	42.12
926B43X5	61	64	68.62	929B02H6	5	7	46.08
926B45X5	79	81	82.07	929B02H6	15	17	0.39
926B46X6	35	37	52.55	929B02H6	145	147	9.88
926B47X6	77	79	69.21	929B02H6	55	57	4.95
926B48X5	88	91	73.15	929B02H6	65	67	8.22
926C01H2	104	106	32.84	929B02H6	75	77	6.75
926C01H2	94	96	24.61	929B02H6	125	127	23.57
926C01H2	144	146	20.47	929B02H6	115	117	16.66
926C01H3	94	96	33.85	929B02H6	85	87	6.37
926C01H4	144	146	49.63	929B02H6	135	137	15.46
926C01H4	74	76	43.13	929B02H6	95	97	2.52
926C01H4	34	36	25.39	929B02H6	35	37	11.67
926C08H6	72	74	63.01	929B02H6	45	47	5.02
926C15H5	12	14	70.05	929B02H6	25	27	37.41
926C15H5	52	54	79.61	929B02H6	105	107	11.01
926C15H5	72	74	67.59	929B14X5	25	27	23.99

Table 3.2 continued

Sample ID	top (cm)	bottom (cm)	$CaCO_3$ (%)	Sample ID	top (cm)	bottom (cm)	$CaCO_3$ (%)
927A23H4	136	138	60.31	929B14X5	45	47	28.34
929A01H1	24	26	42.96	929C01H4	84	86	16.15
929A01H1	4	6	52.21	929C01H4	64	66	9.25
929A01H1	44	46	11.11	929C01H4	24	26	15.67
929A01H1	44	46	11.49	929C01H4	54	56	8.79
929A01H1	14	16	55.47	929C01H4	74	76	21.72
929A01H1	124	126	20.52	929C01H4	114	116	19.04
929A01H1	64	66	13.40	929C01H4	94	96	11.90
929A01H1	34	36	30.95	929C01H4	144	146	12.66
929A01H1	54	56	11.58	929C01H4	14	16	11.85
929A01H1	74	76	16.47	929C01H4	134	136	14.29
929A01H1	94	96	11.49	929C01H4	124	126	12.42
929A01H1	84	86	11.76	929C01H4	34	36	10.98
929A01H1	114	116	12.37	929C01H4	104	106	17.37
929A01H1	134	136	16.85	929C01H4	44	46	3.02
929A01H1	144	146	21.05	929C01H5	54	56	31.40
929A01H1	104	106	13.31	929C01H5	74	76	0.64
929A01H2	142	144	3.79	929C01H5	94	96	22.52
929A01H2	64	66	2.76	929C01H5	44	46	17.30
929A01H2	104	106	18.09	929C01H5	114	116	35.48
929A01H2	14	16	20.90	929C01H5	24	26	18.50
929A01H2	44	46	18.67	929C01H5	124	126	41.70
929A01H2	24	26	7.98	929C01H5	4	6	5.53
929A01H2	4	6	18.89	929C01H5	134	136	46.80
929A01H2	54	56	10.46	929C01H5	84	86	3.20
929A01H2	114	116	10.28	929C01H5	144	146	33.10
929A01H2	94	96	8.06	929C01H5	34	36	1.64
929A01H2	124	126	22.28	929C01H5	104	106	27.74
929A01H2	34	36	15.15	929C01H5	64	66	10.44
929A01H2	134	136	13.82	929C01H5	14	16	14.50
929A01H2	84	86	0.70	929C01H6	94	96	23.27
929A01H2	74	76	3.62	929C01H6	144	146	26.55
929A01H3	44	46	1.90	929C01H6	14	16	7.65
929A01H3	34	36	5.79	929C01H6	84	86	31.29
929A01H3	64	66	0.07	929C01H6	34	36	0.66
929A01H3	4	6	18.22	929C01H6	64	66	37.42
929A01H3	64	66	0.07	929C01H6	114	116	15.76
929A01H3	14	16	27.43	929C01H6	24	26	24.01
929A01H3	54	56	0.07	929C01H6	4	6	9.17
929A01H3	24	26	19.65	929C01H6	134	136	25.53
929A03H2	50	52	47.95	929C01H6	44	46	8.62
929A03H2	50	52	47.93	929C01H6	104	106	20.37
929A03H3	50	52	7.22	929C01H6	54	56	27.34
929A03H3	50	52	7.40	929C01H6	74	76	47.38
929B01H3	133	135	16.56	929C01H6	124	126	23.35
929B01H3	103	105	9.76	929C01H7	84	86	0.03
929B01H3	63	65	2.32	929C01H7	64	66	0.06
929B01H3	73	75	3.10	929C01H7	4	6	28.97
929B01H3	83	85	0.15	929C01H7	44	46	8.11
929B01H3	123	125	27.70	929C01H7	14	16	28.85
929B01H3	93	95	8.05	929C01H7	24	26	28.36
929B01H3	113	115	15.01	929C01H7	74	76	0.04
929B01H3	143	145	0.58	929C01H7	34	36	26.57
929B01H4	113	115	5.27	929C01H7	54	56	0.15

Table 3.3 Regression equations for estimating % calcium carbonate.

Equation No.	Site (depth*)	N	Terms**	Coefficient	Intercept	r^2	RMSE (%)
1	925 (shallow)	416	R440	3.01	17.92	0.74	6.6
			MS	-1.96			
			MSsq	0.035			
2	926 (shallow)	347	R540	6.00	-17.02	0.75	6.2
			MS	-2.55			
			MSsq	0.0435			
			R540sq	-0.0870			
			D760sq	9117.86			
3	927 (shallow)	431	R890	2.62	-21.86	0.71	5.8
			D550	-210.33			
			D510	265.57			
			D520sq	-1293.04			
4	928 (shallow)	434	R920	4.26	-41.75	0.69	6.8
			D560	-324.24			
			D500	456.21			
			D480sq	10332.27			
			D610	701.39			
			D650	-621.00			
			R920sq	-0.03			
5	929 (shallow)	157	R900	-7.89	6.47	0.81	5.5
			MS	-1.51			
			MSsq	0.017			
			D620	1244.35			
			R550	10.87			
			D600	1167.43			
			D600sq	-14065.62			
			D400sq	194.57			
6	925 (moderate)	131	MS	-0.712	46.40	0.80	4.2
			R480	7.58			
			D640sq	61108.15			
			D450	177.76			
			R490	-6.76			
7	926 (moderate)	155	R470	6.91	40.43	0.76	4.7
			R450sq	-0.113			
			D830	136.48			
			D600sq	56831.16			
			D540	-1550.58			
			D770	319.11			
			D540sq	7280.53			
			D600	-1018.20			
8	All (moderate)	337	R860	7.14	-71.18	0.76	5.6
			R750sq	-0.26			
			R880sq	0.17			
			D840sq	-7881.54			
			D450	107.11			
			D600sq	9800.72			
9	All (deep)	156	R650	13.59	-29.97	0.91	4.1
			R650sq	-0.05			
			MS	-0.82			
			R920	5.68			
			R690	-13.94			
			R440	-0.88			
10	All samples	2287	R640	5.62	-31.19	0.83	7.6
			D530sq	1428.03			
			R640sq	-0.05			
			D530	-437.37			
			MS	-0.62			
			MSsq	0.002			

Notes: * Depth refers to depth below sea floor. ** Term Codes: R = % reflectance term; D = first derivative of reflectance term; MS = magnetic susceptibility; sq = squared term; numbers are wavelengths in nm (e.g. R260sq = the square of %reflectance in an averaged 10-nm-wide band centered at 260 nm).

step-wise, beginning with the term most highly correlated with measured % $CaCO_3$. Terms were retained in regression equations only if significant above a 95% confidence level.

Why use reflectance and susceptibility together? Percent reflectance is a measure of "brightness" at a specific wavelength. Calcium carbonate is highly reflective across our wavelength range (Gaffey, 1986). Other trace components, for example biogenic opal, are also highly reflective. Many noncarbonate constituents (such as clays, oxides) are less reflective than carbonate, but may have a variety of spectral shapes. Percent reflectance is positively correlated with carbonate content and is the dominant term in all but one estimating equation reported here (Table 3.3, Equation 6). The first derivative of the reflectance spectrum with respect to wavelength measures spectral shape, or changes in slope, which are affected primarily by noncarbonate sedimentary constituents, for example, iron oxides and oxyhydroxides (Deaton and Balsam, 1991). Magnetic susceptibility is roughly inversely correlated with carbonate content, since pure calcium carbonate has low susceptibility. It has different biases than reflectance, for example, it may be affected by sedimentary redox conditions. We found that the combination of these variables yields a more accurate estimate of calcium carbonate than any variable type alone.

The strategy used on Leg 138 (Mix et al., 1995b) for developing transfer functions was to divide the groundtruth data set into two parts: a calibration data set, from which a regression equation was developed, and a verification data set, which was used to test the equation using data not included in the initial regression. After early tests with this approach, which showed (1) that our calibrations work on uncalibrated data sets, and (2) the appropriate variables and number of terms in an equation, we combined these two subsets of the groundtruth data to obtain more robust results.

Time series analysis methods

We compare a dissolution index and a terrigenous dilution index with global ice volume (a Pacific benthic oxygen isotope record) in the frequency domain. All spectra were calculated using fast Fourier transform techniques (Bloomfield, 1976). Evolving spectra are compilations of approximately 80 power spectra. Each individual spectrum was calculated from a 1 m.y.-long time series beginning with 0-1 Ma. Successive time series overlap by all but 50 k.y. Overlapping the time series means that adjacent individual frequency spectra are not independent, but this presentation shows the frequency evolution of these signals over the past 5 m.y. The age scales on evolving spectra represent the mean age of the time series chosen for spectral analyses (i.e., 0.5 Ma indicates the average power spectrum for 0-1 Ma).

RESULTS

Our strategy is to develop high resolution time series of carbonate dissolution and noncarbonate dilution indices via comparisons of the proxy carbonate records among Ceara Rise sites. Steps to this end include (1) estimating proxy carbonate over the past 5 m.y., (2) expressing the proxy time series for each site on a common depth and age scale, (3) developing mass accumulation rate ratios for carbonate and noncarbonate, and (4) comparing these relative mass accumulation rates to global ice volume changes in the frequency domain.

Calibrating the equations

The groundtruth carbonate percentage data set was subdivided in three ways: by site, by depth-in-hole, and by latitude. In the shallowest cores (i.e., cores 1H-4H from multiple holes at one site), where many groundtruth samples were measured, better statistical results were obtained by separating the data by site than by combining data from different sites. The logic behind separating the calibration data set by depth-in-hole is (1) the amplitude of the magnetic susceptibility signal decreases downcore (a compaction effect), and (2) the dominant component in the noncarbonate fraction of the sediment changes downcore. By grouping data in depth (or time) the effects of compaction and changing noncarbonate sedimentation on reflectance and susceptibility are partially defrayed. Three calibration equations include data from more than one site. Data from moderate depths (approximately cores 7H-12H) were grouped (Equation 8), data from deep cores (13H or deeper) were grouped (Equation 9), and Equation 10 (Figure 3.2) includes all data from all sites.

Root-mean-square errors (RMSE) for equations 1-9 range from ±4% to ±7%. Equations from more deeply buried intervals generally have the smallest errors (Table 3.3). Ranges of measured carbonate values are also smaller in these data sets because few measured values had less than 20% $CaCO_3$. The low RMSE estimates for equations 6, 7, 8, and 9 are due partially to limited ranges of carbonate values. The fraction of variance explained (r^2) in each calibration ranges from 0.69 to 0.91 (Table 3.3). A significant fraction of the estimated error in the calibration is due to slight depth mismatches among the proxy and groundtruth data sets. Thus the RMSE values reported here are probably worst-case estimates

These RMSEs compare favorably with previous efforts. Using similar techniques, the RMSE was 9.3% for estimating carbonate in the eastern Equatorial Pacific, where the carbonate signal is complicated by both opal and terrigenous sedimentary components (ODP Leg 138; Mix et al., 1995b). Lower errors here are partially due to the new instrumentation (see methods section) and probably also due to the simpler sedimentary regime at Ceara Rise. Balsam and Deaton (personal communication, Sept., 1994) were able to estimate carbonate to within 6% at ODP Site

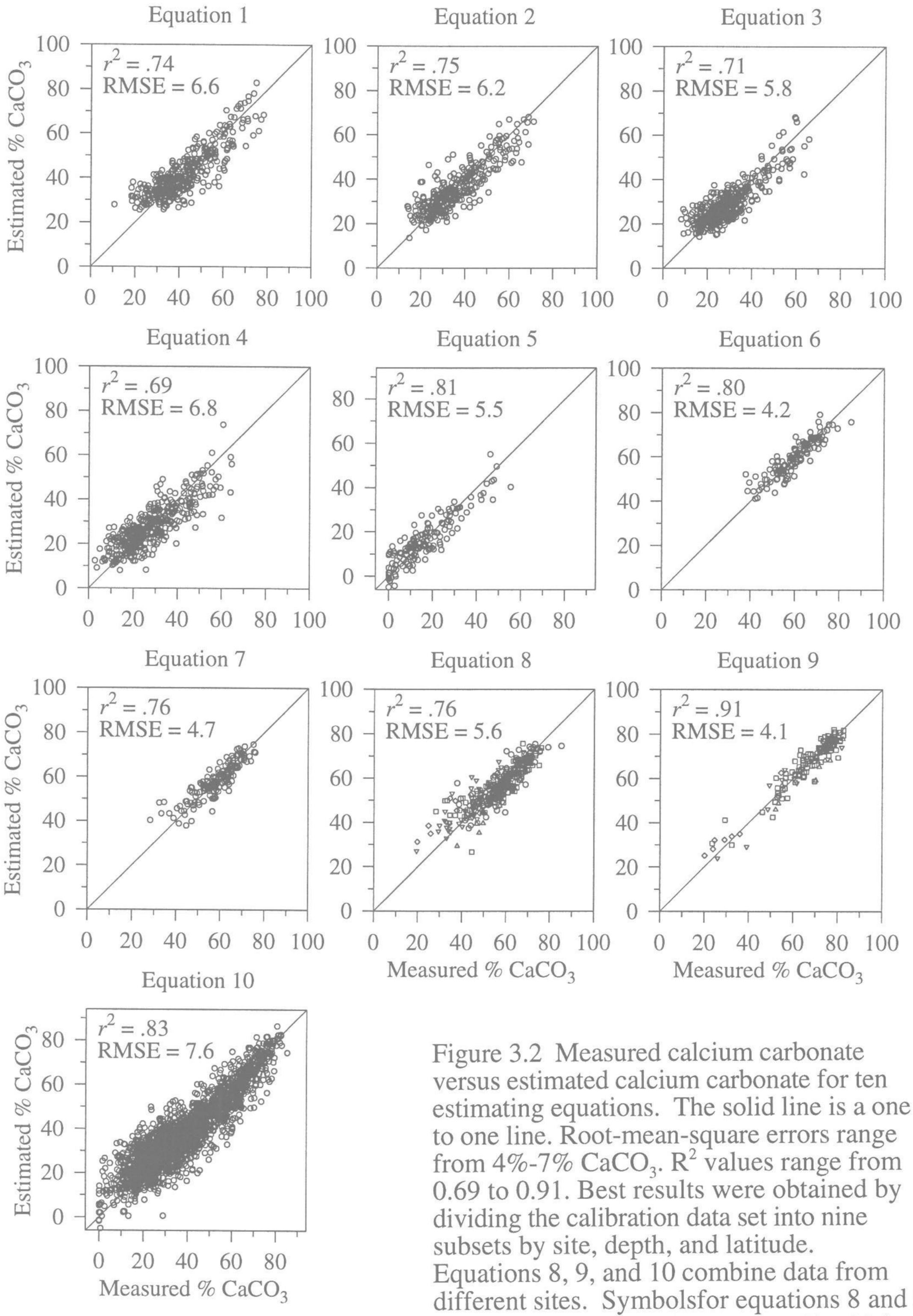

Figure 3.2 Measured calcium carbonate versus estimated calcium carbonate for ten estimating equations. The solid line is a one to one line. Root-mean-square errors range from 4%-7% $CaCO_3$. R^2 values range from 0.69 to 0.91. Best results were obtained by dividing the calibration data set into nine subsets by site, depth, and latitude. Equations 8, 9, and 10 combine data from different sites. Symbolsfor equations 8 and 9 are: circles = Site 925; squares = Site 926; triangles pointing up = Site 927; triangles pointing down = Site 928; diamonds = Site 929;. Equation 10 is a regional calibration including all data from all sites. See Tables 3.3, 3.4, and 3.5 for details and statistics of equations.

847 in the equatorial Pacific, using laboratory reflectance measurements on dried powdered samples, similar to our results.

Low carbonate values are most difficult to estimate, and have the largest residuals (Figure 3.2). In these samples, carbonate contents are often overestimated. This may be because both susceptibility and reflectance depend on the type of noncarbonate constituents present, which becomes important when the non-carbonate components dominate the total.

One might expect the best estimating equation to include all available laboratory data, thus increasing the degrees of freedom. Such a strategy seems reasonable in a limited geographical area such as Ceara Rise where the patterns of sedimentation are relatively simple (i.e., a balance between biogenic carbonate and terrigenous material). The equation including all the data (Equation 10, Figure 3.2, Table 3.3) has an r^2 of 0.83, the second highest of the ten equations, and an RMSE of ±7.6%, which is about 2% greater than our average error obtained using more localized data sets. Our experiments indicate that better results (in terms of error) can be obtained by limiting our calibration data sets in space and time as described above. This suggests that significant differences in the mineralogy of sediment sources exist even within this relatively small area.

Sources of variability on Ceara Rise alone may be related to proximity to the Amazon Fan (the northern sites receive more terrigenous material than the southern sites) or compositional differences in the terrigenous fraction over time. These differences within a relatively small area imply that a global carbonate proxy based on reflectance and susceptibility is unlikely to be as accurate as local calibrations. The calibrations obtained here thus will probably not apply to different and more complex sedimentary regimes, such as those including significant fractions of opal or organic matter. Balsam and Deaton (pers. comm., Sept., 1994) noted the difficulty of obtaining an accurate regional carbonate calibration when they combined coretop and last glacial maximum (LGM) samples from sites throughout the Atlantic basin. They were able to estimate % $CaCO_3$

with an RMSE = 11% using prepared discrete samples. Given the better success of their technique at a single site, Site 847, they note that the Atlantic calibration suffers from interaction with varying noncarbonate constituents.

A simple comparison of the ten equations is to apply each to the other nine data sets and compare the fraction of variance explained, r^2 (Table 3.4). As expected, the highest r^2 values between measured and estimated % carbonate for a given data set are obtained using the equation based on those data (the diagonal of Table 3.4). Two equations (6 and 7) give poor estimations of other data sets, down to r^2 equal to zero for equation 7 applied to data set 9. The most robust equation is equation 10, based on an average r^2 across the 10 data sets (Table 3.4, column 11). This equation can be considered a regional calibration equation that could be applied to any Ceara Rise sediments. The tradeoff for stability is a higher error associated with equation 10.

What do our regression equations have in common? Most of the ten equations choose as their dominant term reflectance in either the lower visible wavelengths (440-540 nm) or the near infrared (860-920 nm). Magnetic susceptibility is the first or second term in 4 equations. Equations at adjacent sites, for example Site 925 and 926 (Equations 1 and 2) tend to be similar. Differences in the equations indicate that a variety of different minerals dilute carbonate and that the reflectance bands are not unique.

The common features in the equations highlight general relationships between carbonate content and the proxies. The variable most highly correlated to carbonate in these equations is usually some term for percentage reflectance (of differing wavelength) with a small positive coefficient. A positive relationship to reflectance is logical given the high reflectivity of calcium carbonate. All coefficients for susceptibility are negative in keeping with the general inverse relationship between magnetic susceptibility and carbonate content. Susceptibility squared has small positive coefficients in 4 equations.

Table 3.4 r^2 values for each equation applied to each calibration data set.

Burial	Shallow					Moderate			Deep	all	
Sites	925	926	927	928	929	925	926	all	all	all	
Data set No.	1	2	3	4	5	6	7	8	9	10	Mean
Equation No.											
1	0.74	0.71	0.65	0.55	0.32	0.71	0.01	0.02	0.70	0.09	0.45
2	0.72	0.75	0.67	0.60	0.40	0.73	0.01	0.01	0.77	0.06	0.47
3	0.68	0.68	0.71	0.64	0.60	0.68	0.65	0.66	0.71	0.74	0.68
4	0.69	0.67	0.70	0.69	0.65	0.55	0.54	0.61	0.48	0.69	0.63
5	0.65	0.64	0.65	0.61	0.81	0.70	0.02	0.06	0.63	0.29	0.51
6	0.09	0.07	0.21	0.12	0.33	0.80	0.08	0.22	0.41	0.18	0.25
7	0.12	0.07	0.23	0.13	0.19	0.72	0.76	0.66	0.00	0.19	0.31
8	0.41	0.34	0.58	0.47	0.48	0.75	0.71	0.76	0.18	0.55	0.52
9	0.64	0.65	0.61	0.59	0.60	0.73	0.13	0.34	0.91	0.72	0.59
10	0.71	0.70	0.68	0.60	0.60	0.72	0.73	0.72	0.88	0.83	0.72

Notes: Equations and data sets are grouped by depth. Data set numbers correspond to equation numbers (the data set used to calibration an equation). On the diagonal of the matrix are r^2 values for each equation applied to the corresponding calibration data set. The highest columnwise r^2 values are on the diagonal. The most robust equation based on mean r^2 is equation 10, which includes all data from all sites.

This squared term may be helpful in constraining the low end of estimated carbonate values.

Equations 3 and 4 have the highest mean r^2 of the first nine equations (0.68 and 0.63 respectively), and do not share the features of the other 3 "shallow" equations beyond the first percent reflectance term (Table 3.3). The second term in these equations, the first derivative at 550 nm and 560 nm with a negative coefficient, may be a clue to their success when applied to the other data sets. The first derivative near 550 nm is likely to be affected by the presence of iron oxides and oxyhydroxides (Deaton and Balsam, 1991). These constituents are present in higher amounts in low carbonate intervals, and color the sediment brownish-red. Most of the sediments included in this study (0-5 Ma) are oxidized. Equations 3 and 4 therefore may record the presence of oxides in the noncarbonate fraction. This feature is common to all the sites over the time period studied, but may have a nonlinear relationship to carbonate, which could yield different sensitivities in different equations.

Data used to develop equations 1-5 cover the same sediment burial depth range at each of the five sites (Cores 1H-4H). Correlation trends (upper left corner of Table 3.4; 5 by 5 matrix) have some dependence on site depth and location. For example, $r^2 = 0.71$ for equation 1 (Site 925) applied to data set 2 (Site 926). These two sites are located at the southern end of Ceara Rise and are geographically closest to one another. Correlations for the equation used in Site 925 (Equation 1) applied to the remaining sites follow a water depth trend with the next highest correlation to data set 3 (Site 927, $r^2 = 0.65$) and the lowest correlation with data set 5 (Site 929, $r^2 = 0.32$). Equation 2 (Site 926) follows a pattern similar to that of equation 1. Equation 3 (Site 927) exhibits its highest correlations with the data sets from other shallow sites (Sites 925 and 926, data sets 1 and 2). However, it does a better job with the deepest site data (Site 929, data set 5) than with data from Site 928 (data set 4) which is closer in depth and geography. Its higher correlation with the data set from Site 929 may mean that these two sites receive a similar terrigenous component from the Amazon Fan.

Down-core estimates

We estimated percent calcium carbonate content down-core at each site using equations 1-9 (Figure 3.3). The equations used for each range in depth and time at each site are tabulated in Table 3.5. Because these equations were calibrated in limited space and depth, transitions between equations at depth were necessary for each site. For intervals with gaps in laboratory carbonate data, (such as between "shallow" and "moderate" depth equations) we applied the two equations calibrated to either side of the gap and switched between regression equations where carbonate estimates given by these two equations were equal. Otherwise, the equation applied to a particular section of core was calibrated on data from that core.

Time series of estimated carbonate are visually similar among the sites. Using the orbitally tuned age models of Bickert et al. (1997) and Tiedemann and Franz (1997), most carbonate events occur synchronously at all locations. Assuming that the shallowest site (Site 925 at 3041 m) which is presently well above the regional lysocline, has undergone minimal dissolution for this period, the similarity of %$CaCO_3$ variations at all depths implies that the first order carbonate cyclicity is primarily a productivity and/or dilution signal rather than a dissolution signal.

Although the shapes of the signals at all sites are similar, the range of carbonate values changes considerably with depth. Carbonate at the shallowest site (925) ranges from about 20%-80%, while at the deepest site (929) the range is about 0%-65%. This difference could reflect either enhanced dilution at depth due to preferential input of noncarbonate material to the deeper sites, and/or to enhanced dissolution of carbonate at depth. To isolate these processes, we analyze the relative mass accumulation rates of

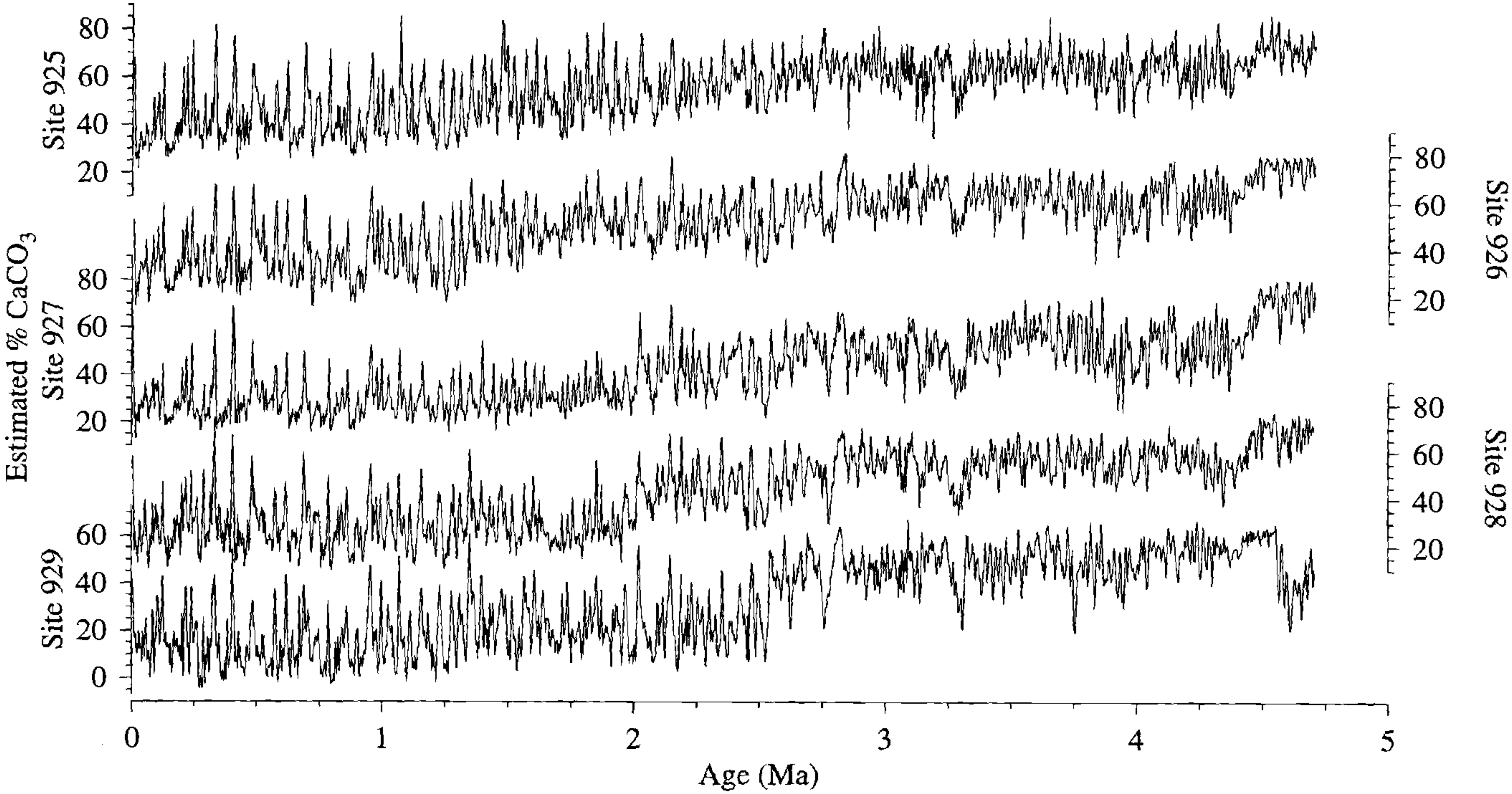

Figure 3.3 Downcore estimates of % calcium carbonate, 0-5 Ma, Sites 925-929 represented on orbitally tuned age models for each site (see Bickert et al., 1997 and Tiedemann and Franz, 1997). Major carbonate events appear to occur synchronously across the depth transect, although the average carbonate content at shallow sites (925-927), is higher than the average % carbonate at the deeper sites. These differences are due to a combination of dissolution of carbonate at depth and dilution by terrigenous material primarily at the northern sites.

Table 3.5: Age and depth ranges for equations.

Site	Equation No.	Depth range (mcd)	Age range (Ma)
925	1	0-65.03	0-2.025
925	6	65.03-147.91	2.025-4.710
926	2	0-48.98	0-1.585
926	7	48.98-115.88	1.585-3.731
926	9	115.88-154.07	3.731-5.009
927	3	0-78.23	0-2.023
927	8	78.23-137.40	2.023-3.784
927	9	137.40-173.75	3.784-5.008
928	4	0-65.26	0-2.027
928	8	65.26-133.73	2.027-4.269
928	9	133.73-150.11	4.269-5.005
929	5	0-83.82	0-2.545
929	8	83.82-133.25	2.545-4.541
929	9	133.25-138.86	4.541-4.908

carbonate and noncarbonate components at the deep and shallow sites, assuming equal export production of carbonate shells to all sites.

Depth-depth correlations

Our operational goal is to compare carbonate and non-carbonate accumulation rates across the depth transect on orbital time scales. This could be done in two ways. First, one could create a detailed age model in each site, calculate mass accumulation rates of each sedimentary component, and then compare absolute rates between sites. This method is not feasible, because age models are not sufficiently accurate in all sites to calculate absolute accumulation rates with sufficient precision. Second, one could correlate records between sites in the depth domain, calculate the relative depth intervals occupied by a correlated event (i.e., the fractional accumulation rate relative to some reference site), and then apply an age model to this record. The assumption here is that events expressed as variations in sedimentary composition are correlated in time. We use this second method, because it allows much higher time resolution of events and provides robust estimates of relative accumulation rate independent of age model. If age models are improved in the future, the relative accumulation rate estimates made here can simply be re-cast onto the new time scale without changing their structure or amplitude.

A simple example to illustrate our strategy is shown in Figure 3.4. Figure 3.4A illustrates a simple time series, a “distorted” signal, with labeled "events" (maxima and minima) which correspond to the events in a reference signal. Note that events "a" and "b" in the distorted signal occur shallower in depth than the same events in the reference signal. Event "c" occurs at a similar depth in both series, and events "d" and "e" occur shallower in the reference signal. Assuming that the events are synchronous, we can "map" one signal to the other in depth. The depth-depth map for these two signals is shown in Figure 3.4B (solid line). The straight dashed line represents the original linear

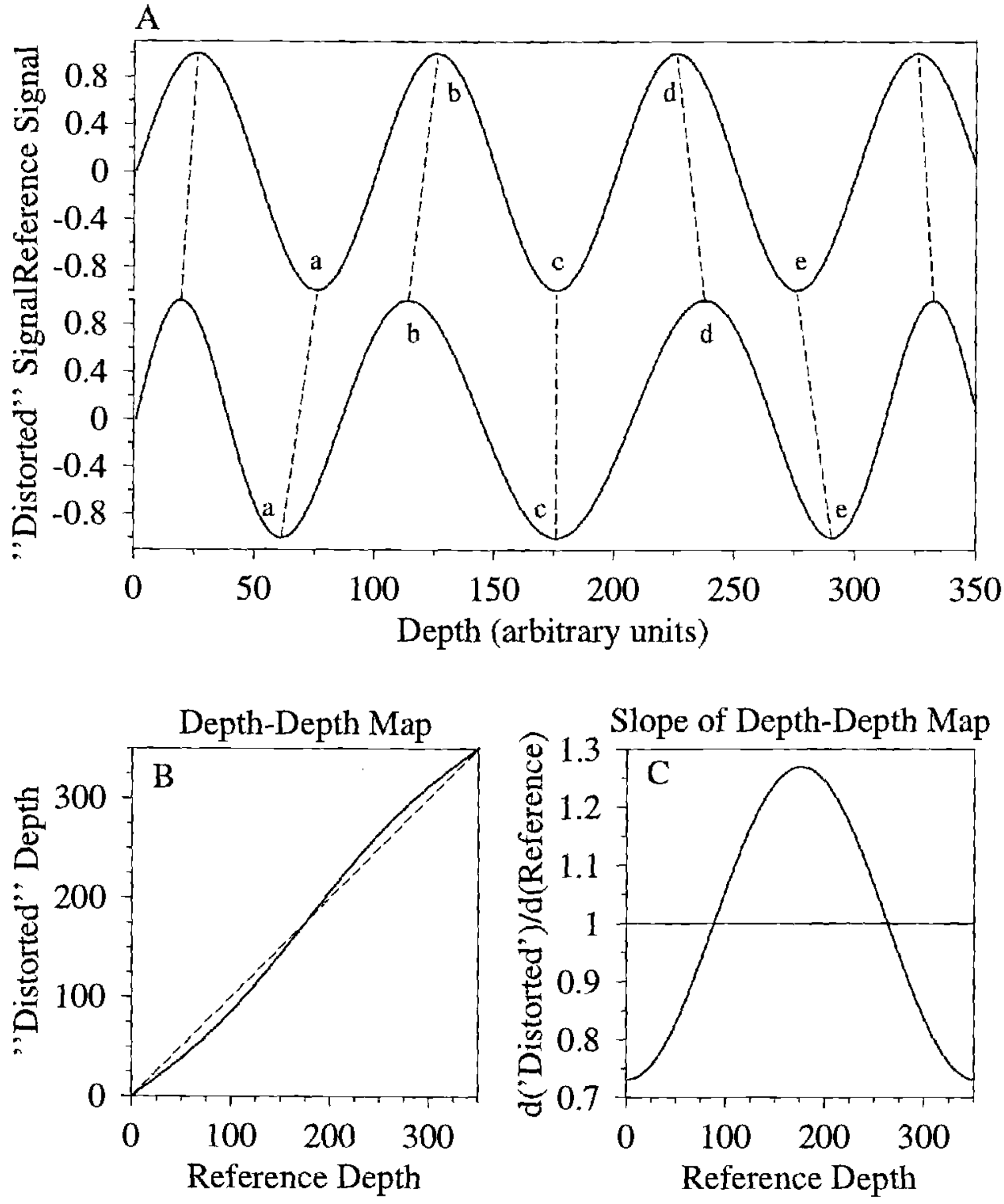

Figure 3.4 Example of depth-depth correlation strategy. (A) A "distorted" signal correlated with dashed lines to a "reference" signal, (B) a depth-depth mapping function of the "distorted" to "reference" signal, (C) the slope of the depth-depth map, or the relative sedimentation rate. See text for details.

depth-depth relationship. The map crosses the dashed line at event "c" which is synchronous in depth. The slope (or first derivative) of the curved line in Figure 3.4B is the relative sedimentation rate, or the sedimentation rate for the distorted signal/sedimentation rate for the reference signal (Figure 3.4C). The slope of the depth-to-depth mapping function equals one where the sedimentation rates for the two signals are equal (at about 75 and 275 in arbitrary depth units). Where the slope is greater than one (the center part of Figure 3.4C), the sedimentation rate is higher for the distorted signal. Where the slope is less than one, the sedimentation rate is higher for the reference signal (the ends of Figure 3.4C). If, for example, the reference is a "shallow" site and the distorted signal is a "deep" site, then the center part of Figure 3.4C could represent dilution of the carbonate signal at the "deep" site relative to the reference site (extra sediment). The ends of Figure 3.4C could represent dissolution at the "deep" site relative to the shallow site (removal of material).

To put all the sites onto a common depth scale, we correlated the %carbonate records from each site to the record at Site 926, using the mcd (meters composite depth) scale from all cores (Figure 3.5). Correlations of records are continuous, using inverse correlation method of Martinson et al. (1982). Site 926 is a reasonable choice for a depth reference site because it is intermediate in water depth among the sites and has the longest record of the reflectance proxy.

Relative sedimentation rates

Once all the sites are expressed relative to a common depth scale (that of Site 926) we can compare sedimentation rates at all the sites relative to any chosen reference. We choose Site 925 as the reference for relative sedimentation rate (Figure 3.6) because as the shallowest site it has experienced the least carbonate dissolution of any of the sites. Relative sedimentation rates are defined as $d(\mathrm{depth}_{92*})/d(\mathrm{depth}_{925})$, where 92* means

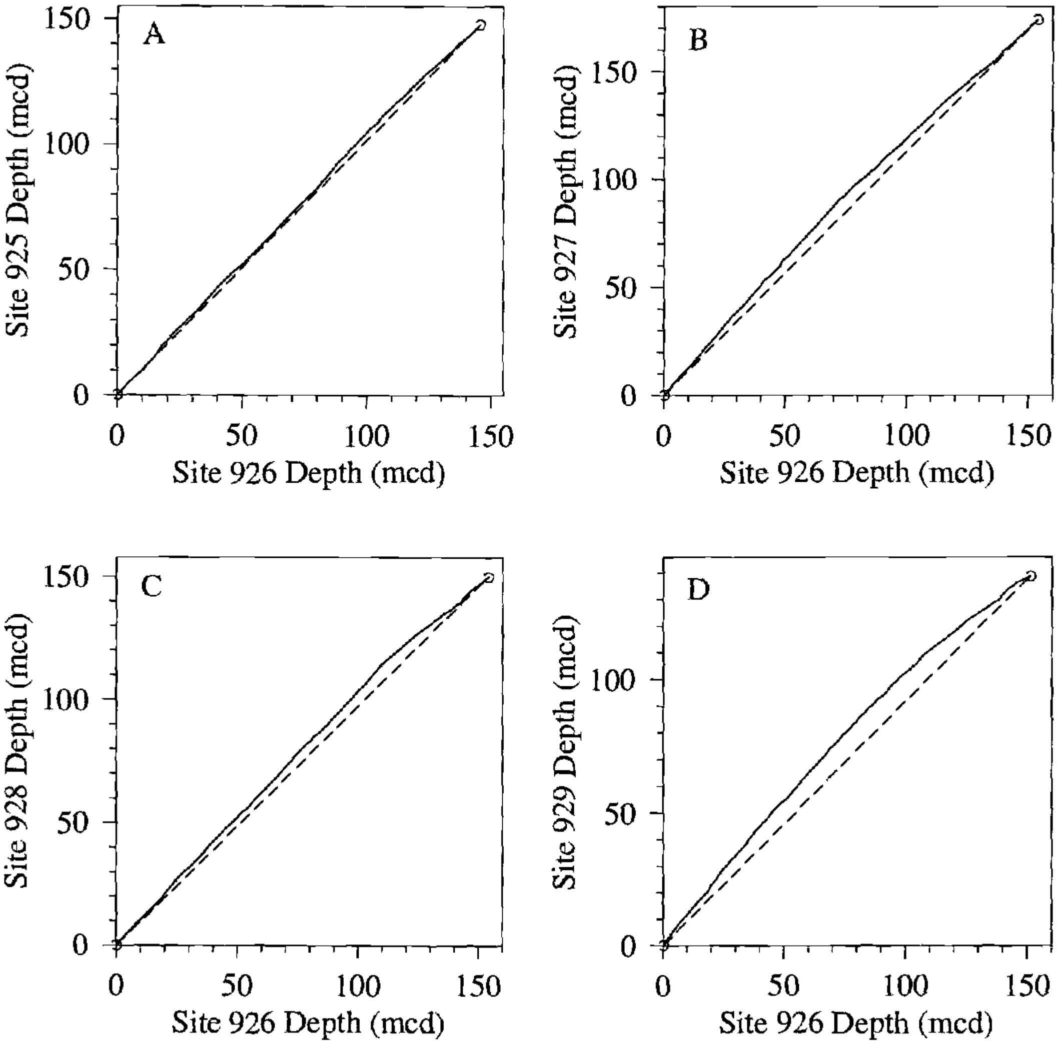

Figure 3.5 Depth-depth correlations in meters composite depth. Sites 925 (A), 927 (B), 928 (C), and 929 (D) estimated carbonate time series were mapped in depth to Site 926, using the strategy shown in Figure 3.4. The age scale is the orbitally tuned age model for Site 926 (see Bickert et al., 1997, and Tiedemann and Franz, 1997). Solid curves represent the depth-depth correlations. Straight dashed lines represent a linear mapping, matching endpoints only.

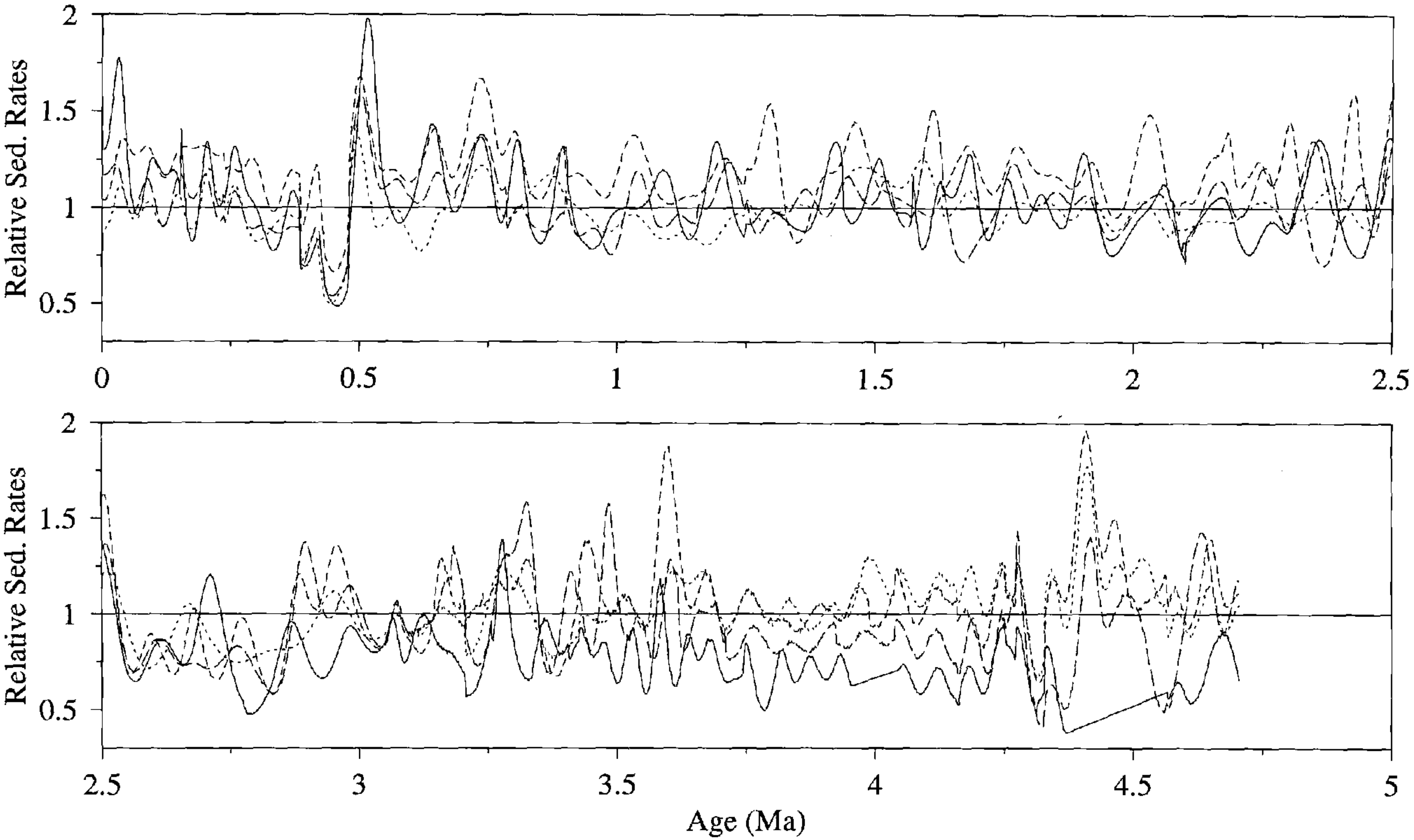

Figure 3.6 Relative sedimentation rates, 0-5 Ma. All sites are relative to 925, which is represented by the horizontal line at one. Small dash = Site 926/Site 925; Medium dash = Site 927/Site 925; Large dash = Site 928/Site 925; Solid = Site 929/Site 925. The relative sedimentation rates for Sites 927 and 929 are highest and most variable throughout the Pleistocene (1.8-0 Ma). Pre-3.6 Ma, relative sedimentation rates drop at the deeper sites indicating a dissolution dominated signal at depth.

926, 927, 928, or 929. Thus values greater than one mean higher sedimentation rates, and values less than one mean lower sedimentation rates than those from equivalent ages in Site 925. These relative sedimentation rates are subsequently represented on the Site 926 age model (Bickert et al., 1997; Tiedemann and Franz, 1997).

The relative sedimentation rates for two of the northern sites (927 and 929 relative to 925) are greater than one during the Pleistocene (Figure 3.6). High relative rates at these sites usually occur during glacial stages (as defined by oxygen isotopes). Both sites are deeper than Site 925 and therefore should be equally or more dissolved than the reference. Site 929 is the deepest site and is most likely to undergo dissolution. Regardless of a possible dissolution signal at depths greater than the reference site, the higher sedimentation rates at Sites 927 and 929 must be due to a greater influx of terrigenous material. This inference makes sense given the proximity of these Sites to the Amazon Fan. During glacial periods, lowered sea level would decrease the distance from the shelf edge to Ceara Rise, making increased transport of terrigenous material to the northern sites likely.

Sedimentation rates at Site 928 are similar to those at Site 925 during the Pleistocene (relative rates near 1.0). Site 928, although north of Site 925, is located upslope of Site 929 and is "shadowed" from the Amazon Fan by the ridge of Ceara Rise (Figure 3.1). The similarity of sedimentation rates at Sites 928 and 925 could either be due to (1) similar accumulation of both carbonate and terrigenous material at the two sites, i.e., no extra dissolution at the deep site and the same influx of terrigenous material to both sites, or (2) a coincidental balance of greater carbonate dissolution and terrigenous dilution both affecting Site 928. The following discussion of relative mass accumulation rates supports the second option.

Site 926 also has sedimentation rates similar to Site 925 throughout most of the Plio-Pleistocene. These two sites are located closest geographically at the southern end of

Ceara Rise and are farthest from the Amazon Fan, thus likely to receive less terrigenous material.

The earliest part of the record, from about 5-3.5 Ma, has a different relationship in relative sedimentation rates than the Pleistocene. Relative sedimentation rates generally decrease with depth during this period, with the lowest relative rates occuring at Site 929. Downslope transport of both carbonate and terrigenous material could cause some redistribution of sediments on Ceara Rise. However, downslope transport should increase sedimentation rates at depth relative to the reference. Based on the observed relative sedimentation rates, the removal of material at depth more than compensates for any additional sediments originating upslope. Even if there were no extra terrigenous flux to the deepest site (northern Site 929), the low relative sedimentation rates at the deeper sites must be due to nondeposition or dissolution of carbonate. Given the assumption of equal export productivity to all the sites because of the limited geographical range of this study, dissolution at depth is the more likely process to account for low relative sedimentation rates at depth. Qualitatively, the magnitude of the dissolution signal increases with water depth during this period of the Pliocene (Figure 3.6).

Relative carbonate mass accumulation rates

We take a closer look at the effects of dissolution by examining the relative carbonate mass accumulation rates (MARs) at each site (again relative to Site 925) in Figure 3.7. These relative rates are calculated as :

$$\%\ \mathrm{CaCO_3}\ (92^*) \times \mathrm{d(depth92^*)}\ /\ \%\ \mathrm{CaCO_3}\ (925) \times \mathrm{d(depth925)} \tag{1}$$

or, the ratio of estimated percent carbonate at the two sites times the sedimentation rate ratio discussed above. In this calculation, we ignore bulk densities, which would be

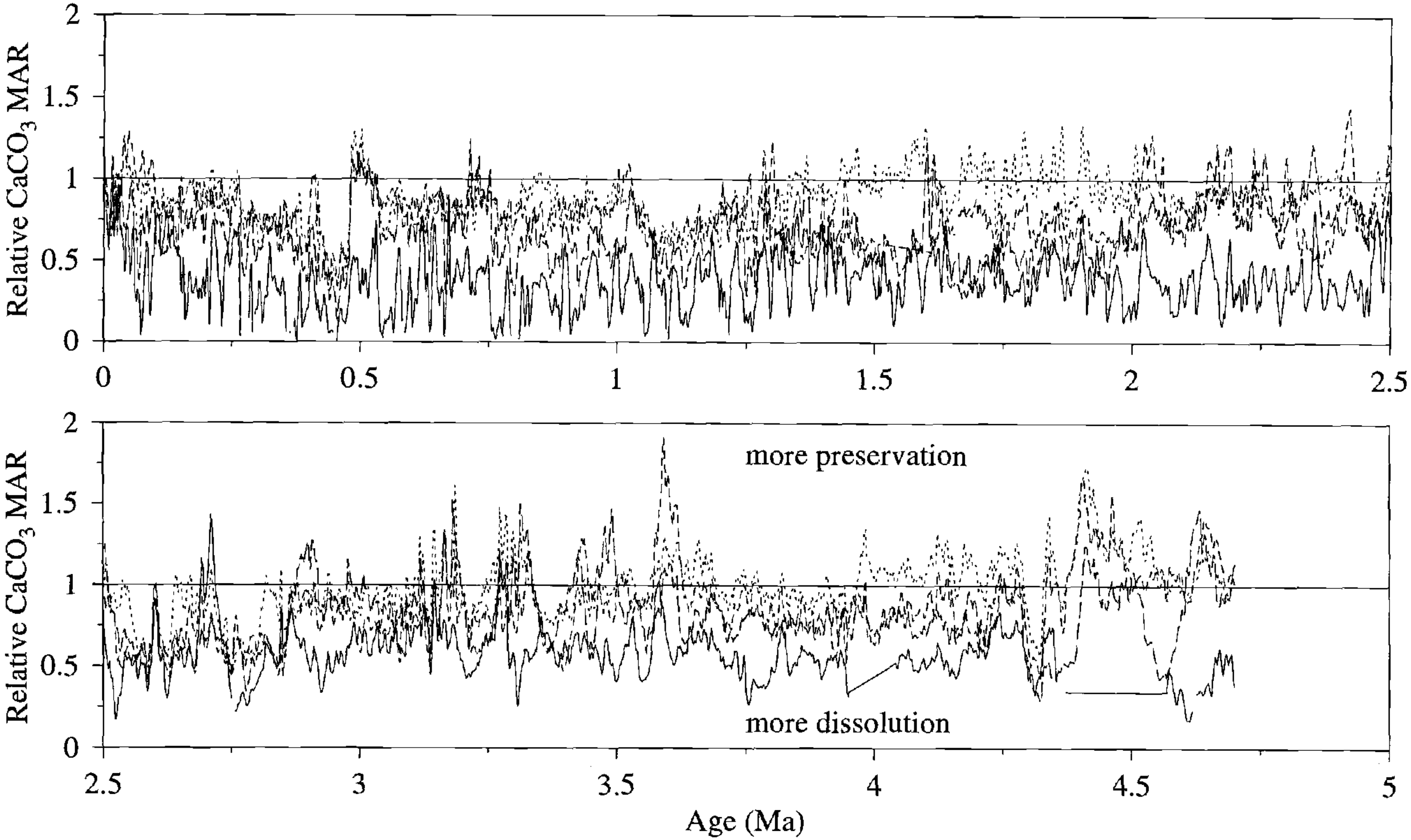

Figure 3.7 Relative calcium carbonate mass accumulation rates, 0-5 Ma, calculated by the ratio of estimated %CaCO$_3$ values multiplied by the relative sedimentation rate between two sites. All sites are represented relative to 925. Small dash = Site 926/Site 925; Medium dash = Site 927/Site 925; Large dash = Site 928/Site 925; Solid = Site 929/Site 925. The mean relative mass accumulation rate of carbonate decreases with depth, with 929/925 (solid) averaging the lowest. The Site 929 record serves as a carbonate dissolution index.

included in a normal mass accumulation rate calculation. The two main sedimentary components, carbonates and clays, have similar bulk densities. Also intervals of high or low carbonate among all the sites are correlated (via the depth-depth correlations in Figure 3.5). For these reasons, the bulk density ratio between two sites will have a negligible effect on the relative mass accumulation rate compared to the effects of changing relative %carbonate and changing relative sedimentation rates. Low resolution bulk densities measured shipboard support this assumption (Curry, Shackleton, Richter, et al., 1995). Additionally, based on the amplitude of high-resolution GRAPE data measured shipboard, we can imagine a worst-case-scenario, where, for example, a poor depth-depth map has matched two samples at the extremes of the bulk density range. Given a generous range in these sediments of 1.6-1.7 g/cm^3, the ratio of bulk densities would alter relative mass accumulation rates by only about 5%.

Accumulation of carbonate is nearly always lower at the deepest site than at the reference site, indicating that dissolution of calcite has occurred at and below 4356 m water depth in the western tropical Atlantic for most of the Plio-Pleistocene (Figure 3.7, solid curve). A similar pattern of carbonate dissolution occurs at the next deepest site (928, 4012 m water depth) from 2.6-0 Ma, The amplitude of this dissolution signal is smaller with a mean relative accumulation rate closer to one than at Site 929 indicating that Site 928 has on average been less severely dissolved than the deepest site.

Relative carbonate accumulation rates at the shallower sites (926 and 927, 3598 m and 3314 m water depth respectively) also indicate periods of dissolution compared to Site 925. One particular event occurs about 450-430 ka (oxygen isotope stage 12), during which time carbonate accumulation was significantly higher at the shallowest site (925) than at any other site. This feature might indicate a particularly shallow lysocline, perhaps due to a weak contribution of NADW to the deep tropical Atlantic during isotope stage 12, which has been recognized as a particularly severe glaciation (Shackleton, 1987).

The dissolution signal was less variable from 5-3.6 Ma. The two deeper sites (928 and 929) are almost continuously dissolved with respect to the reference. Relative accumulation at the two shallower sites (926 and 927) stays close to one during this part of the Pliocene. The dissolution trend with depth is an indication that Pliocene bottom waters were in general corrosive to carbonate. These relative mass accumulation rates indicate a rough depth cutoff for corrosive bottom water between 3600 and 4000 m water depth (the depths of Site 926 and 928 respectively).

Relative terrigenous mass accumulation rates

Dilution by terrigenous material affects the carbonate signals at different sites primarily as a function of location. Relative terrigenous mass accumulation rates show that differential terrigenous accumulation at Sites 927-929 (the northern sites) is responsible for the higher relative sedimentation rates at these sites (Figure 3.8). Terrigenous accumulation ratios are calculated as

$$(100 - \%\ \mathrm{CaCO_3}\ (92^*)) \times d(\mathrm{depth}92^*) / (100 - \%\ \mathrm{CaCO_3}\ (925)) \times d(\mathrm{depth}925). \quad (2)$$

The same assumption discussed above of low relative variability of bulk density is used in this calculation.

From about 3.6 Ma to the present, terrigenous mass accumulation rates for the three northern sites (927-929) are on average higher than the reference. The largest differences in terrigenous mass accumulation rate are at the deepest site and to first order occur during glacial periods. Continental shelf subaerial exposure and erosion could account for the coincidence of increased terrigenous flux with sea level lowering.

From about 3.6-4.4 Ma, the relative terrigenous MARs at the northern sites were less variable than during the Pleistocene. Depth mapping uncertainties are partially

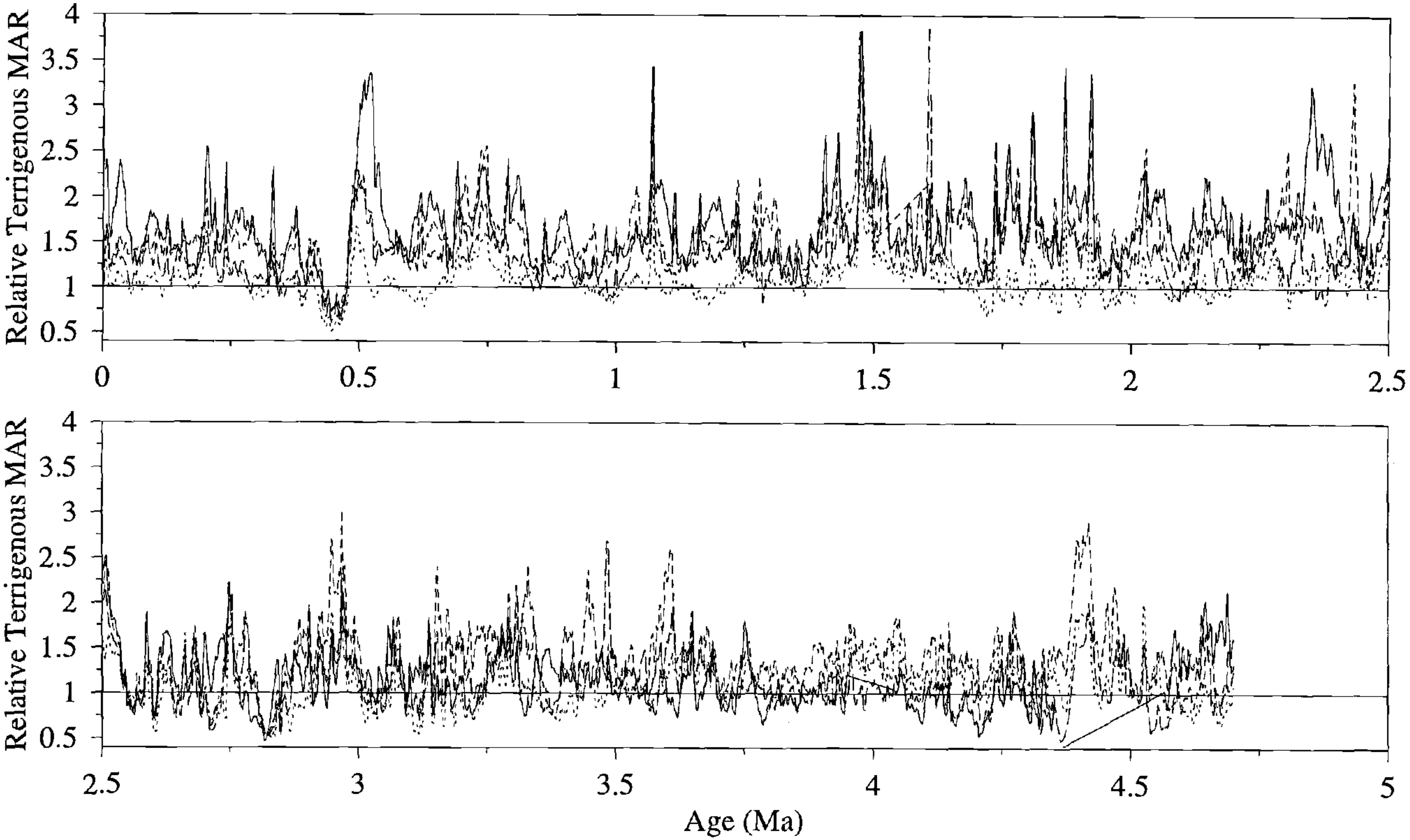

Figure 3.8 Relative terrigenous mass accumulation rates, 0-5 Ma, calculated by the ratio of (100 - estimated % $CaCO_3$) values multiplied by the relative sedimentation rate between two sites. All sites are represented relative to 925. Small dash = Site 926/Site 925; Medium dash = Site 927/Site 925; Large dash = Site 928/Site 925; Solid = Site 929/Site 925. The mean relative mass accumulation rate of non-carbonate is highest at the northern sites (927-929). The Site 929 record has the highest amplitude of varibility and serves as an index of terrigenous dilution.

responsible for the apparent increase in relative terrigenous MAR at Site 929 at 4.4-4.55 Ma, and at Site 928 at 4.6-4.75 Ma. Any increase in relative terrigenous accumulation is more than offset by dissolution of carbonate at the deep sites in the early Pliocene, as seen in relative sedimentation rates (Figure 3.6).

Site 926, the southern site closest to the reference site, displays the least relative terrigenous MAR variability over the past 5 m.y. These north-south differences indicate that terrigenous dilution is primarily a function of proximity to the Amazon Fan, the major source of terrigenous material.

DISCUSSION

We have developed two indices of climate variability, a dissolution index and a relative terrigenous flux index, both of which affect the difference in carbonate content at deep sites on Ceara Rise as compared with shallow sites. The preferred dissolution index is the relative carbonate MAR record from deep Site 929 relative to shallow Site 925. The amplitude of this signal is largest because the deepest site is most affected by dissolution. The preferred relative terrigenous MAR signal is also from Site 929 relative to Site 925. This is an indicator of terrigenous flux to the north and deep part of Ceara Rise.

These indices are shown with the benthic oxygen isotope record from ODP Site 849 in the eastern equatorial Pacific (Figure 3.9; Mix, et al., 1995a). The logical oxygen isotope record to use in this study would be from Ceara Rise sites to avoid any incompatibilities between age models from different sites. However, the Pacific Site 849 record and the oxygen isotopes for 0-1 Ma from Ceara Rise Site 926 (W. Curry, unpublished data) are virtually identical and are in phase. All of these data are presented on the Site 926 age model. Given the excellent correlation between the Site 849 and Site 926 isotopes, it is not inconsistent to use the Pacific oxygen isotope record. This allows us to compare the Ceara Rise data to a longer continuous record of isotopic variation.

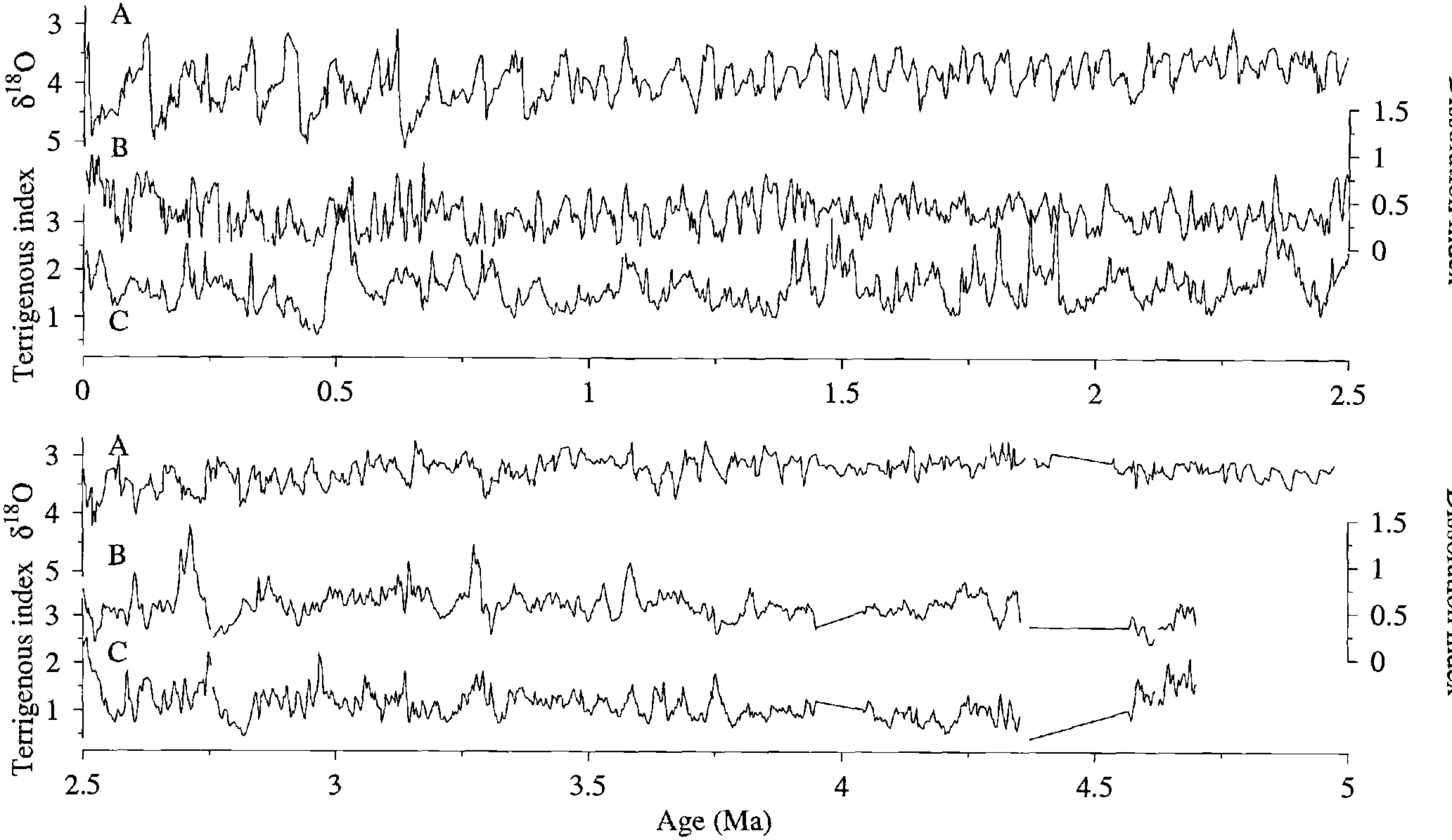

Figure 3.9 Time series 0-5 Ma of: (A) oxygen isotopes (Site 849 in the eastern equatorial Pacific (Mix et al., 1995a)) a global ice volume proxy, (B) relative carbonate mass accumulation rates Site 929/925 (Figure 3.7) which serves as a dissolution index, and (C) relative terrigenous mass accumulation rates Site 929/925 (Figure 3.8) which serves as a terrigenous dilution index. Values of the dissolution index less than one indicate dissolution at the deep site. Values of the terrigenous index greater than one indicate a higher influx of terrigenous material to the deep northern site.

The frequency evolution of each of these indicies is compared with Site 849 $\delta^{18}O$ (Mix et al., 1995a). The oxygen isotope record primarily reflects global ice volume changes, and the orbital periodicities of 100 k.y., 41 k.y., and 23 k.y. dominate Pleistocene climate variability (e.g. Imbrie et al., 1984). Significant power in the 41 k.y. orbital band extends back to at least 4 Ma in the oxygen isotope record from Site 849 (Figure 3.10A). The 100 k.y. and precessional 23 k.y. cycles are strongest during the past 1 m.y.

Carbonate dissolution, water mass variability, and global carbon cycles

The record of carbonate dissolution in the western tropical Atlantic has been inferred to be affected by changes in deep-water circulation (Curry and Lohmann, 1983; Curry et al., 1988; Raymo et al., 1990: Oppo and Fairbanks, 1987). Curry and Lohman (1990) compared dissolution patterns in the eastern and western Atlantic basins and concluded that dissolution in the tropical Atlantic is primarily a function of deep-water circulation changes. Peterson and Prell (1985) also interpreted Indian Ocean dissolution indices to be linked to regional circulation. A more widespread process that could control dissolution patterns is global atmospheric CO_2 cycling (Shackleton, 1977). If massive deforestation transferred much terrestrial carbon to the ocean, globally synchronous dissolution events should occur. These events would occur on interglacial-glacial transitions (Shackleton, 1977). By comparing Atlantic and Pacific dissolution cycles, Crowley (1985) concluded that synchronous dissolution has occurred during ice growth. However, Crowley's dissolution cycles have not always been in phase during the last half-million years, indicating that there is some imprint of regional circulation on carbonate preservation records.

The modern depth of the lysocline at Ceara Rise is primarily controlled by the depth of the mixing zone between NADW and AABW (Curry and Lohman, 1990). If we

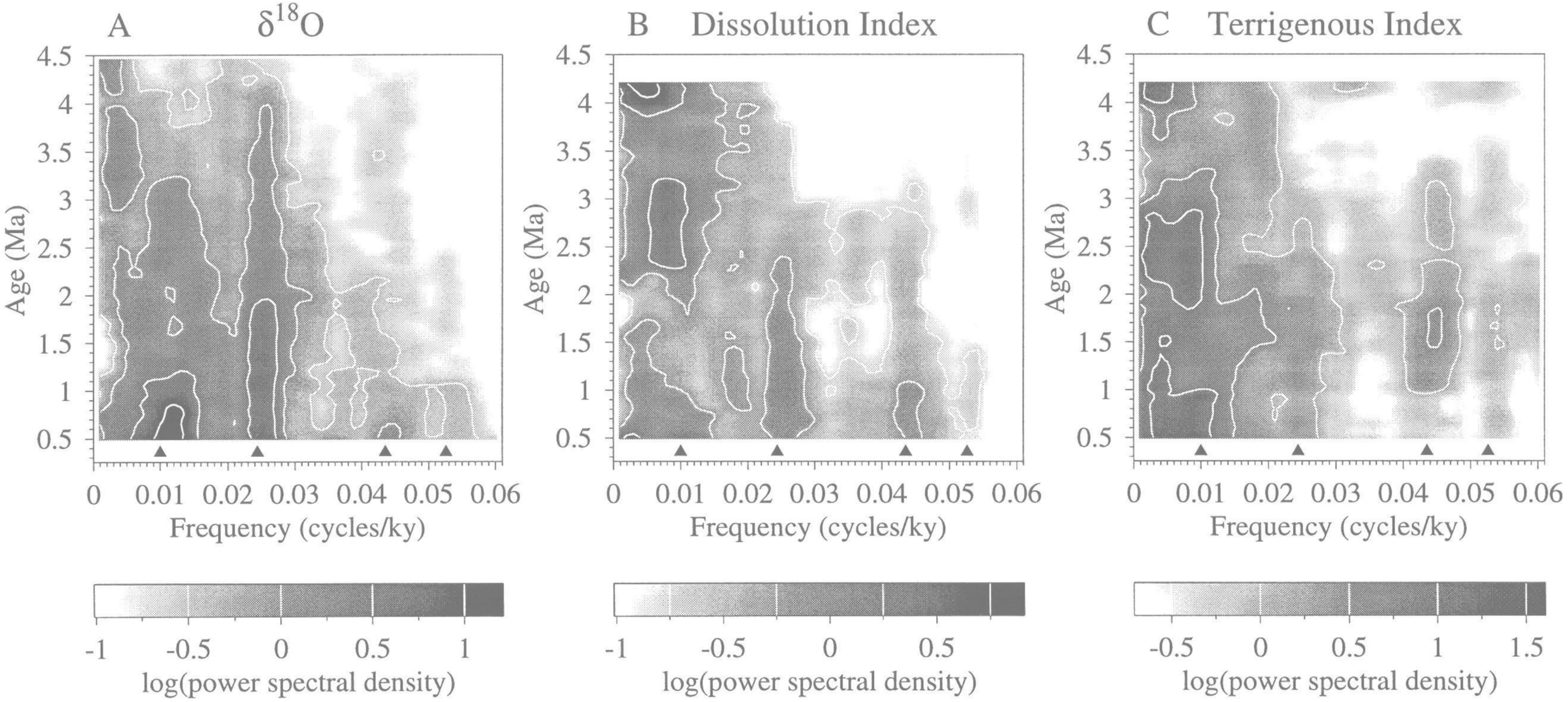

Figure 3.10 Evolving spectra. These maps of frequency evolution are composed of up to 80 individual time series 1 m.y. in length. Each successive time series overlaps the previous one by all but 50 k.y. Age on the y-axes is the average age of the time series (e.g. age = 0.5 Ma represents the time series from 0-1 Ma). Units for the vertical axes are log(estimated power spectral density). (A) Oxygen isotope record from ODP Site 849, 0-5 Ma. Orbital frequencies dominate the spectrum over this time interval. Sampling interval = 2 ky, bandwidth = 0.0053 with 11 degrees of freedom. 95% confidence interval = 0.75 in log units. (B) Calcium carbonate dissolution index ($CaCO_3$ relative MAR, Site 929/Site 925). Time series parameters as in (A). (C) Terrigenous flux proxy (Terrigenous relative MAR, Site 929/Site 925). This signal is dominated by long period fluctuations. Time series parameters as in (A).

assume that this water mass boundary was present here in the past, with similar water mass characteristics, then Ceara Rise, far from deep water source regions, may be an ideal location for monitoring temporal variability in the contributions of AABW and NADW to the deep western Atlantic. The dissolution index, relative mass accumulation rates of calcium carbonate estimated by proxies, should be sensitive to this water-mass balance. If water masses are the dominant control on dissolution, then the timing of dissolution events would define events of low NADW relative to AABW at the Ceara Rise.

In addition, the timing of this dissolution index in relation to ice volume could support the idea of a large influx of terrestrial carbon to the oceans on interglacial-glacial transitions. Orbital frequencies dominate the index (Figure 3.10B). The 100 k.y. period in the dissolution index is strong for the past 1 m.y., similar to ice volume changes, but is also significant from about 2.25-3.5 Ma. Significant variance is concentrated in the obliquity band (41 k.y.) for about the past 1.75 m.y. Precession (23 k.y.) has the highest amplitude variability also during the past 1 m.y. when northern-hemisphere glacial cycles have dominated global climate changes. Significant variance is concentrated in all three orbital frequency bands from about 2-3 Ma.

If this is a water mass signal, variability in the dissolution index supports the concept of decreased NADW production associated with ice-age cycles in the Pleistocene (Oppo and Fairbanks, 1987; Raymo et al., 1990). Cross spectral analysis of the dissolution index with oxygen isotopes for 0-1 Ma shows that the two signals are coherent at all three orbital frequencies (Table 3.6). Maximum dissolution occurs during ice growth, before maximum glacial conditions, i.e. leading $\delta^{18}O$ maxima by ~71° at the 100 k.y. period, ~68° at 41 k.y. period, and ~23° at the 23 k.y. period (Table 3.6). This result is in good agreement with Imbrie et al.'s (1992, 1993) calculated phase relationships between Cd/Ca (Boyle and Keigwin, 1982) in the deep south Atlantic and

Table 3.6 Cross spectral results for the dissolution index with Site 849 oxygen isotopes, 0-1 Ma.

		100 k.y.		41 k.y.		23 k.y.	
Index	Source	Coherence	Phase	Coherence	Phase	Coherence	Phase
Ceara Rise: Carbonate dissol. index	This paper	0.94	-71±11	0.80	-68±22	0.88	-25±16
South Atlantic: -Cd/Ca	Imbrie, 1992	0.92	-77±13	0.78	-49±23	0.80	-27±22
North Atlantic: %NADW	Imbrie, 1992	0.87	+16±15	0.86	+5±16	0.83	+41±17

Notes: Negative phase indicates that the index leads ice volume. (e.g. maximum dissolution leads maximum ice volume by 71° at 100 k.y. periodicities). Positive phase indicates that the index lags ice volume. Coh. = Coherence. Phase units are degrees.

global oxygen isotopes (ice volume lags -Cd/Ca by ~77° at the 100 k.y. period, by ~49° at the 41 k.y. period, and by ~27° at the 23 k.y. period).

The fact that this dissolution index leads ice volume supports a key prediction of SPECMAP (Imbrie et al., 1992), that northern hemisphere climatic forcing was translated via deep water to the southern ocean early during ice growth via early reduction in NADW production. This result, however, disagrees with the history of deep water circulation obtained from N. Atlantic carbon isotopes (Imbrie et al., 1992, 1993; Raymo et al., 1990) in which NADW reduction lags ice volume at all the orbital frequencies (Table 3.6).

Although the timing is consistent with SPECMAP's prediction, we still cannot rule out terrestrial carbon inputs. Dissolution events at Ceara Rise could respond in part to global carbon transfer to the oceans on ice growth. If the total dissolved CO_2 in the oceans increased quickly, then the lysocline at Ceara Rise may not have been coincident with the NADW-AABW transition in the past. Comparisons with carbon isotope data (see papers in Shackleton et al., 1997) from Ceara Rise will help elucidate which process mainly drives the dissolution gradient.

Terrigenous sedimentation, sea level, and South American climate

Part of the difference in carbonate signals between Sites 925 and 929 is clearly due to terrigenous input to the deep northern site (929). The effects of relative dilution on the carbonate record are represented by the relative terrigenous MAR signal between Site 929 and Site 925. Again, this signal has the highest amplitude, largely due to its location and depth. Over the extent of the records, most of the frequency variability in the relative terrigenous index is concentrated at long periods (100 k.y. or greater; Figure 3.10C), with some power at precessional periods.

For the past 1 m.y., the terrigenous index can be compared qualitatively to ice volume. Larger influxes of terrigenous material occur at the northern sites on Ceara Rise roughly during glacial periods (Figure 3.9). If the relative terrigenous flux is linked to sea level, this relationship might imply that maximum erosion of terrigenous material occurs when sea level is low (i.e., close to the shelf edge). Material that was stored on the continental shelf during high-stands of sea level could erode as sea level drops. However, if shelf erosion increases as sea level lowers, one might expect that all sites on Ceara Rise would be equally affected and the relative terrigenous MAR would not vary. Much of the material from the Amazon is carried north up the coast of South America, away from the southern Ceara Rise sites, however, by the Guiana Current.

A difficulty with the interpretation that relative terrigenous flux is linked to sea level is that high-amplitude, long period variability is also present in the pre-Pleistocene record (Figure 3.10C), when ice volume (and sea level) changes were small. If sea level cannot be implicated in the Pliocene and early Pleistocene, some other climate process must dominate terrigenous flux. Crowley et al. (1992) suggest a possible mechanism based on results of energy balance models. At low latitudes the sun passes overhead twice annually, which amplifies long period temperature fluctuations in the tropics. Model output of maximum temperature variations over large tropical land masses indicate a 100-k.y. period response based on insolation forcing. Temperature changes could affect continental weathering and erosion patterns by altering rainfall variability at this long period. Such effects could explain the dominant low frequency variance in the relative terrigenous flux record pre-Pleistocene, independent of ice volume and sea level. Mix et al., (1995c) found that sedimentation rate variability in the eastern tropical Pacific was consistent with the Crowley et al. hypothesis (1992). Climate variability in the tropics at 100-k.y. periods could be independent of ice volume with the effects recorded off both coasts of South America.

CONCLUSIONS

1. Long time series of carbonate variability can be estimated empirically from nonintrusive proxy data (reflectance and magnetic susceptibility) with RMS errors ranging from 4%-7% $CaCO_3$. These errors are smaller than previously possible using similar proxy techniques and are acceptable given the wide range of carbonate variability in Ceara Rise sediments. A regional calibration equation is robust among the sites, but localized calibrations can improve statistical measures of equation success (higher r^2, lower RMSE).

2. Accumulation rates of calcium carbonate decrease with increasing water depth on Ceara Rise, indicating that the deeper sites have undergone some degree of dissolution for the past 5 Ma. The amplitude of the dissolution signal and the mean strength of dissolution both increase in the Pleistocene.

3. Dissolution varies at the deeper sites on G-I time scales during the Pleistocene. Dissolution events lead maximum ice volume at all orbital frequencies. Phase relationships are consistent with a deep south Atlantic nutrient proxy used by Imbrie et al. (1992, 1993) indicating early climate responses in the Southern Ocean. If deep ocean circulation has driven dissolution from 0-1 Ma, then export of NADW decreased early relative to maximum ice, perhaps forming a link between northern hemisphere climate forcing and documented early responses in the southern ocean. This result indicating early deep water changes is quite different than the view of deep water variability derived from carbon isotope data near the source of NADW. One strength of the dissolution index presented here is the location of Ceara Rise in the mixing zone between northern and southern source deep water. Carbonate dissolution signals here should be very sensitive to the balance of NADW and AABW contributions to western tropical Atlantic deep water if the lysocline boundary coincided with the mixing zone 0-1 Ma as it does today. In addition, the dissolution signal may in part record a global transient response of

the carbonate system to the transfer of carbon between the terrestrial and oceanic reservoirs.

4. Carbonate percentages are affected by terrigenous influx preferentially at sites nearest the Amazon Fan. Terrigenous fluxes to the deep sites relative to those at shallow Site 925 were highest during glacial stages in the Pleistocene. The prevalence of 100 k.y. period cycles pre-1 Ma, at times older than large fluctuations in northern-hemisphere ice volume, suggests that sea level is not the primary mechanism controlling terrigenous sedimentation at the northern Ceara Rise. The long-period relative terrigenous flux cycle alternatively could be related to a low-latitude continental climate process acting independently of ice, particularly in the Pliocene-early Pleistocene.

ACKNOWLEDGEMENTS

Thanks to: Jerry McManus and William Balsam for helpful reviews of this manuscript, Bill Rugh for much instrumental help, and Walter Hale and Alex Wueblers for their assistance at the ODP Bremen Core Repository. Carbonate data used in this manuscript were provided by Terri King, Bill Curry and Rindy Ostermann. This work was supported by USSSP grant #154-20868b.

4.

Pleistocene Precipitation Balance in the Amazon Basin Recorded in Deep Sea Sediments

Sara E. Harris and Alan C. Mix

Reprinted in its entirety with permission from Academic Press from:
Quaternary Research (manuscript in press),
copyright Academic Press, Orlando, FL.

ABSTRACT

Terrigenous sediments from Ceara Rise in the western tropical Atlantic record Pleistocene Amazon Basin climate variability. Iron oxides and oxyhydroxides in this region originate mainly from chemically-leached Amazon lowland soils. Concentrations of carbonate-free goethite and hematite consistently peak during transitions from glacial to interglacial periods, suggesting an increased proportion of erosive products derived from the Amazon lowlands compared to the physically weathered highlands. Lowland Amazon Basin precipitation changes, monitored by the percentage of goethite relative to total iron oxides, lead ice age extremes with maximum aridity during ice growth and maximum precipitation during ice melt. Rapid climate changes over the Amazon Basin may reflect shifts in the position of the Intertropical Convergence Zone (ITCZ) forced by northern hemisphere insolation at precessional (1/23,000 yr^{-1}) and obliquity (1/41,000 yr^{-1}) frequencies. Variance in the orbital eccentricity bands (1/100,000 yr^{-1} and 1/413,000 yr^{-1}) may be explained by nonlinear amplification of insolation forcing at precessional frequencies. The early response of Amazon precipitation to insolation, ahead of high latitude ice volume ($\delta^{18}O$) at all orbital frequencies, suggests that tropical aridity is part of the chain of events leading to ice ages, rather than a response to glacial forcing.

INTRODUCTION

To assess Amazon Basin response to glacial-interglacial climate forcing, we link marine and continental climate records over the most recent climate transition, then extend the analysis through the Pleistocene (0-2.6 myr) using long, continuous, well-dated marine sedimentary records from Ceara Rise in the western tropical Atlantic. Consistent glacial-interglacial climate patterns emerge, demonstrating that Amazonia experienced arid periods during Northern Hemisphere ice growth and that lowland precipitation levels increased during glacial terminations.

Much of Amazonia was colder during the last glacial maximum (LGM) than today. Stable isotopes from Peruvian ice cores imply LGM high altitude temperatures 8-12°C cooler than today (Thompson et al., 1995) while noble gases in ground water suggest LGM lowland Brazil air temperatures about 5°C cooler (Stute et al., 1995). In the northern and central Andes, ice age snowlines (Clapperton, 1993) and treelines (van der Hammen, 1974) may have descended 1000 m or more, and montane vegetation may have grown at lower altitudes (Lui and Colinvaux, 1985; Bush et al., 1990).

Evaporite deposits (Kronberg et al., 1991) and paleo-dune features in Amazonia (Clapperton, 1993) imply drier conditions during the last glacial cycle. Many lowland lakes lack LGM sediments, suggesting lake dessication (Servant et al., 1993; van der Hammen, 1974; van der Hammen and Absy, 1994). Some possibly preserved lowland LGM lake sediments are highly oxidized, implying lower lake levels (Colinvaux et al., 1996), but a recent study of age models in lowland lake sediments concludes that the LGM is represented by a hiatus at all known lowland lake sites (Ledru et al., 1998). Grassland vegetation and savanna forest may have been more expansive, in place of today's dense rainforest (Clapperton, 1993), although pollen deposited on the Amazon Fan suggests little glacial-interglacial change in vegetation of the riparian zone (Haberle, 1997). Unweathered plagioclase (Damuth and Fairbridge, 1970) in pre-Holocene sediments from the western tropical Atlantic and the Amazon Fan supports a drier climate and reduced forest cover in Amazonia.

Precipitation levels in much of lowland Amazonia likely increased during the transition from the LGM to the present. Lacustrine sedimentation resumed and arboreal pollen percentages peaked in some areas from about 13-9 ka (Servant et al., 1993).

Foraminiferal $\delta^{18}O$ from the Amazon Fan suggests high discharge and precipitation between 13.5 and 6 ka (^{14}C dates; Showers and Bevis, 1988).

In contrast to lowland lakes, Bolivian altiplano lake levels were high during the LGM and decreased during the transition from glacial to interglacial conditions (Wirrmann and Mourgiart, 1995; Abbott et al., 1997), suggesting different contemporaneous precipitation regimes in the Amazon lowlands and the Bolivian highlands.

Each of the available continental studies represents the climate situation at one or a few isolated points, and discrepancies among them may represent true regional differences in climate response. Lake records are short, discontinuous, difficult to date and correlate accurately, thus basin-wide climate inferences remain uncertain. Previously available marine records are well dated and represent climate variability on a basin-wide scale, however, as with the continental records, most span only the most recent glacial period and transition to the Holocene. Our approach yields an integrated view of Amazon Basin climate at high temporal resolution over many glacial cycles.

Ceara Rise is an aseismic ridge located off the Atlantic coast of South America, southeast of the Amazon Fan (Figure 4.1). Complete sedimentary sequences were recovered at Ocean Drilling Program Sites 925 (4°12'N, 43°29'W, 3041 m water depth) and 926 (3°43'N, 42°54'W, 3598 m water depth) by drilling multiple overlapping holes at each site (Curry et al., 1995). We present data primarily from Site 926, spliced with the upper 2.6 m of Site 925 (approximately 0-50,000 yr), due to poor core conditions which precluded detailed analysis of this interval in Site 926.

Ceara Rise receives sediment from two primary sources: (1) calcareous tests of plankton from overlying surface waters and (2) terrigenous sediment from the Amazon River. Biogenic opal is virtually absent. All cores display a visual light-dark cyclicity arising from the interaction between these two sediment types.

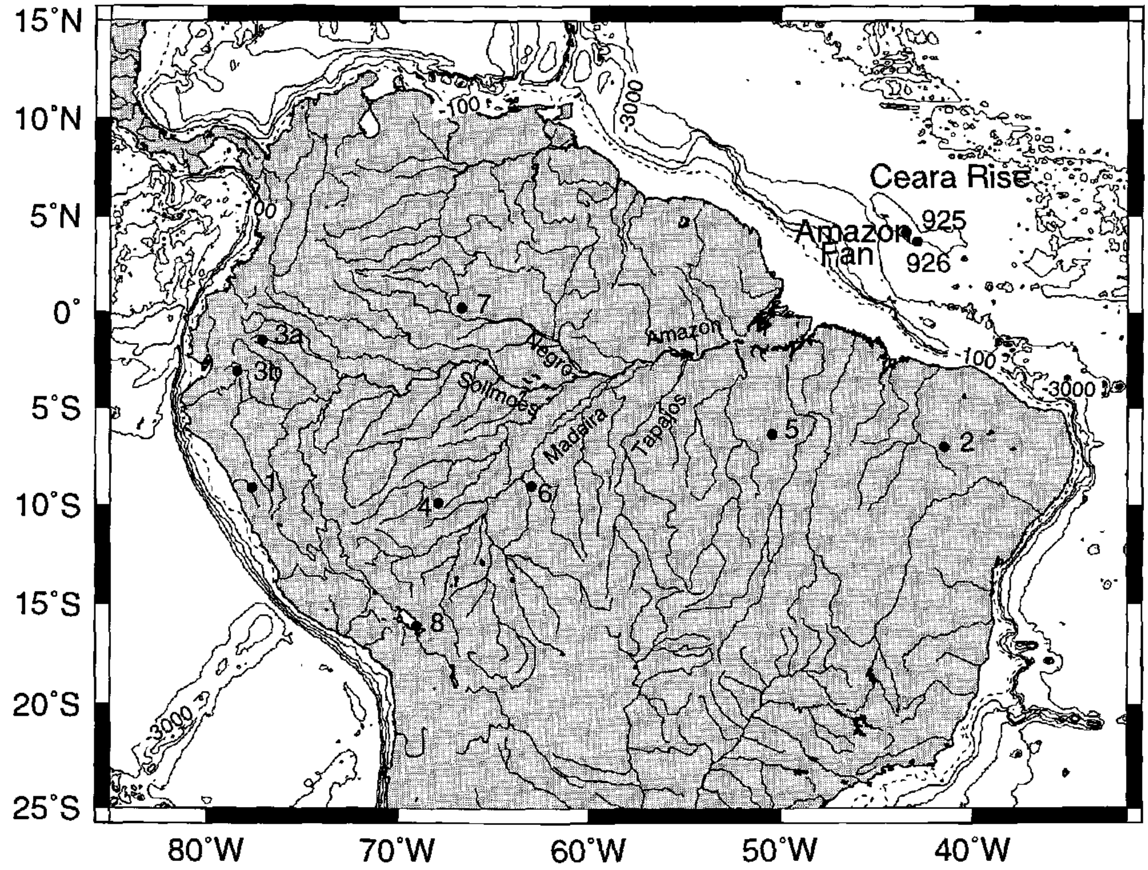

Figure 4.1 Map of South America and western tropical Atlantic with Ceara Rise sites 925 and 926, and continental sites discussed in the text. 1. Peruvian ice cores (Thompson et al., 1995); 2. Ground water temperatures (Stute et al., 1995); 3. a. Mera, b. San Juan Bosco (Lui and Colinvaux, 1985; Bush et al., 1990); 4. Acre Subbasin (Kronberg et al., 1991); 5. Carajas (Servant et al., 1993); 6. Rondonia (Van der Hammen, 1974; Van der Hammen and Absy, 1994); 7. Lake Pata (Colinvaux, 1996); 8. Lake Titicaca (Wirrmann and Mourguiart, 1995; Abbott et al., 1997). Solid bathymetric contours are at 1000 m intervals. Dashed contour at 100 m is the nominal shelf break.

The composition of the terrigenous fraction deposited at Ceara Rise reflects the composition of Amazon suspended sediments, which depends on the source and/or weathering of erosive products. Today, 85-95% of Amazon suspended sediment is from the physically weathered highlands (Gibbs, 1967; Meade et al., 1985). The remaining sediment is from tributaries draining lowland areas where the mineral composition of soils results from intense chemical weathering. More than 75% of Amazon Basin soils are mixtures of quartz (resistant to chemical weathering), kaolinite and gibbsite (clay minerals resulting from strong leaching of cations from the soil), and hematite and goethite (iron oxides formed via chemical weathering reactions; Jordan, 1985).

We use the changing composition of oxides in the terrigenous fraction in the marine record to infer past climate conditions in Amazonia. %Goethite in the non-carbonate fraction serves as a proxy for lowland versus highland erosion. The fraction of goethite relative to hematite plus goethite (G/(G+H)) serves as a proxy for lowland precipitation and vegetation as described below (Kampf and Schwertmann, 1983). Although goethite is an oxyhydroxide, for simplicity the term "iron oxides" refers here to both hematite and goethite, and both are discussed on a carbonate-free basis unless otherwise noted.

METHODS

Reflectance spectra

We measured reflectance spectra from the wet surfaces of split cores at 5 cm resolution using the Oregon State University Split Core Analysis Track modified from Mix et al. (1992). The instrument measures light reflected from split sediment core surfaces at 0.68 nm spectral resolution, spanning upper ultra violet (UV), visible (VIS) and near infrared (nIR) wavelengths (250-950 nm). A split core moves automatically along a track and stops at user-chosen intervals for measurement. Two light sources, a deuterium lamp for the UV and a quartz-tungsten-halogen lamp for the VIS and nIR, illuminate the core surface via fiber optic cables. A Spectralon® coated integrating sphere captures diffuse and specular reflectance from the core surface which is measured by a thermoelectrically cooled Charge-Coupled-Device detector.

Three reflectance measurements are taken at each sample location: background (BLK), internal standard (IW, approximately 100% reflectance), and sample (SMP). Percent reflectance is initially calculated at each wavelength as 100*(SMP-BLK)/(IW - BLK), then corrected to true %reflectance using a polynomial fit to a set of four external calibration standards with known reflectivities (2%, 40%, 75%, and 100% reflectance; data and standards obtained from Labsphere, Inc.). For more detail, see Harris et al. (1997).

The spectra are band-averaged to 10 nm resolution centered on wavelengths ending in 5, e.g. 405, 415, 425 nm (e.g. Figure 4.2A). Reflectance analyses commonly use derivatives of the spectrum relative to wavelength to emphasize spectral shape. First derivative values at each wavelength band are calculated from band averaged data using the centered difference method (e.g. Figure 4.2B; Press et al., 1992).

Estimating goethite and hematite from factor analysis

Reflectance spectroscopy is the most promising method for estimating concentrations of goethite and hematite in deep sea sediments. The presence of small amounts of hematite and/or goethite measurably alters the first derivative spectrum of the sample in the visible range (Deaton and Balsam, 1991).

R-mode factor analysis confirms that different mineral assemblages can be independently estimated from first derivative spectra. Samples in the factor analysis are 4397 first derivative spectra, one fifth of the total reflectance data set from Ceara Rise

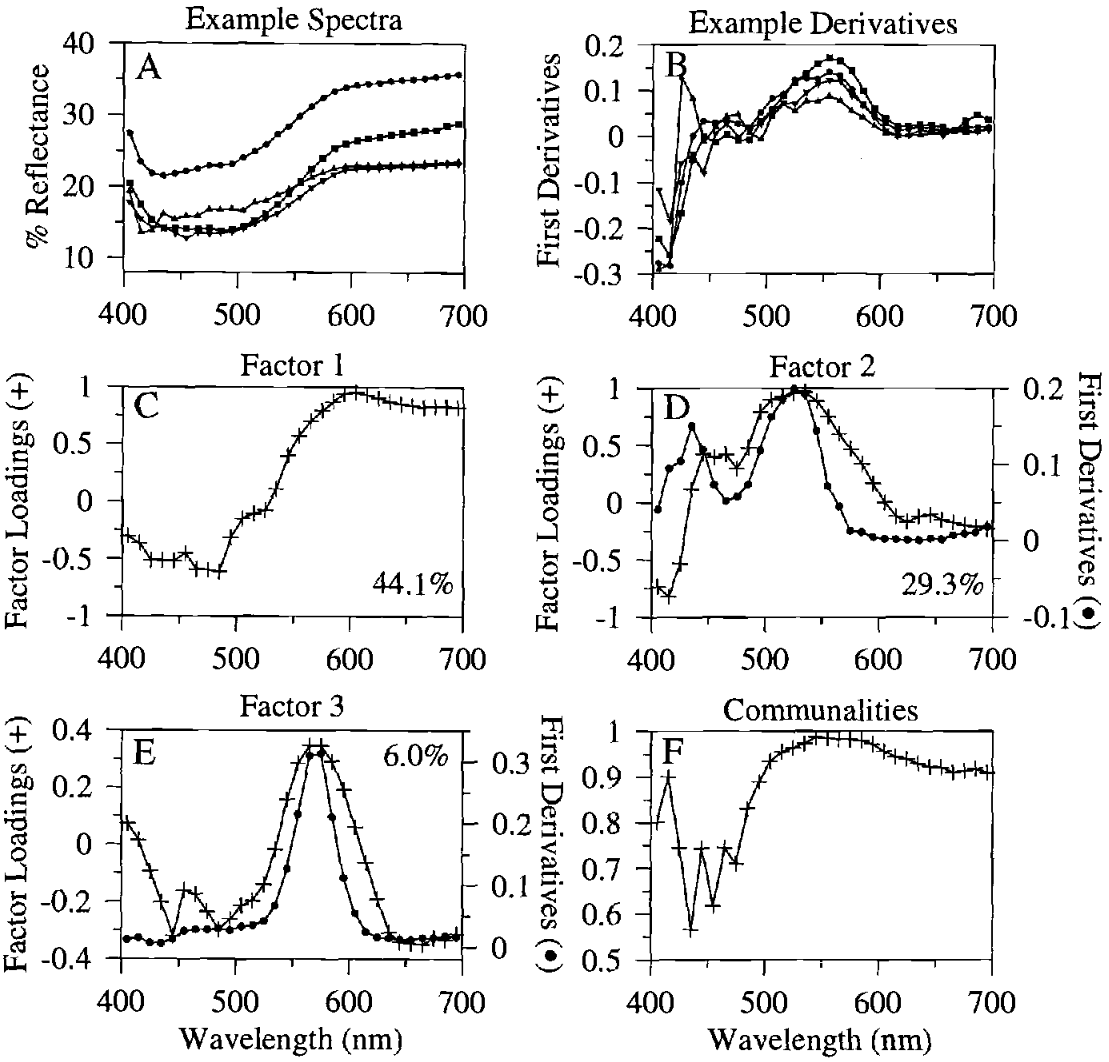

Figure 4.2 (A) Examples of reflectance spectra from four Ceara Rise samples. %Reflectance of Ceara Rise samples is typically lower at shorter wavelengths ("blue") and higher at longer wavelengths ("red"). Squares: Sample with high % goethite and high % hematite; circles: sample with high % goethite and low % hematite; downward triangles: sample with low % goethite and high % hematite; upward triangles: sample with low % goethite and low % hematite. (B) First derivative spectra calculated from the four reflectance spectra in Figure 4.2A by the centered difference method. Symbols as in A. C-F: Results of R-mode factor analysis. (C) Factor 1 represents variability in the non-carbonate sediment matrix. (D) Factor 2 (+) is similar in shape to the first derivative spectrum of 0.5% goethite in a North Atlantic sediment matrix (•) with a major peak near 525-535 nm and a minor peak near 445 nm (data from Deaton and Balsam, 1991). (E) Factor 3 (+) is similar in shape to the first derivative spectrum of 0.3% hematite in a North Atlantic sediment matrix (•) with a major peak at 565-575 nm (data from Deaton and Balsam, 1991). (F) Communalities for the three factor model are greater than 0.95 over the range of major goethite and hematite first derivative spectral peaks.

sites. Variables include first derivatives of reflectance spectra at 10 nm intervals ranging from 405-695 nm (visible range).

In an R-mode factor model, the factor loadings are orthogonal, therefore algebraically independent (Figure 4.2C-E). Downcore time series (factor scores) are not constrained to be orthogonal. The three factors explain 79% of the variability in first derivative spectra. Factor 2 (Figure 4.2D) has peaks at about 525-535 nm and at about 445 nm, similar to first derivative spectra of goethite in a variety of sedimentary matrices, while factor 3 (Figure 4.2E) has a prominent peak at 565-575 nm, matching hematite in a variety of matrices (Deaton and Balsam, 1991). This means that hematite and goethite can be estimated independently in our data set. Factor 1 (Figure 4.2C) is not clearly related to a specific mineral, but represents variability in the dominant non-carbonate sedimentary matrix relative to highly reflective calcium carbonate. Communalities (the proportion of variability at each wavelength explained by the 3 factor model), are greater than 0.95 for wavelengths spanning the main diagnostic goethite and hematite peaks (Figure 4.2F).

We calibrated this factor model by applying it to published first derivative spectra with known concentrations of hematite and goethite in a variety of sedimentary matrices which include varying amounts of calcite and quartz, both highly reflective materials (Balsam and Deaton, 1991; Deaton and Balsam, 1991). Calcite plus quartz is included as a variable in these equations because the sediment brightness affects the equation coefficients. This approach yields the following calibration equations (Figure 4.3):

$$\ln(\%\text{goethite}) = 3.98*f2 - 0.026*f2*CQ - 4.64 \qquad (1)$$

$$\ln(\%\text{hematite}) = 3.31*f3 - 0.022*CQ + 0.955*f1 - 0.018*f3*CQ - 2.86 \qquad (2)$$

where f1, f2, and f3 equal factor scores for factors 1, 2, and 3, and CQ equals the sum of calcite plus quartz (in percent) in the calibration matrices. Factors 2 and 3 are positively correlated to %goethite and %hematite respectively, while CQ terms in each equation have

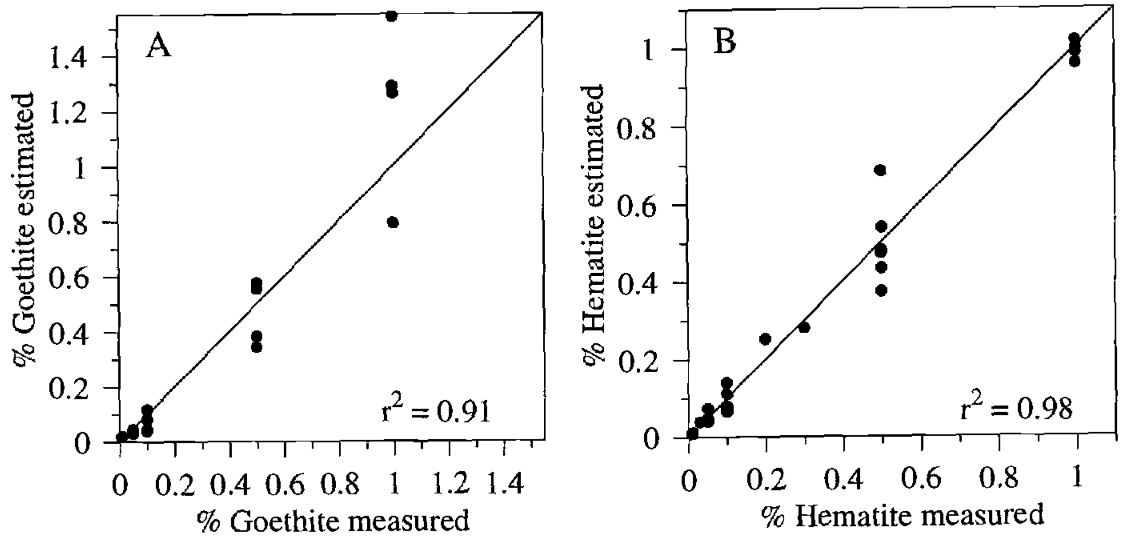

Figure 4.3 (A) Results of goethite calibration (equation 1). $R^2 = 0.91$, $p<0.0001$. The root mean square error (rmse) over the full range is ±0.16 %goethite (n=20), while over the range ≤0.5% measured goethite, which encompasses the downcore estimates, rmse=±0.06 %goethite (n=16). (B) Results of hematite calibration (equation 2). $R^2 = 0.98$, p=0. Rmse for the full range is ±0.05 %hematite (n=26) while over the range ≤0.2, which encompasses the downcore estimates, rmse=±0.02 %hematite (n=15).

negative coefficients. This relationship is expected since brighter sedimentary matrices (higher CQ) enhance the first derivative signature of these oxides. The significance of factor 1 in the hematite equation may be explained if this factor contains information about variability in the non-carbonate matrix, including hematite, and possibly because factor 3 explains only a small portion of the total variance (6%).

These equations, applied to reflectance spectra from Ceara Rise sediments, estimate concentrations of hematite and goethite, with %$CaCO_3$, estimated from reflectance spectra and magnetic susceptibility (Harris et al., 1997) substituting for CQ. This substitution is appropriate because %reflectance (brightness) and %$CaCO_3$ are positively correlated and in phase. The downcore variability of %hematite and %goethite is statistically robust in both the time and frequency domains regardless of calibration matrix or the functional form of the equations, and therefore interpretable in terms of climate change.

Time series analysis

Using time series analysis techniques, we compare time series of carbonate-free %goethite and %hematite, goethite in total iron oxides (G/(G+H); this paper), %$CaCO_3$ (Harris et al., 1997), -$\delta^{18}O$ (W. Curry, unpublished data), and June insolation at 65°N ($Q65N_{Jun}$, calculated from the $La93_{(1,1)}$ orbital solution; Laskar et al., 1993) in the frequency domain. Time series were first smoothed with a 6000 yr Gaussian window and interpolated to 2000 yr intervals. Frequency spectra are calculated from a Fast Fourier Transform (Bloomfield, 1976) for the interval 0-0.9 myr, over which the time series are stationary, and from 0.2-2.6 myr to examine long period variability. Age models are from orbital tuning of Site 926 magnetic susceptibility records (Bickert et al., 1997). The age model agrees well with tuned age models from the equatorial Pacific (Shackleton et al., 1995). All cross spectral comparisons among time series from the sedimentary record are from Site 926. Because the records are compared from the same samples within one site, errors in phase estimates induced by time scale errors are minimized.

RESULTS

Calcium carbonate and terrigenous flux

Variability in the total terrigenous flux to Ceara Rise is approximated by the percentage of non-carbonate material. Surface water productivity remained low throughout the late Pleistocene with relatively lower productivity during glacial stages (Ruhlemann et al., 1996), thus some productivity overprint is present. Carbonate dissolution is thought to be small at these sites over this time period (Harris et al., 1997). For at least the last glacial cycle, glacial-interglacial differences in terrigenous mass accumulation rate are greater than glacial-interglacial differences in carbonate mass accumulation rate (Francois et al., 1990). Therefore, the Pleistocene carbonate cyclicity probably is driven primarily by dilution of carbonate with riverine terrigenous sediments.

Processes linked to sea level which may act to bring more terrigenous material to Ceara Rise during lowstands include a seaward location of the shoreline (decreased transport distance), continental shelf erosion, and possibly glacial period eastward retroflection of the North Brazil Current (Showers and Bevis, 1988). Low %$CaCO_3$ (high terrigenous flux) coincides with low -$\delta^{18}O$ (low sea level) and vice versa (Figure 4.4). Variance in both these time series is concentrated at the orbital frequencies of 1/100,000 yr^{-1}, 1/41,000 yr^{-1}, and 1/23,000 yr^{-1} (Figure 4.5A). The %$CaCO_3$ record also contains significant variance at the 1/19,000 yr^{-1} frequency, which is small in the -$\delta^{18}O$

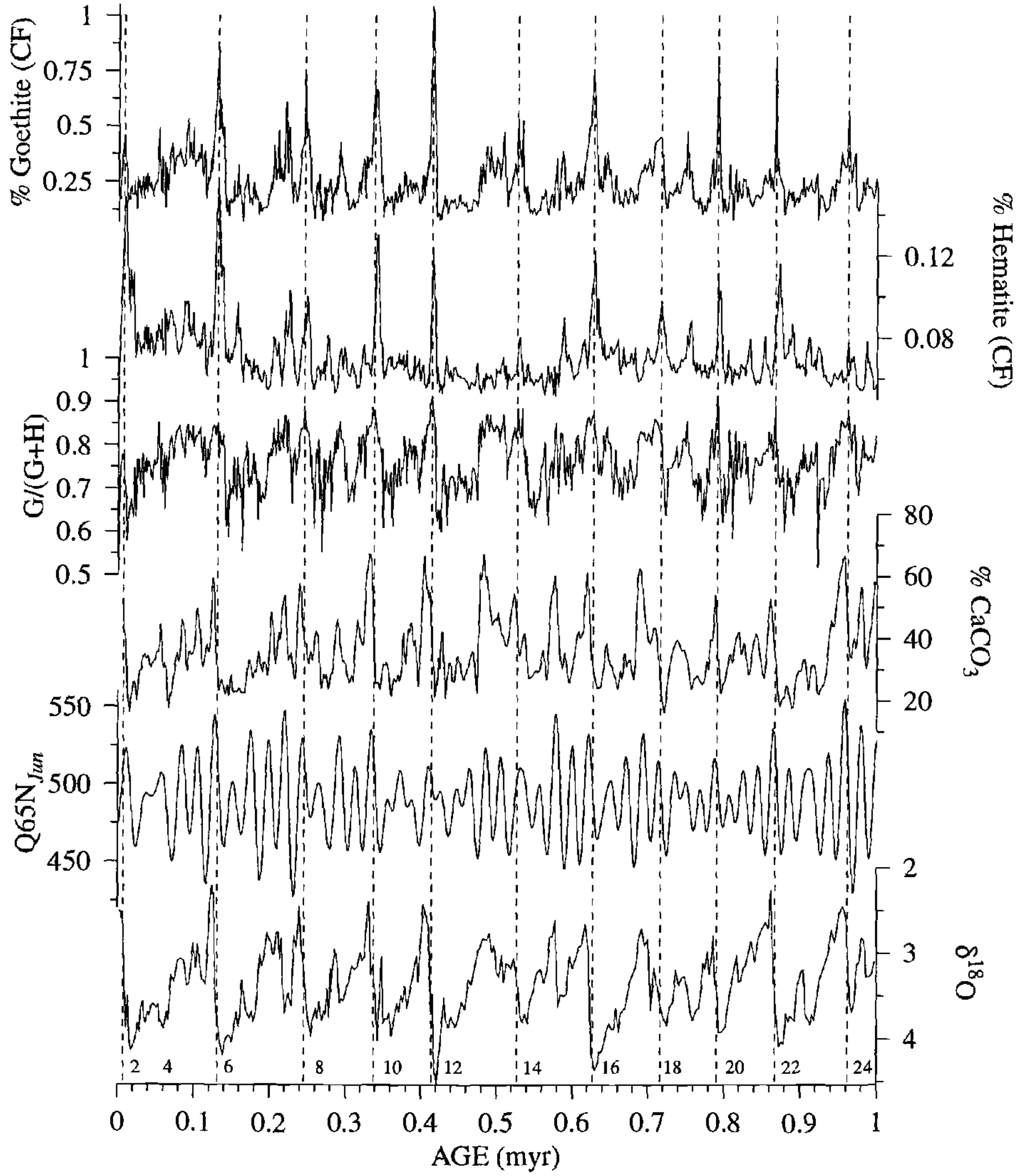

Figure 4.4 Time series of estimated % goethite and % hematite, both on a carbonate-free basis (CF), % goethite in total iron oxides, G/(G+H), calculated from % goethite and % hematite sampled at 2000 yr intervals after 6000 yr Gaussian smoothing, estimated %$CaCO_3$ (Harris et al., 1997), June insolation at 65°N (W/m^2; Laskar et al., 1993), and $\delta^{18}O$ plotted with a reverse vertical axis (Curry, W., unpublished data, primarily *C. wuellerstorfi*). Dashed vertical lines correspond to peaks in % goethite, which typically coincide with glacial terminations and $Q65N_{Jun}$ maxima. Small numbers above horizontal axis indicate oxygen isotope stages.

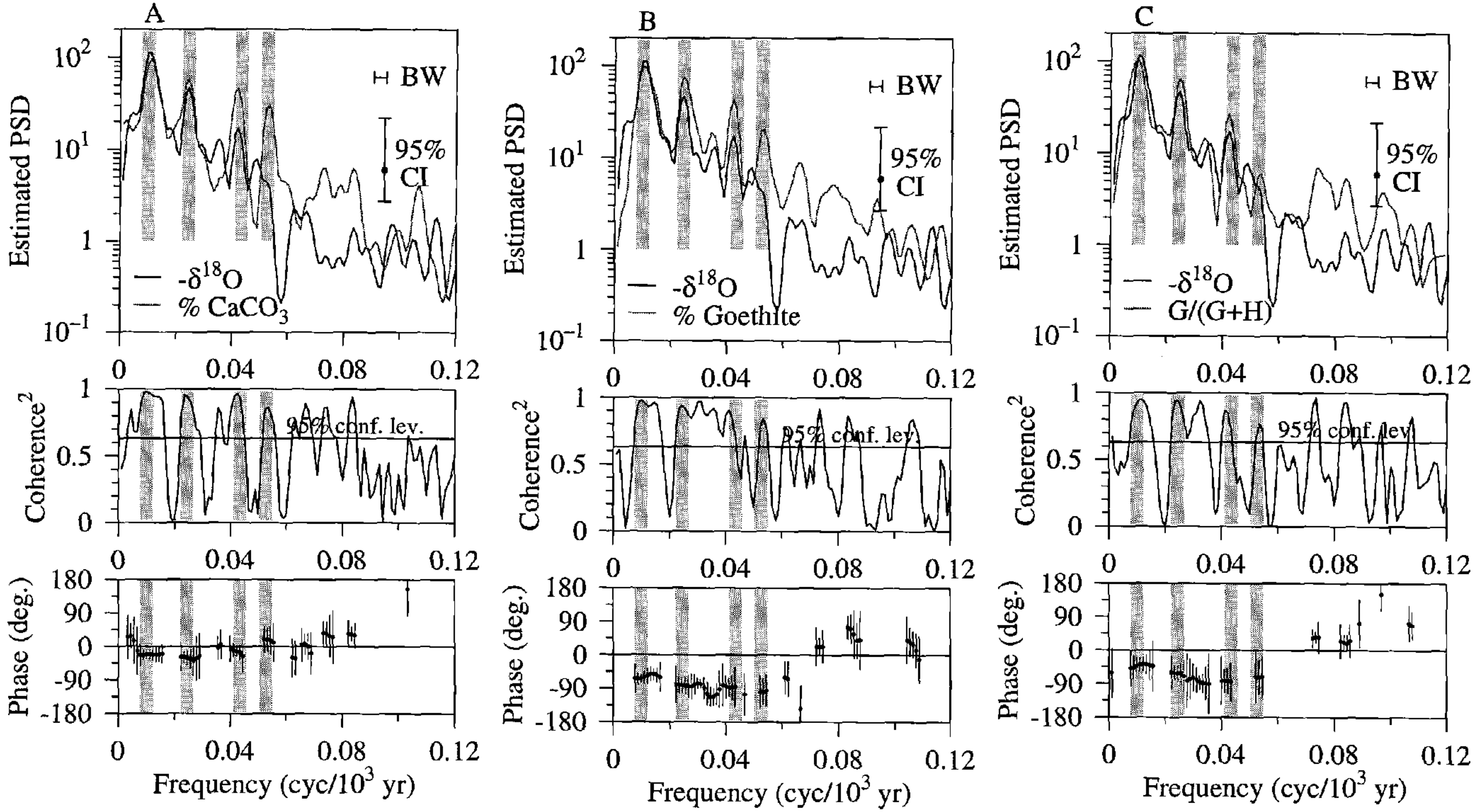

Figure 4.5 Variance, coherence, and phase spectra from cross spectral analysis of: (A) -$\delta^{18}O$ and %$CaCO_3$, (B) -$\delta^{18}O$ and % goethite, and (C) -$\delta^{18}O$ and G/(G+H). All time series analyzed from 0-0.9 myr, sampled at 2 kyr intervals after 6 kyr Gaussian smoothing. Bandwidth = 0.0044, 8 degrees of freedom. Gray vertical bars indicate position of 1/100, 1/41, 1/23, and 1/19 kyr^{-1} frequencies. Width of the gray bars equals the bandwidth. Positive phase indicates that the first time series listed (black lines) leads the second time series (gray lines). 95% confidence intervals on phase estimates.

record. The two time series are nearly in phase at all orbital frequencies, consistent with a sea level control on %CaCO$_3$ by terrigenous dilution (Figure 4.5A).

Iron oxides

Over the past million years, maxima in goethite and hematite percentages, calculated on a carbonate-free basis, occur during transitions from glacial to interglacial stages (Figure 4.4). These iron oxide maxima demonstrate that lowland erosion increases relative to the total load during major ice melting events at high northern latitudes.

The generally in-phase relationship between %CaCO$_3$ (high values associated with low terrigenous flux) and sea level (proportional to -δ^{18}O) coupled with carbonate-free iron oxides leading -δ^{18}O (Figure 4.5) shows that iron oxide concentrations in the terrigenous fraction are not linked to total terrigenous flux. If increases in %goethite and %hematite were solely a function of increases in the terrigenous flux to Ceara Rise, then peaks in iron oxides in total sediment would coincide with low %CaCO$_3$ and low sea level, and carbonate-free values would be constant, neither of which is the case (Figure 4.4). The iron oxide concentrations reflect changes in the composition, rather than the magnitude, of the terrigenous flux. They document climatic conditions in the Amazon Basin, rather than local sea level control of terrigenous sedimentation at Ceara Rise.

In lowland soils, goethite is favored over hematite with decreasing temperature, increasing precipitation and/or increasing soil organic carbon content (Kampf and Schwertmann, 1983). Thus, the fraction of goethite in total iron oxides (G/(G+H)); Figure 4.4) is a measure of lowland climate. Lowland glacial temperatures (Stute et al., 1995) are too high (>20°C) for a significant temperature effect on this ratio, therefore, precipitation and soil organic carbon content control G/(G+H) on glacial-interglacial scales in Amazonia. Precipitation and soil organic carbon are related because moist areas are more vegetated.

Temporal variations in G/(G+H) from Ceara Rise are visually similar to -$\delta^{18}O$ (Figure 4.4) but G/(G+H) maxima precede sea level highstands and minima precede lowstands. Peaks in G/(G+H) are broader than deglacial %goethite or %hematite peaks and G/(G+H) values tend to remain relatively high into interglacial periods, indicating continued high levels of precipitation. Variance in all three iron oxide records is concentrated at orbital frequencies. Negative phase estimates indicate that changes in the oxides lead -$\delta^{18}O$ (sea level) at all coherent frequencies (Figures 4.5B and 4.5C).

DISCUSSION

Origin of the iron oxides

We refer to a terrigenous origin for the iron oxides found in Ceara Rise sediments. However, thin (1-5 cm) sedimentary layers rich in iron found in sediment cores from throughout the western tropical Atlantic at the termination of the last ice age have also been attributed to an in situ, diagenetic origin (McGeary and Damuth, 1973; Richardson, 1974). Two observations support a terrigenous source. First, if diagenetic iron accumulates at the base of the present oxidized layer, reducible iron must continually migrate upward to keep pace with sedimentation (Wilson et al., 1986), dissolving diagenetic layers deeper in the sediment. Even if erasure of diagenetic layers buried below the oxidized zone were slow, the iron oxide abundance would decrease downcore. In conflict with this prediction, %goethite and %hematite oscillate downcore with little or no loss of amplitude in Pleistocene sediments (Figure 4.4) and display higher amplitude variability in Miocene sediments (Chapter 5). Second, the zones of high hematite and goethite percentages we observe are typically about 25 cm wide. Typical diagenetic iron-rich layers are only a few cm wide (McGeary and Damuth, 1973) because they form at specific depths relative to pore-water oxygen gradients, below the near-surface bioturbation layer.

Coretops reveal a plume of goethite extending into the western Atlantic from the mouth of the Amazon River (Balsam and Deaton, 1991) indicating a riverine terrigenous origin. Hematite and goethite are both prevalent in Amazon soils (Jordan, 1985) which links the two to a common source. Although aeolian hematite from Africa is also present in Atlantic core top sediments, the plume of African hematite is far north of Ceara Rise, at about 20°N latitude (Sarnthein et al., 1982) outside this study area.

Source and weathering of terrigenous material

The Andean highlands of Peru (Solimoes River) and Bolivia (Madeira River) presently supply most of the suspended sediment at the mouth of the Amazon (Gibbs, 1967; Meade et al., 1985), although most probably is stored temporarily on floodplains en route (Meade, 1994) and undergoes some degree of weathering (Johnsson and Meade, 1990). Steep Andean topography coupled with high rainfall (up to 5000 mm/yr), volcanism and earthquakes encourages physical weathering on eastern Andean slopes. Lowland rivers today supply a small portion of total suspended sediment, although up to 70% of the total water runoff (Meade, 1994).

If material derived from the highlands and lowlands maintained distinctive compositions on glacial-interglacial time scales, then the bulk composition of suspended sediment at the mouth of the Amazon would depend only on the respective contributions from each source. Taking %goethite as a signature of a lowland source, increased goethite concentrations in the deep sea sediment terrigenous fraction reflect increases in the lowland source and/or decreases in the highland source. Two mechanisms may alter this balance: (1) continental storage and release of Andean sediment, related to sea level fluctuations, and (2) changes in precipitation distribution.

Sea level may contribute to changing the balance between lowland and highland source in the following manner. R. Stallard (1988; personal communication, 1998) hypothesizes that Andean material may be trapped up the Amazon valley as sea level rises, effectively increasing the influence of lowland river sources. This rapidly deposited Andean material would erode when sea level falls, diluting the lowland signature and producing a surge of Andean material during transitions from interglacial to glacial conditions. This process predicts that the total terrigenous flux should be at a minimum when sea level is rising. However, over the most recent glacial cycle, maximum terrigenous flux at Ceara Rise, derived from ^{230}Th accumulation, occurred during the LGM (Francois et al., 1990). The spikes in %goethite and %hematite do not coincide with minimal terrigenous flux, therefore it appears that sediment trapping in the Amazon valley is not a major influence on the mineralogy of the terrigenous component in Ceara Rise sediments.

Changes in the precipitation balance may influence the relative contributions from highland and lowland sources by drying out or wetting highland source areas and lowland source areas separately. Assuming that the deglacial terrigenous flux was about two-thirds the glacial maximum value (Francois et al., 1990) and the relative deglacial lowland contribution was three times the glacial contribution (based on deglacial %goethite peaks, Figure 4.4), the lowland deglacial flux would have to be twice the glacial flux, while the highland flux was halved. These flux changes may be plausible given recent interannual variability in highland and lowland river sediment loads (Richey et al., 1986), although data are sparse.

Precipitation and temperature can also affect chemical weathering. Cooler temperatures and lower precipitation slow chemical weathering rates, preserving more physical weathering products that would break down under warm humid conditions

(Martinelli et al., 1993). Such environmental changes could alter the average lowland soil composition without changing the balance of source regions. If %goethite in the total sediment load is dominantly weathering- rather than source-controlled, increases in %goethite imply increased chemical weathering.

Source and weathering influences are not mutually exclusive. Material stored on the continent via a sea level driven control would be affected by weathering depending on the length of storage and rapidity of deposition and burial. Increased lowland precipitation promotes an increase in chemical weathering products both by dilution of the mainstem Amazon with lowland erosive products and by weathering of material derived from the highlands.

Pleistocene Amazonian climate

While goethite and hematite concentrations in the terrigenous fraction depend on Andean erosion, the relative proportion of oxides, G/(G+H), is a proxy for lowland precipitation and vegetation without a highland signature. This is because most of the oxides are derived from lowland soils. Precipitation and soil carbon increases imply rainforest expansion since forests depend on high precipitation levels (Clapperton, 1993) and forest soils typically contain higher organic carbon concentrations than grassland soils (Haase, 1992). At all orbital frequencies, %hematite, %goethite and G/(G+H) lead ice volume by several thousand years (Figures 4.5 and 4.6). Wet periods in the Amazon lowlands with increased forest cover and higher soil organic carbon contents occur during ice melt, and dry periods occur during ice growth. For the most recent glacial termination, this finding of wet conditions during deglacial periods is supported by oxygen isotopic evidence for increased freshwater discharge to the Atlantic (Showers and Bevis, 1988) and pollen evidence for lowland forest expansion (Servant et al., 1993).

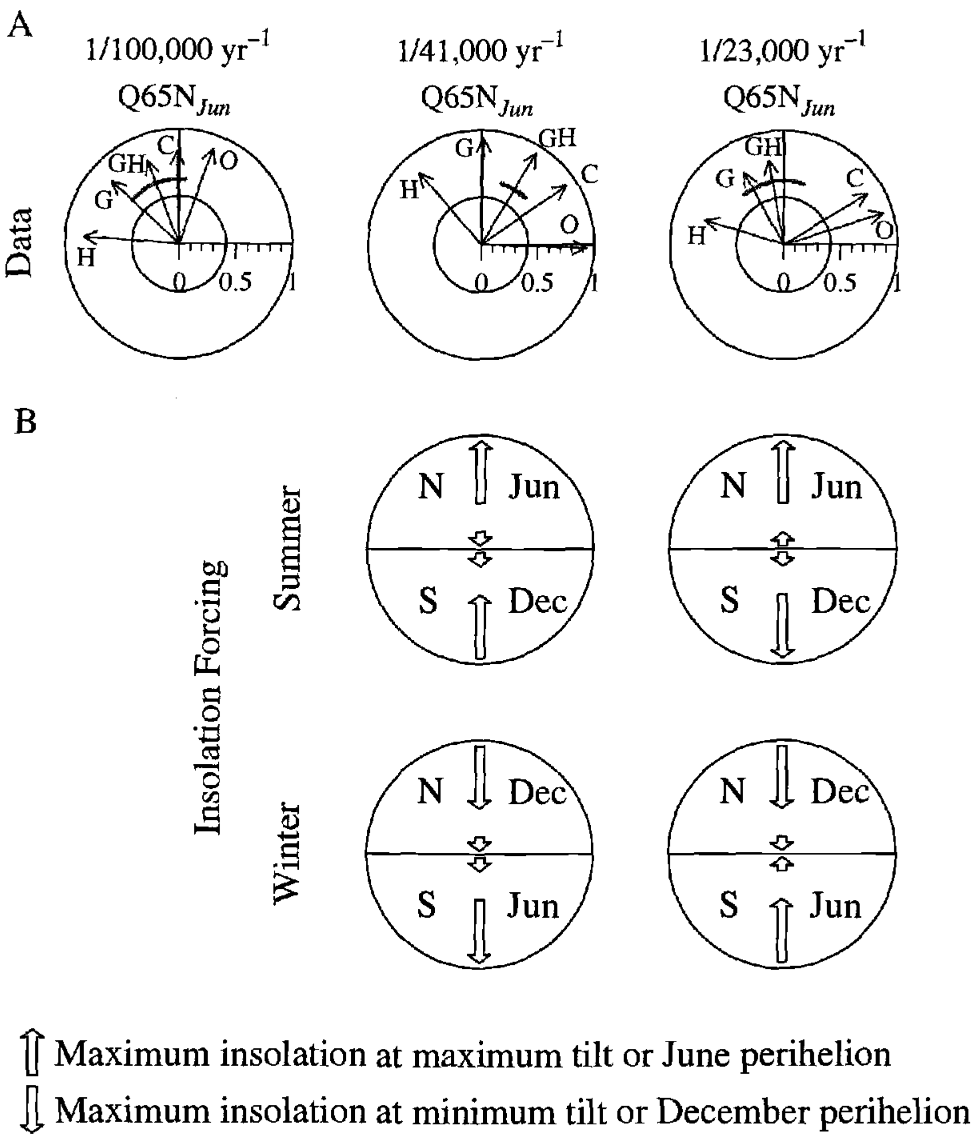

Figure 4.6 (A) Phase vectors in degrees for sedimentary time series relative to June insolation at 65°N at the main orbital frequencies ("Data" panel, see Table 4.1). $Q65N_{Jun}$ is defined at 12 o'clock, with vectors to the left (right) indicating a lead (lag) of the climate index relative to $Q65N_{Jun}$ within a frequency band. H = %hematite, G = %goethite; GH = G/(G+H); C = %$CaCO_3$, and O = $-\delta^{18}O$. Arrow length indicates coherence^2 defined by the horizontal length scale from 0-1. The inner circle indicates the 80% confidence cutoff for significant coherence. 80% confidence ranges in phase angle are shown for G/(G+H) relative to $Q65N_{Jun}$ as gray arcs. Maxima in % goethite and G/(G+H) occur during ice melt and the sequence of events is consistent at all orbital frequencies. (B) Phase vectors of insolation (June and December) at low and high latitude. Summer insolation at northern high latitudes is the only insolation forcing with both tilt and precession phases consistent with the climate response in G/(G+H) (both arrows pointing up). See text for phase model details.

Table 4.1 Cross spectral analysis results. All time series except insolation (Laskar et al., 1993) are from Site 926, 0-0.9 Ma, smoothed with a 6000 yr Gaussian window and sampled at 2000 yr intervals; n = 450, bandwidth = 0.0044. Cutoff for significant coherence^2 = 0.41 ($1-\alpha = 0.80$). Positive phase means the first time series listed leads. 80% confidence intervals on phase.

Orbital Period	100,000 yr		41,000 yr		23,000 yr	
Data	Coh[a]	ph,° (10^3 yr)[b]	Coh[a]	ph,° (10^3 yr)[b]	Coh[a]	ph,° (10^3 yr)[b]
Q65N[c] v. $-\delta^{18}O$	0.88	19±18 (5)	0.93	92±14 (10)	0.92	72±14 (17)
Q65N v. +%$CaCO_3$	0.81	-2±24 (-0.6)	0.91	56±15 (6)	0.86	59±20 (4)
Q65N v. Goethite (CF[d])	0.80	-47±25 (-13)	0.93	1±17 (0.1)	0.72	-29±32 (-2)
Q65N v. Hematite (CF[d])	0.84	-86±21 (-24)	0.83	-41±22 (-5)	0.72	-73±32 (-5)
Q65N v. G/(G+H)	0.77	-21±27 (-6)	0.93	31±17 (4)	0.75	-10±29 (-0.6)

[a] Coherence^2; [b] Phase in degrees ± 80% confidence error bars with phase in thousands of years in parentheses; [c] June insolation at 65°N; [d] carbonate-free.

We add that this climate pattern occurs consistently throughout the late Pleistocene and at all dominant frequencies of orbital variability.

This phasing of the oxides with respect to -δ^{18}O suggests that ice volume alone cannot drive tropical climate change, since the oxide index leads -δ^{18}O. A mechanism called upon to force both low and high latitude climate signals must lead, or be in phase with, both the oxide and isotope records. The tropical atmosphere might respond rapidly to such forcing while slow ice sheet dynamics would cause ice volume to lag.

Orbital modulation of solar insolation, which has strongly influenced global climate during the late Pleistocene (e.g. Hays et al., 1976), may force precipitation variability in the Amazon Basin. A combination of Earth's orbital eccentricity, axial tilt, and orbital position when the equinoxes occur (precession) induce insolation variations. These parameters modify the quantity and the seasonal and latitudinal distribution of solar energy received by the Earth.

Over the past million years, maximum %goethite, the proxy for relative lowland erosion, and G/(G+H), the precipitation proxy, are statistically in phase with or slightly lag maximum northern hemisphere summer insolation at high latitude ($Q65N_{Jun}$) at 1/41,000 yr^{-1} and 1/23,000 yr^{-1} frequencies (Figure 4.6, "Data"; Table 4.1). Assuming that maximum precipitation should correspond to maximum insolation, $Q65N_{Jun}$, commonly cited as the "pacemaker" of continental ice sheets (Hays et al., 1976), represents the only insolation forcing (with latitude and season) that has an appropriate phase with respect to Amazon climate proxies at both obliquity and precessional frequencies. This conclusion is based on a phase model after Imbrie et al. (1989; Figure 4.6).

The "Insolation Forcing" panel in Figure 4.6 shows a summary of models for insolation forcing as a function of hemisphere, latitude and season. Arrows are phase vectors for maximum insolation at tilt and precession frequencies at low and high latitudes, summer and winter. Each circle represents a globe, and the location of each of the four vectors on each circle represents a region of the globe: northern high latitude, northern low latitude, southern low latitude and southern high latitude. The direction of the arrows designates the phase of maximum insolation relative to maximum tilt or June perihelion. Arrows pointing up indicate that maximum insolation for a particular latitude and season occurs at maximum tilt or June perihelion. Arrows pointing down indicate that maximum insolation for a particular latitude and season occurs at minimum tilt or December perihelion. The only insolation forcing with both tilt and precession phases consistent with the climate response in G/(G+H) is summer (June) insolation at northern high latitudes (both arrows pointing up).

How might $Q65N_{Jun}$ drive Amazon Basin climate to explain the phases of both %goethite and G/(G+H) in the dominant orbital bands? One hypothesis is that the austral summer (wet season) position of the ITCZ during the most recent glacial termination was farther north than today, driven by minimal summer continental heating of low latitude South America (Martin et al., 1997). With the ITCZ farther north, less precipitation would fall in the central Bolivian Andes which are the headwaters of the Madeira River. Since the Madeira supplies a large portion of the total erosive products to the Amazon today (Meade et al., 1985), a more northerly position of the ITCZ in the past skews the erosional balance toward the Amazon lowlands while increasing lowland precipitation. The opposition of lowland and Bolivian altiplano deglacial lake levels also supports this hypothesis (Servant et al., 1993; Wirrmann and Mourguiart, 1995).

While a mechanism for precipitation variability involving changing the position or intensity of the ITCZ appears reasonable, it cannot be forced by summer (Dec.) insolation at 10°S or 20°S as hypothesized by Martin et al. (1997) because the phases of G/(G+H) at tilt and precession frequencies disagree with these insolation curves (Figure 4.6). Rather than a local continental control of the ITCZ position, we propose an oceanic circulation process, forced by northern hemisphere high latitude insolation. Enhanced North Atlantic

Deep Water (NADW) formation during deglacial periods and a stronger thermohaline circulation, driven by $Q65N_{Jun}$, would increase heat transport from the southern to northern hemisphere (e.g. Rind and Chandler, 1991), cooling sea surface temperatures in the southern ocean (Crowley, 1992). Warming water north of the equator would shift the mean position of the ITCZ northward, producing the observed pattern of Amazon precipitation inferred from G/(G+H). This mechanism is supported by the early phases (preceding ice volume) of equatorial sea surface temperatures both in the Atlantic (Imbrie et al., 1989) and in the eastern Pacific (Pisias and Mix, 1997) although, admittedly, the phase match to the Amazon Basin is not precise, and past changes in oceanic heat transport are not well understood. We are left with the conclusion, based on phase considerations, that northern hemisphere insolation at high latitudes drives Amazon basin climate cycles at tilt and precession frequencies, and precipitation cycles respond rapidly to such forcing.

Explaining the strong 100,000 yr cycle of Pleistocene climate change given minimal external forcing is a classic problem (e.g. Imbrie et al., 1993). Insolation forcing at 1/100,000 yr^{-1} is small and the phase is later than expected for a forcing mechanism, since maximum insolation at this frequency lags Amazon climate parameters and barely leads $-\delta^{18}O$ (Figure 4.6). However, an effect of precession forcing may explain the strong eccentricity climate response in Amazonia, which differs from the high latitude ice volume response. Several studies have shown that "clipped" precession cycles transfer power from precession bands to the 1/100,000 yr^{-1} and 1/413,000 yr^{-1} periods of eccentricity (Pokras and Mix, 1987; Short et al., 1991; Crowley et al., 1992), due to a greater climate response to insolation maxima than to minima. Our data support the theory that the Amazon climate system may respond in such an assymetrical manner: G/(G+H) contains significant variance in the 1/413,000 yr^{-1} band over the interval 0.2-2.6 myr, a time period long enough to resolve a 413,000 yr climate cycle (Figure 4.7).

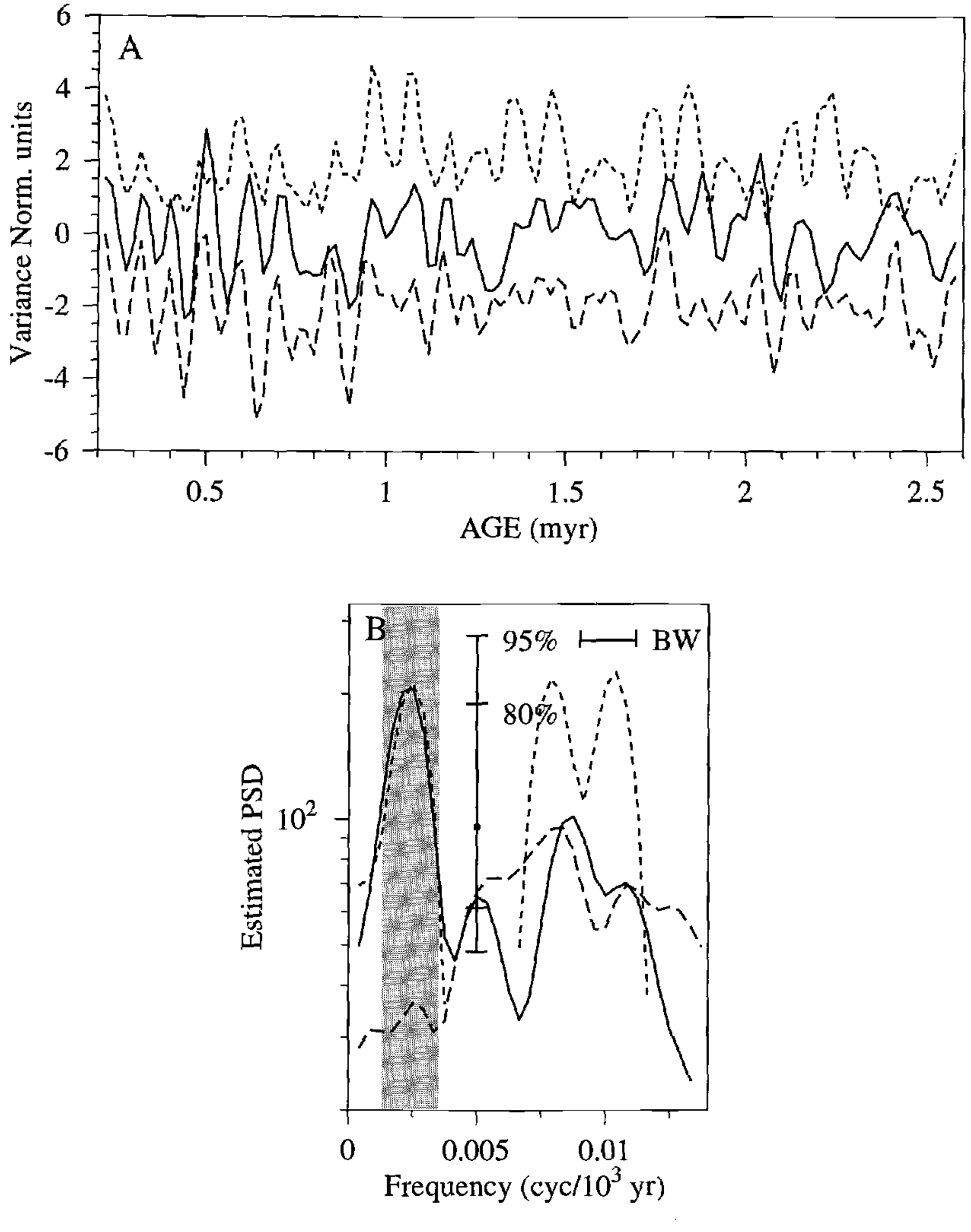

Figure 4.7 (A) Time series of G/(G+H) (solid), $-\delta^{18}O$ (long dash), and June insolation at 65°N (short dash), from 0.2 to 2.6 myr. Time series were detrended, normalized to zero mean and unit variance, then lowpass filtered to remove all frequencies higher than 1/70,000 yr^{-1}. Means are offset for convenience. (B) Frequency spectra of G/(G+H) (solid), $-\delta^{18}O$ (long dash), and June insolation at 65°N (short dash), analyzed from 0.2 to 2.6 myr, an interval long enough to include several 413,000 yr cycles. Vertical gray bar is centered at 1/413,000 yr^{-1} and its width equals the bandwidth. Significant variance at this frequency, a component of eccentricity, is present in the insolation record and the G/(G+H) precipitation proxy, but absent from $-\delta^{18}O$.

Significant variance at this frequency is absent from ice volume ($-\delta^{18}O$) records. Therefore, we infer that the long period cycles of aridity in Amazonia could be driven by a nonlinear amplification of precessional forcing perhaps due to selective sensitivity to the rainy season and feedbacks related to recycling of water by vegetation (Salati and Vose, 1984). Alternatively, a "clipped precession" response in the geologic record may result from high sediment discharge during the rainy season (Meade, 1994) thus amplifying that season's effect on the marine sedimentary record, relative to the dry season when discharge is low.

Because of its early phase at all orbital frequencies, low latitude climate change may itself be part of the mechanism driving changes in high latitude ice. An arid Amazonia during ice growth (low G/(G+H)) implies loss of tropical rainforest extent which would result in a large transfer of carbon from terrestrial biomass storage to the oceans (Shackleton, 1977). Replacement of rainforest areas in lowland Amazonia by savanna-type vegetation (Clapperton, 1993) would increase the region's albedo and reduce water vapor in the atmosphere by reducing evapotranspiration. However, in some regional model output, the net effect of reducing tropical forest cover is increased local surface temperatures, since the effect of increased albedo is overcome by a decrease in evaporative cooling (Polcher and Laval, 1994; Lean and Warrilow, 1989). Such a temperature increase would be counter global cooling trends during ice growth. This modeled warming effect has been questioned by Crowley and Baum (1997), thus it remains uncertain how tropical vegetation change might act as a global feedback mechanism. The results presented here suggest that tropical atmospheric and oceanic circulation, which are manifested in the Amazon region, may be part of the chain of events that contribute to global 100,000 yr climate cycles.

CONCLUSIONS

Goethite and hematite in Ceara Rise sediments are derived primarily from the Amazon lowlands. Increases in goethite and hematite during major deglacial transitions imply relative increases in erosion from lowland sources. We suggest that the major climate variable controlling changes in relative erosion is variability in the highland-lowland balance of precipitation. During the Late Pleistocene, high levels of lowland Amazon precipitation as measured by G/(G+H) coincided with ice melting events and maximum June insolation at 65°N. At precessional and obliquity frequencies, these precipitation changes may be driven by high northern latitude summer insolation, although the physical mechanism is unclear. Insolation forcing at 65°N is consistent with the same forcing for deep Atlantic circulation on glacial-interglacial time scales that may translate climate changes via the deep ocean resulting in early climate responses in the southern hemisphere and tropics (Imbrie et al., 1992, 1993; Harris et al., 1997). At eccentricity frequencies, insolation may provide the forcing for Amazon Basin climate if the climate responds nonlinearly to precession forcing, transfering power to 100,000 yr and 413,000 yr periods. This theory is supported by the presence of significant variance at 1/413,000 yr^{-1} frequencies in lowland precipitation documented here. Analysis of these long times series shows that late Pleistocene climate extremes in Amazonia precede northern hemisphere ice extremes, suggesting that tropical climate changes may affect, rather than respond to, global ice age climate cycles.

ACKNOWLEDGMENTS

Helpful reviews of this manuscript were provided by N. Shackleton and R. Stallard. Comments from G. Seltzer and N. Pisias also improved the manuscript. Thanks to W. Curry for the use of his unpublished oxygen isotope data and to Walter Hale and Alex Wueblers for their assistance at the Ocean Drilling Program Core

Respository in Bremen. Collection of reflectance data was supported by USSSP grant #154-20868b and later work by NSF-OCE 95-30094.

5.

Amazon Drainage Tectonic and Climatic History, Middle Miocene to Present

Sara E. Harris, Alan C. Mix and Nicklas G. Pisias

ABSTRACT

Two episodes since the middle Miocene mark major changes in erosion patterns from South America to the Atlantic Ocean. Step-like transitions in the magnitude of terrigenous flux and the composition of terrigenous material deposited at Ceara Rise in the western tropical Atlantic occur at about 8 Ma and 4.5 Ma. These steps likely reflect major tectonic deformation in eastern Andean provinces which altered the source area for the Amazon drainage. Orbital scale climate variability is superimposed on the long-term changes induced by tectonic processes. For much of the 13 My record, high precipitation in the Amazon lowlands, recorded by iron oxide minerals, is linked to high %$CaCO_3$ in Ceara Rise sediments, and both are associated with high summer insolation in the high latitude northern hemisphere. However, during two intervals, the early Pliocene (~4.5-5.0 Ma) and late Plio-Pleistocene (2.5-0 Ma), precipitation cycles are decoupled from %$CaCO_3$. Phase and amplitude considerations suggest that during the early Pliocene interval, Amazon Basin precipitation was responding to summer insolation in southern hemisphere low latitudes, driving a monsoon circulation pattern, perhaps in association with newly uplifted Andes. From ~2.5-0 Ma precipitation cycles lead %$CaCO_3$ at all orbital frequencies, reflecting sea level control of %$CaCO_3$ at Ceara Rise, while precipitation maintains constant phase relative to northern hemisphere insolation forcing. The initiation of large fluctuations in northern hemisphere ice volume about 2.5 Ma modify calcium carbonate by terrigenous dilution at low sea level, but do not directly influence tropical precipitation cycles.

INTRODUCTION

Development of a cross-continental drainage on South America may be causally linked to tectonic events in the Andes (Hoorn et al., 1994). Based on an estimated age of the Amazon Cone (Damuth and Kumar, 1975) and the timing of burial of carbonate platforms under siliciclastics off the coast of northeast Brazil (Campbell, 1992), the present drainage of the Amazon River to the Atlantic Ocean initiated during the late Miocene, although this event was not well dated.

In general, tectonic deformation in the Andes progressed eastward with time. From the middle Miocene to the present, two major periods of compressive deformation in the Peruvian Andes are recognized: Quechua stages 2 (c. 8.5-9.5 Ma), and 3 (c. 3.8-6 Ma) (Megard et al., 1984). Compression and erosion in the Eastern Cordillera is associated with Quechua 2, while deformation in the Subandean fold and thrust belt is associated with the later Quechua 3 event (Megard, 1987). In the Bolivian Andes, $^{40}Ar/^{39}Ar$ dates bracketing an erosional unconformity show that prior to about 10 Ma, deformation in the central Bolivian Andes was concentrated in the Altiplano and Eastern Cordillera (Gubbels et al, 1993), while dates for deformation in eastern Andean provinces, the Interandean zone and Subandes, range from 10 to post-5 Ma (Gubbels et al, 1993; Kley, 1996). Fission track data indicate a dramatic increase in uplift rates in the Eastern Cordillera and Altiplano from 15-10 Ma, with the upward trend continuing to the present (Benjamin et al., 1987), implying increases in exhumation and erosion of Andean material. Crough (1983) estimated that 2.5-5.0 vertical kilometers of material have eroded from the Bolivian Andes in the past 12 Ma.

Such tectonic events influenced the development of the Amazon River drainage and thus the erosion of terrigenous material to the Atlantic. Here we examine the signature of changing terrigenous sedimentation in the western tropical Atlantic from the middle Miocene to the present (13-0 Ma), in order to better constrain the timing of Andean tectonic events and Amazon erosional and climatic patterns. High frequency climate fluctuations in the orbital bands are superimposed on long-term sedimentary trends. We investigate the evolving relationships among insolation, %$CaCO_3$ in Atlantic deep sea sediments, and average precipitation conditions throughout the lowland Amazon basin to understand the processes driving both Amazon lowland precipitation and %$CaCO_3$ since the middle Miocene.

The evidence we present here is from 290 m of the deep-sea sedimentary sequence recovered at Ocean Drilling Program (ODP) Site 926 (3°43'N, 42°54'W, 3598 meters water depth) at the southern end of Ceara Rise in the western tropical Atlantic (Figure 5.1). Terrigenous sediments from South America and biogenic carbonate microfossil tests dominate the sedimentary matrix in this region, and document tectonic and climatic changes on land. Long-term changes in clay mineralogy and terrigenous mass accumulation rates document the initiation and development of Andean erosion to the Atlantic. The iron oxide composition of the terrigenous fraction through time reflects both (1) long-term changes in drainage area impacting the average climate of lowland Amazonia and (2) orbital scale lowland climate cycles.

METHODS

Clay mineralogy

Clay mineralogy was measured with a Scintag DMC-105 x-ray diffractometer in two size fractions, (1) <2 µm and 2-20 µm. Samples were pre-treated with buffered acetic acid to remove calcium carbonate. Ultrasonic dissagregation and repeated centrifugation separated the <2 µm from the 2-20 µm fraction. All samples were saturated with $MgCl_2$. Preparation of oriented mounts followed procedures of Moore and Reynolds (1985).

Chlorite/kaolinite (C/K) peak area ratios for both the <2 and 2-20 µm fractions were calculated from the kaolinite-chlorite doublet near 3.5 Å. Illite/kaolinite (I/K) peak area ratios were calculated using the kaolinite peak at 3.5 Å and the illite peak at 10 Å.

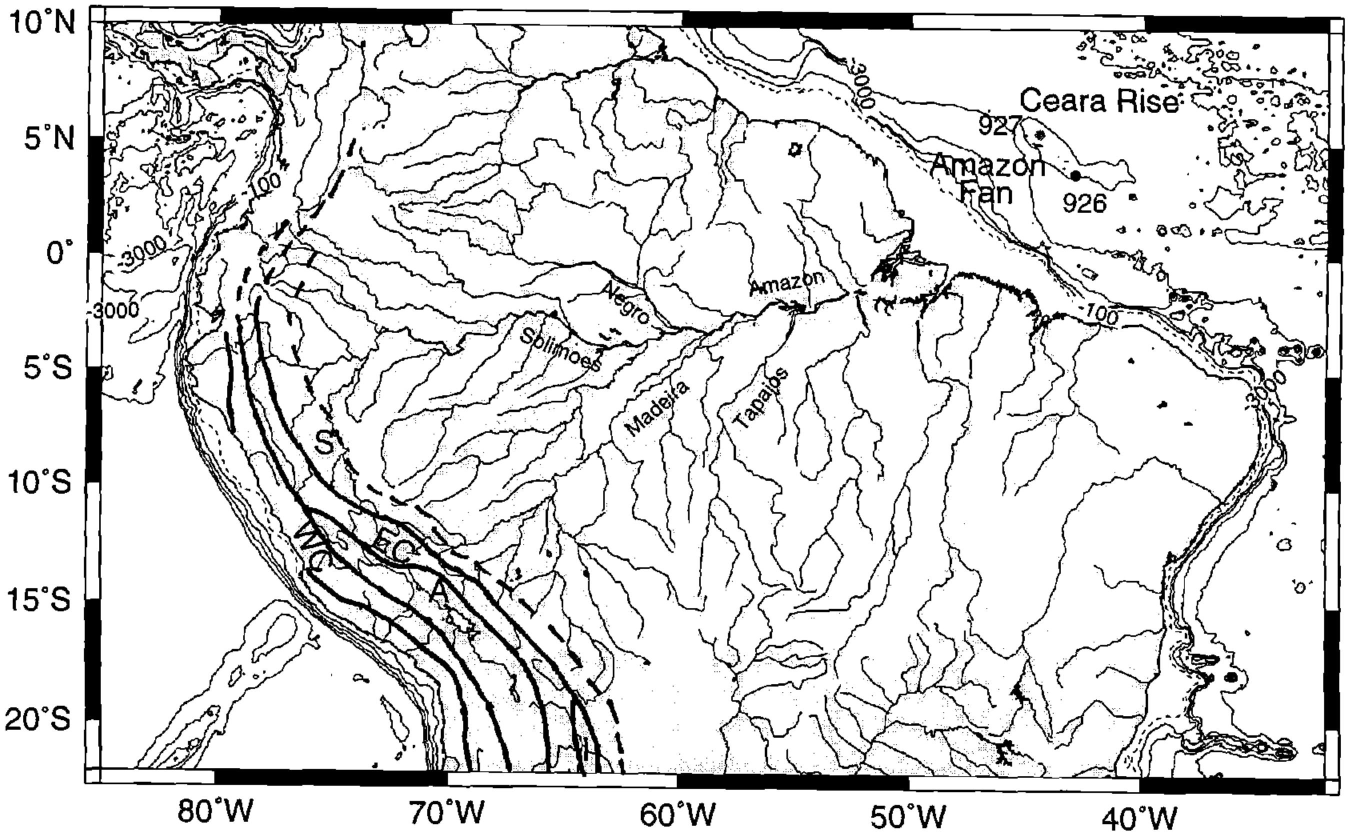

Figure 5.1 Map of South America and Ceara Rise. Sedimentary records are from Site 926. Andean provinces are marked to show geographic relationships. WC=Western Cordillera, A=Altiplano, EC=Eastern Cordillera, I=Interandean Zone, S=Subandean fold and thrust belt.

Following Biscaye (1965), glycolated traces were used to calculate ratios for the <2 μm fraction. C/K and I/K are proxies for the relative proportions of physical weathering products (chlorite and illite) derived from Andean sources, versus chemical weathering products (kaolinite) derived from leached lowland soils (Gibbs, 1967).

Carbonate, hematite and goethite from reflectance spectroscopy

Visible reflectance spectra measured at 5 cm intervals from the surfaces of wet split cores provide a rapid, non-intrusive means for estimating concentrations of calcium carbonate, hematite and goethite in marine sediments (Harris et al., 1997; Harris and Mix, in press). The average age spacing between samples ranges from 1.6 ky (Pleistocene) to 3.5 ky (Miocene). Reflectance- and magnetic susceptibility-based estimates of % calcium carbonate (Harris et al., 1997) allow expression of % hematite and % goethite on a carbonate-free basis.

The ratio of goethite/goethite+hematite, G/(G+H), is a climate parameter for areas with tropical chemically weathered soils. High G/(G+H) indicates high precipitation levels and/or high soil organic carbon content in the terrigenous source area (Kampf and Schwertmann, 1983). The ratio may also be affected by temperature variability, although Pleistocene glacial lowland Amazon temperatures, which are likely some of the lowest experienced in tropical South America since the Miocene, are too high (>20°C, Stute et al., 1995) to significantly affect G/(G+H). Because organic carbon content and moisture availability are generally correlated in these settings, G/(G+H) serves as a precipitation index for the integrated lowland regions of the Amazon or pre-Amazon drainage areas.

Terrigenous mass accumulation rates

Terrigenous mass accumulation rates (TMAR) are calculated as

$$\text{TMAR} = (100\text{-}\%\text{CaCO}_3) * \text{DBD} * \text{LSR} \quad (1)$$

where $\%CaCO_3$ is the weight percentage of calcium carbonate estimated from reflectance and magnetic susceptibility proxies (Harris et al., 1997). DBD is dry bulk density in g/cm^3, calculated from ODP shipboard gamma ray attenuation porosity evaluator (GRAPE) data, iteratively corrected for porosity variability using a grain density of 2.65 g/cm^3, following Weber et al. (1997). At Site 926, GRAPE measurements of wet bulk density agreed well with discrete samples over the interval 0-13.2 Ma (Curry et al., 1995), which justifies the use of GRAPE for bulk density estimates at this site. Orbitally tuned age models (Bickert et al., 1997; Tiedemann and Franz, 1997; Shackleton and Crowhurst, 1997) provide linear sedimentation rates (LSR) at typical resolution of one precession or one obliquity cycle. To construct the age model, magnetic susceptibility maxima (proxy for high terrigenous concentration, low $\%CaCO_3$) were tuned to Northern Hemisphere summer insolation minima, using the Laskar $90_{(1,1)}$ orbital solution (Laskar et al., 1993). In the interval from 2.5-0 Ma, 2 ky was subtracted from the tuned ages in order to match the phase of oxygen isotope data with Pacific records (Bickert et al., 1997). Due to the resolution of the age model and the low amplitude variability of DBD, $\%CaCO_3$ controls TMAR at high frequencies. Therefore, only long term changes in TMAR will be discussed.

RESULTS AND DISCUSSION

Sediment oxidation state

Prior to 12 Ma, sediments at Site 926 are reduced (light gray shading on Figure 5.2), with sediment colors ranging from greens to grays. Post-12 Ma sediments are

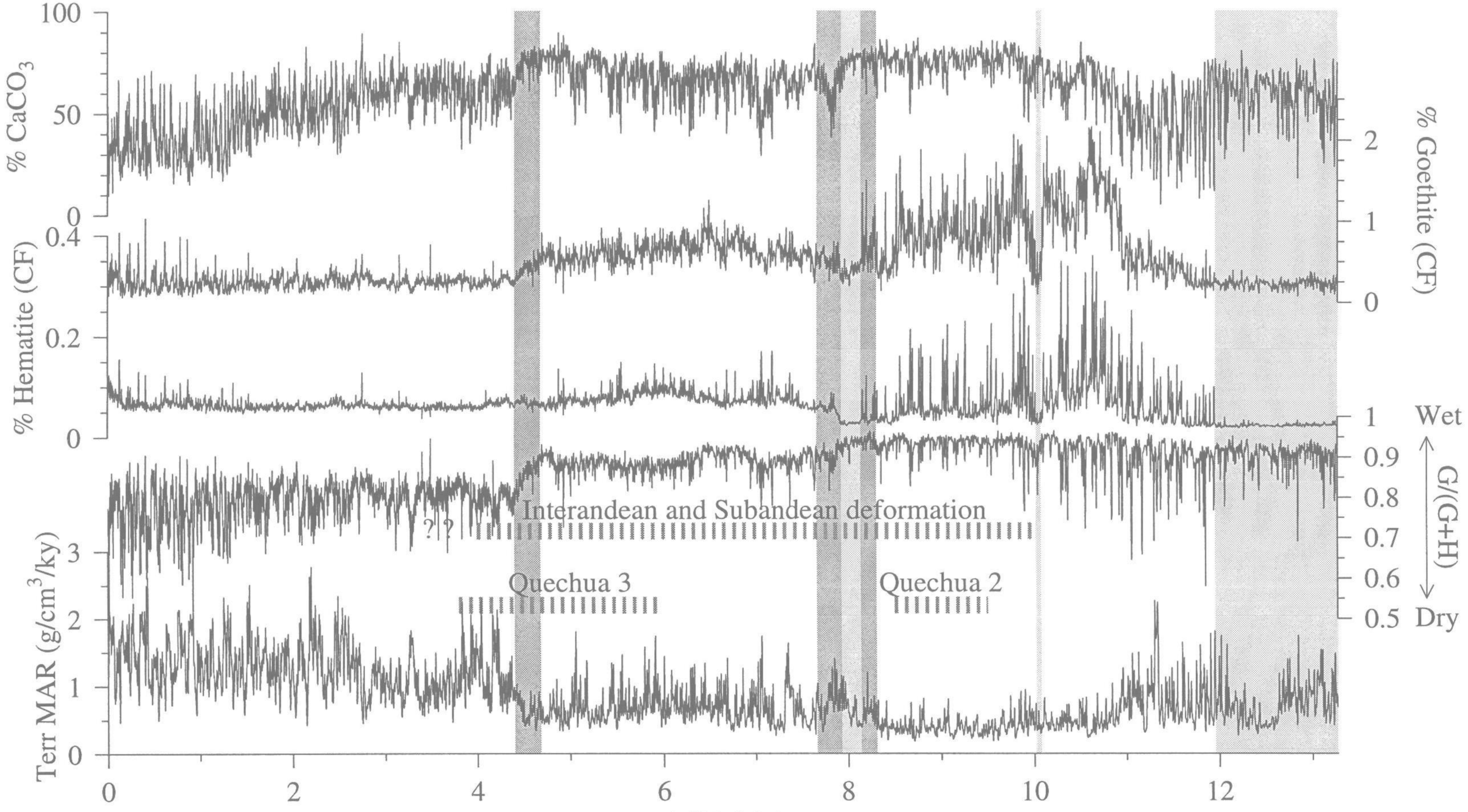

Figure 5.2 Time series from 0-13.2 of estimated %CaCO$_3$, estimated % goethite, estimated % hematite, goethite/goethite+hematite (G/(G+H)), and estimated terrigenous mass accumulation rates (Terr MAR). CF = carbonate-free. Vertical light gray bars encompass portions of the sedimentary record in which sediments are reduced and estimates of iron oxides may be suspect. Darker gray vertical bars encompass estimated dates for major tectonic changes as indicated by the data presented in this paper. The dark gray vertical bar near 8 Ma includes the period covered by the light gray bar. Horizontal striped bars show the range of dates for tectonic deformation events observed in the Peruvian and Bolivian Andes.

typically oxic and brown to gray colored. The pre-12 Ma reduction is coincident at the two Ceara Rise sites (926 and 927, not shown) from which we have data extending to sediments of this age, indicating regional rather than local sedimentary conditions. Estimates of % hematite and % goethite are both very low in this interval, suggesting either that the estimating equations we use are only viable in oxidized sediments or that sediment diagenesis removes terrigenous oxides on long time scales. The ratio of G/(G+H) shows no major change across the transition at 12 Ma, which may imply that the ratio is more robust than the estimates from which it is calculated, though we avoid interpretation of G/(G+H) in pre-12 Ma sediments. The fact that little change occurs in the clay mineral ratios of I/K and C/K between 8 and 22 Ma (Figure 5.3) suggests that no major change in the composition of terrigenous material occurred at 12 Ma and the low estimates of iron oxides are an artifact of the oxidation state of the sediments.

Sediment oxidation state may also be the major factor causing low % hematite and % goethite estimates near 10 Ma, and from 7.9 to 8.1 Ma (Figure 5.2). Low values of % goethite and % hematite in these intervals are anomalous compared to values above and below these horizons, reaching values as low (goethite) or lower (hematite) than Pleistocene lows. No clay mineralogy samples were analyzed for the interval near 10 Ma and the sample analyzed from the 7.9 to 8.1 Ma interval has low C/K and C/I ratios in both size fractions. The ratio values are similar to values in older sediments (Figure 5.3), thus, it is unlikely that a large influx of iron-oxide-poor physical weathering products diluted the hematite and goethite signals.

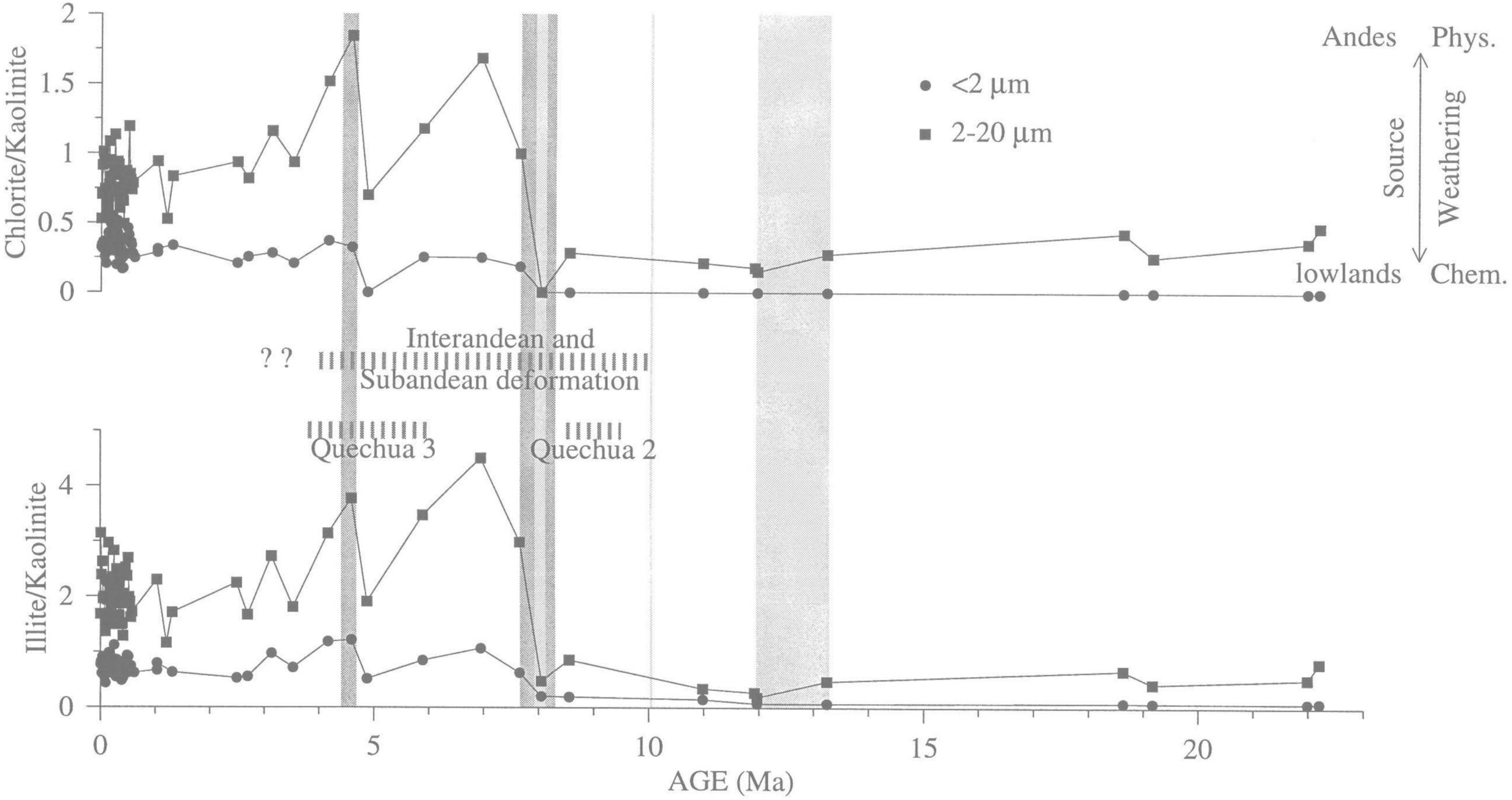

Figure 5.3 Time series of clay mineral ratios extending to 22 Ma. Vertical and horizontal bars as in Figure 5.2. Chlorite/kaolinite and illite/kaolinite ratios indicate the relative proportions of physical weathering products (chlorite and illite) to chemical weathering products (kaolinite) deposited at Ceara Rise through time. Little change occurs in these clay mineral ratios before 8 Ma. Data are shown for two size fractions, <2 µm and 2-20 µm.

Terrigenous sources and Andean tectonics

Conditions at 8 Ma and older

Prior to 8 Ma, the terrigenous material deposited at Ceara Rise was highly chemically weathered, with low chlorite/kaolinite and illite/kaolinite ratios (Figure 5.3). Although these data are low resolution, they represent the likely range of variability in this interval because samples analyzed have a large range of values for %$CaCO_3$, G/(G+H), and carbonate-free %hematite and %goethite. A bias based on samples preferentially selected from one climatic extreme is unlikely. In addition to clay mineral data, carbonate-free % hematite and % goethite were high prior to 8 Ma, the highest values observed since the middle Miocene (Figure 5.2). This abundance of chemical weathering products implies that the main source of terrigenous material to Ceara Rise prior to 8 Ma was deeply weathered lowland soils, perhaps from coastal areas, with little or no input from highland Andean sources.

Today the coastal regions receive more rainfall than the basin-wide lowland average (Salati, 1985) and soils are typically cation-poor. If the G/(G+H) ratio is an indicator of mean precipitation, then the NE coast of South America was more humid prior to 8 Ma (mean G/(G+H) = 0.91) than the average Pleistocene lowland Amazon Basin (mean G/(G+H) = 0.78, 0-2 Ma; Figure 5.2).

For nearly 3 My prior to the increase at 8 Ma, TMAR values are low, meaning low rates of erosion from South America to Ceara Rise (Figure 5.2). Some high TMAR values between 11 and 12 Ma rival Pleistocene values. Based on the constancy of clay mineralogy, we do not believe these early high TMAR values are a signal of Andean erosion.

The erosive event near 8 Ma is marked by changes in the magnitude and composition of the terrigenous flux (dark gray bar, Figures 5.2 and 5.3). Terrigenous mass accumulation rates begin to increase slightly at ~8.3 Ma (Figure 5.2) while clay mineral ratios chlorite/kaolinite and illite/kaolinite increase dramatically between 8.1 and 7.7 Ma (Figure 5.3). Post 8 Ma, a fundamental shift in the relationship between % goethite and % hematite occurs, as shown by a drop in the G/(G+H) ratio. This suggests that the coastal sources with high G/(G+H) ratios became progressively diluted with lower G/(G+H) material, likely from inland areas with lower precipitation and/or lower soil organic carbon, as the Amazon began draining a larger and more diverse area. If goethite, hematite, and low chlorite/kaolinite and illite/kaolinite ratios represent highly weathered material from coastal rivers, the changes in lithology near 8 Ma mark the beginning of significant contributions of physically weathered terrigenous material from highland Andean sources in addition to lowland sources.

This timing is later than a fundamental shift in elemental chemistry of the terrigenous fraction at Ceara Rise. Dobson et al. (1997) bracketed a change in the chemical (rare earth element) make-up of terrigenous sediments between 13.5 and 9.4 Ma, from a dominantly continental shield source to an Andean source. They also noted that the first increase in terrigenous mass accumulation rates at about 8 Ma postdated this chemical change, and suggested that cross-continental gradients were insufficient to carry large amounts of terrigenous material even though the chemical composition of that material had changed earlier. The timing of the chemical shift is not mirrored in mineralogy, implying that either (1) chemical weathering between 9.4 and 8 Ma was stronger in the Amazon Basin than post 8 Ma and affected the mineralogy without significantly altering the new Andean chemical signal, or (2) due to a low gradient, the new source signal was too small prior to the increase in terrigenous mass accumulation rates at 8 Ma to be detected in mineralogical analyses. These possibilities are not mutually exclusive. Clearly, major episodes of erosion of Andean material to the Atlantic postdated the chemical shift.

The mineralogical changes observed near 8 Ma postdate the Quechua 2 compressional event in the Peruvian Andes where the oldest post-deformation volcanics were dated at 9.0±0.3 Ma (Megard, 1984). The shift also occurred later than the initiation of deformation in the Interandean zone and Subandean fold and thrust belt, although it is bracketed within the range of dates for deformation in these eastern Andean zones. Changes in chemistry between 13.5 and 9.4 Ma (Dobson, et al., 1997) bracket the beginning of Interandean/Subandean zone deformation and therefore may be a better early indicator of the initiation of a cross-continental drainage than clay mineralogy and terrigenous mass accumulation rates, although the latter two record the start of major erosive events.

Event at 4.5 Ma

Beginning at ~4.5 Ma, terrigenous MAR increases by a factor of 2-3 (dark gray bar, Figures 5.2 and 5.3), starting a long-term increase which continues to the present. This trend in TMAR may be attributed to a long-term increase in Andean exhumation rates (Benjamin, 1987). Between 4.9 and 4.6 Ma, chlorite/kaolinite and illite/kaolinite increase temporarily, implying a stronger highland source (Figure 5.3). G/(G+H) decreases over a period of approximately 400 ky (~4.8-4.4 Ma), suggesting lowland drying (Figure 5.2). This time may mark the expansion of the Amazon basin to include most or all of the present drainage area and a corresponding change to average drier conditions in the lowland Amazon Basin. These sedimentological changes may coincide with the end of the Quechua 3 compressional event. Undeformed volcanics overlying strata deformed in this event were dated at 3.8±0.4 Ma and 4.9±0.4 Ma (Megard, 1984). The shifts in mineralogy and TMAR also coincide with post 5 Ma deformation in the Subandean fold and thrust belt (Kley, 1996). Given the dates of deformation in the Andes and erosion to the Atlantic, a tectonic link to this erosional event is more clear than a link to Quechua 2 near 8 Ma.

If Andean tectonic events were responsible for major reshaping of the drainage basin, then erosion to the Atlantic lags current estimates of deformation by up to 1 My (event at 8 Ma) or occurs at the end of deformation events (event at 4.5 Ma). The broad range of dates for deformation in the Bolivian Interandean Zone and Bolivian and Peruvian Subandes encompasses these two sedimentary transitional periods. The Eastern Cordillera, Altiplano and other more western Andean provinces are thought to have deformed prior to 10 Ma, but major transport of sediment to the Atlantic did not occur until tectonic deformation reached the eastern zones of the Andes. The high resolution data we present narrows the range of dates for the initiation of major erosive events from these Andean provinces to (1) 7.7-8.3 Ma and (2) 4.4-4.8 Ma.

Andean tectonic events in relation to global trends

These long-term changes in sedimentary composition and terrigenous flux since the middle Miocene coincide with some major global oceanic and climatic shifts. A significant increase in global oceanic $^{87}Sr/^{86}Sr$ ratios in the interval from 5.5-4.5 Ma (Hodell et al., 1989) is concurrent with increases in Andean erosion and delivery of dissolved chemical constituents to the ocean. The $^{87}Sr/^{86}Sr$ ratios of modern Amazon tributaries are likely too low to cause the large Cenozoic (since about 40 Ma) increase in oceanic Sr ratios (Palmer and Edmond, 1992). However, barring major age model discrepancies, the mean flux of Himalayan material to the ocean (a large source of radiogenic Sr) was low from 4.5-5.5 Ma (Rea, 1992). The diminished Himalayan signal during this time of increased Andean erosion implies that Andean tectonics may have contributed to the early Pliocene shift in Sr ratios documented by Hodell et al. (1989).

Andean orogenic events are part of a larger picture of global tectonism since the middle Miocene, including tectonic activity in the Himalaya (Rea, 1992). If mountain building and the resulting exhumation and chemical erosion contributed to long-term draw down of atmospheric CO_2 (Raymo et al., 1988) during the Cenozoic, then these Andean tectonic events may have contributed to the expansion of C4 plants 7-5 Ma (Cerling et al., 1993), deepening of the global average carbonate compensation depth and decreases in oceanic $\delta^{13}C$ since the Miocene as summarized by Raymo et al. (1988 and references therein).

Orbital scale climate variability

While long-term low-frequency changes in G/(G+H) likely reflect changes in tectonics and the extent of the source area on timescales of 10^6 years, higher frequency variability indicates climate perturbations within the context of a reasonably constant source area. High frequency changes in $\%CaCO_3$ are controlled by the combined effects of carbonate production, dissolution, and terrigenous dilution. We compare G/(G+H) to $\%CaCO_3$ in the frequency domain to demonstrate changing amplitude and phase relationships both (1) between them and (2) relative to insolation forcing. The evolution of these relationships shows variations through time in the processes controlling G/(G+H), $\%CaCO_3$, or both. The following discussion centers on the evolution of coherent amplitude and phase using cross spectral analysis of 128 time slices from 13.2-0 Ma, each 500 ky long and overlapped with bordering time slices by 400 ky.

G/(G+H) and $\%CaCO_3$ both contain concentrations of variance at the orbital frequencies of $1/100\ ky^{-1}$, $1/41\ ky^{-1}$, $1/23\ ky^{-1}$. At these frequencies, the two time series display some similar downcore variability in estimated power spectral density (Figure 5.4), with the greatest differences in the precession band. Coherent phase estimates with 90% confidence error bars show that, with a few exceptions, prior to about 5.5 Ma and

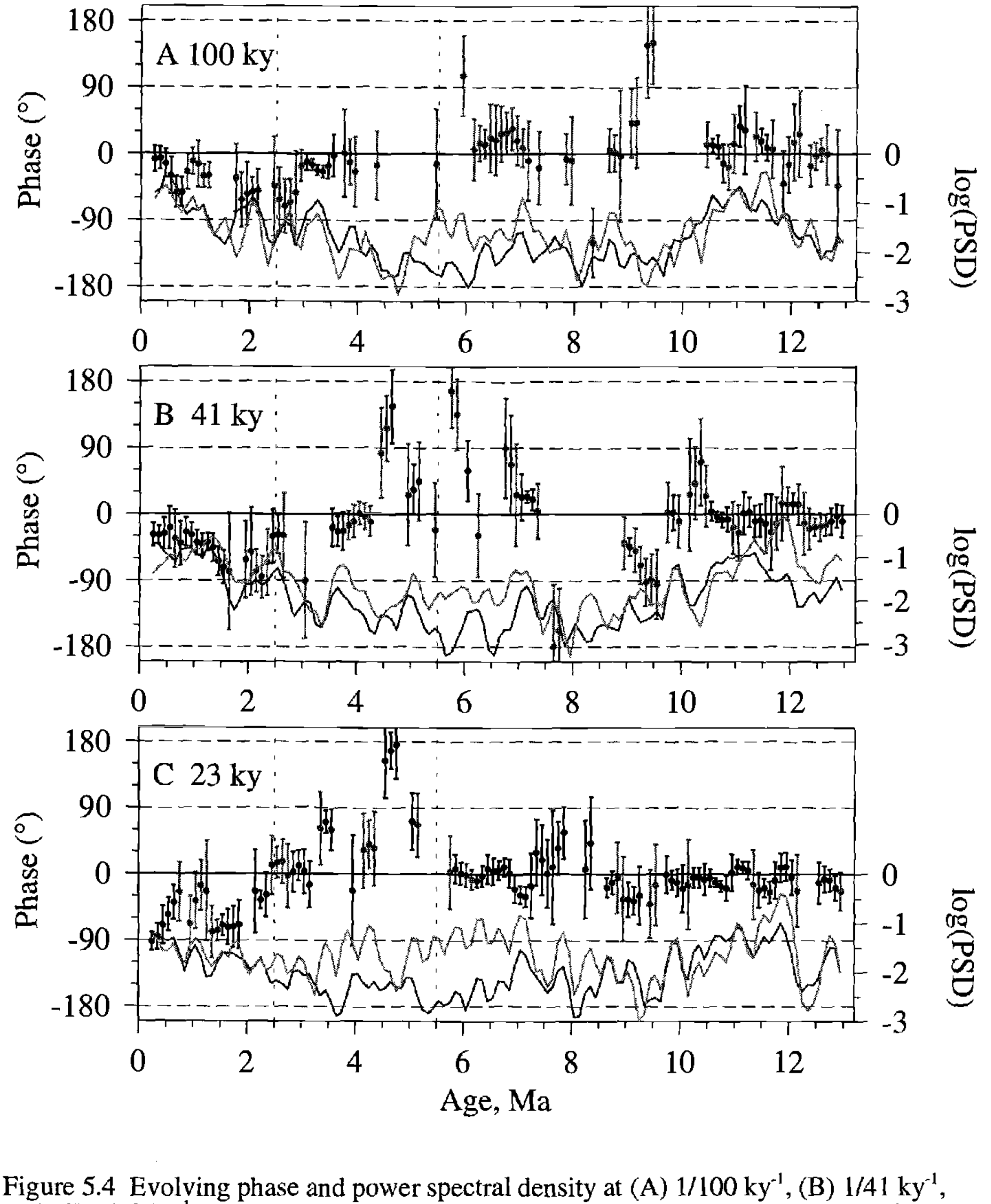

Figure 5.4 Evolving phase and power spectral density at (A) 1/100 ky^{-1}, (B) 1/41 ky^{-1}, and (C) 1/23 ky^{-1} for cross spectral analysis of %CaCO$_3$ versus G/(G+H). Each phase bar is plotted at the mean age of a 500-ky time slice. Both gray and black phase bars indicate coherence above 90%, black phase bars indicate that both %CaCO$_3$ and G/(G+H) spectra have significant concentrations of variance at the respective frequency. Negative phase means G/(G+H) leads %CaCO$_3$. Error bars are shown at the 90% confidence level. Light gray lines are log(power spectral density) for %CaCO$_3$ and dark gray lines are log(power spectral density) for G/(G+H), arbitrary units.

from about 2.5-4.5 Ma, %$CaCO_3$ and G/(G+H) are in phase at 1/100 ky^{-1}, 1/41 ky^{-1}, and 1/23 ky^{-1} frequencies (Figure 5.4). Wet periods in the proto-Amazon and Amazon drainages coincide with high %$CaCO_3$ in Ceara Rise sediments during those intervals. The opposite phase relationship is observed at both tilt and precession frequencies near 4.5-5.0 Ma indicating that dry conditions briefly coincided with high %$CaCO_3$. The two are not coherent in the 1/100 ky^{-1} eccentricity band in this interval. Starting about 2.5 Ma, G/(G+H) begins to lead %$CaCO_3$, approaching a phase angle of about -90° at 1/23 ky^{-1}, and -30° at 1/41 ky^{-1}. At the 1/100 ky^{-1} frequency related to eccentricity, the phase dips temporarily, then returns to zero in the late Pleistocene.

What are the causes of these changing phase relationships? Do they reflect a change in the processes controlling G/(G+H), carbonate, or both? To approach this question, we compare the tilt and precession phases of both these components to summer (June) insolation at 65°N ($Q65N_{Jun}$) as a representative external driving mechanism. We chose this latitude and season for consistency with the age model's orbital tuning target (Bickert et al., 1997; Tiedemann and Franz, 1997, Shackleton and Crowhurst, 1997).

The age model was tuned with the assumption that the climate system, reflected in bulk sediment composition, responded to insolation forcing with no phase lag in the pre-Pleistocene for lack of a plausible mechanism, such as ice volume, to cause a lag (Shackleton and Crowhurst, 1997). The phase between %$CaCO_3$ and insolation is fixed by this assumption (magnetic susceptibility minima mapped to northern hemisphere summer insolation maxima). The precession frequency phase (0°) of carbonate relative to $Q65N_{Jun}$ prior to about 2.5 Ma is consistent with the tuning (Figure 5.5), and the assumption of no phase lag appears to be reasonable given that at 1/23 ky^{-1}, prior to 5.5 Ma, the precipitation proxy, G/(G+H), is also in phase with $Q65N_{Jun}$, and at 1/41 ky^{-1} the two are in phase over much of the coherent record (Figure 5.6). Local precipitation should respond rapidly to insolation forcing, as no inherent lag is expected in the

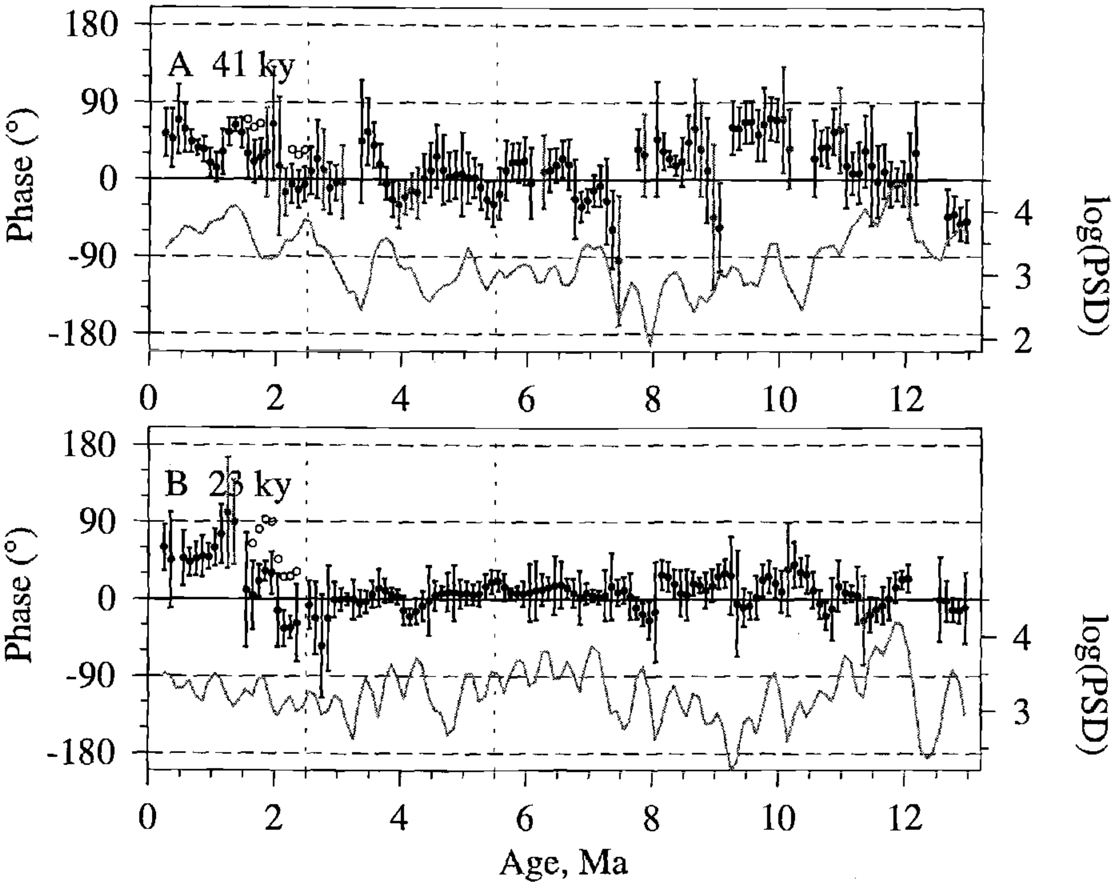

Figure 5.5 Evolving phase and power spectral density at (A) 1/41 ky^{-1}, and (B) 1/23 ky^{-1} for cross spectral analysis of $Q65N_{Jun}$ versus %$CaCO_3$. Positive phase means $Q65N_{Jun}$ leads %$CaCO_3$. Open circles indicate position of postulated phases after adding 40° to 1/41 ky^{-1} phases and 60° to 1/23 ky^{-1} phases from 1.5-2.5 Ma. Other symbols as in Figure 5.4.

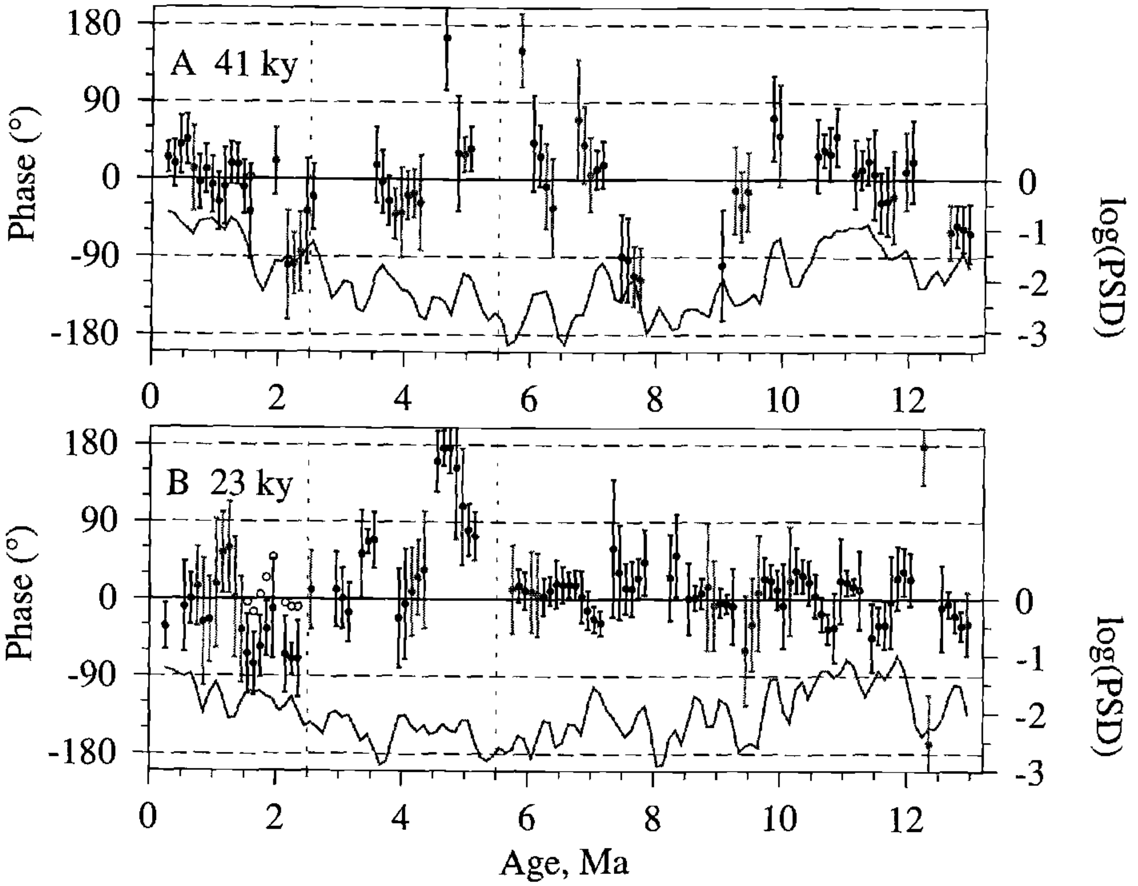

Figure 5.6 Evolving phase and power spectral density at (A) 1/41 ky^{-1}, and (B) 1/23 ky^{-1} for cross spectral analysis of Q65N$_{Jun}$ versus G/(G+H). Positive phase means Q65N$_{Jun}$ leads G/(G+H). Open circles indicate position of postulated phases after adding 40° to 1/41 ky^{-1} phases and 60° to 1/23 ky^{-1} phases from 1.5-2.5 Ma. Other symbols as in Figure 5.4.

atmospheric processes driving precipitation. The intervals where G/(G+H) and $Q65N_{Jun}$ are in phase at both tilt and precession frequencies (> 5.5 Ma and < 4.5 Ma, see below and Figure 5.6) supports the concept of northern hemisphere summer insolation at high latitude driving low latitude climate with Amazon Basin precipitation maxima, or high G/(G+H), occurring during insolation ($Q65N_{Jun}$) maxima (Imbrie et al., 1989).

A different pattern emerges in the interval from about 1.5-2.5 Ma. If $Q65N_{Jun}$ is the driver of these climate cycles, then the phase lead of G/(G+H) with respect to insolation (about -60° at $1/23\ ky^{-1}$, see Figure 5.6) is unrealistic ("response" leads "forcing"). This relationship indicates that the processes driving carbonate concentration likely change in this interval, rather than a decoupling of G/(G+H) from insolation forcing, for which a mechanism is lacking. The phase assumptions in the age model in this interval cause the apparent lead in G/(G+H) relative to insolation. This discrepancy occurs near the transition from an assumed lag in the age model (2 ky subtraction from 2.5-0 Ma; Bickert et al., 1997) and assumed zero lag (>2.5 Ma; Tiedemann and Franz, 1997). We suggest that a more reasonable phase of $\%CaCO_3$ relative to insolation in the interval 1.5-2.5 Ma should be near 60° more positive at $1/23\ ky^{-1}$ and 40° more positive at $1/41\ ky^{-1}$ (open circles in Figure 5.5), similar to the younger Pleistocene record. Such shifts would place G/(G+H) in phase with $Q65N_{Jun}$ during this interval (open circles in Figure 5.6). The implications of this age model adjustment would be (1) increasing sea level control on $\%CaCO_3$ by terrigenous dilution from 2.5 Ma to the present, with a lag caused by long ice sheet response times, and (2) continued fast response of precipitation in the Amazon Basin to insolation forcing of the low latitude atmosphere (Figures 5.5 and 5.6).

If the discrepancy from 1.5-2.5 Ma can be resolved in this manner, then the phase shift between $\%CaCO_3$ and G/(G+H) from 2.5-0 Ma (Figure 5.4) is due to a change in the dominant process controlling carbonate, rather than G/(G+H). We are left with the dilemma of the out-of-phase relationship between G/(G+H) and insolation (Figure 5.6) in the interval from about 4.5-5.0 Ma. This phase relationship indicates that during the early Pliocene dry conditions in the Amazon lowlands coincide with high northern hemisphere summer insolation, in contrast to the rest of the record. We suggest four possibilities to explain the phase: (1) this period coincides with a major shift in average G/(G+H) (Figure 5.2), and the spotty coherence and anomalous phase in this interval may be associated with tectonic activity at this transitional time, (2) the G/(G+H) time series is non-stationary over this interval, thus invalidating the spectral analysis approach we have used, (3) another carbonate-controlling process was operating at this time causing a phase shift of carbonate concentration with respect to insolation which is erased in the age model construction, or, (4) precipitation in the Amazon Basin was responding to a different forcing than before or after this interval.

The first option, tectonic interference, lacks a mechanism whereby tectonic activity could force precipitation cycles on orbital time scales, although tectonics may play a role in this interval, as described below. The second option, non-stationarity, is certainly an issue over the entire 13.2 My. However, this 180 degree phase is robust to different data pretreatments and consistent over 3 time slices, suggesting that the time series are reasonably stationary over a 500 ky interval. The third possibility, a change in process controlling carbonate, rather than G/(G+H), may be linked to strengthened dissolution control of %$CaCO_3$. In the early Pliocene, low percentages of coarse fraction of carbonate indicate a shallow lysocline and overall greater dissolution control on carbonate content (Tiedemann and Franz, 1997). If dissolution were the primary control on %$CaCO_3$ in this interval, and dissolution cycles were out of phase with $Q65N_{Jun}$, then the apparent phase shift between insolation and G/(G+H) would be an artifact of age model assumptions. However, because %$CaCO_3$ and -$\delta^{18}O$ maintain an constant internal in-phase relationship over this interval (Tiedemann and Franz, 1997), we reject the hypothesis of out-of-phase dissolution control and age model problems in this interval.

We are left with the conclusion that from ~4.5-5.0 Ma, the phase of G/(G+H) changed relative to $Q65N_{Jun}$. In search of a plausible climatic explanation for this temporary phase shift, we adopt a conceptual modeling strategy of Imbrie et al. (1989). The amplitude and phase of insolation forcing at tilt and precession frequencies varies as a function of latitude and season. We first summarize the phase vector possibilities for all combinations of latitude (high versus low), hemisphere (north versus south) and season (summer versus winter) in the 1/41 ky^{-1} and 1/23 ky^{-1} frequency bands. Then, we examine three candidates for insolation forcing based on their phases at these frequencies. Finally, we suggest the most plausible forcing mechanism based on amplitude and phase considerations.

Is there a combination of latitudinal and seasonal insolation forcing that could account for the G/(G+H) phase in both the tilt and precession bands? Assuming again that low latitude precipitation responds without delay to insolation forcing, with wet conditions corresponding to insolation maxima, candidate insolation curves must exhibit an out-of-phase relationship with $Q65N_{Jun}$ at these frequencies, as does G/(G+H). Three candidates are revealed by phase vectors in Figure 5.7: (1) December (winter) insolation at low northern latitude (for example, $Q10N_{Dec}$), (2) December (summer) insolation at low southern latitude (for example, $Q10S_{Dec}$), and (3) December (winter) insolation at high northern latitude (for example, $Q65N_{Dec}$).

Among these three possibilities, the main difference between high ($Q65N_{Dec}$) and low ($Q10S_{Dec}$ and $Q10N_{Dec}$) latitude forcing is that high latitude northern hemisphere insolation in December is dominated by the tilt cycle and low latitude December insolation in both hemispheres is dominated by the precession cycle. For these seasons, the amplitude of the tilt cycle is similar among these three, while the amplitude of precession is approximately 100 times larger at low latitude than high latitude (Figure 5.8). We

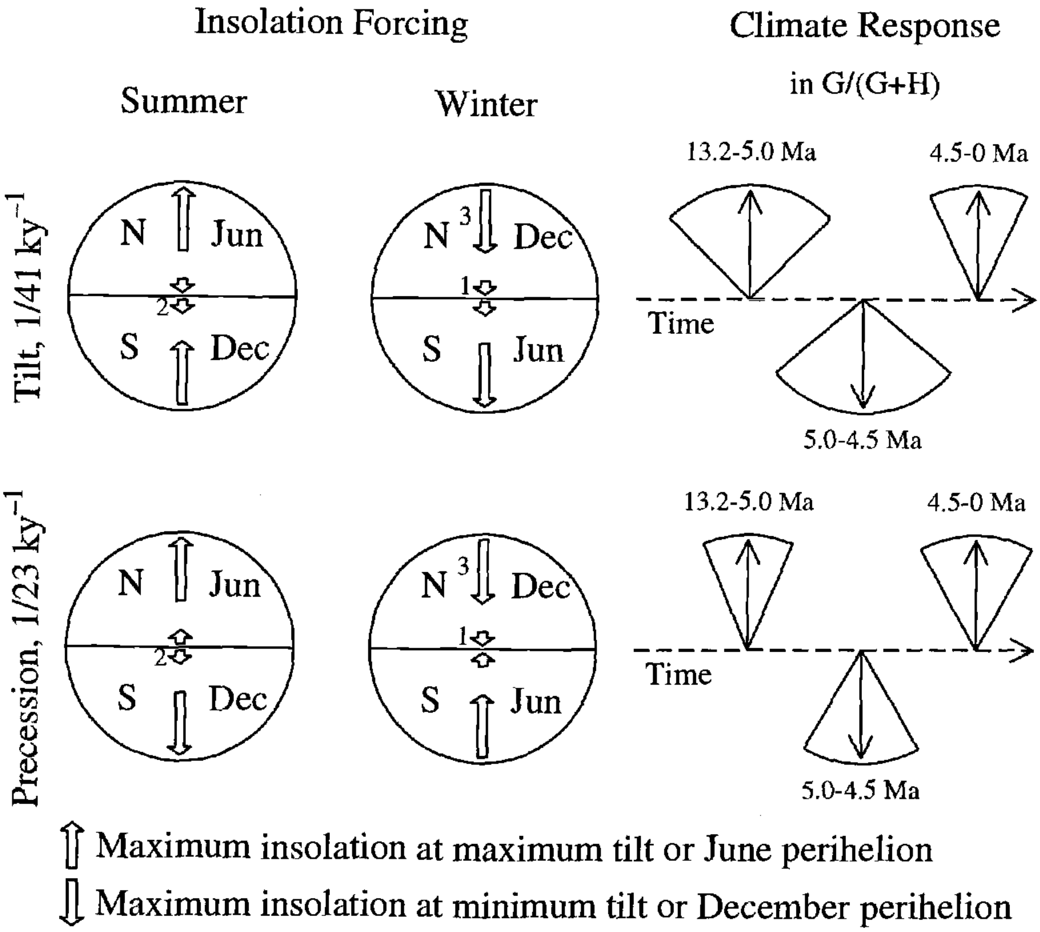

Figure 5.7 Summary of models for insolation forcing as a function of hemisphere, latitude and season. Arrows are phase vectors for maximum insolation at tilt and precession frequencies at low and high latitudes, summer and winter. Each circle represents a globe. The location of each of the four vectors on each circle represents a region of the globe: northern high latitude, northern low latitude, southern low latitude and southern high latitude. Note that the globes are composites of "summer" and "winter" seasons, thus northern and southern hemispheres are labeled either June or December, depending on the season. The direction of the arrows designates the phase of maximum insolation relative to maximum tilt or June perihelion. Arrows pointing up indicate that maximum insolation for a particular latitude and season occurs at maximum tilt or June perihelion. Arrows pointing down indicate that maximum insolation for a particular latitude and season occurs at minimum tilt or December perihelion. For example, during summer at northern hemisphere high latitudes, maximum insolation related to the tilt cycle occurs at maximum tilt and maximum insolation related to the precession cycle occurs at June perihelion.

The climate response is represented by the phase of G/(G+H) with the same phase conventions. The observed range of phases is indicated by the size of each pie-shaped wedge. From 13.2-5.0 Ma and from 4.5-0 Ma, G/(G+H) is in phase with summer insolation at northern high latitude at both tilt and precession frequencies (arrows pointing up). The phase of G/(G+H) in the interval 4.5-5.0 Ma is opposite northern high latitude summer insolation phase at both frequencies (arrows pointing down). Three insolation curves fit this phase: (1) December insolation at low northern latitude, (2) December insolation at low southern latitude, and (3) December insolation at high northern latitude.

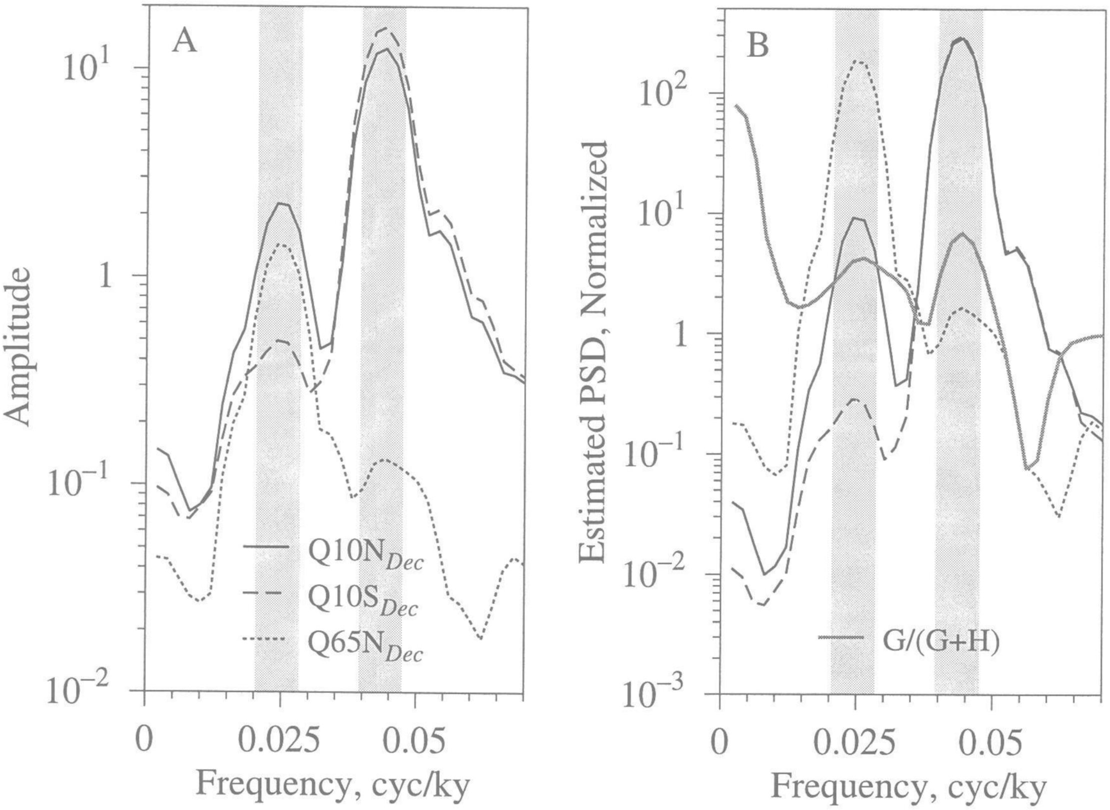

Figure 5.8 (A) Amplitude spectra of insolation curves representing the three candidates for forcing early Pliocene tropical precipitation cycles calculated from the interval 4.4-4.9 Ma. Gray vertical lines are located at 1/41 ky-1 and 1/23 ky-1 frequencies and the bar width equals the bandwidth (bw=0.008). The three curves display similar amplitude forcing at the 1/41 ky^{-1} tilt cycle. We eliminate Q65N$_{\mathrm{Dec}}$ from consideration based on the very low amplitude forcing in the precession band at this latitude and season. (B) Variance normalized power spectra for the three candidate insolation curves and the climate response, G/(G+H). G/(G+H) displays nearly equal power at tilt and precession frequencies, while Q65N$_{\mathrm{Dec}}$ is dominated by tilt and Q10N$_{\mathrm{Dec}}$ and Q10S$_{\mathrm{Dec}}$ are both dominated by precession.

therefore reject a forcing of Amazon precipitation by winter high northern latitude insolation based on the very low amplitude of $Q65N_{Dec}$ at precession relative to tilt frequencies.

The remaining possibility is low latitude December insolation forcing. This early Pliocene time period is characterized as a globally warm interval with minimum polar ice volume (Shackleton et al., 1995). The presence and intensity of NADW formation during this time is questionable. Strong carbonate dissolution at Ceara Rise sites suggests minimal formation of northern component deep water (Tiedemann and Franz, 1997), while carbon isotopes hint that NADW was strong (Billups et al., 1997). Perhaps high northern latitude climate was relatively stable during this interval, allowing a local insolation effect to drive Amazon precipitation briefly. If precipitation were driven by a local monsoon-type atmospheric circulation pattern, then southern hemisphere summer (December) low latitude insolation is a more likely candidate than northern hemisphere winter (December) low latitude insolation, because summer continental heating would drive monsoon precipitation.

Required for this circulation pattern is a high land mass. Analogous to the Indian monsoon, a high land mass (e.g. the Tibetan Plateau) amplifies this type of circulation pattern by enhancing the seasonal contrast between land and sea (Ruddiman et al., 1989). Prior to 5 Ma, when precipitation cycles appear to be driven from high northern latitudes, the Andes mountain belt may not yet have reached an altitude sufficient to drive monsoon precipitation. If the Andes reached a "threshold" altitude just prior to (Quechua 3) or during the erosive event near 4.5 Ma, then the new presence of high topography may have contributed to switching the forcing to low latitude insolation. This interpretation relies on an assumption that exhumation/erosion at this time was associated with true uplift, which is unknown. Post-4.5 Ma, some process driven from high latitudes, perhaps increased variability in the deep Atlantic conveyor, would have to overcome the high topography effect, possibly aided by decreasing tropical sea surface temperatures.

To summarize the progression of orbital-scale climate relationships, from the middle Miocene to Pliocene, high % carbonate in Ceara Rise sediments is generally in phase with wet Amazon or proto-Amazon lowland conditions. If a significant control on carbonate concentration were terrigenous flux from South America, this phase relationship indicates that higher rates of erosion from South America occurred during dry periods, when reduced vegetation cover could destabilize soils. If the major controls on carbonate were productivity and/or dissolution, then there is no mechanistic link between lowland precipitation and carbonate concentration. In the early Pliocene, dry conditions in Amazonia are in phase with high carbonate concentrations and high $Q65N_{Jun}$. The phase inversion indicates that during this interval Amazon precipitation cycles were responding to a forcing different than $Q65N_{Jun}$, perhaps local southern hemisphere summer low latitude insolation. During the Plio-Pleistocene (about 2.5-0 Ma), high concentrations of carbonate are in phase with high sea level and lag wet lowland conditions. Given the age model assumptions, and direct comparisons of both parameters to insolation, this phase change appears to be caused by a shift in $\%CaCO_3$ to a later phase, consistent with increasing control of carbonate concentration by sea-level driven terrigenous flux.

CONCLUSIONS

The signature of major eastward cross-continental transport of terrigenous sediments via the Amazon River drainage appears in western tropical Atlantic sediments at 8 Ma, when terrigenous mass accumulation rates begin a long-term increase and clay mineralogy changes dramatically. At 4.5 Ma, the rate of Andean erosion again begins to increase significantly, a trend which continues to the present. The event near 8 Ma postdates compression event Quechua 2, while the event near 4.5 Ma occurs at the end of Quechua 3. Both are spanned by deformation in the Subandes and Interandean zones.

Major erosion of Andean material to the Atlantic appears to be associated with tectonic deformation in the eastern Andean provinces. The step-wise character of sedimentological changes suggests discrete tectonic events near 8 and 4.5 Ma, rather than continuous change. We bracket the initiation of these erosion events at 7.7-8.3 Ma and 4.4-4.8 Ma.

Climate conditions in lowland sediment source areas have become progressively drier since the middle Miocene. This trend is probably linked to the expansion of the drainage basin to include more diverse terrains and climate zones, although long term drying due to tropical ocean cooling may also be a factor.

At frequencies of 1/41 ky^{-1} and 1/23 ky^{-1}, phase relationships between average lowland precipitation conditions and %$CaCO_3$ in Ceara Rise sediments evolved. From 13.2 to about 2.5 Ma, excluding about 4.5-5.0 Ma, %$CaCO_3$ was high during lowland wet periods. From 2.5-0 Ma, lowland precipitation cycles lead %$CaCO_3$, and wet periods occur on the transitions from low carbonate to high carbonate concentrations. The phase shift likely is due to an increase in the control of terrigenous dilution on %$CaCO_3$, driven by higher amplitude sea level variability after the intensification of Northern Hemisphere glacial cycles. During the early Pliocene interval (~4.5-5.0 Ma), Amazon Basin precipitation cycles appear to respond to local low latitude December (southern hemisphere summer) insolation, driving a monsoon circulation perhaps aided by the newly uplifted Andes.

ACKNOWLEDGMENTS

Thanks to the ODP Leg 154 shipboard scientific party, and to Michael Weber for assistance with the GRAPE bulk density correction, and Reed Glasman for use of his XRD prep lab. This work was supported by NSF-OCE 95-30094.

6.

Summary

The goal of this thesis was to understand links and feedbacks between tropical climate and the global climate system on time scales ranging from tens of thousands of years (orbital scale) to millions of years (tectonic scale). Such studies have become possible only with the advent of (1) deep sea drilling of long continuous sedimentary records, and (2) application of non-intrusive proxy techniques to interpret lengthy records at high resolution.

Reflectance spectroscopy and magnetic susceptibility data were calibrated using laboratory data to estimate concentrations of calcium carbonate, hematite, and goethite in Ceara Rise sediments. These estimates were subsequently used for paleoclimate analyses and interpretation. While errors on non-intrusive proxy estimates are larger than errors for discrete laboratory samples, we gain time series of exceptional length and detail with a proxy approach. Reflectance spectroscopy appears to be one of the most promising methods for estimating hematite and goethite in deep sea sediments.

We used proxy estimates of calcium carbonate to assess the relative carbonate accumulation between shallow and deep water Ceara Rise sites. Lower accumulation of carbonate at deep sites is indicative of stronger carbonate dissolution. Assuming that dissolution trends with time are a function of the relative presences of North Atlantic Deep Water (NADW) and Antarctic Bottom Water (AABW) bathing Ceara Rise, then our analysis indicates that NADW was weakest during transitions from interglacial to glacial conditions, and strongest during deglacial transitions during the late Pleistocene. The SPECMAP group (Imbrie et al., 1992; 1993) hypothesized that early climate change triggered in the high latitude North Atlantic was somehow translated to the southern hemisphere, where most early climate responses are observed during the Pleistocene. The early phase observed here in deep water circulation could provide this link.

Amazon Basin precipitation cycles are monitored by the fraction of goethite relative to goethite plus hematite G/(G+H), during the late Pleistocene. Wet periods coincided with ice melt and dry periods coincided with ice growth. This finding conflicts with suggestions from lowland continental records that Amazon Basin climate extremes responded to northern hemisphere ice volume extremes. The phase signature of G/(G+H) at precession and tilt frequencies imply that northern hemisphere summer insolation forces Amazon climate. Changing the location and intensity of the intertropical convergence zone may supply the mechanism to alter precipitation patterns on orbital time scales. Because the tropics lead ice volume, they may in part force high latitude climate by changing low latitude albedo or atmospheric water vapor transport. The presence of a ~400 ky periodicity in the precipitation proxy, which is lacking from ice volume records, implies that the tropics may respond non-linearly to insolation forcing at precession frequencies while ice volume does not.

Comparisons between a lowland Amazon Basin precipitation proxy, G/(G+H), and %$CaCO_3$ over longer time intervals in Ceara Rise sediments reveal that the dominant controls on each have evolved since the middle Miocene (13.2 Ma). High precipitation in the Amazon Basin is in phase with high latitude northern hemisphere summer insolation forcing over much of the record. Prior to about 2.5 Ma, high carbonate is in phase with high precipitation. If %$CaCO_3$ is domininantly controlled by terrigenous dilution, this phase implies that greater erosion occurs during dry periods. After 2.5 Ma, %$CaCO_3$ lags precipitation and is in phase with northern hemisphere ice volume ($-\delta^{18}O$) suggesting that sea level control of terrigenous flux to Ceara Rise dominates the dilution of carbonate without affecting precipitation cycles. In the early Pliocene (4.5-5.0 Ma), insolation control of Amazon Basin precipitation cycles switched to local southern hemisphere summer forcing, perhaps assisted by the advent of high Andean topography, setting up a monsoon-type atmospheric circulation pattern.

Orbital-scale climate variations since the middle Miocene are superimposed on long-term changes in terrigenous composition and mass accumulation rate. A combination of changing sedimentological parameters brackets major Andean erosive events at 7.7-8.3 Ma and 4.4-4.8 Ma, time intervals which lag or occur at the end of dated tectonic deformation events in the Andes. Tectonic changes are slow and appear to have little direct effect on the amplitude or phase of tropical climate cycles at orbital frequencies.

A common theme in these studies is early (preceding northern hemisphere ice volume extremes) climate responses in Atlantic deep water circulation and tropical precipitation. The tropics appear to respond rapidly to insolation forcing, which typically has been high northern latitude summer insolation. Because precipitation is related to fast-acting atmospheric phenomena, no lag between forcing and climate response is expected or observed. Amazon Basin climate represented by the precipitation proxy leads northern hemisphere ice volume, thus eliminating ice volume as a primary driver of late Pleistocene low latitude climate. In contrast, because of its early phase, tropical climate patterns may play a role in driving high latitude northern hemisphere climate during the glacial-interglacial cycles of the late Pleistocene. While the the extent and diversity of the Amazon Basin has evolved since the middle Miocene in response to Andean tectonics, external insolation forcing drives orbital scale climate cycles throughout the record.

BIBLIOGRAPHY

Abbott, M.B., Seltzer, G.O., Kelts, K.R., and Southon, J., 1997. Holocene paleohydrology of the tropical Andes from lake records. *Quaternary Research*, 47, 70-80.

Balsam, W.L., and Deaton, B.C., 1991. Sediment dispersal in the Atlantic Ocean: Evaluation by visible light spectra. *Reviews in Aquatic Sciences*, 4, 411-447.

Balsam, W.L., Otto-Bleisner, B.L., and Deaton, B.C., 1995. Modern and last glacial maximum eolian sedimentation patterns in the Atlantic Ocean interpreted from sediment iron oxide content. *Paleoceanography*, 10, 493-508.

Benjamin, M.T., Johnson, N.M., and Naeser, C.W., 1987. Recent rapid uplift in the Bolivian Andes: Evidence from fission-track dating. *Geology*, 15, 680-683.

Bickert, T., Curry, W.B., and Wefer, G., 1997. Late Pliocene to Holocene (2.6 to 0 Ma) western equatorial Atlantic deep water circulation: inferences from benthic stable isotopes, Leg 154. In: Shackleton, N.J., Curry, W.B., Richter, C., and Bralower, T.J. (Eds.). *Proc. ODP Sci. Results*, 154: College Station, TX (Ocean Drilling Program), 239-253.

Billups, K., Ravelo, A.C., and Zachos, J.C., 1997. Early Pliocene deep-water circulation: stable isotope evidence for enhanced northern component deep water. In: Shackleton, N.J., Curry, W.B., Richter, C., and Bralower, T.J. (Eds.). *Proc. ODP Sci. Results*, 154: College Station, TX (Ocean Drilling Program), 319-330.

Biscaye, P.E., 1965. Mineralogy and sedimentation of recent deep-sea clay in the Atlantic Ocean and adjacent seas and oceans. *Geological Society of America Bulletin*, 76, 803-832.

Bloomfield, P., 1976. Fourier Analysis of Time Series: An Introduction. Wiley and Sons, New York.

Boyle, E.A., and Keigwin, L.D., 1982. Deep circulation of the North Atlantic over the last 200,000 years: Geochemical evidence. *Science*, 218, 784-787.

Bush, M.B., Colinvaux, P.A., Wiemann, M.C., Piperno, D.R., and Liu, K., 1990. Late Pleistocene temperature depression and vegetation change in Ecuadorian Amazonia. *Quaternary Research*, 34, 330-345.

Campbell, A.E., 1992. Unconformities in seismic records and outcrop. Ph.D. thesis, Free University, Amsterdam, 187 pgs.

Cerling, T.E., Wang, Y., and Quade, J., 1993. Expansion of C4 ecosystems as an indicator of global ecological change in the late Miocene. *Nature*, 361, 344-345.

BIBLIOGRAPHY, Continued

Clapperton, C., 1993. Nature of environmental changes in South America at the Last Glacial Maximum. *Palaeogeography, Palaeoclimatology, Palaeoecology*, 101, 189-208.

Clark, R.N., King, T.V.V., Klejwa, M., and Swayze, G.A., 1990. High spectral resolution reflectance spectroscopy of minerals. *Journal of Geophysical Research*, 95, 12653-12680.

Clarke, F.J.J. and Compton, J.A., 1986. Correction methods for integrating-sphere measurement of hemispherical reflectance. *Color Research and Application*, 11, 253-262.

Colinvaux, P.A., De Oliveira, P.E., Moreno, J.E., Miller, M.C., and Bush, M.B., 1996. A long pollen record from lowland Amazonia: forest and cooling in glacial times. *Science*, 274, 85-88.

Crough, S.T., 1983. Apatite fission-track dating of erosion in the eastern Andes, Bolivia. *Earth and Planetary Science Letters*, 64, 396-397.

Crowley, T.J., 1985. Late Quaternary changes in the North Atlantic and Atlantic/Pacific comparisons. *In* Sundquist, E.T., and Broecker,W.S. (Eds.), *The Carbon Cycle and Atmospheric* CO_2*: Natural Variations Archean to Present.* American Geophysical Union, Washington, D.C. 271-284.

Crowley, T.J., Kim, K.Y., Mengel J.G., and Short, D.A. , 1992. Modeling the 100,000-year climate fluctuations in pre-Pleistocene time series. *Science*, 255, 705-707.

Crowley, T.J., 1992. North Atlantic Deep Water cools the southern hemisphere. *Paleoceanography*, 7, 489-497.

Crowley, T.J., and Baum, S.K., 1997. Effect of vegetation on an ice-age climate model simulation. *Journal of Geophysical Research*, 102, 16463-16480.

Curry, W.B., and Cullen, L.J., 1997. Carbonate production and dissolution in the western equatorial Atlantic during the last 1 m.y. In: Shackleton, N.J., Curry, W.B., Richter, C., and Bralower, T.J. (Eds.). *Proc. ODP Sci. Results*, 154: College Station, TX (Ocean Drilling Program), 189-199.

Curry, W.B., Shackleton, N.J., Richter, C., et al., 1995. *Proc. ODP, Init. Repts.*, 154: College Station, TX (Ocean Drilling Program).

Curry, W.B., Duplessy, J.C., Labeyrie, L.D., and Shackleton N.J., 1988. Changes in the distribution of $\delta^{13}C$ of deep water ΣCO_2 between the last glaciation and the Holocene. *Paleoceanography*, 3, 317-341.

Curry, W.B., and Lohmann, G.P., 1983. Reduced advection into Atlantic Ocean deep eastern basins during last glacial maximum. *Nature*, 306, 577-580.

BIBLIOGRAPHY, Continued

Curry, W.B., and Lohmann, G.P., 1990. Reconstructing past particle fluxes in the tropical Atlantic ocean. *Paleoceanography*, 5, 487-505.

Damuth, J.E., and Fairbridge, R.W., 1970. Equatorial Atlantic deep-sea arkosic sands and ice-age aridity in tropical South America. *Geological Society of America Bulletin*, 81, 189-206.

Damuth, J.E, and Kumar, N., 1975. Amazon cone: Morphology, sediments, age, and growth pattern. *Geological Society of America Bulletin*, 86, 863-878.

Deaton, B.C., and Balsam, W.L., 1991. Visible spectroscopy - A rapid method for determining hematite and goethite concentration in geological materials. *Journal of Sedimentary Petrology*, 61, 628-632.

Dobson, D.M., Dickens, G.R., and Rea, D.K., 1997. Terrigenous sedimentation at Ceara Rise. In: Shackleton, N.J., Curry, W.B., Richter, C., and Bralower, T.J. (Eds.). *Proc. ODP Sci. Results*, 154: College Station, TX (Ocean Drilling Program), 465-474.

Francois, R., Bacon, M.P., and Suman, D.O., 1990. Thorium 230 profiling in deep-sea sediments: high-resolution records of flux and dissolution of carbonate in the equatorial Atlantic during the last 24,000 years. *Paleoceanography*, 5, 761-787.

Gaffey, S.J., 1986. Spectral reflectance of carbonate minerals in the visible and near infrared (-0.35-2.55 microns): calcite, aragonite, and dolomite. *American Mineralogist,* 71, 151-162.

Gibbs, R.J., 1967. The geochemistry of the Amazon river system: Part I. The factors that control the salinity and the composition and concentration of the suspended solids. *Geological Society of America Bulletin*, 78, 1203-1232.

Gubbels, T.L., Isacks, B.L., and Farrar, E., 1993. High-level surfaces, plateau uplift, and foreland development, Bolivian central Andes. *Geology*, 21, 695-698.

Haase, R., 1992. Physical and chemical properties of savanna soils in northern Bolivia. *Catena*, 19, 119-134.

Haberle, S., 1997. Upper Quaternary vegetation and climate history of the Amazon Basin: correlating marine and terrestrial pollen records. In: Flood, R.D., Piper, D.J.W., Klaus, A., and Peterson, L.C. (Eds.). *Proc. ODP, Sci. Results*, 155: College Station, TX (Ocean Drilling Program), 381-396.

Harris, S.E., Mix, A.C., and King, T.A., 1997. Biogenic and terrigenous sedimentation at Ceara Rise, western tropical Atlantic, supports Pliocene-Pleistocene deep-water linkage between hemispheres. In: Shackleton, N.J., Curry, W.B., Richter, C., and Bralower, T.J. (Eds.). *Proc. ODP Sci. Results*, 154: College Station, TX (Ocean Drilling Program), 331-345.

Harris, S.E., and Mix, A.C., in press. Pleistocene precipitation balance in the Amazon Basin recorded in deep sea sediments. *Quaternary Research.*

BIBLIOGRAPHY, Continued

Hays, J.D., Imbrie, J., and Shackleton, N.J., 1976. Variations in the Earth's orbit: Pacemaker of the ice ages. *Science*, 194, 1121-1131.

Hodell, D.A., Mueller, P.A., McKenzie, J.A., and Mead, G.A., 1989. Strontium isotope stratigraphy and geochemistry of the late Neogene ocean. *Earth and Planetary Science Letters*, 92, 165-178.

Hoorn, C., 1994. An environmental reconstruction of the palaeo-Amazon River sysem (Middle-Late Miocene, NW Amazonia). *Palaeogeography, Palaeoclimatology, Palaeoecology*, 112, 187-238.

Hunt, G.R., 1977. Spectral signatures of particulate minerals in the visible and near infrared. *Geophysics*, 42, 501-513.

Hunt, G.R., and Ashley R.P., 1979. Spectra of altered rocks in the visible and near infrared. *Economic Geology*, 74, 1613-1629.

Imbrie, J., Hays, D., Martinson, D.G., McIntyre, A., Mix, A.C., Morley, J.J., Pisias, N.G., Prell, W.L., and Shackleton, N.J., 1984. The orbital theory of Pleistocene climate: Support from a revised chronology of the marine ^{18}O record. In: Berger, A.L., et al. (Eds.), *Milankovitch and Climate, Part 1*. Reidel, Norwell, MA. 269-305.

Imbrie, J., McIntyre, A., and Mix, A., 1989. Oceanic response to orbital forcing in the late Quaternary: Observational and experimental strategies. In: Berger, A., (Ed.), *Climate and Geo-Sciences*. Kluwer Academic, Dordrecht. 121-164.

Imbrie, J., Boyle, E.A., Clemens, S.C., Duffy, A., Howard, W.R., Kukla, G., Kutzbach, J., Martinson, D.G., McIntyre, A., Mix, A.C., Molfino, B., Morley, J.J., Peterson, L.C., Pisias, N.G., Prell, W.L , Raymo, M.E., Shackleton, N.J., and Toggweiler, J.R., 1992. On the structure and origin of major glaciation cycles 1. Linear responses to Milankovitch forcing. *Paleoceanography*, 7, 701-738

Imbrie, J., Berger, A., Boyle, E., Clemens, S., Duffy, A., Howard, W., Kukla, G., Kutzbach, J., Martinson, D., McIntyre, A., Mix, A., Molfino, B., Morley, J., Peterson, L., Pisias, N., Prell, W., Raymo, M., Shackleton, N., and Toggweiler, J., 1993. On the structure and origin of major glaciation cycles, 2. The 100,000-year cycle. *Paleoceanography*, 8, 699-735.

Johnsson, M.J., and Meade, R.H., 1990. Chemical weathering of fluvial sediments during alluvial storage: The Macuapanim Island point bar, Solimoes River, Brazil. *Journal of Sedimentary Petrology*, 60, 827-842.

Jordan, C.F., 1985. Soils of the Amazon rainforest. In: Prance, G.T., and Lovejoy, T.E. (Eds.), *Amazonia*. Pergamon, Oxford. 83-94.

Kampf, N., and Schwertmann, U., 1983. Goethite and hematite in a climosequence in southern Brazil and their application in classification of kaolinitic soils. *Geoderma*, 29, 27-39.

BIBLIOGRAPHY, Continued

King, T.A., Ellis, W.G., Murray, D.W., Shackleton, N.J., and Harris, S., 1997. Miocene evolution of carbonate sedimentation at the Ceara Rise: a multivariate data/proxy approach. In: Shackleton, N.J., Curry, W.B., Richter, C., and Bralower, T.J. (Eds.). *Proc. ODP Sci. Results*, 154: College Station, TX (Ocean Drilling Program), 349-365.

Kley, J., 1996. Transition from basement-involved to thin-skinned thrusting in the Cordillera Oriental of southern Bolivia. *Tectonics*, 15, 763-775.

Kronberg, B.I., Benchimol, R.E., and Bird, M.I., 1991. Geochemistry of Acre Subbasin sediments: Window on ice-age Amazonia. *Interciencia*, 16, 138-141.

Laskar, J., Joutel, F., and Boudin, F., 1993. Orbital, precessional and insolation quantities for the Earth from -20Myr to +10Myr. *Astronomy and Astrophysics*, 270, 522-533.

Lean, J., and Warrilow, D.A., 1989. Simulation of the regional climatic impact of Amazon deforestation. *Nature*, 342, 411-413.

Ledru, M., Bertaux, J., and Sifeddine, A., 1998. Absence of last glacial maximum records in lowland tropical forests. *Quaternary Research*, 49, 233-237.

Liu, K., and Colinvaux, P.A., 1985. Forest changes in the Amazon Basin during the last glacial maximum. *Nature*, 318, 83-88.

Martin, L., Bertaux, J., Correge, T., Ledru, M.P., Mourguiart, P., Sifeddine, A., Soubies, F., Wirrmann, D., Suguio, K., and Turcq, B., 1997. Astronomical forcing of contrasting rainfall changes in tropical South America between 12,400 and 8800 cal yr B.P. *Quaternary Research*, 47, 117-122.

Martinelli, L.A., Victoria, R.L., Dematte, J.L.I., Richey, J.E., and Devol, A.H., 1993. Chemical and mineralogical composition of Amazon River floodplain sediments, Brazil. *Applied Geochemistry*, 8, 391-402.

Martinson, D.G., Menke, W., and Stoffa, P., 1982. An inverse approach to signal correlation. *Journal of Geophysical Research*, 87, 4807-4818

McGeary, D.F.R., and Damuth, J.E., 1973. Postglacial iron-rich crusts in hemipelagic deep-sea sediment. *Geological Society of America Bulletin*, 84, 1201-1212.

Meade, R.H., 1994. Suspended sediments of the modern Amazon and Orinoco Rivers. *Quaternary International*, 21, 29-39.

Meade, R.H., Dunne, T., Richey, J.E., Santos, U.M., and Salati, E., 1985. Storage and remobilization of suspended sediment in the lower Amazon River of Brazil. *Science*, 228, 488-490.

Megard, F., Nobel., D.C., McKee, E.H., and Bellon, H., 1984. Mulitple pulses of Neogene deformation in the Ayacucho intermontane basin, Andes of central Peru. *Geological Society of America Bulletin*, 95, 1108-1117.

BIBLIOGRAPHY, Continued

Megard, F., 1987. Structure and Evolution of the Peruvian Andes. In: *The Anatomy of mountain ranges*, Schaer, J.P., and Rogers, J. (Eds.). Princeton University Press, Princeton. 179-210.

Mix, A.C., Rugh, W., Pisias, N.G., Veirs, S., Leg 138 Shipboard sedimentologists, and Leg 138 Scientific Party, 1992. Color reflectance spectroscopy: a tool for rapid characterization of deep-sea sediments. In: Pisias, N.G., Mayer, L.A., Janecek, T.R., Palmer-Julson, A., and van Andel, T.H. (Eds.), *Proc. ODP, Init. Repts*, 138: College Station, TX (Ocean Drilling Program), 67-77.

Mix, A.C., Pisias, N.G., Rugh, W., Wilson, J., Morey, A., and Hagelberg, T.K., 1995a. Benthic foraminifer stable isotope record from Site 849 (0-5 Ma): Local and global climate changes. In: Pisias, N.G., Mayer, L.A., Janecek, T.R., Palmer-Julson, A., and van Andel, T.H. (Eds.), *Proc. ODP, Sci. Res.* 138: College Station, TX (Ocean Drilling Program), 371-412.

Mix, A.C., Harris, S.E., and Janecek T.R., 1995b. Estimating lithology from nonintrusive reflectance spectra: Leg 138. In: Pisias, N.G., Mayer, L.A., Janecek, T.R., Palmer-Julson, A., and van Andel, T.H. (Eds.), *Proc. ODP, Sci. Res.* 138: College Station, TX (Ocean Drilling Program), 413-428.

Mix, A.C., Le, J., and Shackleton N.J., 1995c. Benthic foraminiferal stable isotope stratigraphy of Site 846: 0-1.8 Ma. In: Pisias, N.G., Mayer, L.A., Janecek, T.R., Palmer-Julson, A., and van Andel, T.H. (Eds.), *Proc. ODP, Sci. Res.* 138: College Station, TX (Ocean Drilling Program), 839-854.

Moore, D.M., and Reynolds, R.C., 1985. X-ray diffraction and the identification and analysis of clay minerals. Oxford University Press, Oxford.

Oppo, D.W., and Fairbanks, R.G., 1987. Variability in the deep and intermediate water circulation of the Atlantic Ocean: northern hemisphere modulation of the Southern Ocean. *Earth and Planetary Science Letters*, 86, 1-15.

Ortiz, J., Mix, A., Harris, S., and O'Connell, S., in press. Diffuse spectral reflectance as a proxy for percent carbonate content in North Atlantic sediments. *Paleoceanography.*

Ostermann, D.R., Karbott, D., and Curry, W.B., 1990. Automated system to measure the carbonate concentration of sediments. *Woods Hole Oceanographic Institution, Technical Rept. WHOI-90-03.*

Palmer, M.R., and Edmond, J.M., 1992. Controls over the strontium isotope composition of river water. *Geochimica et Cosmochimica Acta,* 56, 2099-2111.

Peterson, L.C., and Prell, W.L., 1985. Carbonate preservation and rates of climatic change: An 800 ky record from the Indian Ocean. In: Sundquist, E.T., and Broecker,W.S. (Eds.), *The Carbon Cycle and Atmospheric* CO_2*: Natural Variations Archean to Present.* American Geophysical Union, Washington, D.C. 251-269.

BIBLIOGRAPHY, Continued

Pisias, N.G., and Mix, A.C., 1997. Spatial and temporal oceanographic variability of the eastern equatorial Pacific during the late Pleistocene: Evidence from Radiolaria microfossils. *Paleoceanography,* 12, 381-393.

Pokras, E.M., and Mix, A.C., 1987. Earth's precession cycle and Quaternary climatic change in tropical Africa. *Nature,* 326, 486-487.

Polcher, J., and Laval, K., 1994. The impact of African and Amazonian deforestation on tropical climate. *Journal of Hydrology,* 155, 389-405.

Press, W.H., Teukolsky, S.A., Vetterling, W.T., and Flannery, B.P., 1992. Numerical Recipes in Fortran: The Art of Scientific Computing, (second edition), 180-184, Cambridge Press, New York, 963 pp.

Raymo, M.E., Ruddiman, W.F., Shackleton, N.J., and Oppo, D.W., 1990. Evolution of Atlantic-Pacific $\delta^{13}C$ gradients over the last 2.5 m.y. *Earth and Planetary Science Letters*, 97, 353-368.

Raymo, M.E., Ruddiman, W.F., and Froelich, P.N., 1988. Influence of late Cenozoic mountain building on ocean geochemical cycles. *Geology*, 16, 649-653.

Rea, D.K., 1992. Delivery of Himalayan sediment to the Northern Indian Ocean and its relation to global climate, sea level, uplift, and seawater strontium. In: Duncan, R.A. et al. (Eds.), *Synthesis of Results from Scientific Drilling in the Indian Ocean.* American Geophysical Union, Washington. 387-402.

Richardson, D.S., 1974. The origin of iron-rich layers in sediments of the western equatorial Atlantic Ocean. Ph.D. dissertation, Columbia University, New York.

Richey, J.E., Meade, R.H., Salati, E., Devol, A.H., Nordin, C.F.Jr., and dos Santos, U., 1986. Water discharge and suspended sediment concentrations in the Amazon River: 1982-1984. *Water Resources Research,* 22, 756-764.

Rind, D., and Chandler, M., 1991. Increased ocean heat transports and warmer climate. *Journal of Geophysical Research*, 96, 7437-7461.

Ruddiman, W.F., Prell, W.L., and Raymo, M.E., 1989. Late Cenozoic uplift in Southern Asia and the American West: Rationale for general circulation modeling experiments. *Journal of Geophysical Research,* 94, 18379-18391.

Ruhlemann, C., Frank, M., Hale, W., Mangini, A., Mulitza, S., Muller, P.J., and Wefer, G., 1996. Late Quaternary productivity changes in the western equatorial Atlantic: Evidence from 230Th-normalized carbonate and organic carbon accumulation rates. *Marine Geology*, 135, 127-152.

Salati, E., and Vose, P.B., 1984. Amazon Basin: A system in equilibrium. *Science,* 225, 129-138.

BIBLIOGRAPHY, Continued

Salati, E., 1985. The climatology and hydrology of Amazonia. In: Prance, G.T. and Lovejoy, T.E. (Eds.), *Amazonia.* Pergamon, Oxford, 18-48.

Sarnthein, M., Thiede, J., Pflaumann, U., Erlenkeuser, H., Futterer, D., Koopmann, B., Lange, H., and Seibold, E., 1982. Atmospheric and oceanic circulation patterns off northwest Africa during the past 25 million years. In: von Rad, U., Hinz, K., Sarnthein, M., and Seibold, E., (Eds.) *Geology of the northwest African continental margin.* Springer-Verlag, Berlin. 547-604.

Servant, M., Maley, J., Turcq, B., Absy, M.L., Brenac, P., Fournier, M., and Ledru, M.P., 1993. Tropical forest changes during the late Quaternary in African and South American lowlands. *Global and Planetary Change*, 7, 25-40.

Shackleton, N.J., 1977. Carbon-13 in Uvigerina: Tropical rainforest history and the equatorial Pacific carbonate dissolution cycles. In: Anderson, N.R., and Malahoff, A. (Eds.), *The fate of fossil fuel* CO_2 *in the oceans.* Plenum, New York. 401-427.

Shackleton, N.J., 1987. Oxygen isotopes, ice volume and sea level. *Quaternary Science Reviews*, 6, 183-190.

Shackleton, N.J., Crowhurst, S., Hagelberg, T., Pisias, N.G., and Schneider, D.A., 1995. A new late Neogene time scale: application to Leg 138 sites. In: Pisias, N.G., Mayer, L.A., Janecek, T.R., Palmer-Julson, A., and van Andel, T.H. (Eds.), *Proc. ODP, Sci. Results,* 138: College Sation, TX (Ocean Drilling Program), 73-101.

Shackleton, N.J., and Crowhurst, S., 1997. Sediment fluxes based on an orbitally tuned time scale 5 Ma to 14 Ma, Site 926. In: Shackleton, N.J., Curry, W.B., Richter, C., and Bralower, T.J. (Eds.). *Proc. ODP Sci. Results*, 154: College Station, TX (Ocean Drilling Program), 69-82.

Shackleton, N.J., Curry, W.B., Richter, C., and Bralower, T.J. (Eds.), 1997. *Proc. ODP Sci. Results*, 154: College Station, TX (Ocean Drilling Program).

Short, D.A., Mengel, J.G., Crowley, T.J., Hyde, W.T., and North, G.R., 1991. Filtering of Milankovitch cycles by Earth's geography. *Quaternary Research*, 35, 157-173.

Showers, W.J., and Bevis, M., 1988. Amazon Cone isotopic stratigraphy: Evidence for the source of the tropical freshwater spike. *Palaeogeography, Palaeoclimatology, Palaeoecology*, 64, 189-199.

Stallard, R.F., 1988. Weathering and erosion in the humid tropics. In: Lerman, A., and Meybeck, M., (Eds.), Physical and chemical weathering in geochemical cycles. Kluwer Academic, Dordrecht. 225-246.

Stute, M., Forster, M., Frischkorn, H., Serejo, A., Clark, J.F., Schlosser, P., Broecker, W.S., and Bonani, G., 1995. Cooling of tropical Brazil (5°C) during the Last Glacial Maximum. *Science*, 269, 379-383.

BIBLIOGRAPHY, Continued

Thompson, L.G., Mosley-Thompson, E., Davis, M.E., Lim, P.-N., Henderson, K.A., Cole-Dai, J., Bolzan, J.F., and Liu, K.-b., 1995. Late glacial stage and Holocene tropical ice core records from Huascaran, Peru. *Science*, 269, 46-50.

Tiedemann, R., and Franz, S.O., 1997. Deep-water circulation, chemistry and terrigenous sediment supply in the equatorial Atlantic during the Pliocene, 3.3-2.6 Ma and 5-4.5 Ma. In: Shackleton, N.J., Curry, W.B., Richter, C., and Bralower, T.J. (Eds.). *Proc. ODP Sci. Results*, 154: College Station, TX (Ocean Drilling Program), 299-318.

Van der Hammen, T., 1974. The Pleistocene changes of vegetation and climate in tropical South America. *Journal of Biogeography*, 1, 3-26.

Van der Hammen, T., and Absy, M.L., 1994. Amazonia during the last glacial. *Palaeogeography, Palaeoclimatology, Palaeoecology*, 109, 247-261.

Weber, M.E., Niessen, F., Kuhn, G., and Wiedicke, M., 1997. Calibration and application of marine sedimentary physical properties using a multi-sensor core logger. *Marine Geology*, 136, 151-172.

Wilson, T.R.S., Thomson, J., Hydes, D.J., Colley, S., Culkin, F., and Sorensen, J., 1986. Oxidation fronts in pelagic sediments: Diagenetic formation of metal-rich layers. *Science*, 232, 972-975.

Wirrmann, D., and Mourguiart, P., 1995. Late Quaternary spatio-temporal limnological variations in the altiplano of Bolivia and Peru. *Quaternary Research*, 43, 344-354.

APPENDICES

Appendix A

Documentation for Some MATLAB Time Series Analysis Functions

INTRODUCTION

This appendix is a guide to time series analysis functions for use in MATLAB. The source code for all the following special functions is located in:

/home/server/homes/student/sharris/matlab OR /home/tahiti/paleo3/sara/matlab

To access these functions directly from your own work space, copy the source code (files ending in *.m) to:

<your home directory>/matlab/*.m

These functions were written between 1994 and 1998. Documentation was last updated in March, 1998.

MATLAB BASICS AND SOME TIPS

1) STARTING MATLAB:
   To start a MATLAB session, type "matlab".

2) HELP
   MATLAB includes online documentation in two forms:
   1. the "help" command. At the matlab prompt, type "help <function name>". For example, to get brief explanation of the function "mean", type "help mean". A very useful feature of "help" is at the bottom, where related commands are listed under "See also...".
   2. the "doc" command. This command will bring up a netscape-type window in which all the matlab documentation resides. Includes lots of examples and a lot more information than "help".

3) LOOKFOR
   If you don't remember (or don't know) the name of the function you want to use, type "lookfor <keyword>". This can be a little slow, but it's thorough.

4) TYPE
   To look at the actual matlab code for any function, type "type <function name>".

5) Several UNIX commands work directly at a matlab prompt (e.g. ls, cd, pwd, more). You can also access any UNIX command by preceding the command with "!".

6) By adding a semicolon (;) to the end of a command, you suppress writing the output to the screen. Usually a good idea.

7) Comment lines in matlab begin with the percent sign (%)

8) When you load data into matlab, its variable name becomes the file name up to the first period in the file name. E.g. the file "carb926.dat" becomes variable "carb926". Matlab can't deal with filenames that begin with numbers, like "926carb.dat".

9) Frequently used commands (see "help" for details):
   LOAD, PLOT, PRINT, SAVE

SPECIAL FUNCTIONS FOR TIME SERIES ANALYSIS

General comments

Functions are set up in a common format:

```
[<output>] = <function name>(<input>);
```

You must define the input variables and assign variable names to the output variables. Character strings, such as the variables str, w_type, and filt_type, must be enclosed in single quotes (' ')

The examples given use a data file called iso849.dat which is also located in /home/server/homes/student/sharris/matlab. This file has three columns, age, $\delta^{18}O$ and $\delta^{13}C$ from ODP Site 849 (Mix et al., 1995) and includes data from 0.004-4.974 Ma at 2 ky intervals.

List of functions

FFTSPEC	Power spectrum of a time series, semi-interactive
FFTSPEC2	Power spectrum of a time series, non-interactive
EVSPEC	"Evolving" spectra of overlapping segments of a time series
EVSPEC2	"Evolving" spectra of overlapping segments of a time series, mean and variance normalized
XSPEC	Cross spectrum of two time series, semi-interactive
XSPEC2	Cross spectrum of two time series, non-interactive
XTRACT_MILANK	Extracts information around Milankovitch frequencies, using output from XSPEC or XSPEC2

The most useful functions are probably fftspec2 and xspec2. Examples are given for each function.

fftspec

This function calculates the frequency spectrum of a time series using an fft. This function is somewhat interactive. Type "help fftspec" for on-line information.

[Y,spec,smspec,f,coord,ci,bw] = fftspec(y,N,t,treat,alpha);

Input variables

y : a time series with length N and equally-spaced sampling interval, t.
N : the length (number of samples) of y
t : the sampling interval
treat : data pretreatment. Options are
- treat=0 : do nothing
- treat=1 : apply a data window. Types available are bartlett, blackman, boxcar, chebyshev ('chebwin'), hamming, hanning, kaiser, triangular ('triang').
- treat=2 : linear detrend the time series based on connecting endpoints (reduces leakage).
- treat=3 : prewhiten and post color the time series (reduce leak.)

alpha : The function calculates (1-alpha) confidence intervals. For 95% CIs, enter 0.05.

Output variables

Y : the fft of y
spec : the raw frequency spectrum of y
smspec : the smoothed frequency spectrum
f : the frequency vector in units of cycles/sampling unit (e.g. if your sample spacing is 2 ky, the units of f will be cyc/ky, not cyc/2ky).
coord : The indices of independent estimates (at the Fourier frequencies).
ci : confidence intervals at each f (low, high).
bw : bandwidth

Example for fftspec

Calculate the frequency spectrum of the oxygen isotope time series in data file "iso849.dat" from 0-0.9 Ma. The prompts are shown. Comments begin with %.

```
tahiti% matlab                  % start MATLAB session
>> load iso849.dat
>> whos                         % Check out the variables and their sizes.
>> y = -iso849(1:450,2);        % Take the first 450 lines from the second column.
>> N = 450;
>> t = 2;
>> treat = 1;                   % Apply a data window
>> alpha = 0.05;                % 95% confidence intervals
>> [Y,spec,smspec,f,coord,ci,bw] = fftspec(y,N,t,treat,alpha);

        % NOTE: The above 6 lines could just as well be done in one line as
        % [Y,spec,smspec,f,coord,ci,bw] = fftspec(-iso849(1:450,2),450,2,1,0.05);
        % Now you'll be asked a few questions.

Input data widowing type: bartlett  % Use a bartlett data window. See
                                    % notes above for other available
                                    % window types.

        % At this point, a new figure window will appear and the raw
        % frequency spectrum will be plotted

Input half filter width: 2          % Full width = (2*half_width) + 1

Input filter type: hanning          % Use a hanning window for smoothing
                                    % the spectrum. See notes above for
                                    % other available window types.

Input title for plots: Site 849, -del18O, 0-0.9 Ma, 2 ky intervals

        % At this point, in the upper panel, the smoothed spectrum is
        % plotted on a linear-linear scale, with dot-dash lines denoting
        % (1-alpha) confidence intervals. In the lower panel, the spectrum
        % is plotted with log-y and linear-x axes with a bar denoting
        % confidence interval (Figure A.1). Frequency range is from 0 to the Nyquist.
        % The bandwidth (bw) and degrees of freedom (dof) are printed to
        % the screen (NOTE: dof is not saved in the output).
        % A second figure window appears in which is plotted just the
        % spectral estimates at the Fourier frequencies on a log-log plot (Figure A.2).

        % The types of plots vary among these functions. Some plot
        % all the frequencies, some plot only the Fourier frequencies.
        % You can edit the source code or just replot the spectra to
        % get what you want. For example,

>> plot(f,smspec);                      % the whole spectrum, linear-linear OR
>> plot(f([coord],smspec([coord]))      % just Fourier frequencies OR
>> semilogy(f,smspec);                  % log y-axis, linear x-axis OR
>> loglog(f,smspec);                    % both axes log
```

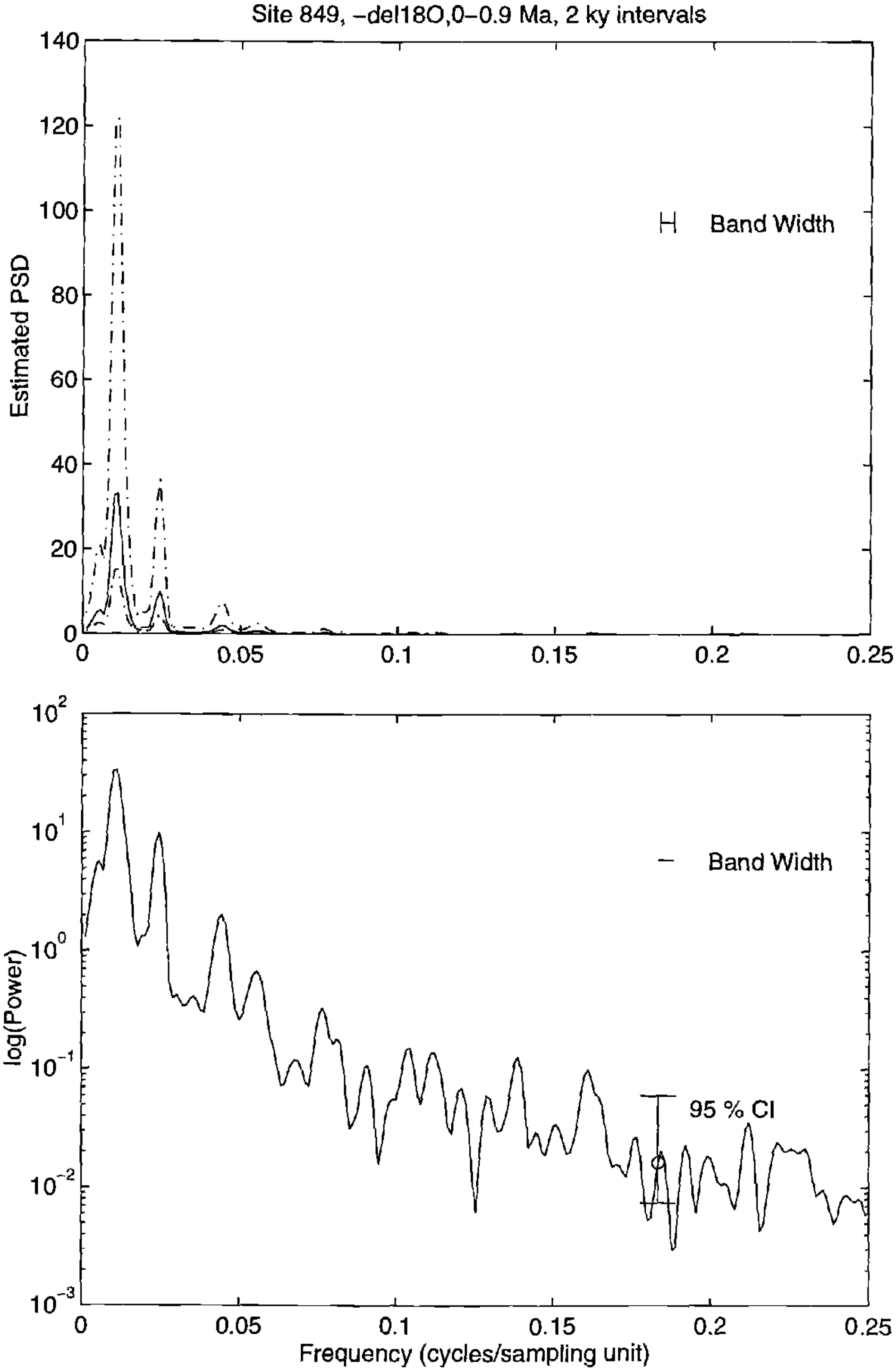

Figure A.1 Output plots from function fftspec.

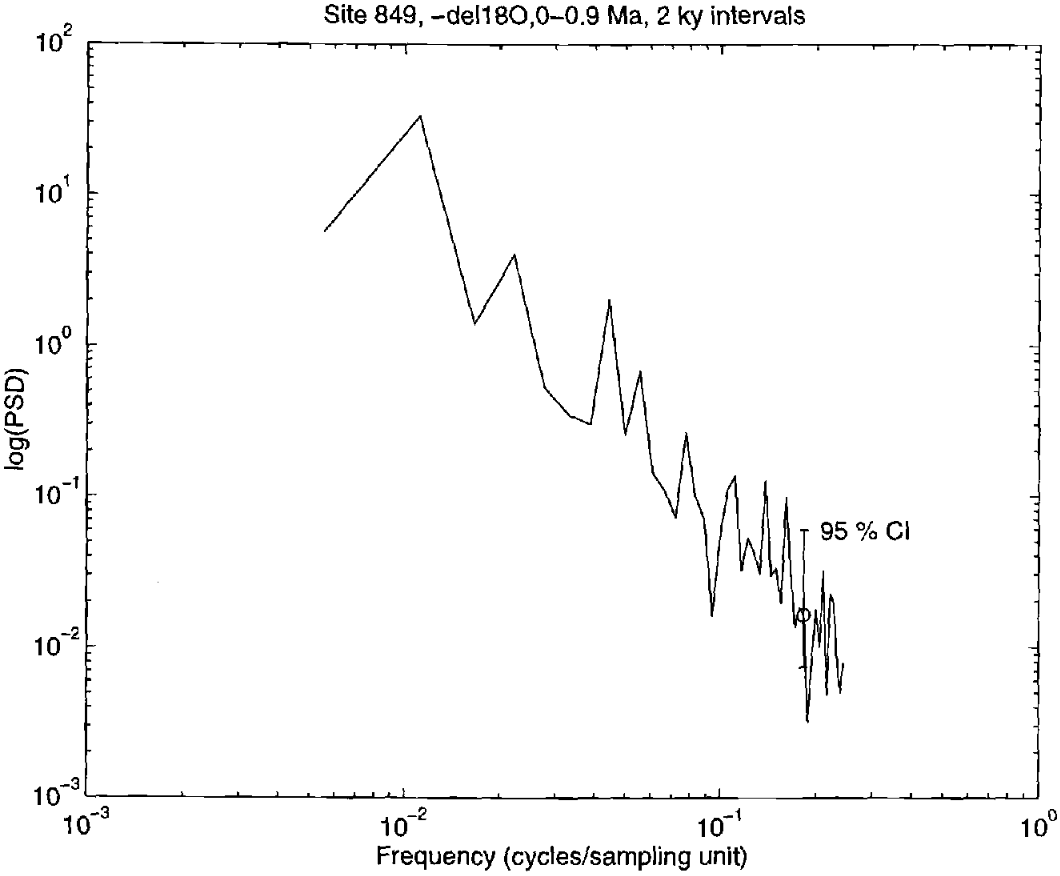

Figure A.2 Output plot from function fftspec.

fftspec2

This function is nearly identical to fftspec, but is not interactive. Plotting is slightly different from FFTSPEC. Type "help fftspec2" for on-line information.

```
[Y,spec,smspec,f,coord,ci,bw] =
        fftspec2(y,N,t,treat,w_type,alpha,filter_type,half_filt,str);
```

Input variables

y : a time series with length N and equally-spaced sampling interval, t.
N : the length (number of samples) of y
t : the sampling interval
treat : data pretreatment. Options are
- treat=0 : do nothing
- treat=1 : apply a data window. Types available are bartlett, blackman, boxcar, chebyshev ('chebwin'), hamming, hanning, kaiser, triangular ('triang').
- treat=2 : linear detrend the time series based on connecting endpoints (reduces leakage).
- treat=3 : prewhiten and post color the time series (reduce leak.)

w_type : window type for data windowing (e.g. 'bartlett'). Must be enclosed in single quotes. NOTE: if you chose treat = 0, you still must input a dummy variable into 'w_type'. You can assign w_type = '';
alpha : The function calculates (1-alpha) confidence intervals. For 95% CIs, enter 0.05.
filter_type : type of filter for smoothing spectrum (e.g. 'hanning'). Must be enclosed in single quotes.
half_filt : half filter width of the filter for smoothing the spectrum. Full filter width = (2*half_filt) + 1.
str : character string for title for plots. Must be enclosed in single quotes (' ').

Output variables

Y : the fft of y
spec : the raw frequency spectrum of y
smspec : the smoothed frequency spectrum
f : the frequency vector in units of cycles/sampling unit (e.g. if your sample spacing is 2 ky, the units of f will be cyc/ky, not cyc/2ky).
coord : The indices of independent estimates (at the Fourier frequencies).
ci : confidence intervals at each f (low, high).
bw : bandwidth

Example for fftspec2

```
>> load iso849.dat
>> y=-iso849(1:450,2);
>> N=450;
>> t=2;
>> treat=1;
>> w_type = 'bartlett';
>> alpha=0.05;
>> filter_type = 'hanning';
>> half_filt = 2;
>> str='Site 849, -del18O, 0-0.9 Ma, 2 ky intervals';
>> [Y,spec,smspec,f,coord,ci,bw] =
fftspec2(y,N,t,treat,w_type,alpha,filter_type,half_filt,str);
```

```
        % Alternatively, do the whole thing on one line:
```

```
>> [Y,spec,smspec,f,coord,ci,bw] = fftspec2(-iso849(1:450,2),450,2,1,'bartlett',
0.05,'hanning',2,'Site 849, -del18O, 0-0.9 Ma, 2 ky intervals');
```

```
        % Only one figure will appear (Figure A.3).  In the top panel is the spectrum on
        % a linear-linear plot with dash-dot confidence intervals.  In the
        % bottom panel is a log-linear plot of the spectrum.  Frequency
        % range is from 0 to the Nyquist.  Only Fourier frequencies are
        % plotted.  See notes on plotting at the end of documentation for
        % FFTSPEC.
```

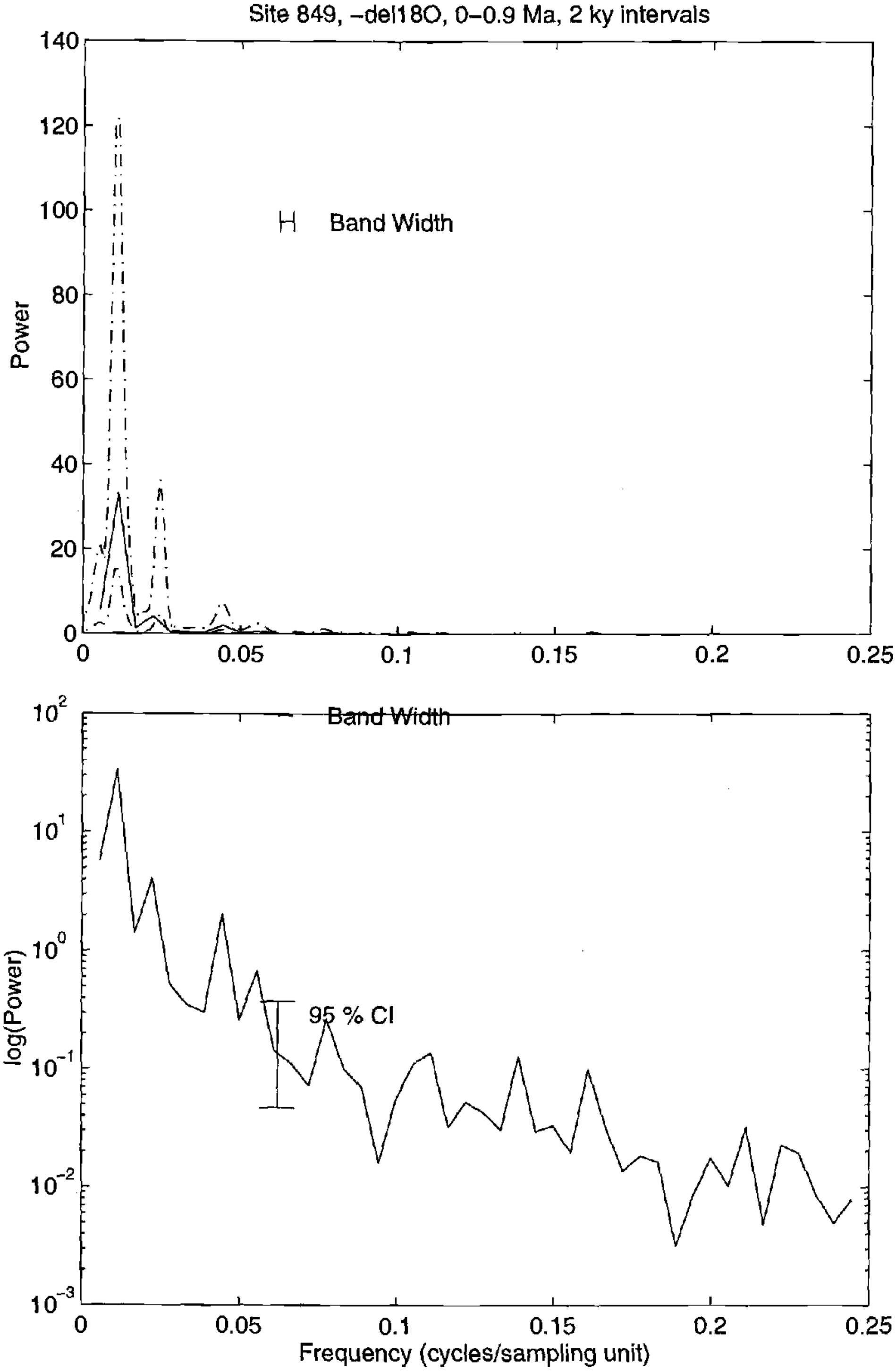

Figure A.3 Output plots from function fftspec2.

evspec

This function will create a matrix of "evolving" spectra. Basically, it uses the same routines as fftspec2 and calculates successive spectra on successive segments of the original time series, with user-chosen overlap between adjacent time series. Type "help evspec" for on-line information.

```
[smevspec,f,coord,ci,bw] =
evspec(y,blk_len,os,t,treat,w_type,alpha,filter_type,half_filt,str,num_blks,time_1);
```

Input variables

y : a time series with length N and equally-spaced sampling interval, t.

blk_len : the length (number of samples) of each segment of y

os : offset between successive segments (number of points, not age). The offset is the difference between the start of the first and second time series segments, not the overlap between the two.

t : the sampling interval

treat : data pretreatment. Options are
- treat=0 : do nothing
- treat=1 : apply a data window. Types available are bartlett, blackman, boxcar, chebyshev ('chebwin'), hamming, hanning, kaiser, triangular ('triang').
- treat=2 : linear detrend the time series based on connecting endpoints (reduces leakage).
- treat=3 : prewhiten and post color the time series (reduce leak.)

w_type : window type for data windowing (e.g. 'bartlett'). Must be enclosed in single quotes. NOTE: if you chose treat = 0, you still must input a dummy variable into 'w_type'. You can assign w_type = '';

alpha : The function calculates (1-alpha) confidence intervals. For 95% CIs, enter 0.05.

filter_type : type of filter for smoothing spectrum (e.g. 'hanning'). Must be enclosed in single quotes.

half_filt : half filter width of the filter for smoothing the spectrum. Full filter width = (2*half_filt) + 1.

str : character string for title for plots. Must be enclosed in single quotes (' ').

num_blks : Total number of time series segments (Number of spectra to be calculated). The number of points in the time series, y, must be greater than of equal to ((os * num_blks) + blk_len - os).

time_1 : Age of the first sample (in the same units as the sampling interval, t).

Output variables

smevspec : A matrix of smoothed frequency spectra, with m rows and n columns, where m = number of frequencies and n = number of spectra (num_blks). Each column is an individual spectrum.

f : the frequency vector in units of cycles/sampling unit (e.g. if your sample spacing is 2 ky, the units of f will be cyc/ky, not cyc/2ky).

coord : The indices of independent estimates (at the Fourier frequencies).

ci : confidence intervals at each f (low, high). The first two columns of ci correspond to the first spectrum, columns 3 and 4 to the second spectrum, etc. Matrix size is m by (2*n) (see smevspec matrix).

bw : bandwidth

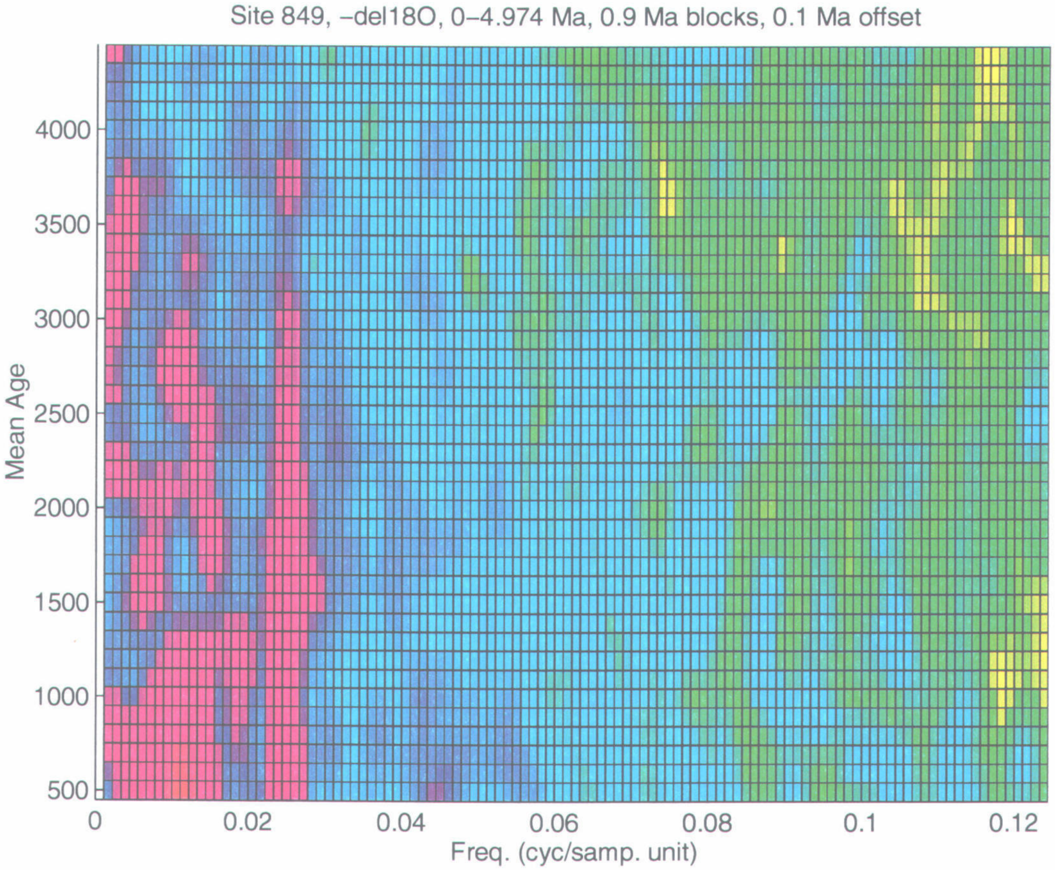

Figure A.4 Output plot from function evspec.

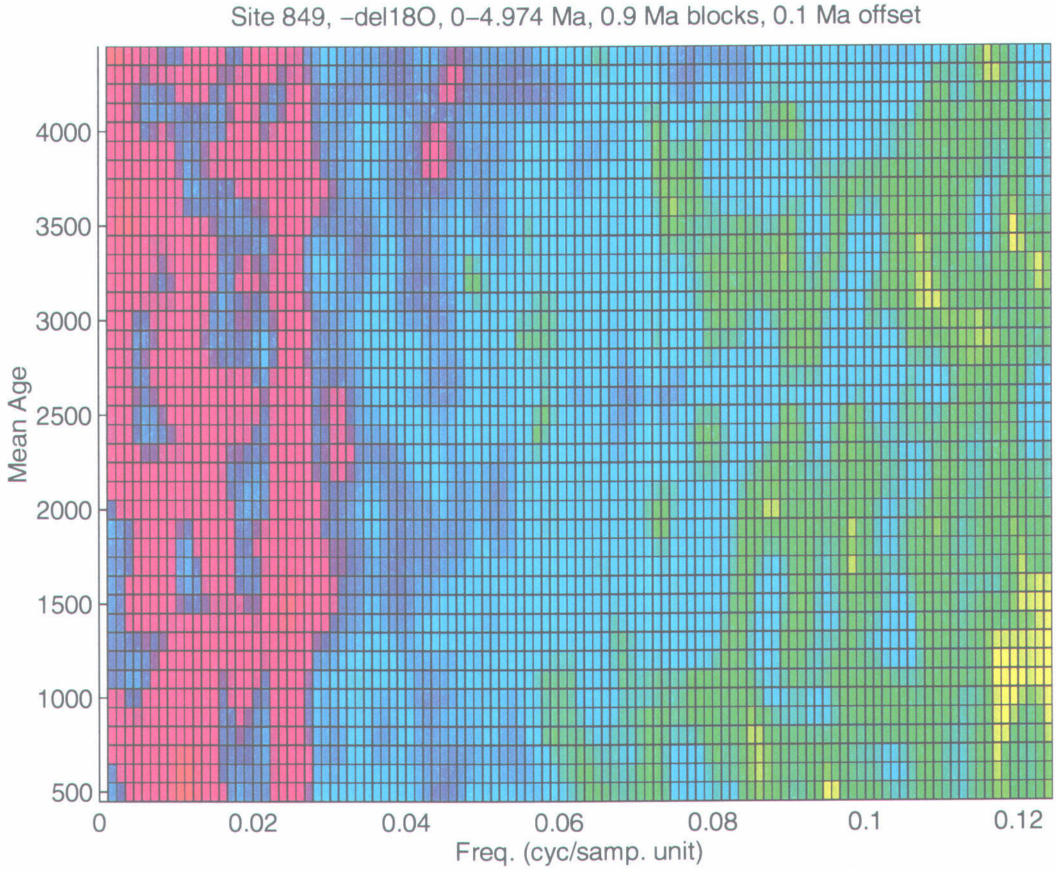

Figure A.5 Output plot from function evspec2.

evspec2

This function will create a matrix of "evolving" spectra. Basically, it uses the same routines as fftspec2 and calculates successive spectra on successive segments of the original time series, with user-chosen overlap between adjacent time series. EVSPEC2 is identical to EVSPEC, except each segment is normalized to have mean = 0 and variance = 1. See documentation for EVSPEC for input and output information. Type "help evspec2" for on-line documentation.

```
[smevspec,f,coord,ci,bw] =
evspec2(y,blk_len,os,t,treat,w_type,alpha,filter_type,half_filt,str,num_blks,time_1);
```

Example for evspec2

```
>> load iso849.dat
>> y=-iso849(:,2);                    % Take all rows in the second column
>> blk_len=450;
>> os=50;
>> t=2;
>> treat=1
>> w_type='bartlett';
>> alpha=0.05;
>> filter_type='hanning';
>> half_filt=2;
>> str='Site 849, -del18O, 0-4.974 Ma, 0.9 Ma blocks, 0.1 Ma offset'
>> num_blks=41;
>> time_1=0.0040;
>> [smevspec,f,coord,ci,bw] =
evspec2(y,blk_len,os,t,treat,w_type,alpha,filter_type,half_filt,str,num_blks,time_1);

        % This function will output to the screen the segment number currently being
        % calculated from 1 to num_blks. ("i = 1", "i = 2", etc.). It will create a 3-D plot
        % of frequency, average age (of segment), and estimated power spectral density
        % (Figure A.5; variance of each time series segment = 1). See functions MESH,
        % SURF, VIEW and CONTOUR for information about 3-D plotting in matlab.
```

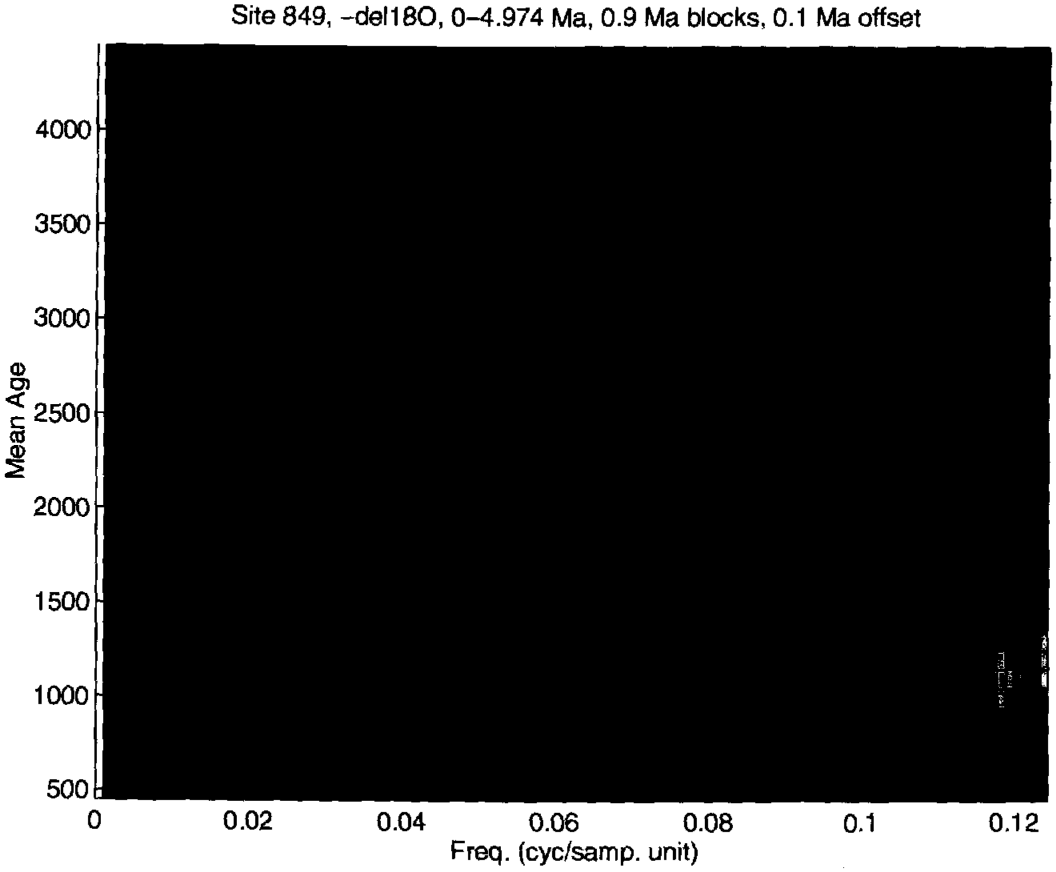

Figure A.5 Output plot from function evspec2.

xspec

This function will calculate the coherence and phase spectra between two time series of equal length with equal sampling interval. This function is somewhat interactive. Type "help xspec" for on-line information.

[smspecx,smspecy,f,coord,ci,bw,Cxy,Gain,fullgain,ph,ciph] =
xspec(x,y,N,t,treat,alpha,cohalpha);

Input variables

x : a time series with length N and equally-spaced sampling interval, t.
y : a time series with same length N as x, and equally-spaced sampling interval, t.
N : the length (number of samples) of x and y
t : the sampling interval
treat : data pretreatment. Options are
  treat=0 : do nothing
  treat=1 : apply a data window. Types available are bartlett, blackman, boxcar, chebyshev ('chebwin'), hamming, hanning, kaiser, triangular ('triang').
  treat=2 : linear detrend the time series based on connecting endpoints (reduces leakage).
  treat=3 : prewhiten and post color the time series (reduce leak.)
alpha : The function calculates (1-alpha) confidence intervals. For 95% CIs, enter 0.05.
cohalpha : Calculates (1-cohalpha) significance level for coherence. For 95% significance, enter 0.05.

Output variables

smspecx : the smoothed frequency spectrum of x.
smspecy : the smoothed frequency spectrum of y.
f : the frequency vector in units of cycles/sampling unit (e.g. if your sample spacing is 2 ky, the units of f will be cyc/ky, not cyc/2ky).
coord : The indices of independent estimates (at the Fourier frequencies).
ci : confidence intervals at each f (low, high for x, then low, high for y).
bw : bandwidth
Cxy : Coherence^2 spectrum
Gain : smoothed gain function from 0 to Nyquist.
fullgain : raw gain function symmetrical about Nyquist.
ph : phase. If time progresses toward the past, as in most geologic time series, then a positive phase means that the first time series (x) leads. If time progresses forward (e.g. physical oceanography time series), then a positive phase means that the second time series (y) leads.
ciph : Confidence intervals on phase (1-cohalpha). Two columns, first lower then upper limits.

Example for xspec

```
>> load iso849.dat
>> x=-iso849(1:450,2);                 % Oxygen isotopes
>> y=iso849(1:450,3);                  % Carbon isotopes
>> N=450;
>> t=2;
>> treat=1;
>> alpha=0.05;
>> cohalpha=0.05;
>> [smspecx,smspecy,f,coord,ci,bw,Cxy,Gain,fullgain,ph,ciph] =
xspec(x,y,N,t,treat,alpha,cohalpha);

             % You will be asked some questions, as in FFTSPEC

Input data windowing type: bartlett              % see example for FFTSPEC

             % The raw spectra for x (solid) and y (dash) will be plotted.

Input half filter width: 2                       % see example for FFTSPEC
Input filter type: hanning                       % see example for FFTSPEC
Input title for plots: Site 849, -del18O v. del13C, 0-0.9 Ma, 2ky int.

        % The bandwidth (bw), degrees of freedom (dof) and cutoff level for (1-
        % cohalpha) coherence^2 (K) will be output to the screen. NOTE: dof and K are
        % not saved in the output. PLOTS (Figure A.6): In the top plot are the smoothed
        % spectra plotted on a log-linear scale. Solid is the first time series (x), dash is
        % the second time series (y). Frequency runs from 0 to the Nyquist. The second
        % plot shows the coherence^2 spectrum with a solid horizontal line at the 1-
        % cohalpha confidence level. The third plot shows phase in degrees, with 1-
        % cohalpha confidence intervals. Phase is only plotted for frequencies where the
        % coherence is significant. The fourth plot shows the gain spectrum plotted only
        % at the Fourier frequencies.
```

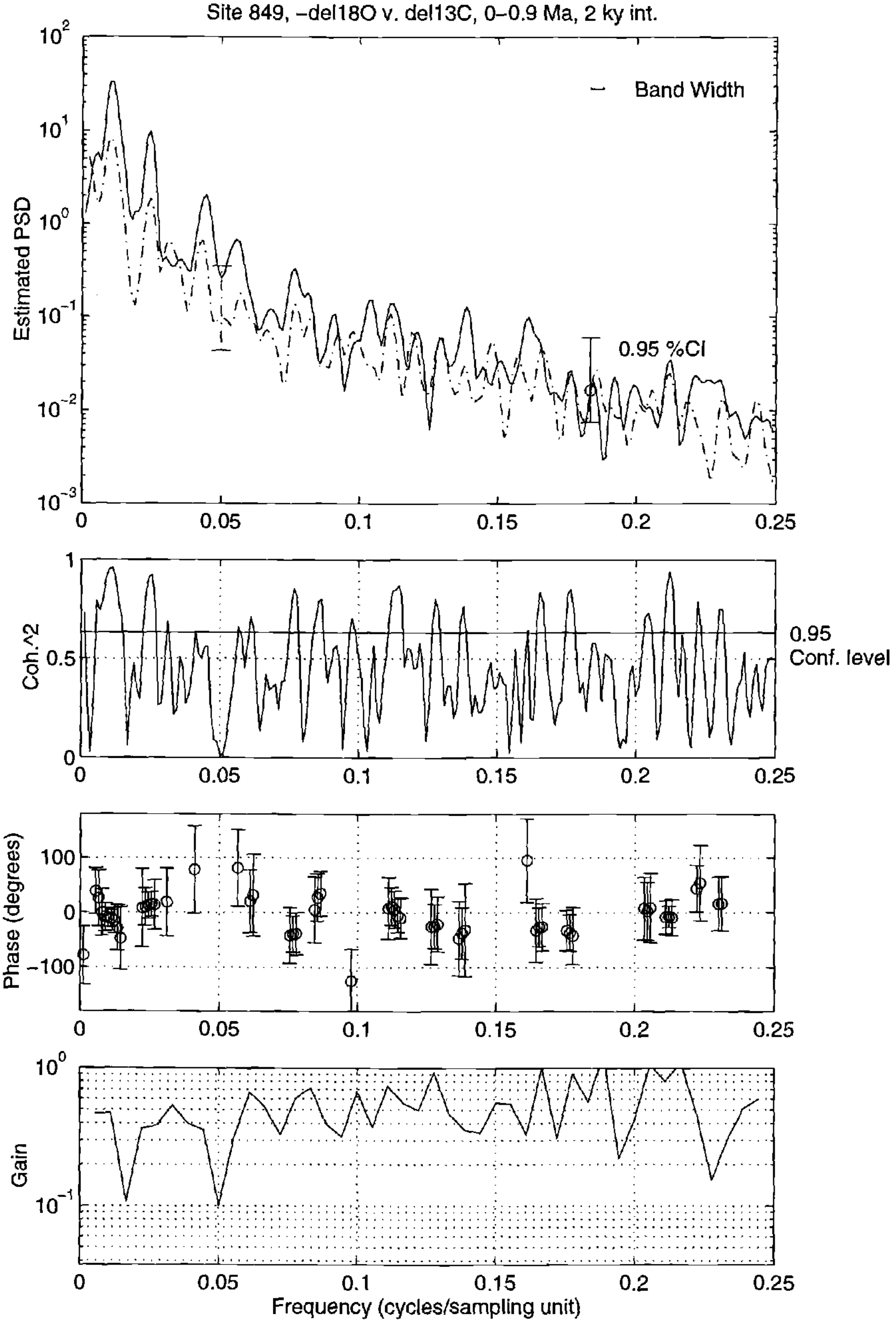

Figure A.6 Output plots from function xspec.

xspec2

This function will calculate the coherence and phase spectra between two time series of equal length with equal sampling interval. This function is not interactive, and gives a bit more output than XSPEC. Type "help xspec2" for on-line information.

```
[smspecx,smspecy,f,coord,ci,bw,Cxy,coord2,Gain,fullgain,ph,ciph] =
xspec2(x,y,N,t,treat,w_type,alpha,cohalpha,filter_type,half_filt,str);
```

Input variables

x : a time series with length N and equally-spaced sampling interval, t.
y : a time series with same length N as x, and equally-spaced sampling interval, t.
N : the length (number of samples) of x and y
t : the sampling interval
treat : data pretreatment. Options are
  treat=0 : do nothing
  treat=1 : apply a data window. Types available are bartlett, blackman, boxcar, chebyshev ('chebwin'), hamming, hanning, kaiser, triangular ('triang').
  treat=2 : linear detrend the time series based on connecting endpoints (reduces leakage).
  treat=3 : prewhiten and post color the time series (reduce leak.)
w_type : window type for data windowing (e.g. 'bartlett'). Must be enclosed in single quotes. NOTE: if you chose treat = 0, you still must input a dummy variable into 'w_type'. You can assign w_type = '';
alpha : The function calculates (1-alpha) confidence intervals. For 95% CIs, enter 0.05.
cohalpha : Calculates (1-cohalpha) significance level for coherence. For 95% significance, enter 0.05.
filter_type : type of filter for smoothing spectrum (e.g. 'hanning'). Must be enclosed in single quotes.
half_filt : half filter width of the filter for smoothing the spectrum. Full filter width = (2*half_filt) + 1.
str : character string for title for plots. Must be enclosed in single quotes (' ').

Output variables

smspecx : the smoothed frequency spectrum of x.
smspecy : the smoothed frequency spectrum of y.
f : the frequency vector in units of cycles/sampling unit (e.g. if your sample spacing is 2 ky, the units of f will be cyc/ky, not cyc/2ky).
coord : The indices of independent estimates (at the Fourier frequencies).
ci : confidence intervals at each f (low, high for x, then low, high for y).
bw : bandwidth
Cxy : Coherence spectrum (Coherence^2).
coord2 : The indices of f for Coherence^2 greater than the 1-cohalpha cutoff.
Gain : smoothed gain function from 0 to Nyquist.
fullgain : raw gain function symmetrical about Nyquist.
ph : phase. If time progresses toward the past, as in most geologic time series, then a positive phase means that the first time series (x) leads. If time progresses forward (e.g. physical oceanography time series), then a positive phase means that the second time series (y) leads.
ciph : Confidence intervals on phase (1-cohalpha). Two columns, first lower then upper limits.

Example for xspec2

```
>> load iso849.dat
>> x=-iso849(1:450,2);                % Oxygen isotopes
>> y=iso849(1:450,3);                 % Carbon isotopes
>> N=450;
>> t=2;
>> treat=1;
>> w_type='bartlett';
>> alpha=0.05;
>> cohalpha=0.05;
>> filter_type='hanning';
>> half_filt=2;
>> str='Site 849, -del18O v. del13C, 0-0.9 Ma, 2ky int.';
>> [smspecx,smspecy,f,coord,ci,bw,Cxy,coord2,Gain,fullgain,ph,ciph] =
xspec2(x,y,N,t,treat,w_type,alpha,cohalpha,filter_type,half_filt,str);

        % The bandwidth (bw), degrees of freedom (dof) and cutoff level for (1-
        % cohalpha) coherence^2 (K) will be output to the screen.  NOTE: dof and K are
        % not saved in the output.  PLOTS (Figure A.7):  In the top plot are the smoothed
        % spectra plotted on a log-linear scale.  Solid is the first time series (x), dash is
        % the second time series (y).  Frequency runs from 0 to one half the Nyquist. If
        % the axes are off, type (for example):

>> subplot(2,1,1)
>> axis([0 0.125 0.01  100])

        % The second plot shows the coherence^2 spectrum with a solid horizontal line at
        % the 1-cohalpha confidence level.  The third plot shows phase in degrees, with
        % 1-cohalpha confidence intervals.  Phase is only plotted for frequencies where
        % the coherence is significant. Gain is not plotted.
```

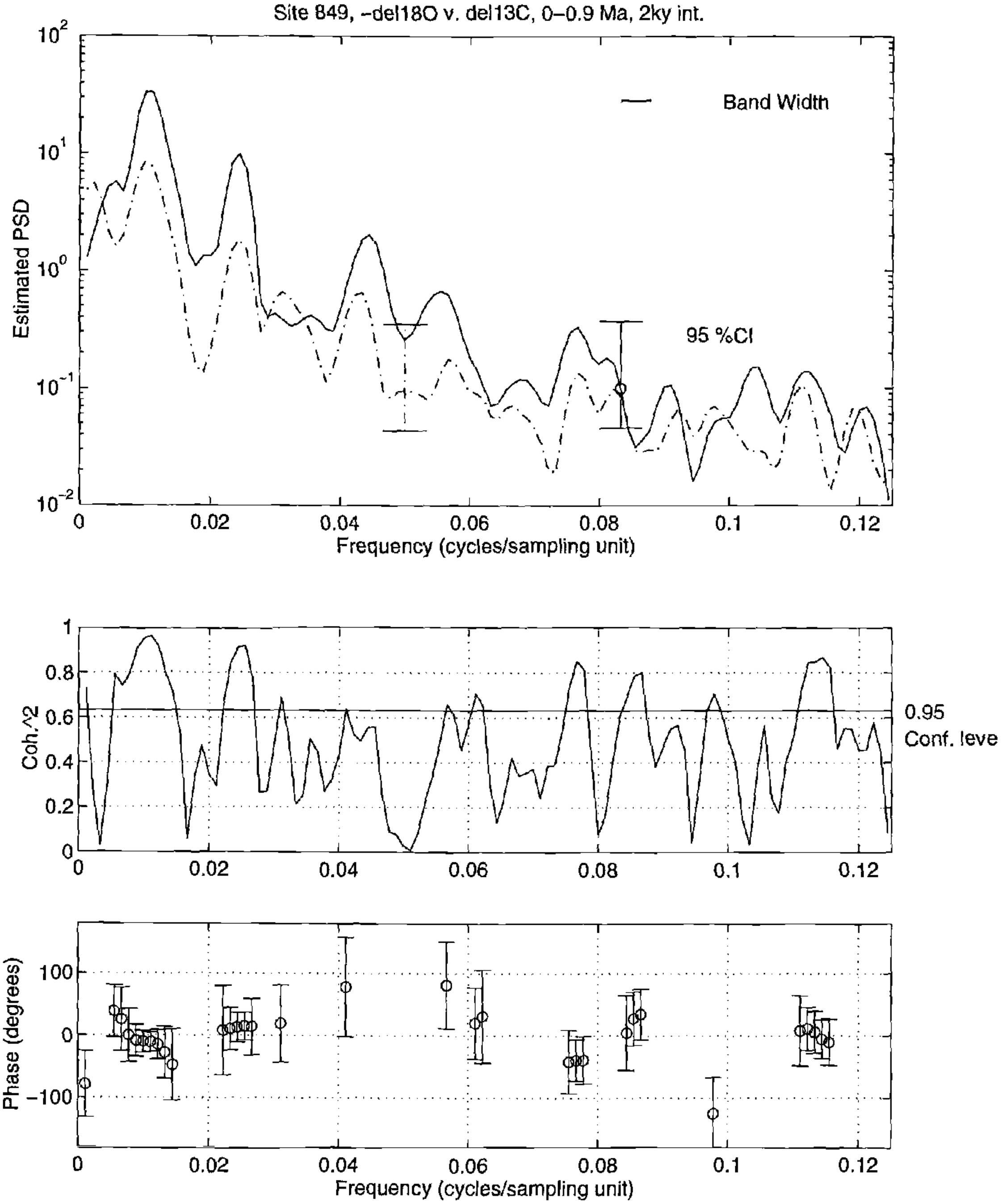

Figure A.7 Output plots from function xspec2.

xtract_Milank

This function extracts frequency, coherence, and phase information from the output of XSPEC2 that corresponds to Milankovitch frequencies within the bandwidth. Type "help xtract_Milank" for on-line information.

```
[Milank] = xtract_Milank(f,Cxy,ph,ciph,bw,coord2);
```

Input variables

f : frequency vector output by xspec2.
Cxy : Coherence sepctrum output by xspec2.
ph : phase spectrum output by xspec2.
ciph : phase confidence intervals output by xspec2.
bw : bandwidth output by xspec2.
coord2 : indices of coherent frequencies output by xspec2.

Output variables

Milank : A matrix with 7 columns as follows: frequency, period, coherence, phase,

2 columns for phase confidence intervals, and the phase error (difference between columns 4 and 5). If columns 5 and 6 are = 0, then the coherence is below the 1-cohalpha confidence level. Frequencies included in this matrix are within 1/2 a bandwidth of the Milankovitch frequencies (1/100, 1/41, 1/23, 1/19 ky^{-1}).

Example for xtract_Milank

To run xtract_Milank, first run xspec2, then type

```
>> [Milank] = xtract_Milank(f,Cxy,ph,ciph,bw,coord2);
>> Milank                    % to show matrix on the screen
```

OTHER AVAILABLE FUNCTIONS

head

Functions like the UNIX "head" command. Will show the first 10 lines of a matlab variable. Does not work if the matrix has fewer than 10 lines.

rmode

Performs r-mode factor analysis.

tail

Functions like the UNIX "tail" command. Will show the last 10 lines of a matlab variable. Does not work if the matrix has fewer than 10 lines.

MATLAB CODE

fftspec

```
function [Y,spec,smspec,f,coord,ci,bw] = fftspec(y,N,t,treat,alpha)

% [Y,spec,smspec,f,coord,ci,bw] = fftspec(y,N,t,treat,alpha);
%
%       Calculates a variance spectrum for column vector y with
%       length N and equally-spaced sampling interval t.  Asks for
%       smoothing filter half-width and type.  Calculates (1-alpha)
%       confidence intervals.
%       The input parameter "treat" refers to data pretreatment.
%       treat=0 : do nothing
%       treat=1 : apply a data window (will ask for type)
%       treat=2 : linear detrend the time series based on
%                 connecting endpoints (reduces leakage).
%       treat=3 : prewhiten and post color the time series (reduce leak.)
%
%       Outputs the smoothed spectrum (smspec), frequency vector (f),
%       confidence intervals (ci), and band width (bw). Plots spectrum on
%       linear and log-linear scales with CIs and bandwidth.  Also outputs
%       steps Y (the fft) and spec (the raw spectrum). "Coord" contains
%       the indices of independent estimates.
%       Plots spectrum on linear, log-linear, and log-log scales with
%       CIs and bandwidth.
%
%       See also FFTSPEC2, XSPEC, XSPEC2, and GAIN

% ERROR message
if nargin < 5,
  error('FFTSPEC requires five input arguments.');
end

% REMOVE THE MEAN FROM THE TIME SERIES
y=y-mean(y);

% DATA WINDOWING
if treat==1
   win_type=input('Input data windowing type: ','s');
   window=eval([win_type,'(' num2str(N) ')']);
   window=window/(sum(window)/N);
   y=y.*window;

% LINEAR DETREND, detrends by connecting endpoints to reduce leakage
%  from low to high frequencies
elseif treat==2
  slope=(y(N)-y(1))/N;
  intercept=y(1);
  B = [intercept;slope];
%  xtemp=[ones(1,N);[t:t:N*t]]';
  xtemp=[ones(1,N);[1:1:N]]';
  yest=xtemp*B;                 % N by 1
  y=y-yest;

% PREWHITEN USING FIRST DIFFERENCE
```

```
elseif treat==3
y2=ones(1,N);
  for j=2:N
    y2(j)=y(j)-y(j-1);
  end
  y2(1)=y2(2);                    % set 1st value = second value
  y=y2;
end

% CALCULATE SPECTRUM
Y=fft(y);

% This runs from the first Fourier frequency to the Nyquist,
% not including 0 (after next line).
Y=Y(2:N/2)/N;
spec=2*N*t*abs(Y).^2;

% FREQUENCY
% likewise, the frequencies should not include zero or the Nyquist
delf=1/(N*t);
f = [delf:delf:1/(2*t)-delf]';

% PLOT
figure;
orient tall;
axes('position',[0.18 0.52 0.64 0.37]);
plot(f,spec);

% FILTER THE SPECTRUM (SMOOTHING)
half_filt = input('Input half filter width: ');
filter_type = input('Input filter type: ', 's');
txt_title = input('Input title for plots: ','s');
HF = 2*half_filt+1;
filter = eval([filter_type,'(' num2str(HF) ')']);
filter = filter/sum(filter);
smspec=conv(spec,filter);
smspec=smspec(half_filt+1:length(smspec)-half_filt);

% CALCULATE THE CENTER FREQUENCIES for the smoothed spectra
% CHECK THIS OUT FOR WINDOWS OTHER THAN BOXCAR
 coord=[HF:HF:length(f)];
 f2=f([coord]);
% This next line matches Dudley's results, but will not work if HF = 1;
% coord=[HF-1:HF:length(f)]; *OLD*
% but, I think it should be the following line, to correspond to Four. freq.
% same as for HF = 1
% coord=[HF:HF:length(f)];
% f2=f([coord]);
%end

% POST-COLOR
if treat==3;
 Hf=2*exp(i*pi*(1/2-f)).*sin(pi.*f);
 Gf=2*sin(pi.*f);
 smspec=smspec./(conj(Gf).*Gf)';
end

% PLOT SMOOTHED SPECTRUM
```

```
plot(f,smspec);
ylabel('Estimated PSD');
title(txt_title);

% DEGREES OF FREEDOM and BAND WIDTH
I = sum(filter.*filter);
%bw = 1/(N*I)
bw = 1/(N*t*I)
dof = round(2/I)

% CONFIDENCE INTERVALS
low_lim=smspec*dof./(chi2inv(1-alpha/2,dof));
upp_lim=smspec*dof./(chi2inv(alpha/2,dof));
ci=[low_lim upp_lim];

% PLOT CIs and BW on LINEAR SCALE
hold on
plot(f,low_lim,'-.');
plot(f,upp_lim,'-.');

temp=0.8*max(upp_lim);
k=coord(round(length(coord)*3/4));
bwdat=[f(k) temp;f(k)+bw temp];
bwleft=[f(k) temp+(0.02*max(upp_lim));f(k) temp-(0.02*max(upp_lim))];
bwrt=[f(k)+bw temp+(0.02*max(upp_lim));f(k)+bw temp-(0.02*max(upp_lim))];
plot(bwdat(:,1),bwdat(:,2),'-');
plot(bwleft(:,1),bwleft(:,2),'-');
plot(bwrt(:,1),bwrt(:,2),'-');
text(f(k+10)+bw,temp,'Band Width');
ylabel('Estimated PSD');
hold off;

%PLOT ON LOG-LINEAR SCALE
temp=0.1*max(spec);
bwdat=[f(k) temp;f(k)+bw temp];
bwleft=[f(k) temp+(0.0002*max(upp_lim));f(k) temp-(0.0002*max(upp_lim))];
bwrt=[f(k)+bw temp+(0.0002*max(upp_lim));f(k)+bw temp-(0.0002*max(upp_lim))];
mid=[f(k) smspec(k)];

axes('position',[0.18 0.1 0.64 0.37]);
semilogy(f,smspec);
cibar=[f(k) low_lim(k);f(k) smspec(k);f(k) upp_lim(k)];
citop=[f(k-5) upp_lim(k);f(k+5) upp_lim(k)];
cibot=[f(k-5) low_lim(k);f(k+5) low_lim(k)];
hold on
semilogy(cibar(:,1),cibar(:,2),'-');
semilogy(citop(:,1),citop(:,2),'-');
semilogy(cibot(:,1),cibot(:,2),'-');
semilogy(mid(:,1),mid(:,2),'o');
semilogy(bwdat(:,1),bwdat(:,2),'-');
semilogy(bwleft(:,1),bwleft(:,2),'-');
semilogy(bwrt(:,1),bwrt(:,2),'-');
text(f(k+10)+bw,temp,'Band Width');
text(f(k+9),upp_lim(k)-0.25*(upp_lim(k)-low_lim(k)),'95 % CI');
xlabel('Frequency (cycles/sampling unit)');
ylabel('log(Power)');
hold off
```

```
%PLOT ON LOG-LOG SCALE
figure
loglog(f2,smspec([coord]));
cibar=[f(k) low_lim(k);f(k) smspec(k);f(k) upp_lim(k)];
citop=[f(k-5) upp_lim(k);f(k+5) upp_lim(k)];
cibot=[f(k-5) low_lim(k);f(k+5) low_lim(k)];
cibar=[cibar(:,1) cibar(:,2)];
citop=[citop(:,1) citop(:,2)];
cibot=[cibot(:,1) cibot(:,2)];
hold on
loglog(cibar(:,1),cibar(:,2),'-');
loglog(citop(:,1),citop(:,2),'-');
loglog(cibot(:,1),cibot(:,2),'-');
loglog(mid(:,1),mid(:,2),'o');
text(f(k+20),citop(1,2),'95 % CI');
xlabel('Frequency (cycles/sampling unit)');
ylabel('log(PSD)');
title(txt_title);
hold off
```

fftspec2

```
function [Y,spec,smspec,f,coord,ci,bw] = fftspec2(y,N,t,treat,w_type,alpha,filter_type,half_filt,str)

% FFTSPEC2
% [Y,spec,smspec,f,coord,ci,bw] = fftspec2(y,N,t,treat,w_type,alpha,filter_type,half_filt,str);
%
%       Calculates a variance spectrum for column vector y with
%       length N and equally-spaced sampling interval t.  Needs
%       smoothing filter type and half width.
%     The title for plots is in variable str.
%     Calculates (1-alpha) confidence intervals.
%       The input parameter "treat" refers to data pretreatment.
%     treat=0 : do nothing
%     treat=1 : apply a data window (input type in "w_type")
%     treat=2 : linear detrend the time series based on
%           connecting endpoints (reduces leakage).
%       treat=3 : prewhiten and post color (reduces leakage)
%
%       w_type is the type of data window (e.g. Bartlett)
%
%       Outputs the smoothed spectrum (smspec), frequency vector (f),
%       confidence intervals (ci), and band width (bw). Also outputs
%       steps Y (the fft) and spec (the raw spectrum). "Coord" contains
%       the indices of independent estimates.
%
%       See also FFTSPEC, XSPEC, XSPEC2, and GAIN

% ERROR message
if nargin < 9,
  error('FFTSPEC2 requires nine input arguments.');
end

% REMOVE THE MEAN FROM THE TIME SERIES
y=y-mean(y);
```

```
% DATA WINDOWING
if treat==1
   win_type=w_type;
   window=eval([win_type,'(' num2str(N) ')']);
   window=window/(sum(window)/N);
   y=y.*window;

% LINEAR DETREND, detrends by connecting endpoints to reduce leakage
%  from low to high frequencies
elseif treat==2
  slope=(y(N)-y(1))/N;
  intercept=y(1);
  B = [intercept;slope];
  xtemp=[ones(1,N);[1:1:N]]';
  yest=xtemp*B;                    % N by 1
  y=y-yest;

% PREWHITEN USING FIRST DIFFERENCE
elseif treat==3
y2=ones(1,N);
  for j=2:N
    y2(j)=y(j)-y(j-1);
  end
  y2(1)=y2(2);              % set 1st value = second value
  y=y2;
end

% CALCULATE SPECTRUM
Y=fft(y);
%  This runs from the first Fourier frequency to the Nyquist,
%  not including 0 (after next line).
Y=Y(2:N/2)/N;
spec=2*N*t*abs(Y).^2;

% FREQUENCY
delf=1/(N*t);
f = [delf:delf:1/(2*t)-delf]';

clf
orient tall;
axes('position',[0.18 0.52 0.64 0.37]);
plot(f,spec);

txt_title = str;
HF = 2*half_filt+1;
filter = eval([filter_type,'(' num2str(HF) ')']);
filter = filter/sum(filter);
smspec=conv(spec,filter);
smspec=smspec(half_filt+1:length(smspec)-half_filt);

% CALCULATE THE CENTER FREQUENCIES for the smoothed spectra
% CHECK THIS OUT FOR WINDOWS OTHER THAN BOXCAR
coord=[HF:HF:length(f)];
f2=f([coord]);

% POST-COLOR
if treat==3;
  Hf=2*exp(i*pi*(1/2-f)).*sin(pi.*f);
```

```
 Gf=2*sin(pi.*f);
 smspec=smspec./(conj(Gf).*Gf)';
end

% PLOT SMOOTHED SPECTRUM
plot(f2,smspec([coord]));
title(txt_title);

% DEGREES OF FREEDOM and BAND WIDTH
I = sum(filter.*filter);
bw = 1/(N*t*I)
dof = round(2/I)

% CONFIDENCE INTERVALS
low_lim=smspec*dof./(chi2inv(1-alpha/2,dof));
upp_lim=smspec*dof./(chi2inv(alpha/2,dof));
ci=[low_lim upp_lim];

% PLOT CIs and BW on LINEAR SCALE
hold on
plot(f,low_lim,'-.');
plot(f,upp_lim,'-.');

temp=0.8*max(upp_lim);
bwdat=[f(N/8) temp;f(N/8)+bw temp];
bwleft=[f(N/8) temp+(0.02*max(upp_lim));f(N/8) temp-(0.02*max(upp_lim))];
bwrt=[f(N/8)+bw temp+(0.02*max(upp_lim));f(N/8)+bw temp-(0.02*max(upp_lim))];
plot(bwdat(:,1),bwdat(:,2),'-');
plot(bwleft(:,1),bwleft(:,2),'-');
plot(bwrt(:,1),bwrt(:,2),'-');
text(f(N/8+10)+bw,temp,'Band Width');
ylabel('Power');
hold off;

%PLOT ON LOG SCALE
axes('position',[0.18 0.1 0.64 0.37]);
semilogy(f2,smspec([coord]));
cibar=[f(N/8) low_lim(N/8);f(N/8) smspec(N/8);f(N/8) upp_lim(N/8)];
citop=[f(N/8-5) upp_lim(N/8);f(N/8+5) upp_lim(N/8)];
cibot=[f(N/8-5) low_lim(N/8);f(N/8+5) low_lim(N/8)];
hold on
semilogy(cibar(:,1),cibar(:,2),'-');
semilogy(citop(:,1),citop(:,2),'-');
semilogy(cibot(:,1),cibot(:,2),'-');
semilogy(bwdat(:,1),bwdat(:,2),'-');
semilogy(bwleft(:,1),bwleft(:,2),'-');
semilogy(bwrt(:,1),bwrt(:,2),'-');
text(f(N/8+10)+bw,temp,'Band Width');
text(f(N/8+9),upp_lim(N/8)-0.25*(upp_lim(N/8)-low_lim(N/8)),'95 % CI');
xlabel('Frequency (cycles/sampling unit)');
ylabel('log(Power)');
hold off
```

evspec

```
function [smevspec,f,coord,ci,bw] =
evspec(y,blk_len,os,t,treat,w_type,alpha,filter_type,half_filt,str,num_blks,time_1)

% EVSPEC
% [smevspec,f,coord,ci,bw] =
evspec(y,blk_len,os,t,treat,w_type,alpha,filter_type,half_filt,str,num_blks,time_1);
%
%       Calculates an evolving variance spectrum for column vector y
%       with equally-spaced sampling interval t. A spectrum is
%       calculated for each segment of the time series, y, of length
%       blk_len.  Successive segments are offset by the number
%       of points defined by the parameter os.  The number of
%       spectra calculated is defined by num_blks. The number
%       of points in the time series, y, must be greater than or equal
%       to ((os * num_blks) + blk_len - os).
%       Needs smoothing filter type and half width defined.
%     The title for plots is in variable str.
%    Calculates (1-alpha) confidence intervals.
%       The input parameter "treat" refers to data pretreatment.
%       Treatment applies to each segment individually.
%     treat=0 : do nothing
%    treat=1 : apply a data window (input type in "w_type")
%    treat=2 : linear detrend the time series based on
%          connecting endpoints (reduces leakage).
%       treat=3 : prewhiten and post color (reduces leakage)
%
%       w_type is the type of data window (e.g. Bartlett)
%       time_1 is the age of the first sample.
%
%       Outputs the smoothed evolving spectra (smevspec), frequency vector (f),
%       confidence intervals (ci), and band width (bw).
%       "Coord" contains the indices of independent estimates.
%
%       See also FFTSPEC, FFTSPEC2, XSPEC, XSPEC2, and EVSPEC2

% ERROR message
if nargin < 12,
  error('EVSPEC requires twelve input arguments.');
end

ts = y;                      % Assign new variable name to whole time series. Avoid renaming in code.
N = blk_len;                 % Avoid renaming in code.
txt_title = str;
start = -os+1;

% GET FILTER
HF = 2*half_filt+1;
filter = eval([filter_type,'(' num2str(HF) ')']);
filter = filter/sum(filter);

% FREQUENCY
delf=1/(N*t);
f = [delf:delf:1/(2*t)-delf]';

% CALCULATE THE CENTER FREQUENCIES for the smoothed spectra
coord=[HF:HF:length(f)];
```

```
f2=f([coord]);

% DEGREES OF FREEDOM and BAND WIDTH
I = sum(filter.*filter);
%bw = 1/(N*I)
bw = 1/(N*t*I)
dof = round(2/I)

%  ASSIGN FINAL MATRIX SIZES
%smevspec = zeros(size(f):num_blks);
%full_ci = zeros(size(f):2*num_blks);
smevspec = zeros(length(f),num_blks);
full_ci = zeros(length(f),(2*num_blks));

%******************************************************
% BEGIN LARGE LOOP, RETURN TO HERE FOR SUBSEQUENT SEGMENTS
for i = 1:num_blks;
 i                                % write segment number to screen
 start = start+os;
 end_seg = start + blk_len - 1;
 y = ts(start:end_seg);

% REMOVE THE MEAN FROM THE TIME SERIES
y=y-mean(y);

% DATA WINDOWING
if treat==1
  win_type=w_type;
  window=eval([win_type,'(' num2str(N) ')']);
  window=window/(sum(window)/N);
  y=y.*window;

% LINEAR DETREND, detrends by connecting endpoints to reduce leakage
%  from low to high frequencies
elseif treat==2
 slope=(y(N)-y(1))/N;
 intercept=y(1);
 B = [intercept;slope];
%  xtemp=[ones(1,N);[t:t:N*t]]';
 xtemp=[ones(1,N);[1:1:N]]';
 yest=xtemp*B;                    % N by 1
 y=y-yest;

% PREWHITEN USING FIRST DIFFERENCE
elseif treat==3
y2=ones(1,N);
 for j=2:N
  y2(j)=y(j)-y(j-1);
 end
 y2(1)=y2(2);              % set 1st value = second value
 y=y2;
end

% CALCULATE SPECTRUM
Y=fft(y);
%  This runs from the first Fourier frequency to the Nyquist,
%  not including 0 (after next line).
Y=Y(2:N/2)/N;
```

```
spec=2*N*t*abs(Y).^2;

clf
plot(f,spec);

% FILTER THE SPECTRUM (SMOOTHING)
smspec=conv(spec,filter);
smspec=smspec(half_filt+1:length(smspec)-half_filt);

% POST-COLOR
if treat==3;
  Hf=2*exp(i*pi*(1/2-f)).*sin(pi.*f);
  Gf=2*sin(pi.*f);
  smspec=smspec./(conj(Gf).*Gf)';
end

% PLOT SMOOTHED SPECTRUM
plot(f2,smspec([coord]));
title(txt_title);

% CONFIDENCE INTERVALS
low_lim=smspec*dof./(chi2inv(1-alpha/2,dof));
upp_lim=smspec*dof./(chi2inv(alpha/2,dof));
ci=[low_lim upp_lim];

%  ASSIGN VALUES TO SMEVSPEC, and FULL_CI
smevspec(:,i) = smspec;
full_ci(:,(i*2-1):(i*2)) = ci;

end                                     % END OF LARGE LOOP

ci = full_ci;

% PLOT in 3-D,
center = time_1+(t*(blk_len-1))/2;
y_3d = [center:t*os:center+(t*os*(num_blks-1))];
surf(f,y_3d,log10(smevspec)');
axis([0 0.5*f(length(f)) min(y_3d) max(y_3d) min(min(log10(smevspec))) max(max(log10(smevspec)))]);

xlabel('Freq. (cyc/samp. unit)');
ylabel('Mean Age');
zlabel('Log(Power Spectral Density)');
title(str);
view(0,90);
```

evspec2

```
function [smevspec,f,coord,ci,bw] =
evspec2(y,blk_len,os,t,treat,w_type,alpha,filter_type,half_filt,str,num_blks,time_1)

% EVSPEC2
% [smevspec,f,coord,ci,bw] =
evspec2(y,blk_len,os,t,treat,w_type,alpha,filter_type,half_filt,str,num_blks,time_1);
%
%       Calculates an evolving variance spectrum for column vector y
%       with equally-spaced sampling interval t. A spectrum is
```

```
%         calculated for each segment of the time series, y, of length
%         blk_len.  Successive segments are offset by the number
%         of points defined by the parameter os.  The number of
%         spectra calculated is defined by num_blks. The number
%         of points in the time series, y, must be greater than or equal
%         to ((os * num_blks) + blk_len - os).
%         Needs smoothing filter type and half width defined.
%       The title for plots is in variable str.
%      Calculates (1-alpha) confidence intervals.
%         The input parameter "treat" refers to data pretreatment.
%         Treatment applies to each segment individually.
%       treat=0 : do nothing
%      treat=1 : apply a data window (input type in "w_type")
%      treat=2 : linear detrend the time series based on
%              connecting endpoints (reduces leakage).
%         treat=3 : prewhiten and post color (reduces leakage)
%
%         w_type is the type of data window (e.g. Bartlett)
%         time_1 is the age of the first sample.
%
%         Outputs the smoothed evolving spectra (smevspec), frequency vector (f),
%         confidence intervals (ci), and band width (bw).
%         "Coord" contains the indices of independent estimates.
%
%         This function is identical to EVSPEC except each segment is
%         normalized to have mean = 0 and variance = 1;
%
%         See also FFTSPEC, FFTSPEC2, XSPEC, XSPEC2, and EVSPEC

% ERROR message
if nargin < 12,
  error('EVSPEC2 requires twelve input arguments.');
end

ts = y;                    % Assign new variable name to whole time series. Avoid renaming in code.
N = blk_len;               % Avoid renaming in code.
txt_title = str;
start = -os+1;

% GET FILTER
HF = 2*half_filt+1;
filter = eval([filter_type,'(' num2str(HF) ')']);
filter = filter/sum(filter);

% FREQUENCY
delf=1/(N*t);
f = [delf:delf:1/(2*t)-delf]';

% CALCULATE THE CENTER FREQUENCIES for the smoothed spectra
coord=[HF:HF:length(f)];
f2=f([coord]);

% DEGREES OF FREEDOM and BAND WIDTH
I = sum(filter.*filter);
%bw = 1/(N*I)
bw = 1/(N*t*I)
dof = round(2/I)
```

```
% ASSIGN FINAL MATRIX SIZES
smevspec = zeros(size(f):num_blks);
full_ci = zeros(size(f):2*num_blks);

%************************************************************
% BEGIN LARGE LOOP, RETURN TO HERE FOR SUBSEQUENT SEGMENTS
for i = 1:num_blks;
 i                                  % write segment number to screen
 start = start+os;
 end_seg = start + blk_len - 1;
 y = ts(start:end_seg);

% REMOVE THE MEAN FROM THE TIME SERIES
y=(y-mean(y))./std(y);

% DATA WINDOWING
if treat==1
  win_type=w_type;
  window=eval([win_type,'(' num2str(N) ')']);
  window=window/(sum(window)/N);
  y=y.*window;

% LINEAR DETREND, detrends by connecting endpoints to reduce leakage
% from low to high frequencies
elseif treat==2
 slope=(y(N)-y(1))/N;
 intercept=y(1);
 B = [intercept;slope];
% xtemp=[ones(1,N);[t:t:N*t]]';
 xtemp=[ones(1,N);[1:1:N]]';
 yest=xtemp*B;                  % N by 1
 y=y-yest;

% PREWHITEN USING FIRST DIFFERENCE
elseif treat==3
y2=ones(1,N);
 for j=2:N
  y2(j)=y(j)-y(j-1);
 end
 y2(1)=y2(2);              % set 1st value = second value
 y=y2;
end

% CALCULATE SPECTRUM
Y=fft(y);
% This runs from the first Fourier frequency to the Nyquist,
% not including 0 (after next line).
Y=Y(2:N/2)/N;
spec=2*N*t*abs(Y).^2;

clf
plot(f,spec);

% FILTER THE SPECTRUM (SMOOTHING)
smspec=conv(spec,filter);
smspec=smspec(half_filt+1:length(smspec)-half_filt);

% POST-COLOR
```

```
if treat==3;
 Hf=2*exp(i*pi*(1/2-f)).*sin(pi.*f);
 Gf=2*sin(pi.*f);
 smspec=smspec./(conj(Gf).*Gf)';
end

% PLOT SMOOTHED SPECTRUM
plot(f2,smspec([coord]));
title(txt_title);

% CONFIDENCE INTERVALS
low_lim=smspec*dof./(chi2inv(1-alpha/2,dof));
upp_lim=smspec*dof./(chi2inv(alpha/2,dof));
ci=[low_lim upp_lim];

% ASSIGN VALUES TO SMEVSPEC, and FULL_CI
smevspec(:,i) = smspec;
full_ci(:,(i*2-1):(i*2)) = ci;

end                                     % END OF LARGE LOOP

ci = full_ci;

% PLOT in 3-D,
center = time_1+(t*(blk_len-1))/2;
y_3d = [center:t*os:center+(t*os*(num_blks-1))];
surf(f,y_3d,log10(smevspec)');
axis([0 0.5*f(length(f)) min(y_3d) max(y_3d) min(min(log10(smevspec))) max(max(log10(smevspec)))]);

xlabel('Freq. (cyc/samp. unit)');
ylabel('Mean Age');
zlabel('Log(Power Spectral Density)');
title(str);
view(0,90);
```

xspec

```
function [smspecx,smspecy,f,coord,ci,bw,Cxy,Gain,fullgain,ph,ciph] =
xspec(x,y,N,t,treat,alpha,cohalpha);

% XSPEC
% [smspecx,smspecy,f,coord,ci,bw,Cxy,Gain,fullgain,ph,ciph] = xspec(x,y,N,t,treat,alpha,cohalpha);
%
%       Calculates a variance cross-spectrum for column vectors x and y with
%       length N and equally-spaced sampling interval t.  Asks for
%       smoothing filter half-width and type.  Calculates (1-alpha) % confidence
%       interval for spectra and (1-cohalpha) confidence level for coherence .
%       "treat" is same parameter as in fftspec. (optional data treatment)
%       treat=0 : do nothing
%       treat=1 : apply a data window (will ask for type)
%       treat=2 : linear detrend the time series based on
%                 connecting endpoints (reduces leakage).
%       treat=3 : prewhiten and post color the time series (reduce leak.)
%
%       Outputs the smoothed spectra (smspecx,smspecy), frequency vector (f),
%       confidence intervals (ci, four columns which are lower and upper
```

```
%       confidence limits for x, then for y), band width (bw),
%       coherence (Cxy), Gain, fullgain (symmetrical about Nyquist),
%     and phase (ph).
%       coord contains the indices of f close to the Fourier frequencies
%       given ensemble averaging (independent spectral estimates)
%       Plots smoothed spectra on log-linear scale, coherence, phase,
%       and gain.
%
%       See also, FFTSPEC, FFTSPEC2, XSPEC2, and GAIN

% ERROR message
if nargin < 7,
  error('XSPEC requires seven input arguments.');
end

% REMOVE THE MEAN FROM THE TIME SERIES
x1=x-mean(x);
y1=y-mean(y);

% DATA WINDOWING
if treat==1
   win_type=input('Input data windowing type: ','s');
   window=eval([win_type,'(' num2str(N) ')']);
   window=window/(sum(window)/N);
   x1=x1.*window;
   y1=y1.*window;

% LINEAR DETREND, detrends by connecting endpoints to reduce leakage
%  from low to high frequencies
elseif treat==2
  slopey=(y1(N)-y1(1))/N;
  slopex=(x1(N)-x1(1))/N;
  interceptx=x(1);
  intercepty=y(1);
  By = [intercepty;slopey];
  Bx = [interceptx;slopex];
  xtemp=[ones(1,N);[1:1:N]]';
  yest=xtemp*By;                    % N by 1
  xest=xtemp*Bx;                    % N by 1
  y1=y1-yest;
  x1=x1-xest;

% PREWHITEN USING FIRST DIFFERENCE
elseif treat==3
x2=ones(1,N);
y2=ones(1,N);
  for j=2:N
    x2(j)=x1(j)-x1(j-1);
    y2(j)=y1(j)-y1(j-1);
  end
  x2(1)=x2(2);              % set 1st value = second value
  x1=x2;
  y2(1)=y2(2);              % set 1st value = second value
  y1=y2;
end

% CALCULATE SPECTRA
% Xx1 runs from 0 to 2*Nyq; Xx runs from 1/(N*t) to Nyq-1 freq.
```

```
Xx1=fft(x1,N)/N;
Xx=Xx1(2:N/2);
Yy1=fft(y1,N)/N;
Yy=Yy1(2:N/2);

% POWER SPECTRAL DENSITY
% EITHER...
%specx=2*N*t*conj(Xx).*Xx;
%specy=2*N*t*conj(Yy).*Yy;
% OR...
Pxx1=2*N*t*abs(Xx1).^2;
Pyy1=2*N*t*abs(Yy1).^2;
Pyy=2*N*t*abs(Yy).^2;
Pxx=2*N*t*abs(Xx).^2;

% FREQUENCY
delf=1/(N*t);
f = [delf:delf: 1/(2*t)-delf]';

% PLOT
figure;
orient tall;
axes('position',[0.18 0.60 0.64 0.33]);
plot(f,Pxx);
hold on
plot(f,Pyy,'--');
hold off

% DEFINE FILTER
half_filt = input('Input half filter width: ');
filter_type = input('Input filter type: ', 's');
txt_title = input('Input title for plots: ','s');
HF = 2*half_filt+1;
filter = eval([filter_type,'(' num2str(HF) ')']);
filter = filter/sum(filter);

% FILTER THE SPECTRA (SMOOTHING)
smspecx=conv(Pxx,filter);
smspecx=smspecx(half_filt+1:length(smspecx)-half_filt);
smspecy=conv(Pyy,filter);
smspecy=smspecy(half_filt+1:length(smspecy)-half_filt);

% CALCULATE THE CENTER FREQUENCIES for the smoothed spectra
% CHECK THIS OUT FOR WINDOWS OTHER THAN BOXCAR
coord=[HF:HF:length(f)];
f2=f([coord]);

% POST-COLOR
if treat==3;
 Hf=2*exp(i*pi*(1/2-f)).*sin(pi.*f);
 Gf=2*sin(pi.*f);
 smspecx=smspecx./(conj(Gf).*Gf)';
 smspecy=smspecy./(conj(Gf).*Gf)';
end

%PLOT SMOOTHED SPECTRA
semilogy(f,smspecx);
hold on
```

```
semilogy(f,smspecy,'-.');
ylabel('Estimated PSD');
title(txt_title);

% DEGREES OF FREEDOM and BAND WIDTH,
I = sum(filter.*filter);
bw = 1/(N*t*I)
dof = round(2/I)

%PLOT BANDWIDTH
temp=max([0.85*max(smspecx);0.8*max(smspecy)]);
k=coord(round(length(coord)*3/4));
mid=[f(k) smspecx(k)];
bwdat=[f(k) temp;f(k)+bw temp];
bwleft=[f(k) temp+(0.02*max(smspecx));f(k) temp-(0.02*max(smspecx))];
bwrt=[f(k)+bw temp+(0.02*max(smspecx));f(k)+bw temp-(0.02*max(smspecx))];
semilogy(bwdat(:,1),bwdat(:,2),'-');
semilogy(bwleft(:,1),bwleft(:,2),'-');
semilogy(bwrt(:,1),bwrt(:,2),'-');
text(f(k+10)+bw,temp,'Band Width');

% PLOT CONFIDENCE INTERVALS
low_limx=smspecx*dof./(chi2inv(1-alpha/2,dof));
upp_limx=smspecx*dof./(chi2inv(alpha/2,dof));
cix=[low_limx upp_limx];
low_limy=smspecy*dof./(chi2inv(1-alpha/2,dof));
upp_limy=smspecy*dof./(chi2inv(alpha/2,dof));
ciy=[low_limy upp_limy];
ci=[cix,ciy];

xpos=k;
ypos=round(N/10);
cibarx=[f(xpos) low_limx(xpos);f(xpos) smspecx(xpos);f(xpos) upp_limx(xpos)];
citopx=[f(xpos-3) upp_limx(xpos);f(xpos+3) upp_limx(xpos)];
cibotx=[f(xpos-3) low_limx(xpos);f(xpos+3) low_limx(xpos)];
cibary=[f(ypos) low_limy(ypos);f(ypos) smspecy(ypos);f(ypos) upp_limy(ypos)];
citopy=[f(ypos-3) upp_limy(ypos);f(ypos+3) upp_limy(ypos)];
ciboty=[f(ypos-3) low_limy(ypos);f(ypos+3) low_limy(ypos)];
semilogy(mid(:,1),mid(:,2),'o');
semilogy(cibarx(:,1),cibarx(:,2),'-');
semilogy(citopx(:,1),citopx(:,2),'-');
semilogy(cibotx(:,1),cibotx(:,2),'-');
semilogy(citopy(:,1),citopy(:,2),'-');
semilogy(ciboty(:,1),ciboty(:,2),'-');
semilogy(cibary(:,1),cibary(:,2),'-.');
conf=([num2str(1-alpha) ' %CI']);
text(f(xpos+9),(upp_limx(xpos)-0.25*(upp_limx(xpos)-low_limx(xpos))),conf);
hold off

% CROSS SPECTRAL DENSITY
% REAL PART IS CO-SPECTRUM, IMAG PART IS QUADRATURE SPECTRUM
Pxy = 2*N*t*Yy.*conj(Xx);
Pxy1 = 2*N*t*Yy1.*conj(Xx1);

% SMOOTH CROSS SPECTRUM
smPxy=conv(Pxy,filter);
smPxy=smPxy(half_filt+1:length(smPxy)-half_filt);
```

```
% POST-COLOR CROSS SPECTRUM
if treat==3;
  smPxy=smPxy./(conj(Gf).*Gf)';
end

% CALCULATE SQUARED COHERENCY SPECTRUM
Cxy=(smPxy.*conj(smPxy))./(smspecx.*smspecy);

%  PLOT
axes('position',[0.18 0.42 0.64 0.14]);
%plot(f2,Cxy([coord])), grid;
plot(f,Cxy), grid;
axis([0 1/(2*t) 0 1]);
ylabel('Coh.^2');
hold on

%CUTOFF COHERENCE LEVEL
%K=(1-cohalpha^(2/(dof-2)))^0.5;
K=(1-cohalpha^(2/(dof-2)))
Kdat=[0 K; 1/(2*t) K];
plot(Kdat(:,1),Kdat(:,2),'-');
text(1/(2*t)+0.02*(1/(2*t)),K,[num2str(1-cohalpha)]);
text(1/(2*t)+0.02*(1/(2*t)),K-0.12,'Conf. level');

% PHASE. POSITIVE PHASE MEANS THAT THE Y (second) TIME SERIES LEADS
% IF time goes forward.  IF time goes backward, as in most geological
% time series, then positive phase means that the X(first) t.s. leads.
% These two lines give the exact same result as the following two lines
%  EXCEPT in the case of ph = 180, when you get ph = 0 instead.
ph = angle(smPxy);
ph = ph * (180/pi);
ph2=ph([coord]);

% FIND COHERENT FREQUENCIES TO PLOT PHASE CIs
coord2=[find(Cxy>=K)];

% PLOT PHASE
axes('position',[0.18 0.24 0.64 0.14]);
plot(f([coord2]),ph([coord2]),'o'), grid;
axis([0 1/(2*t) -180 180]);
%xlabel('Frequency (cycles/sampling unit)');
ylabel('Phase (degrees)');

% CALCULATE CONFIDENCE INTERVALS FOR PHASES
temp=Cxy;
%  Using the chi2 distribution
%delph=asin(sqrt((1/(dof-2))*((1-temp)./temp)*chi2inv((1-cohalpha),2)));

% OR, using the F distribution, USE THIS
delph=asin(sqrt((2/(dof-2))*((1-temp)./temp)*finv((1-cohalpha),2,(dof-2))));

delph=real(delph)*(180/pi);
low_ph=ph-delph;
upp_ph=ph+delph;
ciph=[low_ph,upp_ph];

% PLOT CIs
hold on
```

```
half=1/(2*t)/100;
for i=1:length(coord2)
 j=coord2(i);
 plot([f(j);f(j)],[low_ph(j);upp_ph(j)])
 plot([f(j)-half;f(j)+half],[low_ph(j);low_ph(j)])
 plot([f(j)-half;f(j)+half],[upp_ph(j);upp_ph(j)])
end

% GAIN, used smoothed smPxx and smPxy to calculate gain.
smPxx=conv(Pxx,filter);
smPxx=smPxx(half_filt+1:length(smPxx)-half_filt);

% POST-COLOR smPxx
if treat==3;
 smPxx=smPxx./(conj(Gf).*Gf)';
end

Gain=abs(smPxy./smPxx);
fullgain=abs(Pxy1./Pxx1);
axes('position',[0.18 0.06 0.64 0.14]);
semilogy(f([coord]),Gain([coord])),grid;
axis([0 1/(2*t) (min(Gain)-0.25*min(Gain)) 1]);
ylabel('Gain')
xlabel('Frequency (cycles/sampling unit)');
```

xspec2

```
function [smspecx,smspecy,f,coord,ci,bw,Cxy,coord2,Gain,fullgain,ph,ciph] =
xspec2(x,y,N,t,treat,w_type,alpha,cohalpha,filter_type,half_filt,str);

% XSPEC2
% [smspecx,smspecy,f,coord,ci,bw,Cxy,coord2,Gain,fullgain,ph,ciph] =
%       xspec2(x,y,N,t,treat,w_type,alpha,cohalpha,filter_type,half_filt,str);
%
%       Calculates a variance cross-spectrum for column vectors x and y with
%       length N and equally-spaced sampling interval t.  Needs
%       smoothing filter half-width and type.  STR is a title string for
%       plots.  Calculates (1-alpha) % confidence
%       interval for spectra and (1-cohalpha) confidence level for coherence.
%       The input parameter "treat" refers to data pretreatment.
%     treat=0 : do nothing
%     treat=1 : apply a data window (will ask for type)
%     treat=2 : linear detrend the time series based on
%           connecting endpoints (reduces leakage).
%     treat=3 : prewhiten and post color (reduce leakage)
%
%     w_type is the type of data window (e.g. Bartlett)
%
%       Outputs the smoothed spectra (smspecx,smspecy), frequency vector (f),
%       confidence intervals (ci, four columns which are lower and upper
%       confidence limits for x, then for y), band width (bw),
%       coherence (Cxy), Gain, fullgain (symmetrical about Nyquist),
%     phase (ph), and (1-alpha) CIs for phase at indices in coord2.
%   Positive phase means the first time series (x) leads (for
%   geological time series).
%       Vector "coord" contains the indices of f closest to the Fourier
```

```
%        frequencies given ensemble averaging.
%      Vector "coord2" contains the indices of f for Coherence^2
%      greater than the 1-cohalpha cutoff.
%        Plots smoothed spectra on log scale, coherence and phase.
%
%        See also, FFTSPEC, FFTSPEC2, XSPEC, xtract_Milank and GAIN

% ERROR message
if nargin < 11,
  error('XSPEC2 requires eleven input arguments.');
end

% REMOVE THE MEAN FROM THE TIME SERIES
x1=x-mean(x);
y1=y-mean(y);

% DATA WINDOWING
if treat==1
   win_type=w_type;
   window=eval([win_type,'(' num2str(N) ')']);
   window=window/(sum(window)/N);
   x1=x1.*window;
   y1=y1.*window;

% LINEAR DETREND, detrends by connecting endpoints to reduce leakage
%  from low to high frequencies
elseif treat==2
  slopey=(y1(N)-y1(1))/N;
  slopex=(x1(N)-x1(1))/N;
  interceptx=x(1);
  intercepty=y(1);
  By = [intercepty;slopey];
  Bx = [interceptx;slopex];
  xtemp=[ones(1,N);[1:1:N]]';
  yest=xtemp*By;                  % N by 1
  xest=xtemp*Bx;                  % N by 1
  y1=y1-yest;
  x1=x1-xest;

% PREWHITEN USING FIRST DIFFERENCE
elseif treat==3
x2=ones(1,N);
y2=ones(1,N);
  for j=2:N
    x2(j)=x1(j)-x1(j-1);
    y2(j)=y1(j)-y1(j-1);
  end
  x2(1)=x2(2);             % set 1st value = second value
  x1=x2;
  y2(1)=y2(2);             % set 1st value = second value
  y1=y2;
end

% CALCULATE SPECTRA
Xx1=fft(x1,N)/N;
Xx=Xx1(2:N/2);
Yy1=fft(y1,N)/N;
Yy=Yy1(2:N/2);
```

```
% POWER SPECTRAL DENSITY
Pyy1=2*N*t*abs(Yy1).^2;
Pxx1=2*N*t*abs(Xx1).^2;
Pyy=2*N*t*abs(Yy).^2;
Pxx=2*N*t*abs(Xx).^2;

% FREQUENCY
delf=1/(N*t);
f = [delf:delf:1/(2*t)-delf]';

% PLOT
clf
orient tall;
subplot(2,1,1)                                        % simpler plotting
lim=round(length(f)/2);
plot(f(1:lim),Pxx(1:lim));  % shorten x axis
hold on
plot(f(1:lim),Pyy(1:lim));  % shorten x axis
hold off

txt_title = str;
HF = 2*half_filt+1;
filter = eval([filter_type,'(' num2str(HF) ')']);
filter = filter/sum(filter);

% FILTER THE SPECTRA (SMOOTHING)
smspecx=conv(Pxx,filter);
smspecx=smspecx(half_filt+1:length(smspecx)-half_filt);
smspecy=conv(Pyy,filter);
smspecy=smspecy(half_filt+1:length(smspecy)-half_filt);

% CALCULATE THE CENTER FREQUENCIES for the smoothed spectra
% CHECK THIS OUT FOR WINDOWS OTHER THAN BOXCAR
coord=[HF:HF:length(f)];
f2=f([coord]);

% POST-COLOR
if treat==3;
 Hf=2*exp(i*pi*(1/2-f)).*sin(pi.*f);
 Gf=2*sin(pi.*f);
 smspecx=smspecx./(conj(Gf).*Gf)';
 smspecy=smspecy./(conj(Gf).*Gf)';
end

%PLOT SMOOTHED SPECTRA
%%semilogy(f([coord]),smspecx([coord]));   % PLOT ONLY CENTER FREQS
semilogy(f(1:lim),smspecx(1:lim));         % PLOT ALL FREQS
hold on
%%semilogy(f([coord]),smspecy([coord]),'-.');        % PLOT ONLY CENTER FREQS
semilogy(f(1:lim),smspecy(1:lim),'-.');              % PLOT ALL FREQS
axis([0 1/(4*t) 0.12 200]);
xlabel('Frequency (cycles/sampling unit)');
ylabel('Estimated PSD');
title(txt_title);

% DEGREES OF FREEDOM and BAND WIDTH,
I = sum(filter.*filter);
```

```
bw = 1/(N*t*I)
dof = round(2/I)

%PLOT BANDWIDTH
temp=max([0.85*max(smspecx);0.8*max(smspecy)]);
k=coord(round(length(coord)*1/3));
mid=[f(k) smspecx(k)];
bwdat=[f(k) temp;f(k)+bw temp];
bwleft=[f(k) temp+(0.02*max(smspecx));f(k) temp-(0.02*max(smspecx))];
bwrt=[f(k)+bw temp+(0.02*max(smspecx));f(k)+bw temp-(0.02*max(smspecx))];
semilogy(bwdat(:,1),bwdat(:,2),'-');
semilogy(bwleft(:,1),bwleft(:,2),'-');
semilogy(bwrt(:,1),bwrt(:,2),'-');
text(f(k+10)+bw,temp,'Band Width');

% PLOT CONFIDENCE INTERVALS
low_limx=smspecx*dof./(chi2inv(1-alpha/2,dof));
upp_limx=smspecx*dof./(chi2inv(alpha/2,dof));
cix=[low_limx upp_limx];
low_limy=smspecy*dof./(chi2inv(1-alpha/2,dof));
upp_limy=smspecy*dof./(chi2inv(alpha/2,dof));
ciy=[low_limy upp_limy];
ci=[cix,ciy];

xpos=k;
ypos=round(N/10);
cibarx=[f(xpos) low_limx(xpos);f(xpos) smspecx(xpos);f(xpos) upp_limx(xpos)];
citopx=[f(xpos-3) upp_limx(xpos);f(xpos+3) upp_limx(xpos)];
cibotx=[f(xpos-3) low_limx(xpos);f(xpos+3) low_limx(xpos)];
cibary=[f(ypos) low_limy(ypos);f(ypos) smspecy(ypos);f(ypos) upp_limy(ypos)];
citopy=[f(ypos-3) upp_limy(ypos);f(ypos+3) upp_limy(ypos)];
ciboty=[f(ypos-3) low_limy(ypos);f(ypos+3) low_limy(ypos)];
semilogy(mid(:,1),mid(:,2),'o');
semilogy(cibarx(:,1),cibarx(:,2),'-');
semilogy(citopx(:,1),citopx(:,2),'-');
semilogy(cibotx(:,1),cibotx(:,2),'-');
semilogy(citopy(:,1),citopy(:,2),'-');
semilogy(ciboty(:,1),ciboty(:,2),'-');
semilogy(cibary(:,1),cibary(:,2),'-.');
conf=([num2str((1-alpha)*100) ' %CI']);
text(f(xpos+9),(upp_limx(xpos)-0.25*(upp_limx(xpos)-low_limx(xpos))),conf);
hold off

% CROSS SPECTRAL DENSITY
% REAL PART IS CO-SPECTRUM, IMAG PART IS QUADRATURE SPECTRUM
Pxy = 2*N*t*Yy.*conj(Xx);
Pxy1 = 2*N*t*Yy1.*conj(Xx1);

% SMOOTH CROSS SPECTRUM
smPxy=conv(Pxy,filter);
smPxy=smPxy(half_filt+1:length(smPxy)-half_filt);

% POST-COLOR CROSS SPECTRUM
if treat==3;
  smPxy=smPxy./(conj(Gf).*Gf)';
end

% CALCULATE SQUARED COHERENCY SPECTRUM
```

```
Cxy=(smPxy.*conj(smPxy))./(smspecx.*smspecy);

% PLOT
subplot(4,1,3)                                  % simpler plotting
%%plot(f2,Cxy([coord])), grid;            % PLOT ONLY CENTER FREQS
plot(f(1:lim),Cxy(1:lim)), grid;          % PLOT ALL FREQS
axis([0 1/(4*t) 0 1]);
ylabel('Coh.^2');
hold on

%CUTOFF COHERENCE LEVEL
%K=(1-cohalpha^(2/(dof-2)))^0.5;
K=(1-cohalpha^(2/(dof-2)));
K
Kdat=[0 K; f(N/2-1) K];
plot(Kdat(:,1),Kdat(:,2),'-');
text(f(N/4-1)+0.02*(f(N/4-1)),K,[num2str(1-cohalpha)]);
text(f(N/4-1)+0.02*(f(N/4-1)),K-0.12,'Conf. level');

% PHASE. POSITIVE PHASE MEANS THAT THE X (the first) TIME SERIES LEADS
ph = angle(smPxy);
ph = ph * (180/pi);
ph2=ph([coord]);

% FIND COHERENT FREQUENCIES TO PLOT PHASE CIs
coord2=[find(Cxy>=K)];

% PLOT PHASE
subplot(4,1,4);                                 % simpler plotting
plot(f([coord2]),ph([coord2]),'o'), grid;
axis([0 1/(4*t) -180 180]);
ylabel('Phase (degrees)');
xlabel('Frequency (cycles/sampling unit)');

% CALCULATE CONFIDENCE INTERVALS FOR PHASES
temp=Cxy([coord2]);
% using the F distribution,
delph=asin(sqrt((2/(dof-2))*((1-temp)./temp)*finv((1-cohalpha),2,(dof-2))));

delph=real(delph)*(180/pi);
low_ph=ph([coord2])-delph;
upp_ph=ph([coord2])+delph;
ciph=[low_ph,upp_ph];

% PLOT CIs
hold on
half=1/(4*t)/100;
for i=1:length(coord2)
 j=coord2(i);
 plot([f(j);f(j)],[low_ph(i);upp_ph(i)])
 plot([f(j)-half;f(j)+half],[low_ph(i);low_ph(i)])
 plot([f(j)-half;f(j)+half],[upp_ph(i);upp_ph(i)])
end

% GAIN, used smoothed smPxx and smPxy to calculate gain.
smPxx=conv(Pxx,filter);
smPxx=smPxx(half_filt+1:length(smPxx)-half_filt);
```

```
% POST-COLOR smPxx
if treat==3;
  smPxx=smPxx./(conj(Gf).*Gf)';
end

% DON'T PLOT GAIN
Gain=abs(smPxy./smPxx);
fullgain=abs(Pxy1./Pxx1);
```

xtract_Milank

```
function [Milank] = xtract_Milank(f,Cxy,ph,ciph,bw,coord2);

% xtract_Milank
%        [Milank] = xtract_Milank(f,Cxy,ph,ciph,bw,coord2);
%
%        Extracts Milankovitch frequencies, coherences,
%        phase, and phase confidence intervals w/in bw, using
%        output from XSPEC2.
%        Output matrix, Milank, contains frequency f,
%        period, coherence, phase, 2 columns for phase
%        confidence intervals (1-alpha), and the phase error,
%        which is the difference between columns 4 and 5.
%        If columns 5 and 6 are = 0, then the coherence is below
%        1-coalpha confidence level.

% ERROR message
if nargin < 6,
  error('XTRACT_MILANK requires six input arguments.');
end

fMil=[1/100, 1/41, 1/23, 1/19];

% GET COORDINATES OF DESIRED FREQUENCIES, W/IN ONE BANDWIDTH
i100=find(f>=(fMil(1)-bw/2) & f<=(fMil(1)+bw/2));
i41=find(f>=(fMil(2)-bw/2) & f<=(fMil(2)+bw/2));
i23=find(f>=(fMil(3)-bw/2) & f<=(fMil(3)+bw/2));
i19=find(f>=(fMil(4)-bw/2) & f<=(fMil(4)+bw/2));

iall=[i100;i41;i23;i19];

% GET ciph COORDINATES
j=zeros(1,length(iall));
xciph=zeros(length(iall),2);
for k = 1:length(iall),
  if (find(f([coord2])==f(iall(k)))) ~= []
  j(k)=find(f([coord2])==f(iall(k)));
  end
end

for k = 1:length(iall),
  if j(k) ~= 0,
    xciph(k,:)=ciph(j(k),:);
  end
end
```

```
pherr = abs(xciph(:,1)-ph(iall));

Milank=[f(iall),1./f(iall),Cxy(iall),ph(iall),xciph,pherr];
```

Appendix B

FORTRAN Code for Ocean Drilling Program Leg 154 Reflectance Data Processing

OUTLINE

The four programs included in this appendix are the basic programs used to process Leg 154 reflectance spectroscopy data from the OSU-SCAT, as described in Chapter 2. The programs are:

writeraw.odp
Reads ascii data output from the PC and writes data in direct access binary format.

polycoefs2.ave
Processes standard runs and calculates ball corrections based on average standards.

reffixpl.odp
Calculates final %reflectance for 1024 channels.

band_avg154.lis
Calculates average bands (typically 10 nm) and centered first derivatives.

PROGRAMS

writeraw.odp.f

```
      program write

c     Program write converts .dat files from dos to UNIX
c     Writes .raw files and .id files as Direct Access
c      files.  12-21-93.
c     Reads ODP depth reference files and adds mbsf depths to .raw and .id files
c     SEH. Last Modified 12-94.

c      los=length of section; dis=depth in section (cm);
c      (dic=depth in core); exp= exposure time; int=# of integrations
c      m=slope of lambda eqn.; b=intercept of lambda eqn.;
c      mark=error flag; light=light intensity; strain=strain;
c      cond=conductivity; dis1=real dis value for reading PC file,units are m.
c      mbsf=meters below sea floor.

c     NWRD SHOULD BE 10299
c     IWRD SHOULD BE 24
c     NOTE: the positions of light and cond should be switched for clarity.
c     Order should be cond, strain, light.
c     NOTE: dis currently set to topdep + 1 cm.  This should change if spot
c     size changes. (See line 162)


              parameter (pts=1024,nwrd=10299,iwrd=24)
              character*80 datfile,rawfile,cmd
c      character*80 idfile
```

```
                 character*20 prefix
                 integer*4 date,time,white(pts),sample(pts)
                 integer*2 black(pts)
      integer*2 los,int,leg,count,los1
                 integer*2 site,core,section,topdep,botdep,mark
                 integer*2 dis,light,strain,cond
                 integer*2 mon,day,yr,hr,min,sec
                 real*4 m,b,exp,step
      real*4 mbsf
      real dis1
                 integer asite,acore,system
                 character*1 hole,type,sub,ahole,atype,refsect
                 character*1 charsect
                 integer system

7     write(6,*) 'Enter 1 to process a single file OR'
                 write(6,*) '       2 to process all sections of a corc'
                 read(5,*)inum

c-------OPEN ONE FILE TO READ
                 if (inum.eq.1) then
8                  write(6,*) 'Enter file prefix e.g.925a01h1'
                   read(5,'(a)')prefix
                   datfile=prefix(1:lenstr(prefix))//'.dat'
                   rawfile=prefix(1:lenstr(prefix))//'.raw'
c                  idfile=prefix(1:lenstr(prefix))//'.id'
                   go to 14

c------OR CREATE AND READ FILENAMES FROM A LIST OF .DAT FILES, filename "temp2"
            elseif (inum.eq.2) then
12                 write(6,*) 'Enter siteholecoretype, e.g. 925a01h'
                   read(5,'(a)')prefix
                   cmd='ls '//prefix(1:lenstr(prefix))//'*.dat >! temp2'
                   ier = system(cmd)
                   write(6,'("ier = ",i7)')ier
                   open(10,file='temp2',status='old',err=7)
      else
                   go to 7
      endif

13          read(10,'(a)',end=1000)datfile
            rawfile=datfile(1:(lenstr(datfile)-4))//'.raw'
c           idfile=datfile(1:(lenstr(datfile)-4))//'.id'
                   write(6,'(a)')datfile

c-----DOS2UNIX
14               ier = system('dos2unix '//datfile//'temp')
                 write(6,'("ier = ",i7)')ier
                 ier = system('mv temp '//datfile)
                 write(6,'("ier = ",i7)')ier

                 open(11,file=datfile,access='sequential',status='old',err=7)
     open(12,file=rawfile,status='unknown',access=
```

```
    +    'direct',recl=nwrd)
c                    open(13,file=idfile,status='unknown',access=
c    +    'direct',recl=iwrd)

c-------OPEN DEPTHS FILE
      open(21,file='corelog.depths',status='old',err=9)
                    go to 10
9      write(6,*)'ERROR: cannot find file corelog.depths'
       write(6,*)'File not written'
                    go to 1000

c-------READ HEADER INFO
c  CHECK TO SEE WHY THE FORMAT OF THE FIRST LINE CHANGED!!
c10                  read(11,'(27x,i2,1x,i2,3x,3(i2,1x),i2,26x,i3)')mon,
c    +      day,yr,hr,min,sec,los
10                   read(11,'(27x,i2,1x,i2,3x,3(i2,1x),i2,21x,i3)')mon,
    +      day,yr,hr,min,sec,los
c                    read(11,*)
       read(11,'(15x,f4.1,12x,f4.1,16x,i3,9x,f6.3,12x,f6.1)')
    +      exp,step,int,m,b

c-------FORMATS
40      format(i3,1x,a1,1x,i4,1x,a1,i4,1x,a1,i3,2i6,
    +         f7.2,2i6,i6)
50     format(4x,1024i6)
60      format(i4,1x,a1,1x,i3,1x,a1,2x,a1,1x,i3,f8.2)

c-------CALCULATE DATE AND TIME
      date=(mon*10000)+(day*100)+yr
                    time=(hr*10000)+(min*100)+sec

c-------READ SAMPLE ID STRING AND DATA
       count=1
                    mark=0
15     read(11,fmt=40,end=999)leg,sub,site,hole,core,type,
    +    section,topdep,botdep,dis1,light,strain,cond

c-------TRANSFORM SECTION TO CHARACTER, system# for '1' = 49
      charsect = char(48+section)

c-------ADD MBSF DEPTH
21    read(21,fmt=60,end=1000)asite,ahole,acore,atype,refsect,
    +    los1,depth

c-----CHECK SITE AND HOLE
      if (asite.ne.site.or.ahole.ne.hole) then
       write(6,*)'Wrong depth file. Check site and hole'
        go to 1000
      endif

c-----FIND CORRECT CORE AND SECTION
      if (acore.lt.core) then
        go to 21
```

```
      elseif (acore.eq.core) then

c------CORE CATCHERS
          if (refsect.eq.'C'.and.charsect.eq.'C') then
             mbsf=(0.01*topdep) + depth + .01
             backspace(21)
              go to 100
           endif

          if ((refsect.eq.'C'.and.charsect.eq.'1').or.
     +         (refsect.lt.charsect)) then
             go to 21
          elseif (refsect.eq.charsect) then
            mbsf=(0.01*topdep) + depth + .01
            backspace(21)
             go to 100
          elseif (refsect.gt.charsect) then
            write(6,*)'Section not matched. Check both files'
             go to 1000
          elseif (refsect.eq.'c') then
             go to 21
           endif
      elseif (acore.gt.core) then
        write(6,*)'Core not matched. Check both files'
         go to 1000
      endif

c-------READ DATA
c100            dis=dis1*100.
100             dis=topdep + 1

      read(11,fmt=50)(black(i),i=1,pts)
c               read(11,*)
      read(11,fmt=50)(white(i),i=1,pts)
c               read(11,*)
                read(11,fmt=50)(sample(i),i=1,pts)

c     WRITE

                write(12,rec=count)date,time,los,exp,step,int,m,b,
     +     leg,sub,site,hole,core,type,section,topdep,
     +     botdep,dis,mbsf,light,strain,cond,mark,
     +     (black(i),i=1,pts),
     +     (white(i),i=1,pts),(sample(i),i=1,pts)

c               write(13,rec=count)count,leg,site,hole,core,type,
c    +     section,topdep,botdep,dis,mbsf,mark

                count=count+1
       go to 15
999     if(inum.eq.2)then
       write(6,'("Finished file:",a14)')datfile
                 go to 13
```

```
                        endif
1000     stop
                        end

c*************************************
                        INTEGER FUNCTION LENSTR(LINE)
                        CHARACTER*(*) LINE
                        num = len(line)
                        DO 5 I=num,1,-1
                        IF (LINE(I:I) .NE. ' ') GO TO 10
5       continue
                        i=0
10      lenstr=i
                        end
```

polycoefs2.ave.f

```
                        program polyc2

c       to calculate delta% for corrections to % reflectance values
c       using polynomial coefficients. Saves coefficients in file
c       "polycoefs.---"
c       SEH Last Modified 5-95

                        parameter (inum=4,pts=1024)
                        real*4 fin(pts,inum),del(pts,inum)
                        character*8 now
c---------------------------------------------------

        call correct1(now,fin)
                        call deltacal(fin,del)
                        call deltacor(fin,del,now)
1000    stop
                        end
c---------------------------------------------------
c   START OF SUBROUTINES
c---------------------------------------------------
        subroutine correct1(now,fin)

c       routine to apply correction to measurements of standards

                        parameter (nfile=200,inum=4,pts=1024)
                        character*80 filename,lisfile
                        character*8 now
                        integer*4 white(pts),raw(pts)
                        integer*2 black(pts),count,num(pts)
                        real*4 btemp(pts),wtemp(pts),rtemp(pts),sd(pts)
                        real*4 big(pts,inum,nfile),fin(pts,inum),k100(pts,nfile)
                        real*4 avewhite(pts),temp(pts,nfile),ans(pts)

c--------READ FILE LISTING STANDARD RUNS TO BE USED-------
7                       write(6,*)'Enter name of file containing list of ".dat"'
```

```
                  write(6,*)' standard run files to be used for corrections:'
                  read(5,'(a)')lisfile
                  open(41,file=lisfile,status='old',err=7)
                  count=0

10                read(41,'(a)',end=101)filename
     count=count+1
     go to 11

9    write(6,*)'FILE NOT FOUND. EXITING'
                  go to 1001

c------READ DATA FOR ALL FOUR STANDARDS
11                open(11,file=filename,status='old',err=9)
                  read(11,*)
                  read(11,*)

12    do 25 i=1,inum

41     format(/,4x,1024i6,/4x,1024i6,/4x,1024i6)
                   read(11,fmt=41)black,white,raw

c---------CONVERT TO FLOATING POINT
                  do 13 j=1,pts
                   btemp(j)=float(black(j))
                   wtemp(j)=float(white(j))
                   rtemp(j)=float(raw(j))
13    continue

c---------1ST CORRECTION---------------------
     do j=1,pts
                   big(j,i,count)=100.0*((rtemp(j)-btemp(j))/(wtemp(j)-btemp(j)))
                  enddo

25    continue

c------KEEP 100% measured standard values
                  do 26 i=1,pts
                   k100(i,count)=big(i,inum,count)
26    continue

                  close(11)
     go to 10

101   call sdcull(k100,avewhite,sd,num,count)

c------WRITE FILE 'AVERAGE.WHITE'
                  open(13,file='average.white',status='unknown')
                  do 102 i=1,pts
      write(13,'(i6,2f10.4,i6)')i,avewhite(i),sd(i),num(i)

102   continue
```

```
c-----CALCULATE 2,40,75 and 100% standards normalized to average 100%

      do 35 j=1,inum
                  do 34 k=1,pts
                   do 33 i=1,count
                    big(k,j,i)=big(k,j,i)/(0.01*avewhite(k))
c*****precision test
c                   open(51,file='junk',status='unknown')
c                   write(51,'(f10.2)')big(k,j,i)
c                   close(51)
c                   open(51,file='junk',status='unknown')
c                   read(51,'(f10.2)')temp(k,i)
c                   close(51)
c*******
                    temp(k,i)=big(k,j,i)
33                 continue
34     continue
c----- CALCULATE AVERAGE 2,40,75,and 100% STANDARDS (norm. to average white)
      call sdcull(temp,ans,sd,num,count)
                 if (j.eq.1) then
                   open(21,file='average.02',status='unknown')
                   write(21,'(i6,2f10.4,i6)')(l,ans(l),sd(l),num(l),l=1,pts)
      elseif (j.eq.2) then
                   open(22,file='average.40',status='unknown')
                   write(22,'(i6,2f10.4,i6)')(l,ans(l),sd(l),num(l),l=1,pts)
      elseif (j.eq.3) then
                   open(23,file='average.75',status='unknown')
                   write(23,'(i6,2f10.4,i6)')(l,ans(l),sd(l),num(l),l=1,pts)
      elseif (j.eq.4) then
                   open(24,file='average.100',status='unknown')
                   write(24,'(i6,2f10.4,i6)')(l,ans(l),sd(l),num(l),l=1,pts)
      endif
                 do n=1,pts
                  fin(n,j)=ans(n)
                 enddo

35    continue

         ier = system('date +%y%m%d%H >! tempnow')
         write (6,'("ier = ",i7)')ier
         open(32,file='tempnow',status='unknown')
         read(32,'(a)')now

1001   return
                 end
c--------------------------------------------------
c------------------------------------------------
                 INTEGER FUNCTION LENSTR(LINE)
                 CHARACTER*(*) LINE
                 num = len(line)
                 DO 5 I=num,1,-1
                 IF (LINE(I:I) .NE. ' ') GO TO 10
5     CONTINUE
```

```
       I=0
 10    LENSTR=I
                END

c---------------------------------------------
       SUBROUTINE polcoe(x,y,n,cof)
       INTEGER n,NMAX
       REAL cof(n),x(n),y(n)
       PARAMETER (NMAX=15)
       INTEGER i,j,k
       REAL b,ff,phi,s(NMAX)
       do 11 i=1,n
         s(i)=0.
         cof(i)=0.
 11    continue
       s(n)=-x(1)
       do 13 i=2,n
         do 12 j=n+1-i,n-1
           s(j)=s(j)-x(i)*s(j+1)
 12      continue
         s(n)=s(n)-x(i)
 13    continue
       do 16 j=1,n
         phi=n
         do 14 k=n-1,1,-1
           phi=k*s(k+1)+x(j)*phi
 14      continue
         ff=y(j)/phi
         b=1.
         do 15 k=n,1,-1
           cof(k)=cof(k)+b*ff
           b=s(k)+x(j)*b
 15      continue
 16    continue
       return
       END

C  (C) Copr. 1986-92 Numerical Recipes Software <=-)8.
c---------------------------------------------
c-------------------------------------------------

       subroutine deltacal(fin,del)

c      Subroutine to calculate delta% at all wavelengths. Reads 4 files of expected reflectance
c      from standards at 2%, 40%, 75%, and 100% reflectance (supplied by Labsphere), reads 1
c      file of measured reflectance from these standards. Outputs expected values,
c      and delta% which is expected-measured. This is the first step for the "dark reading error"
c      correction.  12-11-93
c      Last Modified 4-95

               parameter (inum=4,pts=1024)
c              character*120 datform
               real*4 fin(pts,inum),del(pts,inum)
```

```
                real*4 exp(pts,inum)
                real*4 texp(pts,inum)

c-------GET AVERAGE STANDARD DATA
c5    write(6,*)'Enter filename for 2% standard'
c               read(5,'(a)')file2
c               open(51,file=file2,status='old',err=5)
c6    write(6,*)'Enter filename for 40% standard'
c               read(5,'(a)')file40
c               open(52,file=file40,status='old',err=6)
c7    write(6,*)'Enter filename for 75% standard'
c               read(5,'(a)')file75
c     open(53,file=file75,status='old',err=7)
c8    write(6,*)'Enter filename for 100% standard'
c               read(5,'(a)')file100
c               open(54,file=file100,status='old',err=8)
c               write(6,*)'Enter data format'
c               read(5,'(a)')datform

c               do 10 i=1,pts
c                read(51,datform)fin(i,1)
c                read(52,datform)fin(i,2)
c                read(53,datform)fin(i,3)
c                read(54,datform)fin(i,4)
c10    continue

c-------OPEN ABSOLUTE REFLECTANCE FILES (ASCII), FROM LABSPHERE
16    open(21,file='02.abs',status='old',err=14)
     open(22,file='40.abs',status='old',err=14)
     open(23,file='75.abs',status='old',err=14)
     open(24,file='100.abs',status='old',err=14)

c------FORMATS
40    format (2f10.4)
45    format (10x,f10.4)

c-------CHECK 1
     write(6,'(a75)')'  2%     40%     75%     100%'
                write(6,'("Average %reflectance for pixel 500:       ",
   +            4f8.2)')fin(500,1),fin(500,2),
   +    fin(500,3),fin(500,4)

c-------READ ABSOLUTE REFLECTANCE FILES
                do 65 i=1,pts
                 read(21,fmt=45,end=70)exp(i,1)
                 read(22,fmt=45,end=70)exp(i,2)
                 read(23,fmt=45,end=70)exp(i,3)
                 read(24,fmt=45,end=70)exp(i,4)
65    continue

c-------Multiply by 100
                do 66 j=1,inum
                 do 67 i=1,pts
```

```
                    texp(i,j)=100*exp(i,j)
67      continue
66      continue

c-------CHECK 2
        write(6,'("Expected %reflectance for pixel 500:       ",
     +    4f8.2)')texp(500,1),texp(500,2),
     +     texp(500,3),texp(500,4)

c------CALCULATE DEL VALUES
70      do 99 j=1,inum
                    do 100 i=1,pts
                     del(i,j)=(texp(i,j)-fin(i,j))

100     continue
99      continue

c---------CHECK ON SCREEN
                    r02=0
                    r40=0
                    r75=0
                    r100=0
                    do i=495,505
                     r02=r02+del(i,1)
                     r40=r40+del(i,2)
                     r75=r75+del(i,3)
                     r100=r100+del(i,4)
        enddo
                     r02=r02/11.0
                     r40=r40/11.0
                     r75=r75/11.0
                     r100=r100/11.0

        write(6,'("Average ball correction, pixels 495 to 505:",
     +    4f8.2)')r02,r40,r75,r100
        go to 1000

14      write(6,*)'Unable to find .abs file'
                    go to 1000
c15     write (6,*) 'Unable to find .std file'
c                   go to 1000

1000    close(31)
                    return
                    end

c-------------------------------------------------------------
        subroutine deltacor(fin,del,now)

c   Subroutine to calculate polynomial coefficients for delta%reflectance at each wavelength,
c   where delta%reflectance equals
c   (%refl. from digital standardized data) - (%refl. measured for each standard) (at 2%, 40%, 75%,
c    and 100%).  This program will fit a polynomial through four points to calculate the correction
```

```
c    correction coefficients to be used in REFCORRPL to correct for
c    the "dark reading error" correction.   12-11-93
c    Modified: 5-95

           parameter (pts=1024,nwrd=16,inum=4)
           character*80 outfile
           real*4 fin(pts,inum),del(pts,inum)
           real*4 XA(inum),YA(inum),cof(inum)
           character*8 now

c-------CREATE CORRCOEFS.--- FILE
9          outfile='polycoefs.'//now(1:lenstr(now))
           open(33,file=outfile,access='direct',status='unknown',recl=nwrd)

c------CALCULATE ERRORS
           N=4
     do 12 j=1,pts
                   do 13 k=1,inum
       XA(k)=fin(j,k)
                    YA(k)=del(j,k)
13      continue
                   call polcoe(XA,YA,N,cof)
                   write(33,rec=j)cof

12     continue
1000   return
           end

c--------------------------------------------------

     subroutine sdcull(data,nmean,sd,num,icount)

c----- calculates standard deviation of a column of data and replaces
c----- data more than 3 SDs from the mean with -999
c----- Calculates means excluding -999 values.
c     Last Modified 5-95, SEH

                  parameter (icol=1024)
                  real*4 data(icol,icount),sum(icol),sd(icol)
                  real*4 ss(icol),omean(icol),nmean(icol)
                  real*4 min(icol),max(icol)
                  integer*2 num(icol),icount

c-------CALCULATE SDS and MEANS

10      do 11 j=1,icol

c------INITIALIZE

                    sum(j)=0
                  ss(j)=0
                   icount2=0
                   num(j)=0
```

```
c-------MEAN
        do i=1,icount
                    if(data(j,i).gt.-99.0)then
                           sum(j)=sum(j)+data(j,i)
                           icount2=icount2+1
                           endif
        enddo

                    omean(j)=sum(j)/icount2

c-------SUM OF SQUARES and STANDARD DEVIATION
                    do i=1,icount
                     ss(j)=ss(j)+(data(j,i)-omean(j))**2
        enddo

                    sd(j)=(ss(j)/(icount2-1))**0.5

                    max(j)=omean(j)+(3*sd(j))
                    min(j)=omean(j)-(3*sd(j))
c                   max(j)=omean(j)+(2*sd(j))
c                   min(j)=omean(j)-(2*sd(j))

c-------REPLACE DEVIANTS WITH -999

                    do i=1,icount
                           if(data(j,i).gt.max(j).or.data(j,i).lt.min(j)) then
                             data(j,i)=-999.
                             num(j)=num(j)+1

c------Test to see which standard runs are getting culled most frequently
c                            write(6,*)j,i

          endif
        enddo

11                  continue

c-------CALCULATE NEW MEANS

20      do 21 j=1,icol

c------INITIALIZE

                    sum(j)=0
                    icount2=0

c------MEAN
        do i=1,icount
                    if(data(j,i).gt.-99.0)then
                           sum(j)=sum(j)+data(j,i)
                           icount2=icount2+1
```

```
                          endif
           enddo

                       nmean(j)=sum(j)/icount2

21         continue

1000       return
                       end
```

reffixpl.odp.f

```
program reffixpl

c     Program to do refcorr and reffour all at once
c     Uses polynomial fit ball corrections from file polycoefs.---
c     Last modified 5-95

                      character*120 prefix
                      character*1 ans

5                     call refcorr(prefix,num)
                      call reffour(prefix,num)

      write(6,*)'Start again? (y/n)'
                      read(5,'(a)')ans
                      if (ans.eq.'y'.or.ans.eq.'Y') then
                        go to 5
                      endif

                      stop
                      end

c********START OF SUBROUTINES
c*****************************

      subroutine refcorr(prefix,num)

c    Routine to calculate %reflectance from raw counts and to
c    apply all corrections to %reflectance data (black, delta%, and Spectralon)
c    12-12-93. Modified 6-94,7-94, 11-94, 12-94

                      parameter (pts=1024,nwrd=10299,rwrd=2105)
                      character*120 filename,outfile,lisfile,preout,prefix
c                     character*120 reffile
      character*120 polyfile
                      character*170 cmd
                      character*8 adate
                      integer*2 black(pts),fin(pts),light,strain,cond
                      integer*2 site,core,section,topdep,botdep,mark
                      integer*2 leg,count,dis,los,integ
                      real*4 m,b,mbsf,exp,step
```

```
               integer*4 date,time,white(pts),raw(pts)
               character*1 hole,type,sub
               real Spec(pts)
c              character*2 mon,day,yr,mtemp,dtemp,ytemp,hr
c              character*2 htemp
               integer system
c
8     write(6,*) 'Enter 1 to process a single file OR'
     write(6,*) '     2 to process all sections of a core'
               read(5,*)num

c--------- OPEN ONE FILE TO READ-----------------

               if (num.eq.1) then
9                write(6,*) 'Enter .raw filename'
                 read(5,'(a)')filename
                 close(11)
                 open(11,file=filename,access='direct',status='old',
   +      recl=nwrd,err=9)
                 write(6,*) 'Enter output (.ref) filename'
                 read(5,'(a)')outfile
                 close(21)
                 open(21,file=outfile,access='direct',status='unknown',
   +     recl=rwrd)
                 prefix=filename(1:lenstr(filename)-4)
                 go to 20

c---------OR OPEN .lis FILE TO READ A GROUP OF FILES-------

     elseif (num.eq.2) then
12               write(6,*) 'Enter siteholecoretype, e.g. 925a01h'
                 read(5,'(a)')prefix
                 cmd='ls '//prefix(1:lenstr(prefix))//'*.raw >! '
   +       //prefix(1:lenstr(prefix))//'.lis'
                 ier = system(cmd)
                 write(6,'("ier = ",i7)')ier
                 lisfile=prefix(1:lenstr(prefix))//'.lis'
                 close(10)
      open(10,file=lisfile,status='unknown',err=8)
     else
                 goto 8
     endif

c------OPEN OTHER FILES-----------------

c------FIND the LATEST polycoefs.--- file (delta% values)----
20    ier = system('ls polycoefs.* >! coefpl.lis')
               close(33)
               open(33,file='coefpl.lis',status='old')
23             read(33,'(10x,a8)',end=21)adate
      go to 23
21     polyfile='polycoefs.'//adate
                 write(6,'("Corrections are from: ",a)')polyfile
```

```
c-------FORMATS
40      format(1024f6.0)
c41      format(10x,f10.4)
41      format(6x,f10.4)
50      format(100f12.6)
c60      format(41a,50a/1023f6.1)

c---------READ SPECTRALON FILE-----------
c--------CHANGED TO READING AVERAGE EXTERNAL WHITE 'average.white'

35       close(13)
                   open(13,file='average.white',status='old',err=36)
        go to 37
36       write(6,*)'CANNOT FIND FILE average.white'
                   go to 1003

37        do 15 i=1,pts
                   read(13,fmt=41)Spec(i)
15      continue
c----------------------------------------------
       numb=0
       if (num.eq.1) then
        count=1

c---- READ STATEMENT***

22      read(11,rec=count,end=1002)date,time,los,exp,step,integ,
    +      m,b,leg,sub,site,hole,core,type,section,topdep,
    +     botdep,dis,mbsf,light,strain,cond,mark,
    +     (black(i),i=1,pts),
    +     (white(i),i=1,pts),(raw(i),i=1,pts)

c                   call spikecheck(black,white,raw,n)

c                   numb=numb+n

                   call correct(black,white,raw,Spec,fin,polyfile)
                   call spikecheck(fin,n)
                   numb=numb+n

c----- WRITE STATEMENT***
        write(21,rec=count)date,time,los,exp,step,integ,
    +      m,b,leg,sub,site,hole,core,type,section,
    +     topdep,botdep,dis,mbsf,light,strain,cond,mark,fin

                   count=count+1
                  go to 22
                  endif
c----------------------------------------------
      if (num.eq.2) then
26                 count=1
                  read(10,'(a)',end=1000)filename
```

```
                    preout=filename(1:lenstr(filename)-4)
                    outfile=preout(1:lenstr(preout))//'.ref'
                     open(11,file=filename,access='direct',status='old',
     +    recl=nwrd)
                     open(21,file=outfile,access='direct',status='unknown',
     +   recl=rwrd)

c----- READ STATEMENT

24      read(11,rec=count,end=25)date,time,los,exp,step,integ,
     +    m,b,leg,sub,site,hole,core,type,section,topdep,
     +    botdep,dis,mbsf,light,strain,cond,mark,
     +    (black(i),i=1,pts),
     +    (white(i),i=1,pts),(raw(i),i=1,pts)

c                    numb=numb+n

                     call correct(black,white,raw,Spec,fin,polyfile)
                     call spikecheck(fin,n)
                     numb=numb+n

        write(21,rec=count)date,time,los,exp,step,integ,
     +    m,b,leg,sub,site,hole,core,type,section,
     +   topdep,botdep,dis,mbsf,light,strain,cond,mark,fin

                    count=count+1
                     go to 24

25      write(6,30)filename((lenstr(filename)-11):lenstr(filename))
30       format(' Finished file: ',a15)
                    close(21)
                    close(11)
        go to 26
13       write(6,*) 'ERROR reading .lis file'
                     go to 8
                   endif
c
1000    write(6,'("Number of points changed is:",i8)')numb
      go to 1001
1002    write(6,'("Number of points changed is:",i8)')numb
                   close(21)
1001     close(10)
1003     return
                   end

c-----------------------------------------
c     START OF SUBROUTINES FOR REFCORR
c-----------------------------------------

      subroutine spikecheck(fin,n)

c     Modified 7-94 to spikecheck corrected sample spectra
```

```
c       subroutine spikecheck(black,white,raw,n)
c       Checks for spikes within black,white, and sample spectra
c       of a single sample.  Replaces measurements more than 3
c        s.d.'s from the running mean with the running mean.  Counts
c       cumulative number of deviant samples per file (section) and
c        that number is output to the screen in the main program

c       integer*2 black(1024)
c                       integer*4 white(1024),raw(1024)
       integer*2 fin

                        n=0
       call runmean(fin,m)
                        n=n+m
c       call runmean(black,m)
c                       n=n+m
c                       call runmean(white,m)
c                       n=n+m
c                       call runmean(raw,m)
c                       n=n+m
                        return
                        end
c-----------------------------------------------

                        subroutine runmean(temp,num)
                        integer*2 temp(1024)
                        real dat(1024)

c-------CONVERT TO FLOATING PT.
                        do 12 i=1,1024
                         dat(i)=float(temp(i))
12      continue

c-------SET LIMITS for running mean, ilow,ihigh--

                        num=0
                        do 30 i=1,1024
                         ilow = i-5
                         ihigh = i+5
                              if (ilow.lt.1) then
                               ilow = 1
                               ihigh = ilow + 10
          endif
                              if (ihigh.gt.1024) then
                               ihigh = 1024
                               ilow = ihigh - 10
          endif

c-------CALCULATE RUNNING MEAN, SD
                         sum = 0.
                         count = 0.
                         do 19 j=ilow,i-1
                              sum=sum+dat(j)
```

```
                        count = count+1.
19       continue
                  do 20 j=i+1,ihigh
                        sum=sum+dat(j)
                        count = count+1.
20       continue
                  xmean = sum/count
                  ss = 0.
                  do 21 j=ilow,i-1
                   ss=ss+(dat(j)-xmean)**2
21       continue
        do 22 j=i+1,ihigh
                  ss=ss+(dat(j)-xmean)**2
22       continue
                  sd=((1/(count-1))*ss)**0.5

c---------FIND DEVIANTS and replace with mean
                  xmax=xmean+(5*sd)
                  xmin=xmean-(5*sd)
                  if (dat(i).gt.xmax.or.dat(i).lt.xmin) then
                        dat(i)=xmean
                        num=num+1
        endif
30      continue
c---------CONVERT TO INTEGER
                  do 31 i=1,1024
                        temp(i)=int(dat(i))
31      continue

1000     return
                  end

c-----------------------------------------------------
     subroutine correct(black,white,raw,Spec,fin,polyfile)

                  parameter (nmat=16, inum=4, pts=1024)
                  character*80 polyfile
     integer*2 fin(pts),black(pts)
                  integer*4 white(pts),raw(pts)
          real cof(inum),delta
                  real temp(pts),btemp(pts),wtemp(pts),rtemp(pts)
                  real tfin(pts),Spec(pts),corr(pts)

c-------OPEN CORRCOEFS.---
                  open(12,file=polyfile,status='old',access='direct'
   +     ,err=34,recl=nmat)

c-------CONVERT TO FLOATING PT
                  do 12 i=1,pts
                   btemp(i)=float(black(i))
                   wtemp(i)=float(white(i))
                   rtemp(i)=float(raw(i))
12      continue
```

```
c-----CONVERSION from RAW to %, DELTA, and Spectralon corrections--

                  do 30 i=1,pts
                   temp(i)=100*((rtemp(i)-btemp(i))/(wtemp(i)-btemp(i)))

c-------USE NEXT SEVEN LINES TO DO DARK READING ERROR CORRECTIONS
c-------BY (100./Spec(i) (average.white is in %, not fraction)

                   corr(i)=(temp(i))*(100./Spec(i))
                   read(12,rec=i)cof
                   delta=0
                   do 31 k=1,inum
                    delta=delta+(cof(k)*(corr(i)**(k-1)))
31      continue
      tfin(i)=corr(i)+delta

c----USE THIS LINE TO SKIP DARK READING ERROR CORRECTIONS
c                  tfin(i)=(temp(i))*(100./Spec(i))
c-----------------------------------
30    continue
c                 write(6,*)temp(3)
c                 write(6,*)corr(3)
c     write(6,*)tfin(3)

c-------CONVERT BACK TO INTEGER
                  do 13 j=1,pts
                   fin(j)=int(100*tfin(j))
13    continue

c                 write(6,*)fin(3)
                  close(12)
     return

34    write(6,*) 'ERROR opening '//polyfile
                  end

c---------------------------------------------------
     INTEGER FUNCTION LENSTR(LINE)
                  CHARACTER*(*) LINE
                  num = len(line)
     DO 5 I=num,1,-1
                    IF (LINE(I:I) .NE. ' ') GO TO 10
5    CONTINUE
                  I=0
10    LENSTR=I
                  END

c---------------------------------------------------
          subroutine reffour(prefix,imode)

c    After A. Mix's reften program.  Reads section files from refcorr,
```

```
c   outputs ODP header and four %reflectance bands (50nm averages)
c    in the UV, blue, red, and nIR (250-300nm, 450-500nm,650-700nm,
c   900-950nm).  Checks for spikes downcore, marks spikey samples.
c   Plots three bands downcore. These files to be used for barrel sheet plots.
c   Marks spikey samples in .ref and .raw files too.
c   12-12-93. Revised 8-94

        parameter (pts=1024,nraw=10299,nwrd=2105,nref=2105)
        character*120 pre,prefix,filename,outfile,listfile
c       character*20 list
        real tsum(4)
        real*4 m,b,sum(4),dat(pts),mbsf,exp,step
        integer*2 site,core,section,topdep,botdep,mark
        integer*2 light,strain,cond
        integer*2 leg,count,dis,los,integ,temp(pts)
        integer*4 date,time
        character*1 hole,type,sub
        integer icount(4)
        logical makeout

c---- choose manual or auto mode

c       write(6,'(/"Program REFFOUR reads % reflection files",
c   * /" and outputs four, 50nm wide bands")')
c1      write(6,'(/"ENTER 1 for manual file entry")')
c       write(6,'( "     2 to read a file of files")')
c       read(5,*,err=1) imode
c --- get input filename -----------------------------------------------

c    if (imode.eq.1) then
c    if (imode.eq.2) then
c10   write(6,'(/"ENTER data file prefix: ("___".ref)")')
c    read(5,'(a)')prefix
c    elseif (imode.eq.2) then
c11   write(6,'(/"ENTER the Core Prefix, e.g.925a01h ")')
c     read(5,'(a)')list

    if (imode.eq.2) then
     listfile=prefix(1:lenstr(prefix))//'.lis'
                close(15)
     open(15,file=listfile,status='old')
    endif

c --- OPEN FILE for output --LOOP HERE FOR NEXT FILE-------------------

    makeout=.false.
12        if (imode .eq. 2) then
                read(15,'(a)',end=2000) filename
                pre = filename(1:lenstr(filename)-4)
          filename=pre(1:lenstr(pre))//'.ref'
    elseif(imode.eq.1) then
          filename=prefix(1:lenstr(prefix))//'.ref'
         endif
```

```
c         close(11)
          open(11,file=filename,access='direct', status='old',
   +   recl=nwrd,err=13)
          go to 14
13        write(6,'(//" WARNING. FILE ",a,
    *     " NOT FOUND AND SKIPPED"/)')filename(1:lenstr(filename))
          go to 1000

c --- Open file for output sample.

14   if (.not.makeout) then
c       if (imode.eq.2) then
c                             pre=list(1:lenstr(list))
               outfile= prefix(1:lenstr(prefix))//'.four'
c      elseif (imode.eq.1) then
c                     outfile=prefix(1:lenstr(prefix))//'.four'
c       endif
                   close(31)
            open(31,file=outfile,status='unknown')
            makeout = .true.
          endif

c---- nanometer calibration is from variables m and b, read from file
c---- calibration nm = m*(pixel) + b

c         m= -0.6836
c         b= 950.
c** FOR NOW
c         off=0

c---- debug - verify offset
c         write(6,'(" NOTE: offset = ",f10.2)')off

c --- start read/write loop here.

          index = 0
          count=1
c-----READ STATEMENT

20        read(11,rec=count,err=21,end=1000)date,time,los,exp,step,integ,
    +   m,b,leg,sub,site,hole,core,type,section,
    +  topdep,botdep,dis,mbsf,light,strain,cond,mark,temp

c-----CONVERT TO FLOAT
          do 125 i=1,pts
            dat(i)=0.01*(float(temp(i)))
125   continue

    go to 22
21        write(6,'(/" WARNING. ERROR READING LINE ",i3,
    *              " in file ",a," LINE SKIPPED.")')index,
    *              filename(1:lenstr(filename))
```

```
        goto 20
c 22    if (front(1:1) .eq. 'E') goto 1000
c       index=index+1

c--- calculate the four channels

22     inum=0
      do 25 i=1,4
                icount(i)=0
                sum(i)=0
25    continue
      n=1

c     do 33 i=4,1,-1
     do 33 i=1,4
                if (i.eq.1) then
                 x=250.
      elseif (i.eq.2) then
                 x=450.
      elseif (i.eq.3) then
                 x=650.
      elseif (i.eq.4) then
                 x=850.
      endif
           do 30 j=n,pts
             wavelen = (float(j))*m + b
                  if (wavelen.ge.x.and.wavelen.lt.(x+50.)) then
                            inum=inum+1
                            icount(i) = icount(i) +1
                            sum(i) = sum(i) + dat(j)
c         elseif (wavelen.gt.x) then
c                           inum=inum+1
        elseif(wavelen.lt.x) then
                            inum=inum+1
        else
                            go to 32
        endif
30   continue
32         n=inum
33   continue
c
          do 34 i=1,4
                tsum(i) = sum(i)/(float(icount(i)))
34    continue

c --- write the ODP header and the 4 channels

29      format(i4,' _ ',i4,1x,a1,1x,i3,1x,a1,1x,i2,3i6,f8.2,
    +    3i6,i2,4f7.2,i4)
c29      format(i4,' _ ',i4,1x,a1,1x,i3,1x,a1,1x,i2,4i6,i2,4f6.1,i4)
129     format(4f6.1)

      mark=0
```

```
                write(31,fmt=29)leg,site,hole,core,type,section,topdep,
   +    botdep,dis,mbsf,light,strain,cond,mark,(tsum(i),i=1,4),count

c--- go for next sample
            count=count+1
            go to 20
c --- end of this file

1000     numsamples=count-1
         write(6,'(" Lines converted: ",i4)')numsamples
         close(11)

c --- go for next file

         if (imode.eq.2) then
           go to 12
         endif

2000     write (6,'(" Output in file:  ",a)') outfile
                  close(31)
      write (6,*) 'Checking for spikes downcore'
                  call spikecheck2(outfile,inum)
      close(31)

c--------PLOT, ADD THIS IN LATER WHEN DEPTH IS WORKED OUT (or when plotting doesn't
mess up the PC)
c       write(6,*) 'Creating downcore plot'
c                   call refl_barrel3(outfile)
c        close(31)

c--------MARK SPIKEY SAMPLES IN .REF AND .RAW FILES
        if(inum.ne.0)then
                    write(6,*) 'Flagging spikes in .raw and .ref files'
              call retromark(outfile,imode)
                    close(31)
                  endif
         return
         end

c*********************************************
c     SUBROUTINES FOR REFFOUR
c*********************************************

                  SUBROUTINE spikecheck2(outfile,inum)
                  character*120 outfile,dataform,easyform,lisform
                  character*160 cmd
                  character*120 junk
                  real dat(600),datin
                  integer mark(600),count
                  character*150 header
                  character*25 ostuff1,ostuff2
                  integer system
```

```
c------FORMATS WITH f7.2 ARE NEW, FORMATS WITH f6.1 ARE OLD (USE FOR BREMEN
DATA)
c                  data dataform /'(a66,i2,a12,f6.1,a6,i4)'/
                   data dataform /'(a66,i2,a14,f7.2,a7,i4)'/
c                  data easyform /'(80x,f6.1)'/
                   data easyform /'(82x,f7.2)'/
c                   data dataform /'(a30,i2,a12,f6.1,a6,i4)'/
c      data easyform /'(44x,f6.1)'/
      data lisform /'(a66,i2,i5)'/
c
c                  close(21)
c                  close(22)
c                  close(23)
                   ier=system('rm tempfile')
                   write(6,'("ier = ",i7)')ier
                   open(21,file=outfile,status='old')
                   open(22,file='tempfile',status='unknown')
                   open(23,file='spike.lis',status='unknown')
11     read(23,'(a)',end=12)junk
                   go to 11
c
c-------READ .FOUR FILE
12       i=0
20    read(21,easyform,end=30)dat(i+1)
            mark(i+1)=0
            i=i+1
            go to 20
c-------CALCULATE MEAN, SD, MARKS--
30     n=i
                   call runmean2(dat,n,mark,inum)
                   write(6,'(" Number of samples flagged is: ",i5)')inum

c------ASSIGN MARKS AND WRITE TO OUTPUT FILE
                   rewind(21)
                   do 40 k=1,n
                    read(21,dataform,end=500)header,imark,ostuff1,datin,ostuff2,count
                            if (mark(k).ne.0) then
          write(23,lisform)header,mark(k),count
        endif
                             imark=mark(k)
                            write(22,dataform)header,imark,ostuff1,datin,ostuff2,count
40       continue
500     cmd='cp tempfile '//outfile
                   ier=system(cmd)
                   write(6,'("ier = ",i7)')ier

      return
                   end

c--------------------------------------------------
                   SUBROUTINE runmean2(dat,n,xmark,inum)
c------routine cycles through 2 times
```

```
                          real dat(600)
                          integer xmark(600)

c---------SET LIMITS FOR RUNNING MEAN, ILOW,IHIGH

                          inum=0
                          do 40 k=1,2
                          do 30 i=1,n
                            ilow = i-5
                            ihigh = i+5
                                      if (ilow.lt.1) then
                                      ilow = 1
                                      ihigh = ilow + 10
             endif
                                      if (ihigh.gt.n) then
                                      ihigh = n
                                      ilow = ihigh - 10
                                      endif

c-------CALCULATE RUNNING MEAN, SD
                             sum = 0.
                             count = 0.
                             do 19 j=ilow,(i-1)
                                      if (xmark(j).eq.0) then
                                sum=sum+dat(j)
                                 count = count+1.
             endif
19           continue
                             do 20 j=(i+1),ihigh
                                      if (xmark(j).eq.0) then
                                sum=sum+dat(j)
                                 count = count+1.
                             endif
20           continue
                             xmean = sum/count
                             ss = 0.
                             do 21 j=ilow,(i-1)
                                      if (xmark(j).eq.0) then
                               ss=ss+(dat(j)-xmean)**2
                             endif
21           continue
                             do 22 j=(i+1),ihigh
                                      if (xmark(j).eq.0) then
                               ss=ss+(dat(j)-xmean)**2
                             endif
22           continue
                            sd=((1/(count-1))*ss)**0.5

c--------FIND DEVIANTS AND MARK WITH A 1 OR A 2
c--------1= first culls, 2=second culls

                            xmax=xmean+(5*sd)
```

```
                    xmin=xmean-(5*sd)
                    if(dat(i).gt.xmax.or.dat(i).lt.xmin) then
                            if (xmark(i).eq.0) then
                      xmark(i)=k
                      inum=inum+1
                            endif
                    endif
30      continue
40      continue
1000     return
                  end

c-----------------------------------------
          subroutine refl_barrel3(junk)

c  Plots four reflectance bands versus depth in core
c  After ACM's color_barrel.  Last modified 12-94
c  Uses plotting program "gri".

            character*120 junk,dataform,prefix
            integer mark
            integer system

      close(20)
            open(20,file='gri.barrel',status='unknown')
            ier = system('rm tempplot')
            write(6,'("ier = ",i7)')ier
      close(19)
            open(19,file='tempplot', status='unknown')

                  data dataform /'(40x,f8.2,18x,i2,4f7.2)'/
c         start with basic plot commands

            write(20,'(a)')'set page landscape'
            write(20,'(a)')'set x name "Depth (mbsf)"'
            write(20,'(a)')'set y name "% Reflectance"'
            write(20,'(a)')'set x margin 4'
            write(20,'(a)')'set y margin 8'
            write(20,'(a)')'set line width 0.45'
c           write(20,'(a)')'set x axis 0 10 1 0.25'
            write(20,'(a)')'set clip on'
            write(20,'(a)')'set x size 21'
            write(20,'(a)')'set y size 7'

c         OPEN DATA FILE

            prefix=junk(1:lenstr(junk)-5)
            open(11,file=junk,status='old',err=10)
            go to 15

10     write(6,*) 'ERROR READING .four file'
      go to 1000
```

```
c-------CHECK FOR MARKED SAMPLES
15       read(11,dataform,end=17)depth,mark,data1,data2,data3,data4
          if (mark.ne.0) then
          go to 15
          else
          write(19,'(f8.2,4f6.1)')depth,data1,data2,data3,data4
          go to 15
          endif
17        close(19)

         write(20,'(a)')'open tempplot'
         write(20,'(a)')'read columns x * * y'
         write(20,'(a)')'.bottom. = {rpn -10.0 column_min(y) +}'
         write(20,'(a)')'.top. = {rpn 6.0 column_max(y) +}'
         write(20,'(a)')'set y axis .bottom. .top. 5 2.5'
         write(20,'(a)')'.low. = column_min(x)'
         write(20,'(a)')'.high. = {rpn 10.0 column_min(x) +}'
         write(20,'(a)')'set x axis .low. .high. 1.0 0.25'
         write(20,'(a)')'set dash 1'

         write(20,'(a)')'draw axes 1'
         write(20,'(a)')'draw curve'
         write(20,'(a)')'draw line legend "650-700 nm" at 17 16 cm 2'
         write(20,'(a)')'rewind'
         write(20,'(a)')'read columns x * y'
         write(20,'(a)')'set dash 0'
         write(20,'(a)')'draw curve'
         write(20,'(a)')'rewind'
         write(20,'(a)')'draw line legend "450-500 nm" at 17 16.5 cm 2'
         write(20,'(a)')'read columns x y'
         write(20,'(a)')'set dash 3'
         write(20,'(a)')'draw curve'
         write(20,'(a)')'rewind'
         write(20,'(a)')'draw line legend "250-300 nm" at 17 17 cm 2'
         write(20,'(a)')'read columns x * * * y'
    write(20,'(a)')'draw label " '//prefix(1:lenstr(prefix))//
   +    '" centered at 14.5 15.5 cm'
         write(20,'(a)')'set dash 2'
         write(20,'(a)')'draw curve'
         write(20,'(a)')'draw line legend "850-900 nm" at 17 15.5 cm 2'
         write(20,'(a)')'quit'
200      close(20)
         close(10)

         ier = system('gri gri.barrel barrel.ps')
         write(6,'("ier = ",i7)')ier
c        ier = system('lpr -Prm244 barrel.ps')

1000   return
         end

c--------------------------------
    subroutine retromark(fourfile,imode)
```

```
c     Program to mark .raw and .ref files for deviant
c     deviant downcore samples.  Reads .four files for
c     mark.ne.0 and section number. Finds samples in .raw
c     and .ref files
c     and marks them also.  12-17-93.

                    parameter (nraw=10299,nref=2105,pts=1024)
                    character*120 fourfile,rawfile,reffile
                    character*120 prefix
                    character*1 hole,type,sect,sub
                    integer*4 date,time,white(pts),dat(pts)
                    integer*2 los,integ,leg,site,core
                    integer*2 black(pts)
                    integer*2 rdat(pts),light,strain,cond
                    integer*2 section,topdep,botdep,dis
                    integer*2 omark,mark,count
                    real*4 m,b,mbsf,exp,step

c50    format(21x,a1,45x,i1,24x,i4)
50    format(21x,a1,45x,i1,28x,i4)

                    prefix=fourfile(1:lenstr(fourfile)-5)
                    close(31)
                    open(31,file=fourfile,status='old',err=8)
                    go to 9

c--------ERROR MESSAGES
7      write(6,'("ERROR- Cant find",a14," or ",
   +      a14)')rawfile,reffile
                    go to 1000
8     write(6,'("ERROR- Cant find ",a14)')fourfile
      go to 1000

c--------
9     read(31,fmt=50,end=1000)sect,mark,count

c--------CHECK MARK-----
      if (mark.eq.0) then
                    go to 9
      endif
c--------IF MARKED, OPEN .raw and .ref FILES---

                         if(imode.eq.1) then
                         rawfile=prefix(1:lenstr(prefix))//'.raw'
                         reffile=prefix(1:lenstr(prefix))//'.ref'
        else
                     rawfile=prefix(1:lenstr(prefix))//sect//'.raw'
       reffile=prefix(1:lenstr(prefix))//sect//'.ref'
                         endif

20                  open(12,file=rawfile,access='direct',recl=nraw
   +      ,status='old',err=7)
```

```
                open(13,file=reffile,access='direct',recl=nref
     +          ,status='old',err=7)

c-----ADD MARKS TO .RAW AND REF FILES---
        read(12,rec=count,err=900)date,time,los,exp,step,integ,
     +      m,b,leg,sub,site,hole,core,type,section,topdep,
     +      botdep,dis,mbsf,light,strain,cond,omark,
     +      black,white,dat
          omark=mark
        write(12,rec=count)date,time,los,exp,step,integ,
     +      m,b,leg,sub,site,hole,core,type,section,topdep,
     +      botdep,dis,mbsf,light,strain,cond,omark,
     +      black,white,dat
        read(13,rec=count,err=901)date,time,los,exp,step,integ,
     +      m,b,leg,sub,site,hole,core,type,section,topdep,
     +      botdep,dis,mbsf,light,strain,cond,omark,rdat
          omark=mark
        write(13,rec=count)date,time,los,exp,step,integ,
     +      m,b,leg,sub,site,hole,core,type,section,topdep,
     +      botdep,dis,mbsf,light,strain,cond,omark,rdat

c--------
                close(12)
                close(13)
        go to 9

900     write(6,'("ERROR reading direct access file")')
901     write(6,'("ERROR reading .ref file")')
1000    close(31)
                return
                end
```

band_avg154.lis.f

```
program band_avg
c
c    THIS IS IDENTICAL TO BAND_AVG154.F EXCEPT THAT *.REF FILENAMES
C     ARE READ FROM A LISTFILE AND ALL OUTPUT IS PUT INTO ONE LARGE
C     FILE
C
c    This program will smooth % reflectance data by binning
c    raw %reflectance into user chosen bins.  First derivatives
c    are subsequently calculated by a centered technique, resulting
c    in a bandwidth 2*bin width.  The number of first derivative
c    bands calculated is 2 less than the number of reflectance
c    bands, because the endpoints cannot be calculated.
c
c    Input files are Direct Access *.ref files with Leg 154 formats
c
c    Output files are ASCII
c    Options for output are:
c    1) each sample gets (#bands+1) lines (1 header) and three columns
```

```
c        which are: lambda, %reflectance, 1st deriv.
c         (Useful for plotting)
c         With this option, the first and last first derivative points
c         are set to zero.  Ignore them.
c      2) each sample gets one line (header, %reflectance, 1st derivs)
c         (Useful for estimations)
c         With this option, the number of first derivative bands is 2
c        less than the number of reflectance bands, so the first derivative
c        band corresponds to the 2nd center wavelength.
c
c      SEH, Last Modified 12-96
c
c      This program came about from tests done by Joe Ortiz and me in
c      November and Devember, 1996.  The tests and results are documented
c      in /home/tahiti/paleo3/sara/leg154/specdat/smoothtests/conclusions
c      with text in file derivatives.summary and 8 figures
c
C       SEE PROGRAM SMFFT_BANDS154 FOR THE VERSATILE VERSION OF THIS
PROGRAM
c      SEE PROGRAM BANDS_AVG154 FOR THE VERSION OF THIS PROGRAM WITHOUT
INPUT
C       OF A LIST FILE.

c **********************************************************************
            parameter (nref=2105,npts=1024)
      real*4 spectra(npts),first(npts),x(npts)
            character*120 filein,fileout,fmtout,lisfile
            character*1 ans
            real*4 m,b,exp,step,mbsf
            integer*2 site,core,section,topdep,botdep,mark
            integer*2 leg,dis,los,integ,light,strain,cond
            integer*2 tspectra(npts)
            integer*4 date,time,num
            character*1 hole,type,sub
            character*4 cnum
            integer option
            real lambda(npts)
            common width,ocent,x,num

c     CALCULATE NANOMETER WAVELENGTHS (x) of each pixel (npts pixels).

                  do i = 1, npts
         x(i)=0.6836 * i + 249.3164
       enddo

      write(6,*)'BAND_AVG154 calculates band averaged reflectance'
                write(6,*)' data, then calculates first derivatives from'
                write(6,*)' the band averages. Input data should be'
                write(6,*)' direct access, binary files of the'
                write(6,*)' form of .ref files from Leg 154'

5        write (6,'(/"Enter list filename containing a list")')
                write (6,*)'   of *.ref files'
```

```
      read(5,'(a)')lisfile
                  open(31,file=lisfile,status='old',err=5)

c------CHOOSE OUTPUT OPTION
                  write(6,*)'Enter "1" to output three columns for'
                  write(6,*)'  each sample, OR'
                  write(6,*)'Enter "2" to output each sample plus'
                  write(6,*)'  first derivative on one line'
                  read(5,*)option
      write (6,'(/"Enter output filename")')
                  read (5,'(a)')fileout
                  open (12,file=fileout,status='unknown')

c------CHOOSE BAND WIDTH AND CENTER WAVELENGTHS
                   write (6,'(/"Enter band width for averaging (nm)")')
                   write(6,*)'      10 recommended'
                   read (5,*)width
11      write(6,'(/"Enter centerpoint of first band (>250nm)")')
       write(6,*)'      255 recommended'
                   read(5,*)ocent

                   if (ocent.lt.250) then
                    go to 11
                   endif

                   num=700.0064/width

c----- GET NUMBER OF BANDS IN CHARACTERS (for output format).  This is ridiculous!
                   open(21,file='temp',status='unknown')
                   write(21,'(i4)')num
                   close(21)
                   open(21,file='temp',status='unknown')
                   read(21,'(a4)')cnum
                   close(21)
c---------------------------
                   write(6,'(/"The number of averaged bands is:",i5)')num
          write(6,'("The number of 1st derivative bands is:",i5)')(num-2)

c------CALCULATE CENTER WAVELENGTHS FOR AVERAGED BANDS
                   do i=1,num
                    lambda(i)=((i-1)*width)+ocent
                   enddo

c-------READ DA FILES
6                 read (31,'(a)',end=1000)filein
      write(6,'(a16,a80)')'PROCESSING FILE ',filein
                  close(11)
                  open (11,file=filein,status='old',access='direct',
   +   recl=nref,err=7)

                  go to 8
7     write(6,'(a5,a80,a10)')'FILE ',filein,' NOT FOUND'
      go to 6
```

```
8      icount=1
10     read (11,rec=icount,end=6)date,time,los,exp,integ,step,
    +   m,b,leg,sub,site,hole,core,type,section,
    +   topdep,botdep,dis,mbsf,cond,strain,light,mark,
    +   (tspectra(i),i=1,npts)

c-----CONVERT TO FLOATING POINT
       do 12 i=1,npts
                   spectra(i) = 0.01*(float(tspectra(i)))
12     continue

c------BAND AVERAGING
                   call bands154(spectra)

c-------CALCULATE CENTERED FIRST DERIVATIVES
c-------first(1) and first(num) = 0 as placeholders only
                   first(1)=0.0
                   first(num)=0.0
                   do 16 i=2,num-1
                    first(i) = (spectra(i+1)-spectra(i-1))/(2*width)
16       enddo

c-------OUTPUT FILE FORMATS
100     format(i4,i4,a1,i3,a1,i1,2i4)
       fmtout='(i4,i4,a1,i3,a1,i1,2i4,f7.2,i4,'
    +     //cnum//'f7.2,'//cnum//'f8.4)'

c-------OUTPUT FILE OPTION 1 (columns)
           if (option.eq.1) then
            write (12,fmt=100)leg,site,hole,core,type,section,topdep,botdep
            write (12,'(3f10.4)')(lambda(i),spectra(i),first(i),i=1,num)

c-------OUTPUT FILE OPTION 2 (lines)
           elseif(option.eq.2)then
                  write(12,fmtout)leg,site,hole,core,type,section,topdep,botdep
    +   ,mbsf,mark,(spectra(i),i=1,num),(first(i),i=2,(num-1))

           endif
           icount=icount+1
           go to 10

c-------OUTPUT START AND END WAVELENGTHS TO SCREEN
1000     write(6,'("Starting wavelength for reflectance bands:",f9.4)')lambda(1)
                  write(6,'("Ending wavelength for reflectance bands:",f9.4)')lambda(num)
                  write(6,'("Starting wavelength for derivative bands:",f9.4)')lambda(2)
                  write(6,'("Ending wavelength for derivative bands:",f9.4)')lambda(num-1)

      write(6,*)'Start again? (y/n)'
                  read(5,'(a)')ans
                  if(ans.eq.'y'.or.ans.eq.'Y')then
                    go to 5
                  endif
```

```
                    stop
            end

c  ******************************************************
c   START OF SUBROUTINES
c  ******************************************************
c
      subroutine bands154(block)

c   program to average reflectance bands of user-chosen widths,
c   or by user-chosen total number of bands.
c   Last Modified 12-96

            parameter (pts=1024)
             integer num
            real cent,width,end1,end2,ocent
            real block(pts)
            real x(pts)
            common width,ocent,x,num

c------ INITIALIZE
                    cent=ocent
                    i=1
                    sum=0.0
                    count=0.0

c------CALCULATE BAND AVERAGES
                    do 25 j=1,pts
        end1=cent-(0.5*width)
                     end2=cent+(0.5*width)
        if(x(j).ge.end1.and.x(j).lt.end2) then
                              sum=sum+block(j)
                              count=count+1
        endif

        if(x(j).ge.end2.or.j.eq.pts)then
         if(count.gt.0)then
                       block(i)=sum/count
                              sum=block(j)
                              i=i+1
                              count=1
                              cent=cent+width
                      else
                       write(6,*)'OUTSIDE WAVELENGTH RANGE'
         endif
        endif

25      continue

1000   return
          end
```